THREE DIMENSIONAL IMAGE STRUCTURE IN IN-LINE FRAUNHOFER HOLOGRAPHY

A Thesis presented for the partial fulfilment of the requirements for the degree of

DOCTOR OF PHILOSOPHY

(OCTOBER 1991)

SUBMITTED BY: **ABDUL RAOUF**

DEPARTMENT OF PHYSICS,

BRUNEL, THE UNIVERSITY OF WEST LONDON,

UXBRIDGE, MIDDLESEX, UB8 3PH, U.K.

To my beloved parents

TABLE OF CONTENTS

LIST OF FIGURES

LIST OF TABLES

LIST OF SYMBOLS

a	Radius of the particle or disc.
$A_{(x,y)}$	Object describing parameter.
2b	Center to center separation of the discs in a pair.
c	Velocity of light
C_d	Diameter of the discs in group C
C_s	Separation between the inner edges of the discs of group C1 and C2.
d_b	Diameter of the laser beam.
d_c	Diameter of the collimating lens.
d_f	Diameter of the focusing lens.
D_p	Diameter of the pinhole.
D	Density of the emulsion after development.
E	Exposure.
$E_{(x,y)}$	Irradiance of the wave.
f	Focal length of the focusing lens.
F	Focal length of the collimating lens.
G=kH	A multiplication factor.
H	Maximum limit of the aperture.
$I_{max(\theta)}$	Maximum intensity at position θ.
$I_{min(\theta)}$	Minimum intensity at position θ.
$k=2\pi/\lambda$	The wave number.
K_a	Parameter of spherical aberration of the focusing lens Its value for a He-Ne laser (λ=633 nm) is 0.27
L	Length of the laser cavity.
L_H	Coherence length of the laser.
N	Number of far-field distance.
$N_{(extrema)}$	Number of extrema within the image of an individual disc.
$N_{(peaks)}$	Number of peaks within the separation of the discs.

$O_{(x,y)}$	Object wave.
r	Radial distance in the hologram plane.
R	Radial distance in the image plane.
R_s	Resolution of the hologram.
R_o	Reference wave.
t	Coherence time of the laser.
T	Exposure time.
T_o	Constant background in the reconstruction of an in-line hologram.
T_a	Amplitude transmittance.
U	Focusing parameter.
$W_{(edg.)}$	Measurement between the outer most peaks of the image.
$W_{(25\%)}$	Measurement of the image at 25% of its central intensity.
$W_{(50\%)}$	Measurement of the image at 50% of its average intensity.
Z	Depth of the field of in-line hologram.
Z_1	Recording distance of the object from the hologram.
Z_2	Reconstruction distance of the image from the hologram.
$\Delta Z=0$	The focusing condition.
β	Slope of the Ta/E curve.
γ	Slope of the H/D curve.
Ω	Limiting aperture parameter.
ρ	Describe position in the aperture and varies from -1 to +1.
ϕ	Phase difference.
ϕ'	Width of a thin wire.
Φ	Output power of the laser.
$\Psi_{(x,y)}$	Amplitude of the wave.
η_t	Power transfer efficiency of the laser.
θ'_1	Radial component of vector r in hologram plane.
θ'_2	Radial component of vector R in image plane.

ACKNOWLEDGEMENTS

All praise to God, almighty, sustainer of the word, the merciful and kind who enabled me to complete this work. Blessing and peace be upon Jesus, Moses, and the last prophet Muhammad whom God sent for the guidance to mankind to manifest his extreme mercy.

I should like to express my deep appreciation and gratitude to my supervisor Dr. Peter R. Hobson for his supervision, guidance and great patience throughout this project. I am also very grateful to Dr. Chang for his guidance to the experimental work. I am thankful to Prof. D. C. Imrie, Head of the Physics Department for his supervision of all the facilities.

I appreciate the technical assistance and cooperation of Mr. K. Schlachter, Mr. L. E. L. Chandrasekera, Mr. L. A. Lightowler, Mr. C. Selby, and Mr. T. Purser of the Physics Department.

I wish to give my sincerest respect and appreciation to my parents for their affection and encouragement. I also thank my wife for her love and continuing inspiration especially during difficulties and disappointments in my research work.

Finally I am grateful to the Government of Pakistan for the award of S&T scholarship and SUPARCO for the grant of leave for this period of research.

The thesis is written using Macwrite 5.0 on an Apple Macintosh, the 1-D plots are produced using PAW (CERN) and the 2-D plots are produced by using UNIRAS V6.2.

ABSTRACT

In this thesis a new theoretical model for the three dimensional images from a finite aperture in-line Fraunhofer hologram is presented. Existing work only deals with the case of single object, in this thesis this work has been extended to the case of two identical coplanar discs. The resulting image equation is solved numerically for several different limiting apertures and their results are compared with the image intensity data from the holograms recorded on Agfa 8E 75HD film. Excellent quantitative agreement is found, verifying the theoretical predictions.

Three different criteria for determining the disc diameter and disc separation describing their errors are discussed for both numerical and experimental data.

A data acquisition system based upon a digital interfaced with a PC, and high resolution video camera is described.

CHAPTER 1

INTRODUCTION

In-line Fraunhofer holography is an established technique for the study of small particles (upto a few hundred microns in diameter) because it provides a three dimensional image of the object particle. To utilise this technique a hologram is made of the volume containing the particles of interest. This hologram is then replayed to form images of the particles which can then be studied at leisure. This approach is particularly useful when a transient event is to be analysed and the exact location of the particle of interest is not known for example the location of bubbles in bubble chamber experiments or the location of tiny droplets in fog studies. This technique is often discussed in the literature and a recent review [**Hobson P. R. (1988)**] gives a useful bibliography of the many contributions to this field up to that time.

Several models have been constructed to describe the particle images using this technique. Some has been reported so far in which resolving all the three spatial co-ordinates with equal accuracy was important i.e. **Belz and Shofner (1972), Tyler**

and Thompson (1976), Cartwright (1980), Thompson and Malyak (1985) and Schaub (1989). All these imaging models are based on the analysis of a single particle and are only concerned with measuring the size and position of the particle.

Because of the desire to develop a new system capable of resolving the size as well as the separation of small particles in a precise manner, the in-line Fraunhofer hologram formation and reconstruction process for more than one target particle was investigated. The work describe in this thesis is an extension of existing theory enabling the simultaneous measurement of radius and separation of the particles in a precise manner.

A standard way of analysing a system of small particles is to view it directly with a microscope but a holographic imaging system is comparatively better because of its larger depth of field. It has an extra advantage that short lived particles and particles whose position is not known in advance can also be analysed [**Belz R. A (1971)**].

If the target object is illuminated with a coherent wave and the amplitude as well as the phase of the diffracted field is recorded on any recording medium, usually a photographic film, a hologram is formed. A great deal of information concerning the

original object can be obtained by illuminating the hologram with same coherent wave and the reconstructed image can be studied in detail.

It is important to note that far-field holography uses an in-line geometry and no off axis reference beam is required. The reference beam is obtained naturally by the propagation phenomenon responsible for the formation of the hologram and this greatly simplifies the experimental implementation of the technique. The only requirement concerning the geometry is that the hologram must be recorded several far field distances away from the objects of interest and the volume containing the particles of interest is mainly transparent. This is not a limiting constraint unless the objects are larger than few hundred microns in diameter when optical wavelengths are used.

The image model of **Belz and Shofner (1972)** is one of the earliest successful attempts to explain the recording and reconstruction process in mathematical terms having good agreement with the experimental results. They also investigated the effects of the limiting aperture on the resolution, but their mathematical model was restricted to one object only. In this thesis, their image model is extended to more than one recorded

object and various algorithms, such as limiting aperture effect and focal tolerance, are tested. All the mathematical details concerning the recording and the reconstruction phenomena are discussed in Chapter 3. The mathematical results are plotted to test different algorithms. The exact method of computation is discussed in Chapter 5.

The images from holograms of a precision test object were acquired with computer controlled digital oscilloscope by placing a video camera in the hologram plane. The reconstructed images were digitised and analysed on computer where theoretically measured algorithms were tested on real images. All the details of experimental procedure are discussed in Chapter 4.

Chapter 5 gives a comparison between theoretically obtained and experimentally achieved results, and these results are discussed in Chapter 6. Chapter 7 summaries this work and discusses the possibilities of future work in this area of research.

CHAPTER 2

HOLOGRAPHY

Holography was invented by Prof. Denis Gabor in 1947 when he was working to improve the resolution of electron microscope, and is a combination of two Greek words "Holos" and "Graphein" meaning complete writing. It is an exciting technique, developed to furnish dramatic realism in photography, micro-measurements, scientific analysis and to provide a unique memory for a vast amount of information.

Because of its growth and many applications it has become one of the most important area of modern optics. The formation of three dimensional images that gives an impression of true relief is certainly one of the spectacular achievements of holography.

Although different techniques for recording and replay of holograms have been developed, yet they may be classified into two main categories.

i. On-Axis Holography

ii. Off-Axis Holography

2.1 ON-AXIS HOLOGRAPHY

On-axis holography is the first technique which was used by Gabor and is used for transparent objects. In this technique the object is illuminated by a coherent light source. The transmitted light consists of two parts. The first part is a strong plane wave corresponding to the directly transmitted light and is known as the reference wave. The second part is a weak scattered wave due to the object and is known as the object wave.

The complex interference pattern of the two waves is recorded on the photographic film and is given by:

$$E_{(x,y)} = \left|R_o + O_{(x,y)}\right|^2 = R_o^{\,2} + \left|O_{(x,y)}\right|^2 + R_o O_{(x,y)} + R_o O^{*}_{(x,y)} \qquad .....(2.1.1)$$

where R_o is the plane reference wave, in actual experiment the collimated beam from the laser is Gaussian in nature. The central portion of this wave is considered to be approximately a plane wave and is used in the experiments. The $O_{(x,y)}$ is the object wave and $O^{*}_{(x,y)}$ is its complex conjugate.

If the film is processed such that its amplitude transmittance (T_a) is a linear function of intensity and is given by:

$$T_a = T_o + \beta T E_{(x,y)} = T_o + \beta T\left[R_o^{\,2} + \left|O_{(x,y)}\right|^2 + R_o O_{(x,y)} + R_o O^{*}_{(x,y)}\right] \qquad .....(2.1.2)$$

where T_o is a constant background transmittance, T is an exposure time, and β is a slope of the Ta/E curve which is explained later in the chapter.

This developed photographic film is the hologram and when this hologram is illuminated with the same reference wave, the complex amplitude transmitted through the hologram is given by:

$$\Psi_{(x,y)} = R_o.T_a = R_o (T_o + \beta T R_o^2) + \beta T R_o \left|O_{(x,y)}\right|^2 + \beta T R_o^2 . O_{(x,y)} + \beta T R_o^2 . O^*_{(x,y)} \quad .....(2.1.3)$$

The term $R_o(T_o + \beta T R_o^2)$ is a uniform attenuated plane wave transmitted directly through the hologram and acts as a coherent background.

In on-axis holography at least 80% incident wave passes un diffracted through the object sample hence the object wave is small compared to the reference wave. The second term is the attenuated object wave, which is thus very small compared to the other terms and can be neglected.

The term $\beta T R_o^2 O_{(x,y)}$ is the original wave from the object multiplied by a constant factor and is responsible for the reconstruction of the virtual image which forms at the same distance from the hologram as the object was from the

photographic film.

The term $\beta TR_o^2O^*_{(x,y)}$ corresponds to a wavefront which resembles the wavefront diverging from the object, and is responsible for reconstruction of real image. Hence real and virtual images of the object are simultaneously formed on either sides of the hologram and there is no angular separation between them, that is an observer focusing on one image actually sees it superimposed on the out of focus twin image.

The recording and reconstruction process is shown in figure (2.1.1).

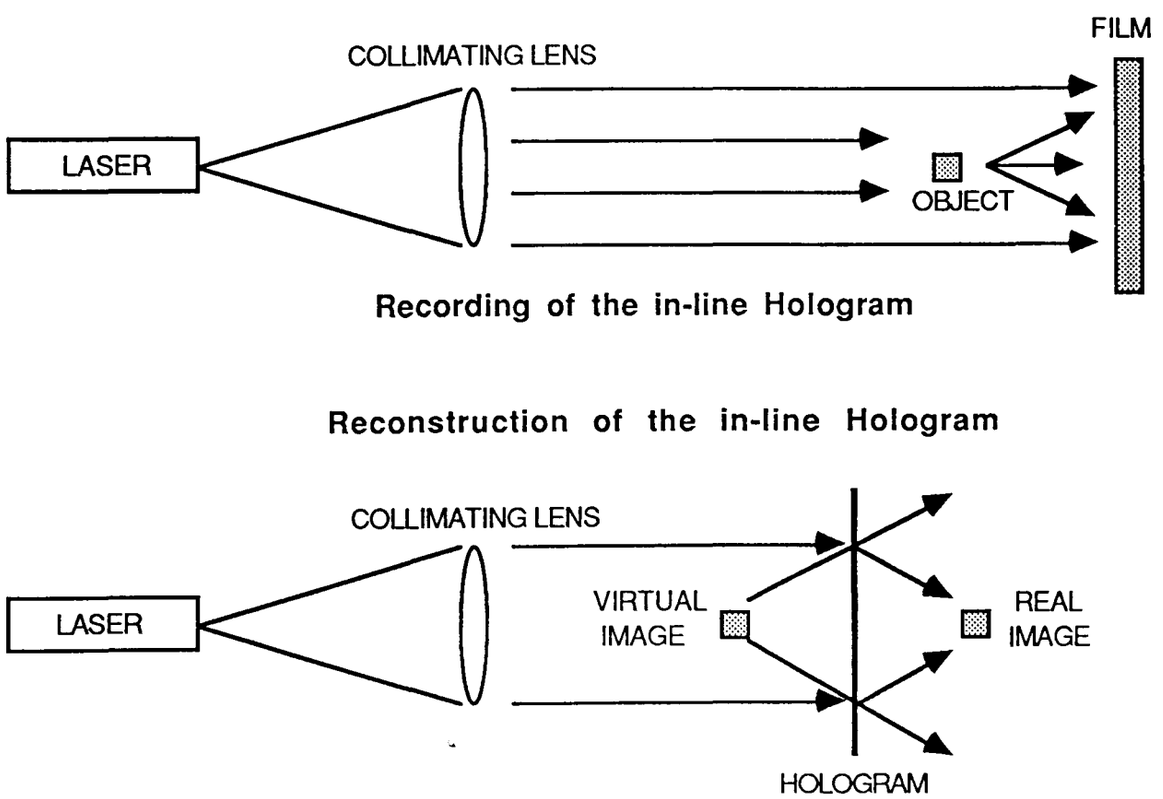

FIG. (2.1.1) Recording and reconstruction of an in-line hologram.

On-Axis holography has its own advantages and disadvantages.

i. On-Axis systems generally use fewer components and occupy smaller table area than off-axis systems.

ii. For an on-axis system, the object and reference beam are practically one beam, thus, alignment of on-axis systems is less critical than the alignment of off-axis systems.

iii. To make a good on-axis hologram at least 80% of the light passing through the object area must be un diffracted. Thus object size and object density will affect the quality of the hologram where off-axis holograms can handle higher object densities **[Witherow W. K. (1979)]**.

iv. On-Axis holograms are harder to view with naked eye than off-axis holograms, mainly due to the fact that angular viewing range is so small.

v. The frequency of the interference fringes recorded on the hologram decreases as the angle between the reference wave and the object wave decreases. Hence, the film resolution is minimised for the case of on-axis holography.

2.2 IN-LINE FRAUNHOFER HOLOGRAPHY

In-Line Fraunhofer holography is confined to the situation where far-field condition is satisfied by the individual objects while the limiting aperture of the whole sample is still in near-field. If a is the radius of a circular disc illuminated by a light of wavelength λ, one far-field is given by $N = 4a^2/\lambda$ [**Robert E. R (1970)**]. If a particle of radius (a =75.0 μm) is illuminated with a He-Ne laser of wavelength (λ=633.0 nm), one far-field distance will be about (N=35.5 mm). For in-line Fraunhofer holography, the object to be recorded must be several far-fields away from the the film plane.

Fraunhofer diffraction patterns with coherent background were discussed by **Parrent and Thompson (1964)** and later the term Fraunhofer hologram was introduced by **Thompson (1965)** to describe this particular type of hologram.

DeVelis J. B. et al.(1966) showed that the effects of the virtual image on the real image were minimal if we remain in the far-field of the individual object, however, the method discussed by them has very little applicability to bigger objects because of the greater far-field distance for such objects. e.g. if a disc of radius (a =1.0 mm) is illuminated with a He-Ne laser of

wave length (λ=633 nm), one far-field distance will be about 6.3 m.

Belz and Shofner (1972) gave an alternative approach to the particle size analysis by investigating the intensity in the neighbourhood of the real image reconstructed from an in-line Fraunhofer hologram. They also included the effects of a limited hologram aperture and focal tolerance to their discussion. It was found theoretically that the minimum error in size measurement occurs when the image is measured where the edge intensity is 25% of the centre intensity. However because of the experimental limitations, real measurements were taken at 50% of the average intensity and proved to have only small errors. The focal tolerance of the aperture limited holograms was found comparable to that of thin lens of equal aperture. The reconstructed images have characteristics that depend upon the amount of information recorded on the hologram, however the amount of information recorded on the hologram could be determined by the film, recording distance, and other recording parameters.

Tyler and Thompson(1976) discussed Fraunhofer holography involving one and two dimensional apertures in detail. This was accomplished by treating the hologram as a diffracting aperture of finite extent, yielding a complete analytical

description of the reconstructed field associated with a Fraunhofer hologram. They showed theoretically that the reconstructed images can be obtained by convolving the Fourier transform of a combined envelope function of finite aperture and film resolution, with the object distribution, but the image obtained is degraded in quality. With coherent illumination, this degradation manifests itself as edge ringing. With partially coherent illumination, edge ringing is not present. They suggested the use of mercury arc in reconstruction from Fraunhofer holograms rather than a laser.

Vikram C. S.(1984-a) has shown that as the image is usually viewed with a video camera, it is highly desirable to have high image contrast. In Fraunhofer holography the contrast depends upon the recording distance and it is fairly close to the maximum possible value if the recording distance is equal to eight or more far-fields.

Vikram C. S. (1984-b) discussed the analysis of images in a plane other than the image plane. This analysis shows that the argument of the Bessel function which is observed in the reconstructed field should be high enough to observe at least one fringe in the pattern whose overall intensity decreases rapidly as the observation plane moves away from the image plane. This analysis of out of focus images may be helpful in determining the

accurate sizes of particles with known shapes.

Cartwright S. L. (1980) reported an interesting case of a small aperture in an otherwise opaque field. To make in-line Fraunhofer hologram, a separate reference beam has to be added. They have made holograms of good quality through this technique because there is separate control over the intensity of two beams.

The resolution in the image reconstructed from a far-field hologram is also dependent upon recording the interference fringes within the envelope of the far-field pattern. Visibility of fringes is an important aspect for the resolution, which depends upon the recording distance and the exposure time. **Dunn P.(1982)** has calculated the visibility at the centre of the hologram for different object shapes and observed that the fringe visibility at the centre of the hologram falls exponentially with increase in N, the number of far-fields, where it is equal to unity when the object is one far-field away (N=1). It also depends upon the size and shape of the object. For one dimensional objects (long wires) the fringe visibility is quite high, whereas for two dimensional objects (square or circular) it is more or less the same, but less than one dimensional objects. The visibility of fringes at the center of the hologram as a function of far-field distance (N) is shown in figure (2.2.1):

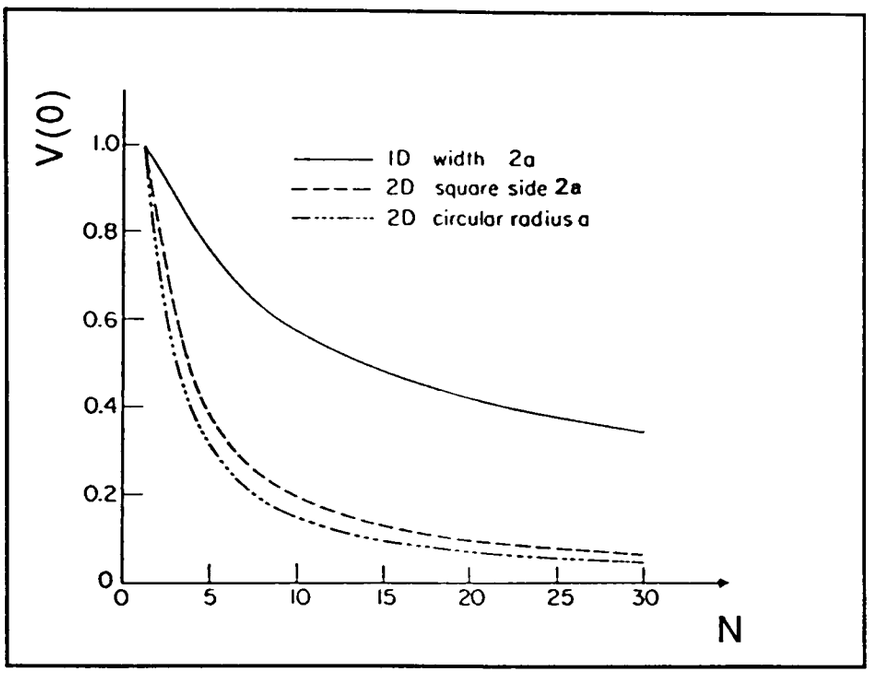

FIG. (2.2.1) visibility of fringes at the center of the hologram as a function of N.

[after Dunn P (1982)].

The visibility of fringes as a function of position can be obtained by the equation:

$$V_{(\theta)} = \frac{I_{max\,(\theta)} - I_{min\,(\theta)}}{I_{max\,(\theta)} + I_{min\,(\theta)}} \qquad .....(2.2.1)$$

Using equation (2.2.1), the general equations for visibility of fringes as function of position V(θ) and visibility of the fringes at the centre of the hologram V(0) can be calculated as:

$$V(\theta) = \frac{2C\,D(\theta)}{1 + C^2 D^2(\theta)} \quad \text{and} \quad V(0) = \frac{2C}{1 + C^2} \qquad .....(2.2.2)$$

parameters C, D(θ), V(0) and V(θ) for different object shapes are as given in the table (2.1).

Particle Shape	C	V(0)	V(θ)	D(θ)
1D 2a	$\frac{1}{\sqrt{N}}$	$\frac{2\sqrt{N}}{N+1}$	$\frac{2\sqrt{N}\,D(\theta)}{N + D(\theta)^2}$	$\frac{\sin\theta}{\theta}$
2D circular	$\frac{\pi}{4N}$	$\frac{8\pi N}{16N^2 + D(\theta)^2}$	$\frac{8\pi N D(\theta)}{16N^2 + \pi^2 D(\theta)^2}$	$\frac{2J1(\theta)}{\theta}$
2D square 2a	$\frac{1}{N}$	$\frac{2N}{N^2+1}$	$\frac{2ND(\theta)}{N^2 + D(\theta)^2}$	$\frac{\sin\theta}{\theta}$
2D rectangle 2a x 4a	$\frac{2}{N}$	$\frac{4N}{N^2+4}$	$\frac{4ND(\theta)}{N^2 + 4D(\theta)^2}$	$\frac{\sin\theta}{\theta}$

TABLE (2.1) Visibility of fringes at the holographic plane [After Dunn P.(1982)].

The role of exposure on the image to background ratio was discussed by **Vikram C. S. et al.(1984-c).** They have suggested that the ratio is very high for lower values of amplitude transmittance and decreases rapidly with its increase. The hologram is replayed on a video monitor which will have a limited dynamic range. There is certain minimum detectable intensity, and there is a saturation level beyond which the monitor output brightness remains constant. The ideal situation is one where the

background intensity is just about the minimum detectable intensity, and thus the object intensity will give the maximum contrast on the monitor. Thus low amplitude transmittance should be used provided the other factors, such as recordability of holographic fringes, dynamic range of video system etc; are not seriously affected.

Ozkul C. (1986) studied the effects of finite aperture on line width measurements and has suggested that recording more than one minima of diffraction pattern was required for satisfactory recording of small objects.

Thompson B. J. (1985) used the Huygens-Fresnel Principle to calculate the intensity distribution for opaque discs illuminated by a coherent laser source and they have used the technique of in-line Fresnel holography to resolve more than one particle. Although they have determined the radius of the particles to a high degree of accuracy, they could not resolve them in depth.

2.3 LIMITATIONS

2.3.1 SYSTEM STABILITY

Stability of the entire hologram recording system must be assured before any attempt can be made to record. Any instability in the recording system can result movement of the

diffraction fringes. If the fringes move during exposure in such a manner that a dark fringe overlaps an adjacent bright fringe, the result is a uniform exposure with no fringe pattern and no hologram is recorded. If the movement of fringes is less than their spacing, the reconstruction is possible but brightness of the image is adversely affected. Movement of any component of the recording system, even air through which the light beam must pass during recording, causes distortion of fringes. Obviously zero movement of all the components is not possible, however a fringe movement of less than 1/10 of a fringe width will not seriously effect the reconstruction brightness of the holographic image, but movement of more than 1/4 of a fringe width will seriously impair the image brightness. **[Lehman M. (1970)]**.

2.3.2 COHERENCE EFFECTS

The basic characteristics of the coherent light image forming system is that complex amplitudes, rather than intensities in the field , add before recording.

When conditions are such that the light is incoherent, it is not possible to detect interference effects. Thus the optical path difference (OPD) must be less than the coherence length of the laser.

The effect of partial spatial coherence is to reduce the

size of the effective on-axis hologram from that given by the case of total coherence, which leads to reduction in resolution upon reconstruction.

Resolution R is given by **[Hobson P. R. (1984)]:**

$$R_s = \frac{\lambda Z}{2 r} \qquad \text{Where} \quad r^2 = \frac{Z L_H}{18} \qquad .....(2.3.1)$$

where r is the radius of the zone plate, L_H is the coherence length of the laser. The Depth of field Z is given by:

$$Z = \frac{4 R_s^2 L_H}{18 \lambda^2} \qquad .....(2.3.2)$$

Thus the depth of field in holography depends upon the coherence length of the laser. **Collier R. J. (1971)** has shown that the effective coherence length of the laser can be determined by plotting a function.

$$f_{(\theta)} = \frac{\text{Sin}\,(M\theta)}{M \,\text{Sin}\,(\theta)} \qquad .....(2.3.3)$$

Where M is the number of modes of the laser and

$$\theta = \frac{c\,t\,\pi}{2L} = \frac{L_H \pi}{2L} \qquad .....(2.3.4)$$

L is the length of the laser cavity, L_H is the coherence length of the

laser, c is the velocity of light and t is the coherence time of the laser. A typical coherence length for a low power He-Ne laser is about 10 cm. For a three mode laser, the computed plot of equation (2.3.3) is shown in the figure (2.3.1):

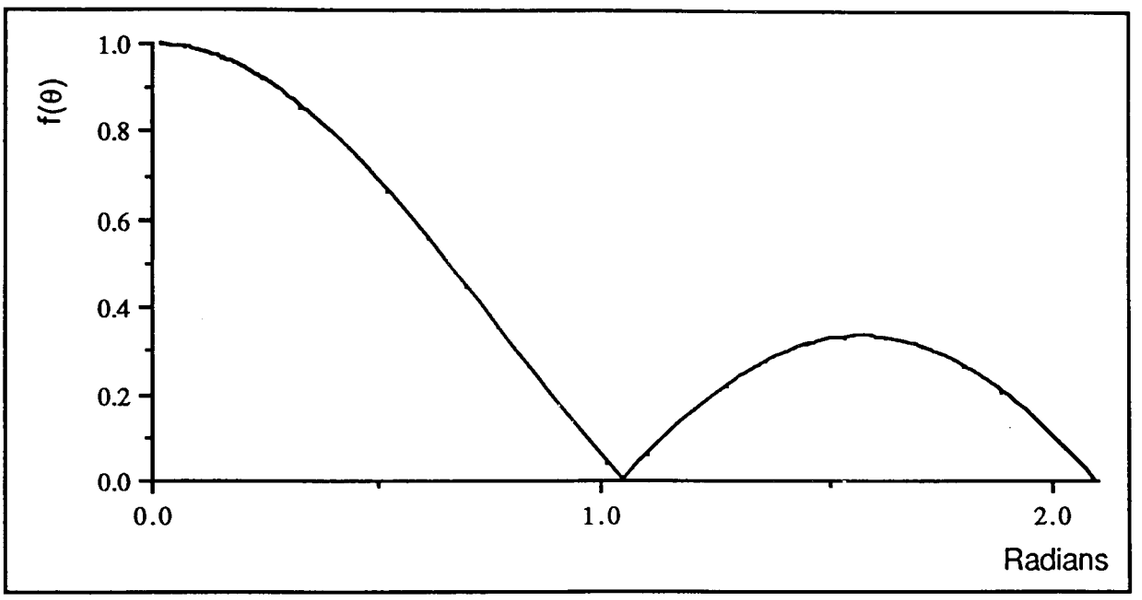

FIG. (2.3.1) Computer plot of equation (2.3.3) for a three mode laser (M=3)

The transverse coherence of the laser can be checked by observing the configuration of a cross-section of the laser beam. For this purpose the beam must be expanded with a lens and spatially filtered with a pinhole filter. If the laser is coherent across its cross-section and operating in TEM_{00} mode, then the output from the pinhole will be a smooth Gaussian intensity distribution. Other modes appearing as double ovals or doughnut patterns, indicate a deficiency in transverse coherence.

Filtering the laser beam is accomplished by placing a pinhole at the focal point of the expanding lens. The appropriate size for the pinhole D_p can be determined from the following equation. [**Lehman M. (1970)**]:

$$D_p = 2(1.22)\frac{\lambda}{d_b} f \qquad .....(2.3.5)$$

where

λ Wavelength of the laser

d_b Diameter of the laser beam incident on the lens

f focal length of the expanding lens

2.3.3 RECORDING MEDIUM EFFECTS

Since holography is a method of recording whereby information is encoded onto a spatial carrier, the recording medium must be capable of resolving the carrier spectrum. The hologram being capable of recording the same volume of information as could only be contained in a large number of photographs. In order to achieve this, a fine grain photographic material and a large amount of exposure energy is required.

Materials such as dichromated gelatin with its greater resolution, and photochromic materials which function normally without any chemical process have been used for hologram

recording. It is questionable whether the silver based sensitiser used on photographic plates is the most suitable material for holography. It is a well known fact that for these materials high sensitivity and high resolution are contrary demands [**Nassentein H, Dedden H. (1969)**]. Their main merit is chemical amplification, making recording possible at even low light levels, and a reasonably constant MTF from DC upto the cut off frequency. The quality of the recording materials can be found by considering photographic parameters and characteristic curves like MTF, H/D, and Ta/E curves.

2.3.3-(a) MODULATION TRANSFER FUNCTION.

The Modulation Transfer Function (MTF) is used as a measure of scattering properties at a particular wavelength, of the emulsion used. In conventional imagery, this would be describable by a spread function in the space domain, but for holographic applications, the frequency domain MTF, is more informative because it is the measure of the contrast of the optical image at a specified spatial frequency [**Wolfe, Marchend and Depalma (1968)**]. A simple definition of MTF is the ratio of transmitted flux to incident flux, on an emulsion exposed and developed under specific conditions at a given spatial frequency [**Biedermann and Johnson (1975)**].

$$MTF_{(\upsilon)} = \frac{TF_{(\upsilon)}}{IF_{(\upsilon)}} \qquad .....(2.3.6)$$

where the transmitted flux $TF_{(\upsilon)}$, is the actual modulation of the intensity distribution within the material and incidence flux $IF_{(\upsilon)}$, is the modulation of the interference pattern. The maximum possible theoretical value of MTF is unity..

Since MTF values cover a range of emulsion and processing characteristics, there is no fixed value for a given material. **Wolfe, Marchend and Depalma (1968)** used experimental data on the volume reflectance and transmittance of emulsion layers of between 3 μm and 33 μm thickness. A mathematical model was thereby constructed which enabled calculated values to be obtained which were in close agreement with those obtained experimentally. Such a process may be useful in assessment of non-photographic records but experimental determination of MTF for photographic materials is definitely more reliable. It can be measured with a specially designed instruments [**Biedermann and Johnson (1975)**].

Van Ligten (1966) by means of both experimental and theoretical treatise, has given a clear guidance on the significance of the MTF in holography. The description stated that the appearance of hologram reconstruction would be the same as a

view of the original object illuminated with a coherent light and seen through a mask of the same form of emulsion MTF placed at the focus of the optical system. This gave a filtering effect showing that the information content of a hologram is limited by the emulsion MTF. The same analysis indicated that the information content was independent of the emulsion contrast. The treatment was carried out separately for both plane and cylindrical waves, yielding the same results.

2.3.3-(b) HURTER-DRIFFIELD (H/D) CURVES

The amount of blackening of an exposed and developed photographic material is measured by the density D defined by

$$D = \text{Log}_{10} \frac{\text{Transmitted Intensity}}{\text{Incident Intensity}} \qquad .....(2.3.7)$$

For a coherent optical system, instead of intensity transmittance, an amplitude transmittance of the material is used. The amplitude is defined as the square root on intensity [**Collier R. J. (1971)**].

The H/D curve is a plot of Log_{10} (exposure) against D. A typical H/D curve is as shown in figure (2.3.2).

The emulsion contrast γ is given by the slope of the straight portion and is the critical characteristic for holographic

applications.

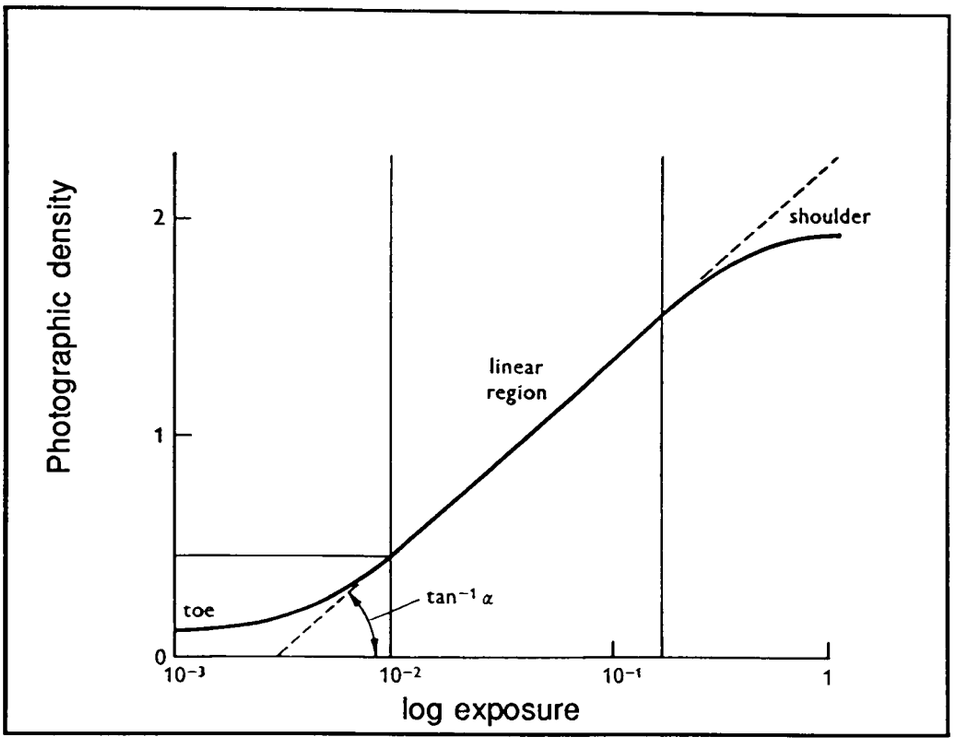

FIG. (2.3.2) A typical H/D curve

If the hologram is recorded from the straight portion of the H/D curve, fringe distortion is experienced, resulting in an effective variation of fringe spacing. The effect of recording on the toe sharpens the dark line, where recording over the shoulder broadens it. Despite of this distortion, the best performance is obtained for a hologram recorded on, or near the toe of the H/D curve.

2.3.3-(c) Ta/E (Amplituded-Transmittance) CURVES

The Amplitude Transmittance T_a of an emulsion is defined as ratio of the amplitude of a monochromatic plane wave

transmitted through the emulsion layer to the incident amplitude of the wave. The amplitude transmittance Ta is in general, a complex quantity because the phase as well as the amplitude of the wave is changed in passing through the emulsion [**Biedermann and Johnson (1975)**]. A typical Ta/E curve is as shown in the figure(2.3.3).

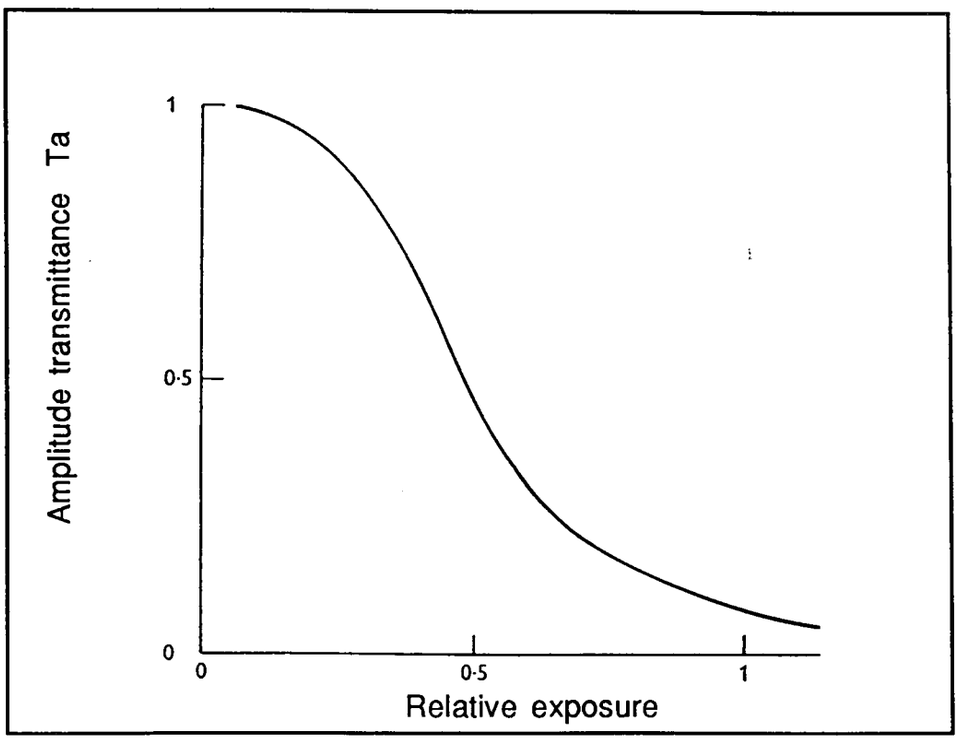

FIG. (2.3.3) A typical Ta/E curve

The straight portion of Ta/E curve is an attractive working zone when mathematical analysis of the recording process is to be undertaken, but the curve is less useful from the practical point of view, since without some form of normalisation, the slope depends upon the emulsion speed and development process. The

best working region corresponds to a very small nonlinear part of the T_a/E curve.

Some advantages are gained by plotting $T_a/Log_{10}E$, which spreads out the toe region of the T_a/E curve which is the portion to be used for the brightest reconstruction. The best working point corresponds to the steepest portion of the $T_a/Log_{10}E$ curve. [**Butters J. N. (1971)**].

After a careful consideration, it is concluded that no characteristic can be recommended for use to the exclusion of the others. The linear region of the H/D curve may be the most suitable for holographic interferometry, since it corresponds to the brightest ratio of 1st order flux to the zero order flux. The maximum image brightness, however corresponds to exposures on the steep straight portion of the $T_a/Log_{10}E$ curve. The T_a/E curve provides a useful characteristic to combine with theoretical analysis of image formation and noise generation.

An appreciation of the form of relationship between H/D, Ta, and MTF may be more easily gained by considering the typical set of combined curves as shown in the figure (2.3.4).

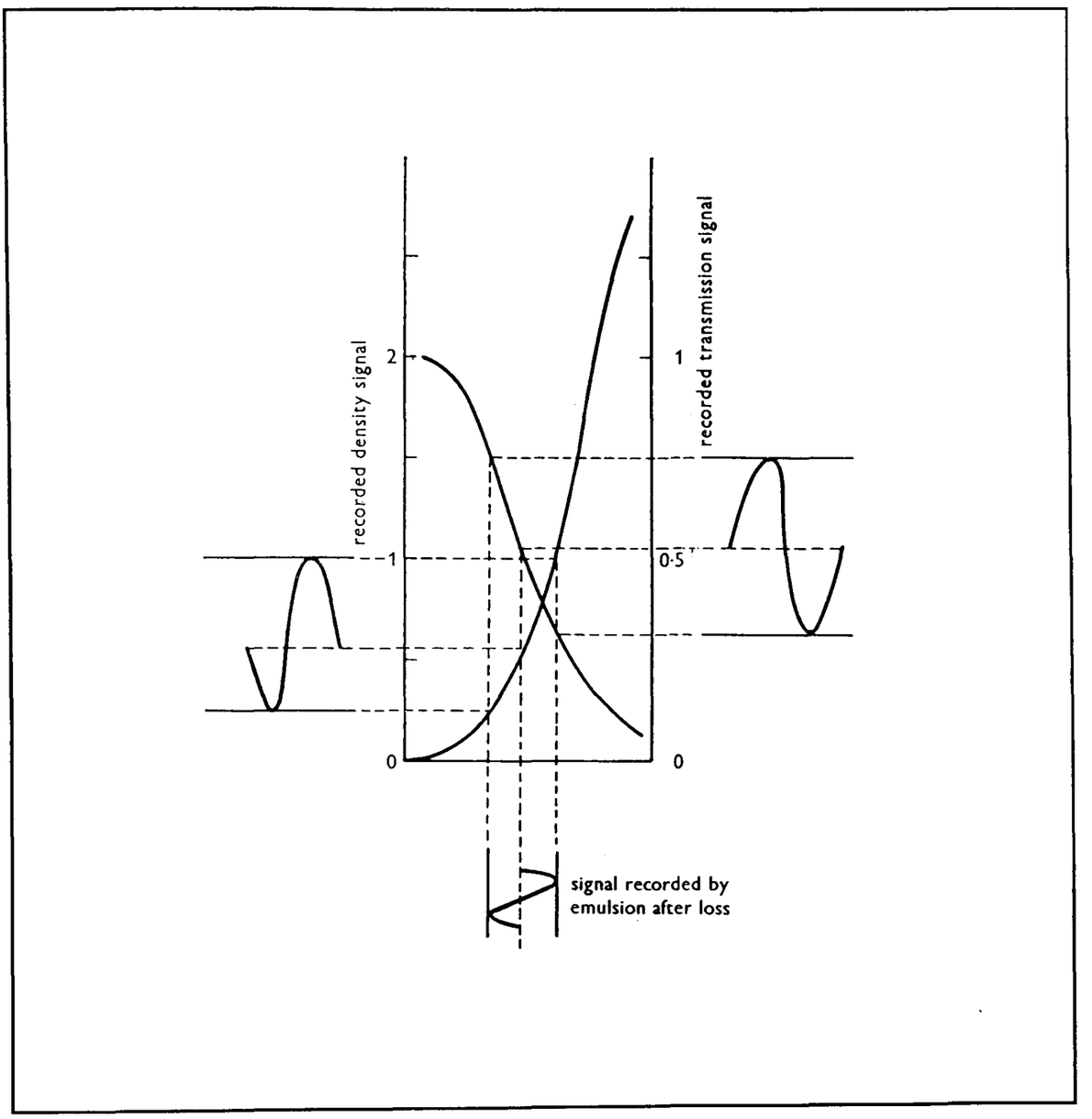

FIG. (2.3.4) Schematic curves showing density and transmission for an emulsion plotted against log E.

CHAPTER 3

THEORETICAL IMAGING MODELS

Several holographic imaging models have been described so far in the literature i.e. **Belz and Shofner (1972), Tyler and Thompson (1976), Cartwright (1980), Thompson and Malyak (1985) and Schaub (1989)** using different imaging techniques but two of them are most appropriate in this work.

(i) Belz and Shofner's model

(ii) Tyler and Thompson's model

Belz and Shofner's model is one of the earliest successful attempts to describe mathematically the construction and reconstruction process of in-line Fraunhofer holography, explaining the characteristics of the predicted images and describing theoretically the effects of a limited aperture on the in-focus and ou-of-focus reconstructed images. The mathematical technique discussed by them is very useful in predicting the effects of limited aperture and other parameters such as recording distance, and focusing parameter, on the reconstructed images.

Tyler and Thompson's model gave an alternative mathematical technique to describe the recording and reconstruction process and is very useful in modelling the

diffraction patterns recorded on the hologram and in computing the reconstructed images.

Both of these models use in-line Fraunhofer holography as the imaging technique, and are restricted to the analysis of a single particle only. Because we are interested in the simultaneous analysis of more than one particle, which is a practical case in the applications of multiple particle case such as bubble chamber experiments, a new imaging model describing images from two co-planer objects is developed in the section 3.3 of this chapter. The recording process of the extended imaging model is based on the theory cited by Tyler and Thompson's model and, because of our interest in the characteristics on in-focus and out-of-focus images, the reconstruction process is based on the theory given by the Belz and Shofner's model. Therefore, both the Belz and Shofner's model and Tyler and Thompson's model are introduced briefly in section 3.1 and 3.2 of this chapter.

3.1 BELZ AND SHOFNER'S MODEL

Belz and Shofner (1972) have investigated the characteristics of an aperture limited in-line holographic image. Having considered the recording and reconstruction geometry as shown in the figure (3.1.1).

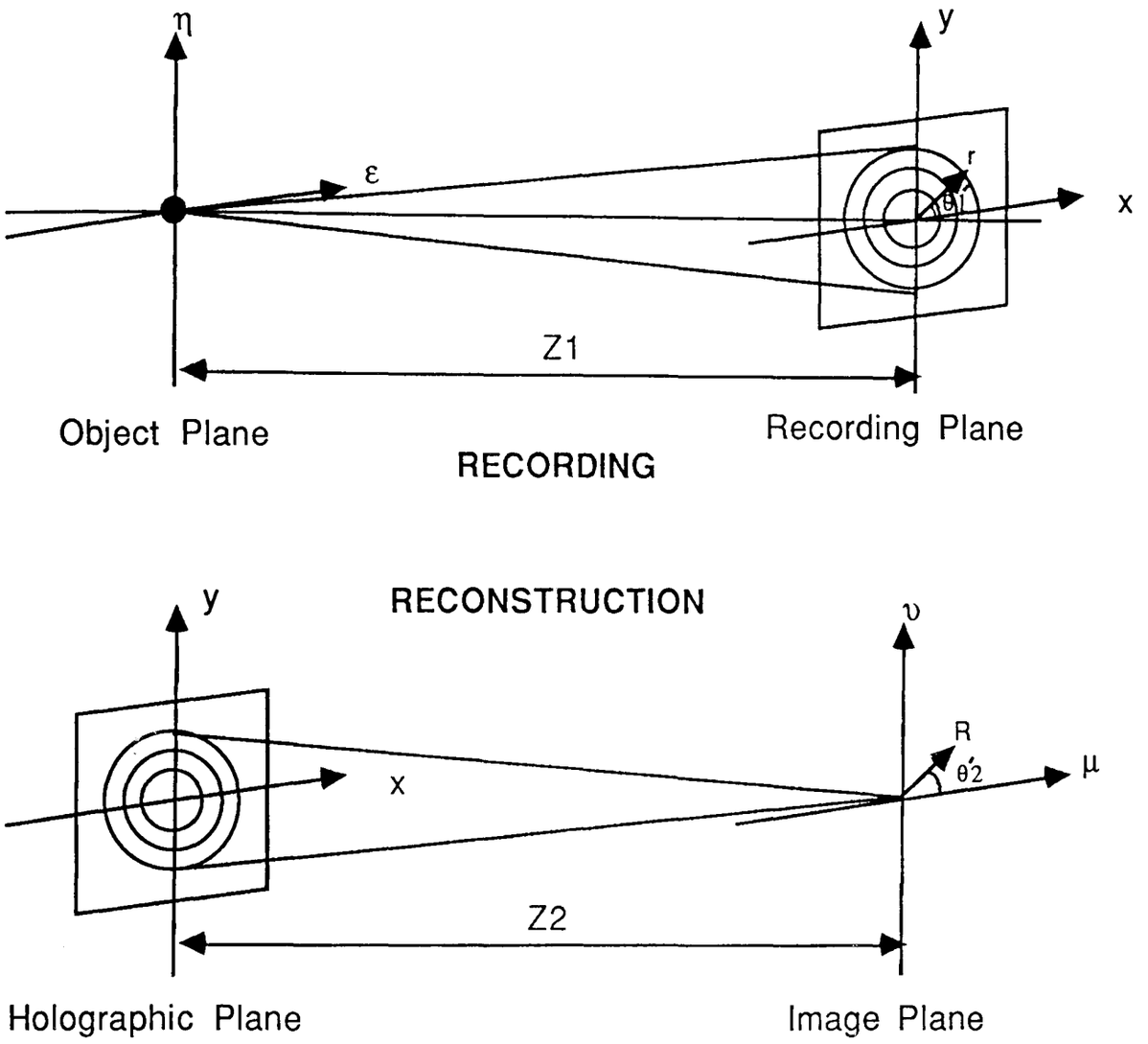

FIG. (3.1.1) Recording and reconstruction geometry.

A circular opaque particle of radius *a* was illuminated by a coherent plane wave of monochromatic light. The diffracted light arising from the particle interferes with the plane background light and the interference fringes are recorded on the film which had a finite circular aperture *H*, at a distance Z_1 from the object to form the hologram. This hologram of finite aperture

is then illuminated with the same plane wave and the image is formed at a distance Z_2 from the hologram where the image intensity was calculated theoretically and is given by: [Appendix E]

$$I_R = C^2 \left\{ \left[\int_0^r J_1\left(\frac{kar}{Z_1}\right) J_0\left(\frac{kRr}{Z_2}\right) \cos\left[\frac{kr^2}{2}\left(\frac{1}{Z_1} - \frac{1}{Z_2}\right) dr\right] \right]^2 + \left[\int_0^r J_1\left(\frac{kar}{Z_1}\right) J_0\left(\frac{kRr}{Z_2}\right) \sin\left[\frac{kr^2}{2}\left(\frac{1}{Z_1} - \frac{1}{Z_2}\right) dr\right] \right]^2 \right\} \quad .....(3.1.1)$$

where $k=2\pi/\lambda$, H is the maximum limit of the aperture, Z_1 is the recording distance, ($r = x^2 + y^2$) and ($R = \mu^2 + \upsilon^2$) are the radial distances in the hologram and image planes respectively. Defining the focusing parameter U, the image coordinate parameter W, and the limiting aperture parameter Ω as:

$$\Omega = \frac{kaH}{Z_1} \quad , \quad U = \frac{kH^2}{2}\left[\frac{1}{Z_1} - \frac{1}{Z_2}\right] \quad , \quad W = \frac{kRH}{Z_2} \quad \text{and} \quad r = \rho H \quad ....(3.1.2)$$

The predicted image intensity is normalised to 100% at $U = 0.0$, $W = 0.0$, and is given by:

$$I_{R(norm)} = \frac{\Omega^2}{[1-J_0(\Omega)]^2} \left\{ \left[\int_0^1 J_1(\Omega\rho)\, J_0(W\rho) \cos\left(\frac{U}{2}\rho^2\right) d\rho \right]^2 + \left[\int_0^1 J_1(\Omega\rho)\, J_0(W\rho) \sin\left(\frac{U}{2}\rho^2\right) d\rho \right]^2 \right\} \quad \text{.....(3.1.3)}$$

where ρ describe the position in the aperture and varies from 0 to 1. The distance Z_2 from the hologram to any plane in the reconstruction can be written as $Z_2 = Z_1 + \Delta Z$ where $\Delta Z = 0$ is the focusing condition for image reconstruction. Thus parameters U and W may be expressed in terms of the limiting aperture Ω and the focusing parameter ΔZ as:

$$U = \frac{\lambda \Omega^2}{2\pi a^2} \Delta Z \quad \text{and} \quad W = \frac{\Omega}{a} R \qquad \text{.....(3.1.4)}$$

The equation (3.1.2) was solved using a 96-point Gaussian quadrature numerical integration and the results of the integration were represented on isophote diagrams showing the contours of constant image intensity. In order to understand the characteristics of in-focus and out-of-focus images, the intensity perpendicular to the optical axis was presented for different values of U.

The calculations were made for first, second, and

fourth zeros of the Bessel function J_1 that is for Ω = 3.832, 7.016 and 13.324, which corresponds to the minimas of the diffraction patterns arising from the object particle, and limits the information recorded on the hologram. The increasing value of Ω correspond to more object detail being recorded. The theory was verified experimentally by the Belz and Shofner placing an aperture on the film during the hologram recording. The object was an opaque paint particle mounted on a glass plate. The aperture radius was constant at (H =3.75 mm) and the amount of recorded information was controlled by varying the distance between the film and the particle that is Z_1 for the corresponding value of Ω, and can be determined by:

$$Z_1 = \frac{KaH}{\Omega} \quad \text{where } H=3.75 \text{ mm, and was kept constant} \qquad .....(3.1.5)$$

This technique of limiting the recorded information by masking the film with an aperture whose radius was kept constant, has a major disadvantage that the recording distance Z_1 cannot be kept constant for different values of Ω which could effect the reconstructed image. Different techniques for limiting the extent of the recorded information, have been discussed in Chapter 4.

The experimental arrangement of the recording and

reconstruction was as shown in the figure (3.1.2).

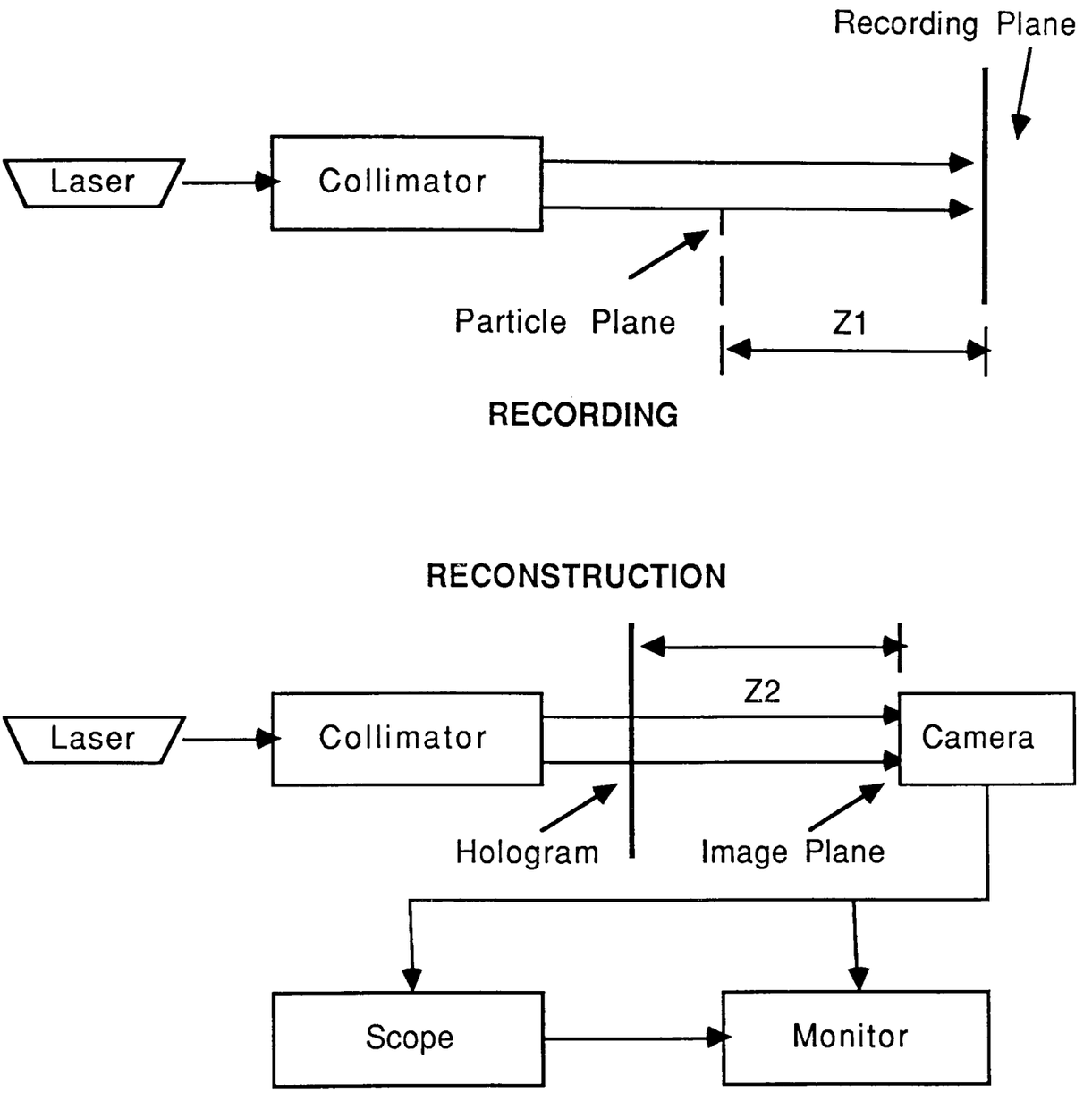

FIG. (3.1.2) Experimental arrangements of recording and reconstruction process.

3.2 TYLER AND THOMPSON'S MODEL

Tyler and Thompson (1976) have investigated the recording and reconstruction process of in-line Fraunhofer

holography for both one dimensional and two dimensional objects.

They used the Huygens-Fresnel principle to calculate the intensity in the hologram plane. According to the Huygens-Fresnel principle, if an object described by an amplitude transmittance $A(\varepsilon,\eta)$ is illuminated by a plane wave of amplitude B and wavelength λ, the field distribution at a distance Z_2 from the object is given by.

$$\Psi(x,y) = -\frac{iB}{\lambda Z_1}\exp(ikZ_1)\int_{-\infty}^{+\infty}\int_{-\infty}^{+\infty}\left[1-A(\varepsilon,\eta)\right]\exp\{\frac{ik}{2Z_1}(x-\varepsilon)^2+(y-\eta)^2\}d\varepsilon\, d\eta \quad \ldots\ldots(3.2.1)$$

but the far-field condition is:

$$\frac{\pi(\varepsilon^2+\eta^2)}{\lambda Z_1} << 1$$

Typical values for the model are a =40 μm, λ=546 nm and Z_1=10 cm.

Thus the intensity at a distance Z_2 for a two dimensional object, under the far-field condition.is given by:

$$I_{(x,y)} = B^2\left\{1+\frac{1}{\lambda^2 Z^2}\tilde{A}(\frac{x}{\lambda Z_1},\frac{y}{\lambda Z_1})\,\tilde{A}^*(\frac{x}{\lambda Z_1},\frac{y}{\lambda Z_1}) - \frac{2}{\lambda Z_1}\left[\sin(\frac{\pi r^2}{\lambda Z_1})\,\mathrm{Re}\,\tilde{A}(\frac{x}{\lambda Z_1},\frac{y}{\lambda Z_1})+\cos(\frac{\pi r^2}{\lambda Z_1})\,\mathrm{Im}\,\tilde{A}(\frac{x}{\lambda Z_1},\frac{y}{\lambda Z_1})\right]\right\} \quad \ldots\ldots(3.2.2)$$

where $r^2 = x^2 + y^2$

and

$$\tilde{A}\left(\frac{x}{\lambda Z_1},\frac{y}{\lambda Z_1}\right) = \int_{-\infty}^{+\infty}\int_{-\infty}^{+\infty} A(\varepsilon,\eta)\exp\{-2\pi i\,[\varepsilon\frac{x}{\lambda Z_1}+\eta\frac{y}{\lambda Z_1}]\}d\varepsilon.d\eta$$

is the Fourier transform of the object. For a disc of radius a, it is given by:

$$\tilde{A}\left(\frac{x}{\lambda Z_1},\frac{y}{\lambda Z_1}\right) = (\pi a^2)\frac{2J_1(\frac{kar}{Z_1})}{\frac{kar}{Z_1}} \qquad \text{.....(3.2.3)}$$

where J_1 is the Bessel function of first order. Hence the intensity in a plane at a distance Z_1 from the object is given by:

$$I_{(x,y)} = B^2\left\{1 - \frac{2\pi a^2}{\lambda Z_1}\sin(\frac{\pi r^2}{\lambda Z_1})\frac{2J_1(\frac{kar}{Z_1})}{\frac{kar}{Z_1}} + \left[(\frac{\pi a^2}{\lambda Z_1})\frac{2J_1(\frac{kar}{Z_1})}{\frac{kar}{Z_1}}\right]^2\right\} \qquad \text{.....(3.2.4)}$$

If the hologram is illuminated with a plane wave of amplitude C, the reconstructed field at a distance Z_2 from the hologram is given by:

$$\Psi_{(\mu,\upsilon)} = -\frac{iC}{\lambda Z_2}\exp(ikZ_2)\int_{-\infty}^{+\infty}\int_{-\infty}^{+\infty} I_{(x,y)}\exp\{\frac{ik}{2Z_2}[(\mu-x)^2+(\upsilon-y)^2]\}.dx.dy \qquad \text{.....(3.2.5)}$$

Thus the image intensity for in-focus condition $Z_1 = Z_2 = Z$ is given by:

$$I_{R(\mu,v)} = \left\{ 1 - \mathrm{circ}\left(\frac{R}{a}\right) + \left(\frac{\pi a^2}{\lambda Z}\right)^2 \left[\frac{2J_1\frac{kaR}{2\lambda Z}}{\frac{kaR}{2\lambda Z}}\right]^2 - \frac{\pi a^2}{2\lambda Z}\left[\frac{2J_1\frac{kaR}{2\lambda Z}}{\frac{kaR}{2\lambda Z}}\right]\exp\left\{i\left(\frac{\pi R^2}{2\lambda Z} - \frac{\pi}{2}\right)\right\} \right\}^2 \quad \text{.....(3.2.6)}$$

where

$$\mathrm{circ}\left(\frac{R}{a}\right) = 1 \quad \text{for } R \le a$$
$$= 0 \quad \text{for } R > a$$

It is important to note that Tyler and Thompson have used a mercury arc (λ = 0.5461 microns) instead of the laser beam for replay.

The equations (3.2.4) and (3.2.6) have been solved numerically and their computer plots compared with the densitometer trace of experimentally achieved results to verify the theory.

3.3 EXTENDED IMAGING

Both of the image models discussed in the previous sections give good mathematical explanation of the in-line Fraunhofer holography but they are restricted to one object only. As it has been mentioned in chapter 1, the restriction of one

object is removed in the model under investigation and in-line Fraunhofer holography is examined for more than one particle.

For mathematical simplicity a system of two opaque discs of same radius *a* separated by distance *2b* is considered. It is important to mention here that both the discs are considered to lie in one plane. The geometry of the recording and reconstruction co-ordinate system is explained in the figure (3.3.1)

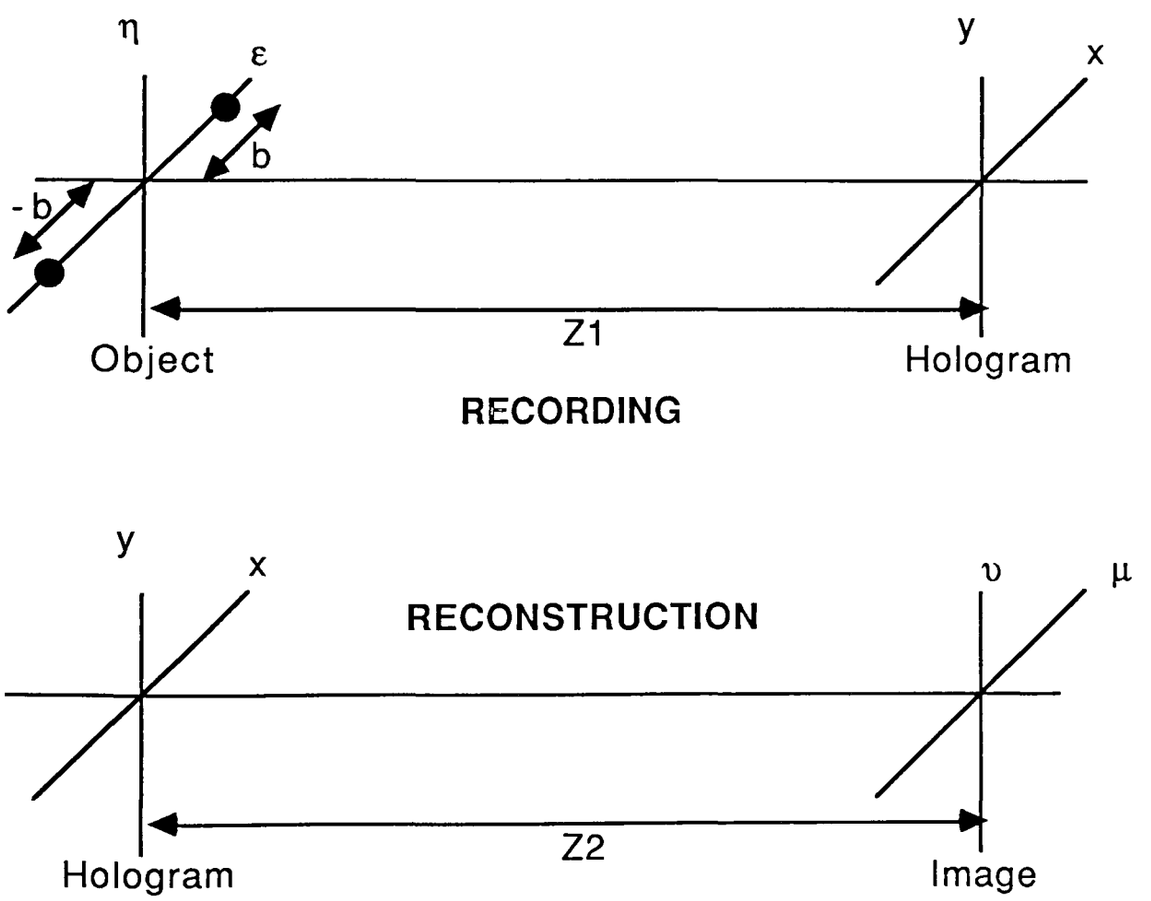

FIG. (3.3.1) Co-ordinate geometry for extended imaging.

3.3.1 RECORDING

It has been shown by **Tyler and Thompson (1976)** that if small opaque disc of radius a is illuminated by a plane wave of amplitude B and wavelength λ, the intensity distribution at a distance Z_1 from the object satisfying the far field condition is given by equation (3.2.2):

$$I_{(x,y)} = B^2 \left\{ 1 + \frac{1}{\lambda^2 Z^2} \tilde{A}\left(\frac{x}{\lambda Z_1}, \frac{y}{\lambda Z_1}\right) \tilde{A}^*\left(\frac{x}{\lambda Z_1}, \frac{y}{\lambda Z_1}\right) - \frac{2}{\lambda Z_1} \left[\sin\left(\frac{\pi r^2}{\lambda Z_1}\right) \mathrm{Re}\, \tilde{A}\left(\frac{x}{\lambda Z_1}, \frac{y}{\lambda Z_1}\right) + \cos\left(\frac{\pi r^2}{\lambda Z_1}\right) \mathrm{Im}\, \tilde{A}\left(\frac{x}{\lambda Z_1}, \frac{y}{\lambda Z_1}\right) \right] \right\} \quad \text{.....(3.2.2)}$$

where $r^2 = x^2 + y^2$

and

$$\tilde{A}\left(\frac{x}{\lambda Z_1}, \frac{y}{\lambda Z_1}\right) = \int_{-\infty}^{+\infty} \int_{-\infty}^{+\infty} A(\varepsilon,\eta) \exp\left\{-2\pi i \left[\varepsilon \frac{x}{\lambda Z_1} + \eta \frac{y}{\lambda Z_1}\right]\right\} d\varepsilon . d\eta$$

is the Fourier transform of the object and Re and Im denotes its real and imaginary parts. The term involving the imaginary part of the Fourier transform is zero for the case where the object is such that its real part is even and its imaginary part is odd.

Consider a pair of two opaque discs each of radius a, with a center to center separation $2b$ such that $b \geq a$ as shown in the figure (3.3.1).

The Fourier addition theorem states that if f(x) and g(x)has Fourier transforms F(s) and G(s), then [f(x) + g(x)] will have Fourier transform F(s) + G(s). **[Bracewell R. N (1978)]**

Therefore, for such a system the Fourier transform of the object may be determined by applying the addition theorem and is given by:

$$\tilde{A}\left(\frac{x}{\lambda Z_1},\frac{y}{\lambda Z_1}\right) = \tilde{A}\left(\frac{x+b}{\lambda Z_1},\frac{y}{\lambda Z_1}\right)+\tilde{A}\left(\frac{x-b}{\lambda Z_1},\frac{y}{\lambda Z_1}\right) \qquad \text{.....(3.3.1)}$$

Hence if such a system is illuminated by a plane wave of amplitude B and wavelength λ, the intensity distribution in the hologram plane at a distance Z_1 from the system of discs is given by:

$$I_{(x,y)} = B^2\left\{\begin{array}{l} 1+\left[\tilde{A}\left(\frac{x+b}{\lambda Z_1},\frac{y}{\lambda Z_1}\right)+\tilde{A}\left(\frac{x-b}{\lambda Z_1},\frac{y}{\lambda Z_1}\right)\right]\left[\tilde{A}^*\left(\frac{x+b}{\lambda Z_1},\frac{y}{\lambda Z_1}\right)+\tilde{A}^*\left(\frac{x-b}{\lambda Z_1},\frac{y}{\lambda Z_1}\right)\right] \\ -\frac{2}{\lambda Z_1}\sin\left(\frac{\pi r^2}{\lambda Z_1}\right)\left[\mathrm{Re}\,\tilde{A}\left(\frac{x+b}{\lambda Z_1},\frac{y}{\lambda Z_1}\right)+\mathrm{Re}\,\tilde{A}\left(\frac{x-b}{\lambda Z_1},\frac{y}{\lambda Z_1}\right)\right] \\ -\frac{2}{\lambda Z_1}\cos\left(\frac{\pi r^2}{\lambda Z_1}\right)\left[\mathrm{Im}\,\tilde{A}\left(\frac{x+b}{\lambda Z_1},\frac{y}{\lambda Z_1}\right)+\mathrm{Im}\,\tilde{A}\left(\frac{x-b}{\lambda Z_1},\frac{y}{\lambda Z_1}\right)\right] \end{array}\right\} \qquad \text{.....(3.3.2)}$$

The Fourier shift theorem states that if f(x) has Fourier transform F(s), then f(x-b) will have Fourier transform $e^{-i2\pi bs}F(s)$.

[Bracewell R. N (1978)].

Therefore, by applying the Fourier shift theorem it can be written that:

$$\tilde{A}\left(\frac{x+b}{\lambda Z_1}, \frac{y}{\lambda Z_1}\right) = e^{i(2\pi bs)}\, \tilde{A}\left(\frac{x}{\lambda Z_1}, \frac{y}{\lambda Z_1}\right)$$

and

$$\tilde{A}\left(\frac{x-b}{\lambda Z_1}, \frac{y}{\lambda Z_1}\right) = e^{-i(2\pi bs)}\, \tilde{A}\left(\frac{x}{\lambda Z_1}, \frac{y}{\lambda Z_1}\right)$$

where $(2\pi bs = \phi)$ is the phase shift for the single disc due to its displacement from origin (0,0,0) by distance b. The total phase difference between the two diffracted waves arising from the two discs is therefore (2ϕ) and is given by:

$$2(2\pi bs) = 2\phi = 2\frac{kbx}{Z_1} \qquad .....(3.3.3)$$

Where $(K = 2\pi/\lambda)$. The intensity distribution in the plane at a distance Z_1 from the system of discs is given by:

$$I_{(x,y)} = B^2 \left\{ \begin{array}{l} 1 + \dfrac{4}{(\lambda Z_1)^2}\left[\tilde{A}\left(\dfrac{x}{\lambda Z_1}, \dfrac{y}{\lambda Z_1}\right)\right]^2 \left[1 + \cos^2(\phi)\right] \\ - \dfrac{4}{\lambda Z_1}\sin\left(\dfrac{kr^2}{2Z_1}\right)\left[\tilde{A}\left(\dfrac{x}{\lambda Z_1}, \dfrac{y}{\lambda Z_1}\right).\cos(\phi)\right] \end{array} \right\} \qquad .....(3.3.4)$$

The Fourier transform of a circular object is as given by equation

(3.2.3) as:

$$\tilde{A}\left(\frac{x}{\lambda Z_1},\frac{y}{\lambda Z_1}\right) = (\pi a^2)\frac{2J_1\left(\frac{kar}{Z_1}\right)}{\frac{kar}{Z_1}} \qquad \text{.....(3.2.3)}$$

hence the intensity recorded on the film in the hologram plane at a distance Z_1 from the discs is given by:

$$I_{(x,y)} = B^2\left\{\begin{array}{l} 1+4\left(\frac{a}{r}\right)^2\left[J_1\left(\frac{kar}{Z_1}\right)\right]^2\left[1+\cos^2(\phi)\right] \\ -4\left(\frac{a}{r}\right)\sin\left(\frac{kr^2}{2Z_1}\right)\left[J_1\left(\frac{kar}{Z_1}\right).\cos(\phi)\right] \end{array}\right\} \qquad \text{.....(3.3.5)}$$

The equation (3.3.5) have been solved numerically and the computer plots of the equation (3.3.5) for two touching discs of radius (a =75 μm and b =75 μm) and for two separated discs of radius (a =75 μm) with center to center separation ($2b$ = 300μm) are shown in the figure (3.3.2).

3.3.2 RECONSTRUCTION

If the amplitude transmittance of the hologram is assumed to be equal to be $I_{(x,y)}$ and is used as a new diffracting aperture, then on illuminating it by a plane wave of amplitude C and wavelength λ, the reconstructed field at a distance Z_2 from the

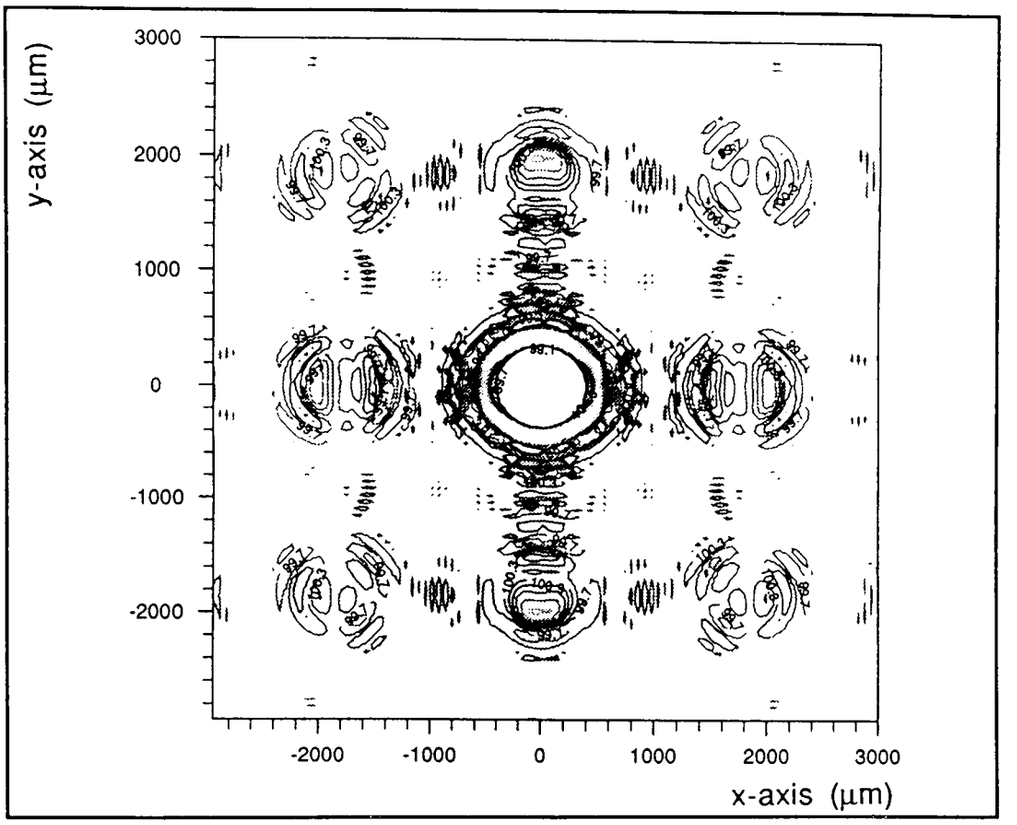

Two touching discs [a=75 μm, b= 75 μm and Z_1=175 mm]

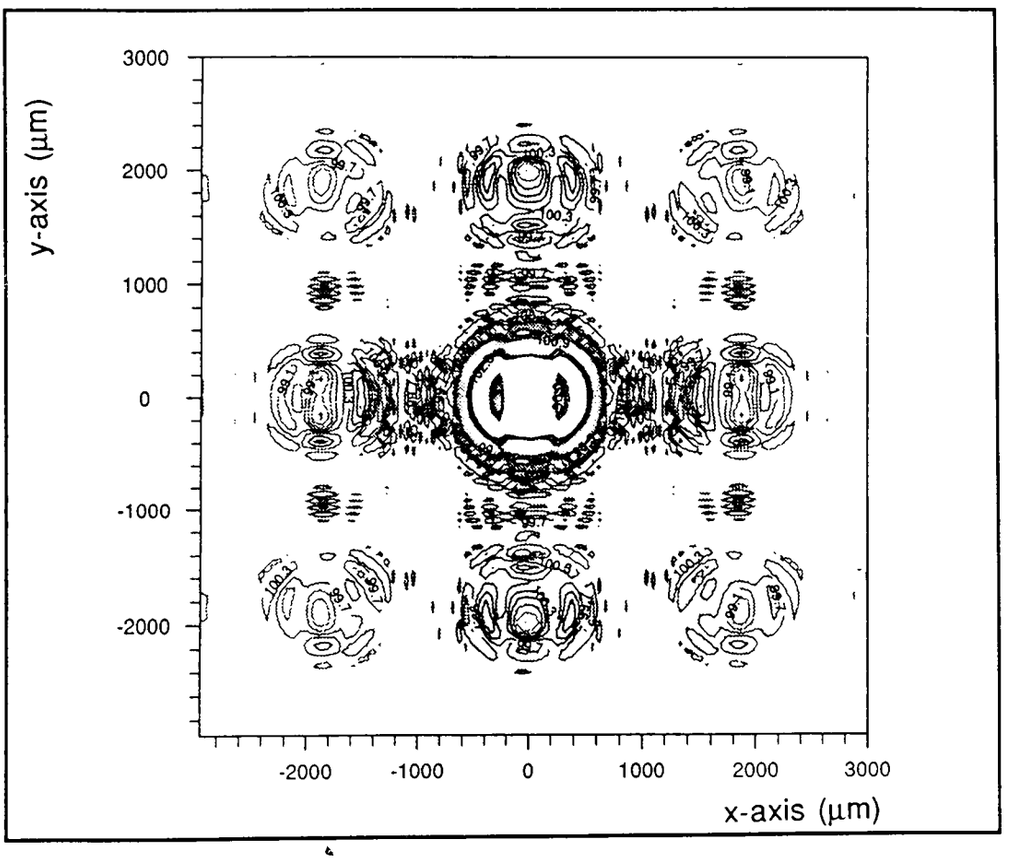

Two separated discs [a=75 μm, b=150 μm and Z_1=175 mm]

FIG. (3.3.2) Computed diffraction patterns on the hologram plane

hologram is given by equation (3.2.5):

$$\Psi_{(\mu,\upsilon)} = -\frac{iC}{\lambda Z_2}\exp(ikZ_2)\int_{-\infty}^{+\infty}\int_{-\infty}^{+\infty} I_{(x,y)}\exp\{\frac{ik}{2Z_2}[(\mu-x)^2+(\upsilon-y)^2]\}dx.dy \quad .....(3.2.5)$$

Under the far-field condition:

$$\frac{\pi(\varepsilon^2+\eta^2)}{\lambda Z_1} << 1$$

where typical values are a = 75 μm , λ = 633 nm and Z_1 = 175 mm.

The simplified equation may be written as:

$$\Psi_{(\mu,\upsilon)} = -\frac{iC}{\lambda Z_2}\exp(ik)\left[Z_2+\frac{\mu^2+\upsilon^2}{2Z_2}\right]\int_{-\infty}^{+\infty}\int_{-\infty}^{+\infty} I_{(x,y)}\exp\{\frac{ik}{2Z_2}[x^2+y^2-2x\mu-2y\upsilon]\}dx.dy \quad .....(3.3.6)$$

For mathematical simplification suppose that:

$$k(Z_2+\frac{\mu^2+\upsilon^2}{2Z_2}) = \theta_1 \qquad .....(3.3.7)$$

$$\frac{k}{2Z_2}(x^2+y^2-2x\mu-2y\upsilon) = \theta_2 \qquad .....(3.3.8)$$

The equation (3.3.6) may be written in a simplified form as:

$$\Psi_{(\mu,\upsilon)} = -\frac{iC}{\lambda Z_2}\exp(i\theta_1)\int_{-\infty}^{+\infty}\int_{-\infty}^{+\infty} I_{(x,y)}\exp(i\theta_2)dx.dy \quad .....(3.3.9)$$

where $I(x,y)$ has been calculated in the previous section and is

given by equation (3.3.5). In this equation the term:

$$4\left(\frac{a}{r}\right)\sin\left(\frac{kr^2}{Z_1}\right)\left[J_1\left(\frac{kar}{Z_1}\right).\cos(\phi)\right]$$

represents the interference between the diffracted waves from the two discs and the coherent background and is responsible for the reconstruction of the image. To simplify the mathematics, suppose that:

$$\frac{1}{\sqrt{x^2+y^2}}J_1\left(\frac{ka\sqrt{x^2+y^2}}{Z_1}\right)=A_1 \qquad \text{.....(3.3.10)}$$

and

$$\frac{k(x^2+y^2)}{Z_1}=\theta_3 \qquad \text{.....(3.3.11)}$$

The term of the intensity recorded on the hologram, responsible for the reconstruction, may be written in a simplified form as:

$$I_{(x,y)}=4\,a\,B^2\,A_1\sin(\theta_3).\cos(\phi) \qquad \text{.....(3.3.12)}$$

The reconstructed field at distance Z_2 from the hologram is determined by substituting the $I_{(x,y)}$ from equation (3.3.12), in equation (3.3.9) and is given by:

$$\Psi_{(\mu,\upsilon)}=-\frac{i4aB^2C}{\lambda Z_2}\exp(i\theta_1)\int_{-\infty}^{+\infty}\int_{-\infty}^{+\infty}A_1\cos(\phi)\sin(\theta_3)\exp(i\theta_2)\,dx\,dy \qquad \text{.....(3.3.13)}$$

sin (θ_3) may be written in complex form and as we are interested in the real image only which is represented by the negative exponential term [**Belz R. A. (1971)** (Page 13)], thus the reconstructed field at a distance Z_2 is given by:

$$\Psi_{(\mu,\upsilon)} = \frac{2aB^2C}{\lambda Z_2} \exp(i\ \theta_1) \int_{-\infty}^{+\infty} \int_{-\infty}^{+\infty} A\cos(\phi)\ \exp[-i(\theta_3 - \theta_2)]\, dx.dy$$

as $\exp(-i\theta) = \cos(\theta) - i\sin(\theta)$, hence it can be written as:

$$\Psi_{(\mu,\upsilon)} = \frac{2aB^2C}{\lambda Z_2} \exp(i\ \theta_1) \left\{ \begin{array}{l} \int_{-\infty}^{+\infty} \int_{-\infty}^{+\infty} A\cos(\phi)\ .\ \cos(\theta_3 - \theta_2)]\, dx.dy \\ -i \int_{-\infty}^{+\infty} \int_{-\infty}^{+\infty} A\cos(\phi)\ .\ \sin(\theta_3 - \theta_2)]\, dx.dy \end{array} \right\} \quad \text{.....(3.3.14)}$$

similarly

$$\overset{*}{\Psi}_{(\mu,\upsilon)} = \frac{2aB^2C}{\lambda Z_2} \exp(i\ \theta_1) \left\{ \begin{array}{l} \int_{-\infty}^{+\infty} \int_{-\infty}^{+\infty} A\cos(\phi)\ .\ \cos(\theta_3 - \theta_2)]\, dx.dy \\ +i \int_{-\infty}^{+\infty} \int_{-\infty}^{+\infty} A\cos(\phi)\ .\ \sin(\theta_3 - \theta_2)]\, dx.dy \end{array} \right\} \quad \text{.....(3.3.15)}$$

The intensity is given by the relation $I_{(\mu,\upsilon)} = \Psi_{(\mu,\upsilon)} \cdot \Psi^*_{(\mu,\upsilon)}$. Hence the intensity in the image plane at a distance Z_2 from the hologram is given by:

$$I_{(\mu,\upsilon)} = \left(\frac{2aB^2C}{\lambda Z_2}\right)^2 \left\{ \left[\int_{-\infty}^{+\infty} \int_{-\infty}^{+\infty} A\cos(\phi) \,.\, \cos(\theta_3 - \theta_2)] \, dx.dy \right]^2 + \left[\int_{-\infty}^{+\infty} \int_{-\infty}^{+\infty} A\cos(\phi) \,.\, \sin(\theta_3 - \theta_2)] \, dx.dy \right]^2 \right\} \quad \text{.....(3.3.16)}$$

where

$$\theta_3 - \theta_2 = \frac{k(x^2 + y^2)}{2}\left(\frac{1}{Z_1} - \frac{1}{Z_2}\right) + \frac{k}{Z_2}(x\mu - y\upsilon)$$

As the information is recorded on a film which has a finite size, suppose a square film with H as an aperture limit such that

$$x = \rho_1 H \quad \text{and} \quad y = \rho_2 H$$

where ρ_1 and ρ_2 varies from -1 to 1, Hence A_1, $(\theta_3 - \theta_2)$, and ϕ in terms of limiting aperture may be written as:

$$A_1 = \frac{1}{H\sqrt{\rho_1^2 + \rho_2^2}} J_1\left(\frac{kaH}{Z_1}\sqrt{\rho_1^2 + \rho_2^2}\right) = \frac{1}{H\sqrt{\rho_1^2 + \rho_2^2}} J_1\left(\Omega\sqrt{\rho_1^2 + \rho_2^2}\right) \quad \text{.....(3.3.17)}$$

$$\theta_3 - \theta_2 = \frac{kH^2}{2}\left(\frac{1}{Z_1} - \frac{1}{Z_2}\right)(\rho_1^2 + \rho_2^2) + \frac{G}{Z_2}(\rho_1\mu - \rho_2\upsilon) = \frac{U}{2}(\rho_1^2 + \rho_2^2) + \frac{G}{Z_2}(\rho_1\mu - \rho_2\upsilon) \text{.....(3.3.18)}$$

$$\phi = \frac{Gb}{Z_1}\rho_1 \quad \text{.....(3.3.19)}$$

where

$$\Omega = \frac{kaH}{Z_1}, \quad G = kH, \quad \text{and} \quad U = kH^2\left(\frac{1}{Z_1} - \frac{1}{Z_2}\right) \quad \text{.....(3.3.20)}$$

here Ω and U are the limiting aperture parameter and focusing condition respectively. The parameter G is only used to reduce the terms in the equations (3.3.17), (3.3.18 and (3.3.19). The image will be in-focus if $U = 0$, that is when $Z_1 = Z_2$. Thus the image intensity at a distance Z_2 from the hologram is given by:

$$I_{(\mu,\upsilon)}=\left(\frac{2aB^2CH}{\lambda Z_2}\right)^2\left\{\left[\int_{-1}^{1}\int_{-1}^{1}\frac{J_1(\Omega\sqrt{\rho_1^2+\rho_2^2})}{\sqrt{\rho_1^2+\rho_2^2}}\cos\left(\frac{G}{Z_1}b\rho_1\right)\cos\left[\frac{u}{2}(\rho_1^2+\rho_2^2)+\frac{G}{Z_2}(\mu\rho_1+\upsilon\rho_2)\right]d\rho_1.d\rho_2\right]^2\right.$$

$$\left.+\left[\int_{-1}^{1}\int_{-1}^{1}\frac{J_1(\Omega\sqrt{\rho_1^2+\rho_2^2})}{\sqrt{\rho_1^2+\rho_2^2}}\cos\left(\frac{G}{Z_1}b\rho_1\right)\sin\left[\frac{u}{2}(\rho_1^2+\rho_2^2)+\frac{G}{Z_2}(\mu\rho_1+\upsilon\rho_2)\right]d\rho_1.d\rho_2\right]^2\right\} \quad ..(3.3.21)$$

The distance Z_2 from the hologram and the image plane may also be written as $Z_2 = Z_1 + \Delta Z$ where Z_1 is the recording distance and ΔZ is difference of the two distances. Thus the focusing parameter U can be written in terms of ΔZ with $\Delta Z = 0$ is the focusing condition.

$$U = kH^2\frac{\Delta Z}{Z_1 . Z_2} = \left(\frac{\Omega}{a}\right)^2\frac{\Delta Z}{k}$$

Equation (3.3.19) gives the image intensity and was solved numerically for different values of Ω and ΔZ and the computer plots of the equation (3.3.19) were compared with the graphs plotted using the data acquired experimentally, for the

experimental verification of the theory. The method of computation is discussed in chapter 5.

Computer plots of equation (3.3.19) for a pair of discs of radius (a =75μm), separated by a distance ($2b$ =225μm) for Ω=19.616 are shown in figure (3.3.3) to figure (3.3.5).

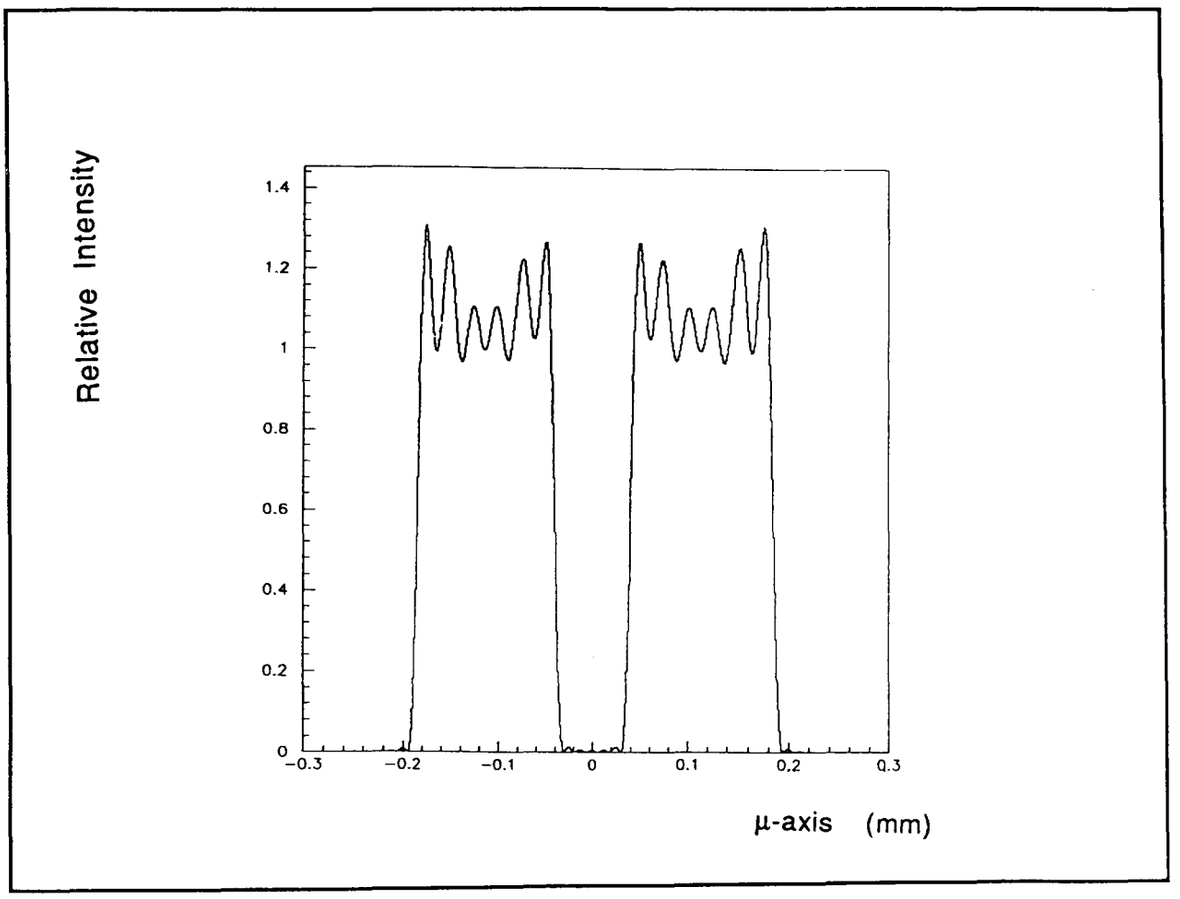

FIG. (3.3.3) Computed line scan through the center of the image

[a =75 μm, $2b$ = 225 μm, Ω=19.616 and υ=0]

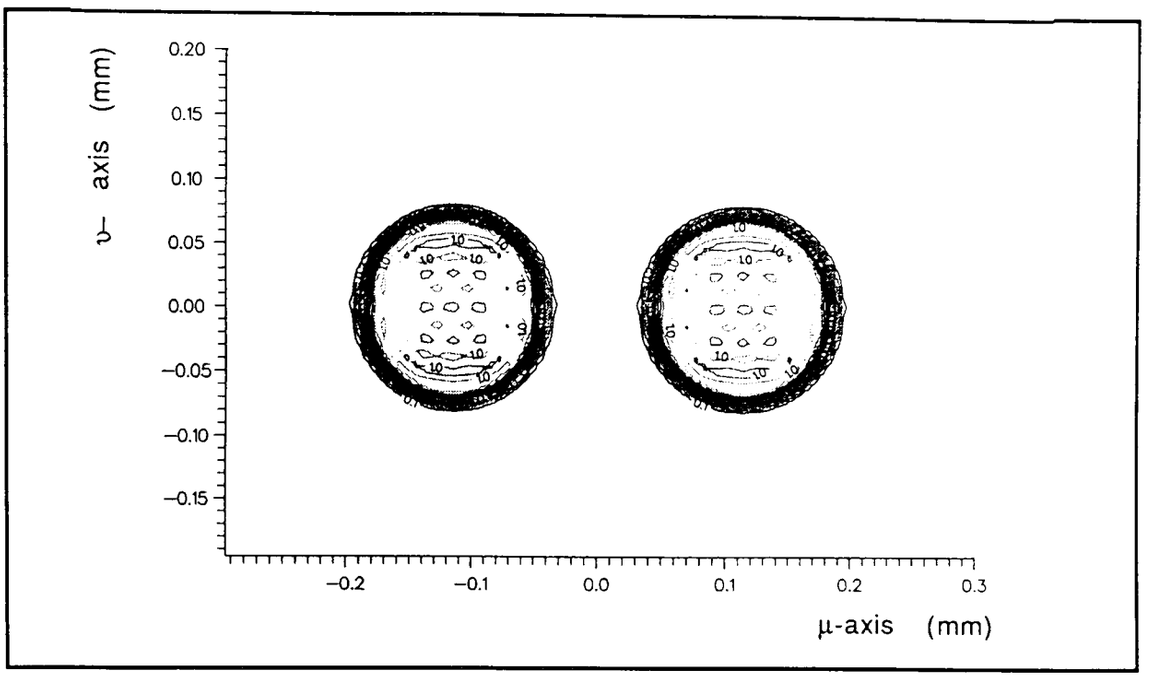

FIG. (3.3.4) Contour plot of equation (3.3.19)

[a =75 μm, $2b$ = 225 μm, Ω=19.616]

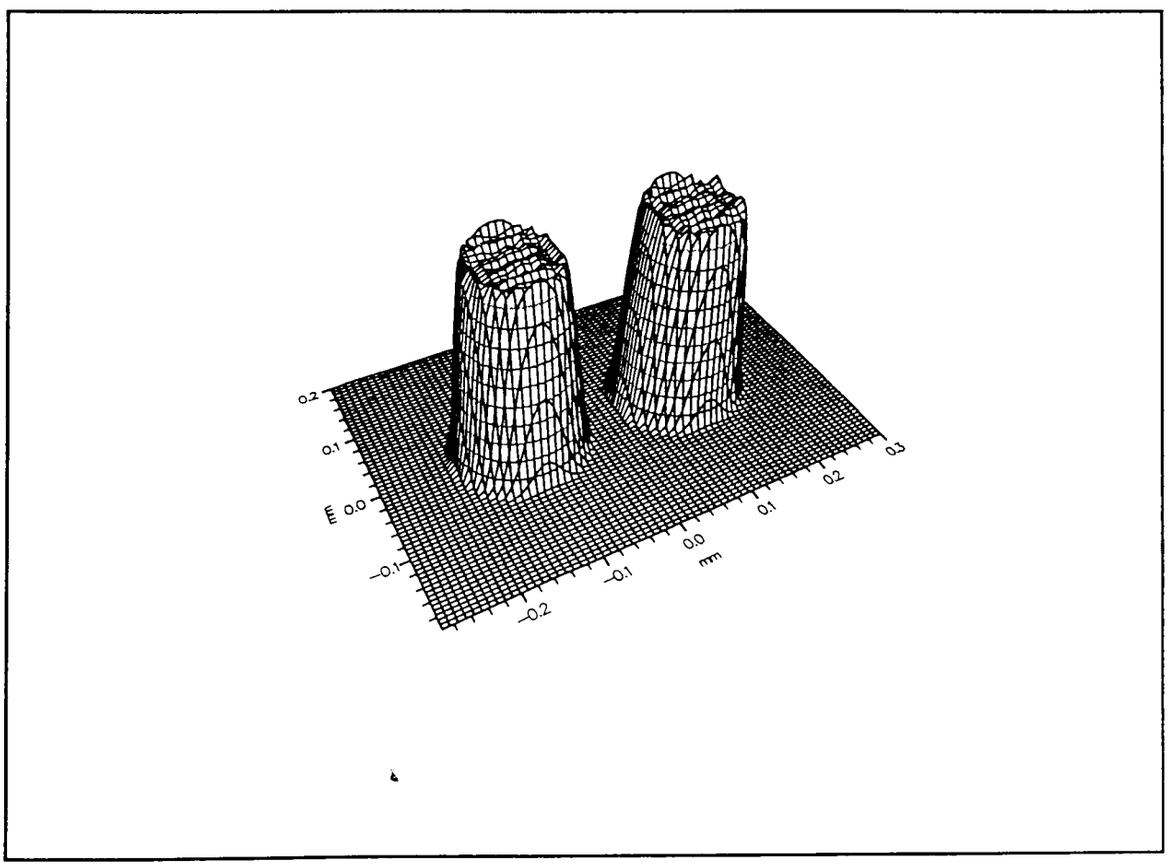

FIG. (3.3.5) Three dimensional plot of equation (3.3.19)

[a =75 μm, $2b$ = 225 μm, Ω=19.616]

3.3.3 AN ALTERNATIVE APPROACH.

As we are also interested in modelling two discs lying in different Z_1 planes, an alternative technique to calculate the intensity of diffraction patterns recorded on the hologram and to determine the image intensity in the reconstruction based on the coordinate geometry as shown in figure (3.3.6) has also been investigated. For the initial analysis, it was supposed that the discs are coplanar ($\Delta s=0$), so that the validity of the alternative technique can be checked by comparing the its predicted results with the computed results of the technique used in extended imaging, cited in sections (3.3.1) and (3.3.2) of this Chapter.

If the whole test volume is illuminated with a plane wave of unit amplitude, interference patterns of the diffracted intensities will be recorded on the film to form a hologram. If I_1 and I_2 are the two diffracted intensities, The interfering intensity in the film plane is therefore given by:

$$I_{(x,y)} = I_1 + 1_2 + 2\sqrt{(I_1 I_2)} \,.\, \cos(2\phi) \qquad \text{.....(3.3.22)}$$

Where (2ϕ) is the total phase difference between the diffracted waves arising from the two discs. Diffracted intensity from an individual disc is available from the literature **Belz R. A. (1972)**

and is given by:

$$I_1 = 1 - 2\left(\frac{a}{r_1}\right)\sin\left(\frac{kr_1^2}{2Z_1}\right)J_1\left(\frac{kar_1}{Z_1}\right) + \left[\left(\frac{a}{r_1}\right)J_1\left(\frac{kar_1}{Z_1}\right)\right]^2 \qquad .....(3.3.23\text{-a})$$

$$I_2 = 1 - 2\left(\frac{a}{r_2}\right)\sin\left(\frac{kr_2^2}{2Z_1}\right)J_1\left(\frac{kar_2}{Z_1}\right) + \left[\left(\frac{a}{r_2}\right)J_1\left(\frac{kar_2}{Z_1}\right)\right]^2 \qquad .....(3.3.23\text{-b})$$

where

$$r_1 = \sqrt{(x-b)^2 + (y)^2} \quad \text{and} \quad r_2 = \sqrt{(x+b)^2 + (y)^2}$$

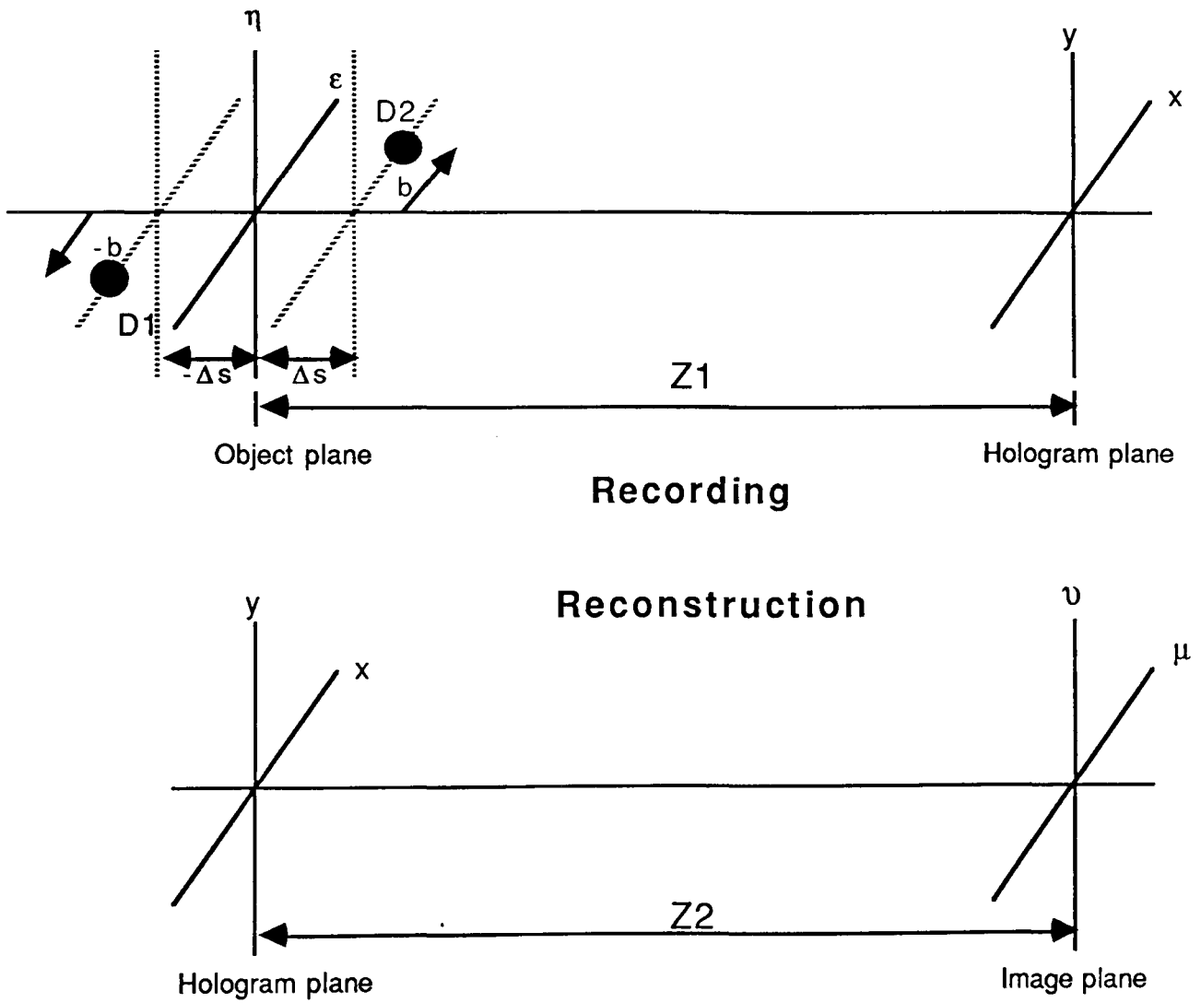

FIG. (3.3.6) Co-ordinate geometry of the possible future work

The third term in the above equations is very small [typically (a = 75 μm), (Z_1 = 175 mm) and r1, r2 ranges upto 5 mm] and can be neglected [**Belz R. A. (1971)**]. By substituting the values of I_1, I_2 and $\sqrt{I_1.I_2}$ the Intensity in the film plane can be determined and is given by:

$$I_{(x,y)} = 4\left\{1 - \left[\frac{a.}{r_1} J_1\left(\frac{kar_1}{Z_1}\right) \sin\left(\frac{kr_1^2}{2Z_1}\right) + \frac{a.}{r_2} J_1\left(\frac{kar_2}{Z_1}\right) \sin\left(\frac{kr_2^2}{2Z_1}\right)\right]\right\} \cos^2(\phi) \quad ...(3.3.24)$$

This is a general equation for intensity in the film plane and can be regarded as the hologram intensity. The term:

$$\left[\frac{a.}{r_1} J_1\left(\frac{kar_1}{Z_1}\right) \sin\left(\frac{kr_1^2}{2Z_1}\right) + \frac{a.}{r_2} J_1\left(\frac{kar_2}{Z_1}\right) \sin\left(\frac{kr_2^2}{2Z_1}\right)\right].\cos^2(\phi)$$

represents the interference between the two diffracted intensities and the coherent background, and is responsible for the reconstruction of real and virtual images. Thus intensity in the holographic plane for reconstruction, may be represented using only this term.

$$I_{(x,y)} = \left[\frac{a.}{r_1} J_1\left(\frac{kar_1}{Z_1}\right) \sin\left(\frac{kr_1^2}{2Z_1}\right) + \frac{a.}{r_2} J_1\left(\frac{kar_2}{Z_1}\right) \sin\left(\frac{kr_2^2}{2Z_1}\right) \right] .\cos^2(\phi) \quad ...(3.3.25)$$

The reconstructed field can be determined by substituting the value of intensity in equation (3.3.6) and adopting the same procedure and is given by:

$$\psi_R = \frac{2}{\lambda Z_2} \exp(i\ \theta_1) \left[\begin{array}{l} \int_{-1}^{1}\int_{-1}^{1} \left(A_2.\sin\theta_4 + A_3.\sin\theta_5\right) \cos^2(\phi)\, d\rho_1 .d\rho_2 \\ -\, i \int_{-1}^{1}\int_{-1}^{1} \left(A_2.\sin\theta_4 + A_3.\sin\theta_5\right) \cos^2(\phi)\, d\rho_1 .d\rho_2 \end{array} \right]$$

Similarly

$$\psi_R^* = \frac{2}{\lambda Z_2} \exp(i\ \theta_1) \left[\begin{array}{l} \int_{-1}^{1}\int_{-1}^{1} \left(A_2.\sin\theta_4 + A_3.\sin\theta_5\right) \cos^2(\phi)\, d\rho_1 .d\rho_2 \\ +\, i \int_{-1}^{1}\int_{-1}^{1} \left(A_2.\sin\theta_4 + A_3.\sin\theta_5\right) \cos^2(\phi)\, d\rho_1 .d\rho_2 \end{array} \right]$$

Image intensity at a distance Z_2 from the hologram is therefore; given by $I_R = \psi_R \cdot \psi_R^*$. Thus the image intensity at a distance Z_2 from the hologram in terms of limiting aperture and focusing condition, may be written as:

$$I_{R(\mu,\upsilon)} = \left(\frac{2a}{H\lambda Z_2}\right)^2 \left\{ \left[\int_{-1}^{1}\int_{-1}^{1} \left(A_2.\cos\theta_4 + A_3\cos\theta_5\right)\cos^2(\phi)\, d\rho_1 d\rho_2\right]^2 + \left[\int_{-1}^{1}\int_{-1}^{1} \left(A_2\sin\theta_4 + A_3\sin\theta_5\right)\cos^2(\phi)\, d\rho_1 d\rho_2\right]^2 \right\} \quad ...(3.3.26)$$

where A_2, A_3, θ_4, and θ_5 are the parameters introduced for mathematical simplicity and to reduce the terms in equation (3.3.26): These parameters are defined as:

$$A_2 = \frac{a\, J_1\left(\Omega \sqrt{\left(\rho_1 - b/H\right)^2 + \left(\rho_2\right)^2}\right)}{\sqrt{\left(\rho_1 - b/H\right)^2 + \left(\rho_2\right)^2}} \quad \text{and} \quad A_3 = \frac{a\, J_1\left(\Omega \sqrt{\left(\rho_1 + b/H\right)^2 + \left(\rho_2\right)^2}\right)}{\sqrt{\left(\rho_1 + b/H\right)^2 + \left(\rho_2\right)^2}}$$

$$\theta_4 = \frac{U}{2}\left(\rho_1^{\,2} + \rho_2^{\,2}\right) + \frac{G}{2}\left(\mu\rho_1 + \upsilon\rho_2\right) - \phi\rho_1$$

$$\theta_5 = \frac{U}{2}\left(\rho_1^{\,2} + \rho_2^{\,2}\right) + \frac{G}{2}\left(\mu\rho_1 + \upsilon\rho_2\right) + \phi\rho_1$$

The parameters *U* and *G* are defined in equation (3.3.20). The equation (3.3.26) has been solved numerically and the computed results were compared with the predicted results of the previous techniques. The alternative technique was not found appropriate for predicting the reconstructed image intensity. The main source of errors has not yet been investigated.

CHAPTER 4

EXPERIMENTAL TECHNIQUES

The experiments are divided into two main parts. In the first part, a complete data acquisition system was developed to acquire the data from the reconstructed images. This was then compared with the theory cited in chapter 3.

The second part consists of a discussion about the overall optical system, characteristics of the recording medium including the design of the test object, and techniques of placing the aperture to record an aperture limited hologram.

4.1 DATA ACQUISITION SYSTEM

The usual experimental procedure of in line holography is that the object is illuminated by a collimated beam and the interference patterns of the light diffracted from the object and the coherent background are recorded on the film which is then used for the study of the diffraction fringes. In the experiments under discussion the technique is slightly expanded that is after recording the hologram, a video camera is placed in the plane of the real image allowing this to be displayed on a TV monitor. This image is captured by a computer controlled digital oscilloscope

Hewlett-Packard HP54501A using the Asystant GPIB software. The schematic diagram of the overall system is shown in figure (4.1.1).

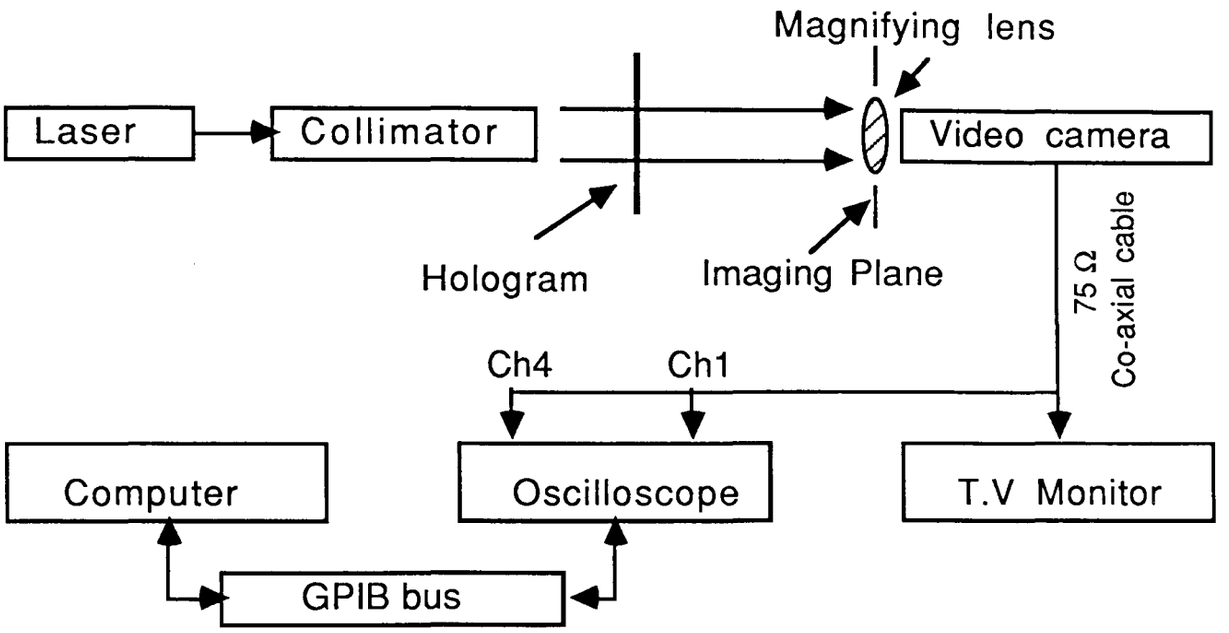

FIG (4.1.1) Schematic diagram of the data acquisition system.

The real images were magnified by introducing a microscope objective [15 mm/0.25 NA, 0/∞] from Ealing Opto Electronics, at a distance of 17 cm from the camera. These magnified images were projected on the camera and the data was transferred to the TV monitor and channel 1 and channel 4 of the digital oscilloscope HP54501A simultaneously using a 75 Ω co-axial cable. Channel 1 of the oscilloscope is used for triggering and Channel 4 is used to display the video signal and its

acquisition. Because of the different channels for triggering and data acquisition, the user has independent control over the two functions.

The camera used to display the image on the TV monitor was selected very carefully. A CCD camera EEV46410 and a video camera 109A from Link Electronics, fitted with an RCA Ultricon (Appendix A), were tested by analysing the diffraction patterns arising from a 25 μm diameter wire. The performance of the two cameras was tested by plotting the dark current and the optical noise with the laser. Figure (4.1.2) and figure (4.1.3) shows the dark current and the optical noise respectively. It is clear that although the dark current of the CCD camera EEV46410 is small (i.e -3.7 mA for the CCd camera and -2.0 mA for the video camera), the performance of the video camera 109A is better when it was used with the laser source. The fact was also confirmed by recording the diffraction patterns arising from a thin wire (ϕ'=25μm). The diffraction patterns recorded by both cameras are shown in figure (4.1.4). It can be seen that if coherent background can be subtracted both cameras are equally good, however if this is not possible, as in holography, the CCD camera is much poorer. This poor performance of the CCD camera was due to interference

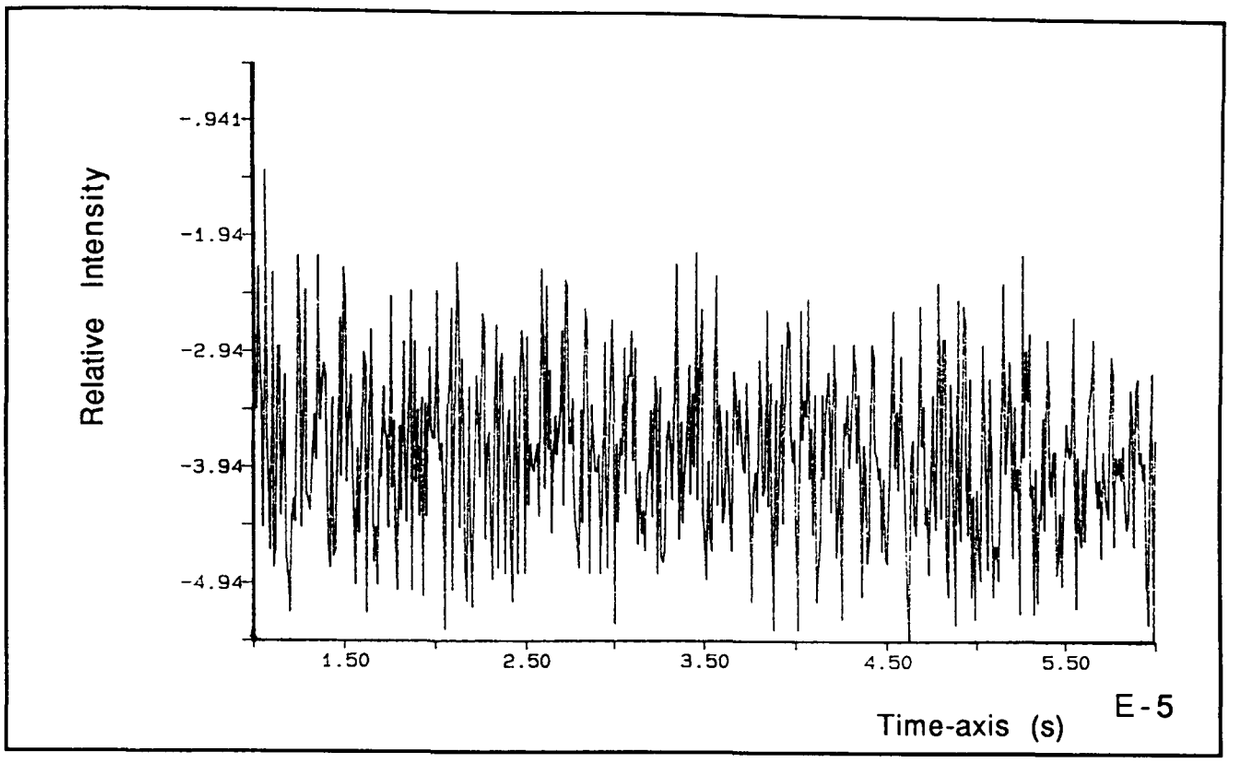

Dark current of the CCD camera EEV46410

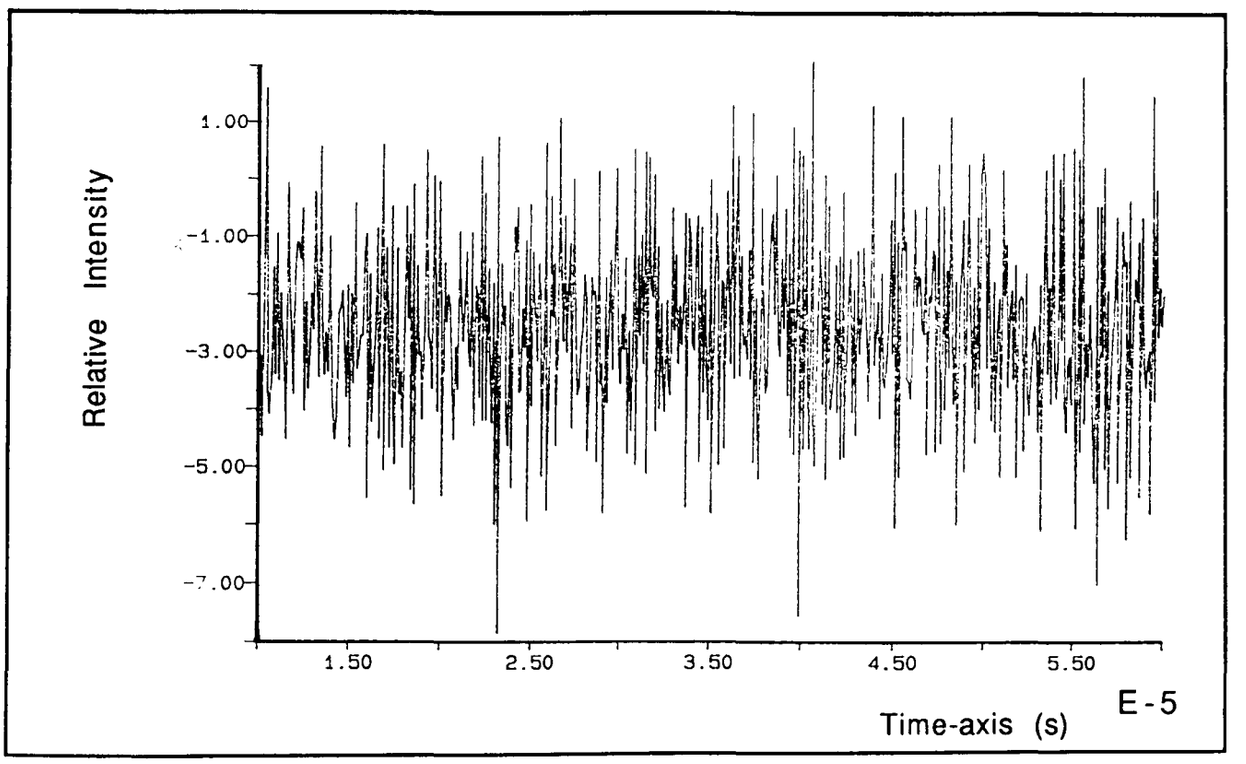

Dark current of the video camera 109A from Link Electronics

FIG. (4.1.2) Comparison of the dark current of the two cameras

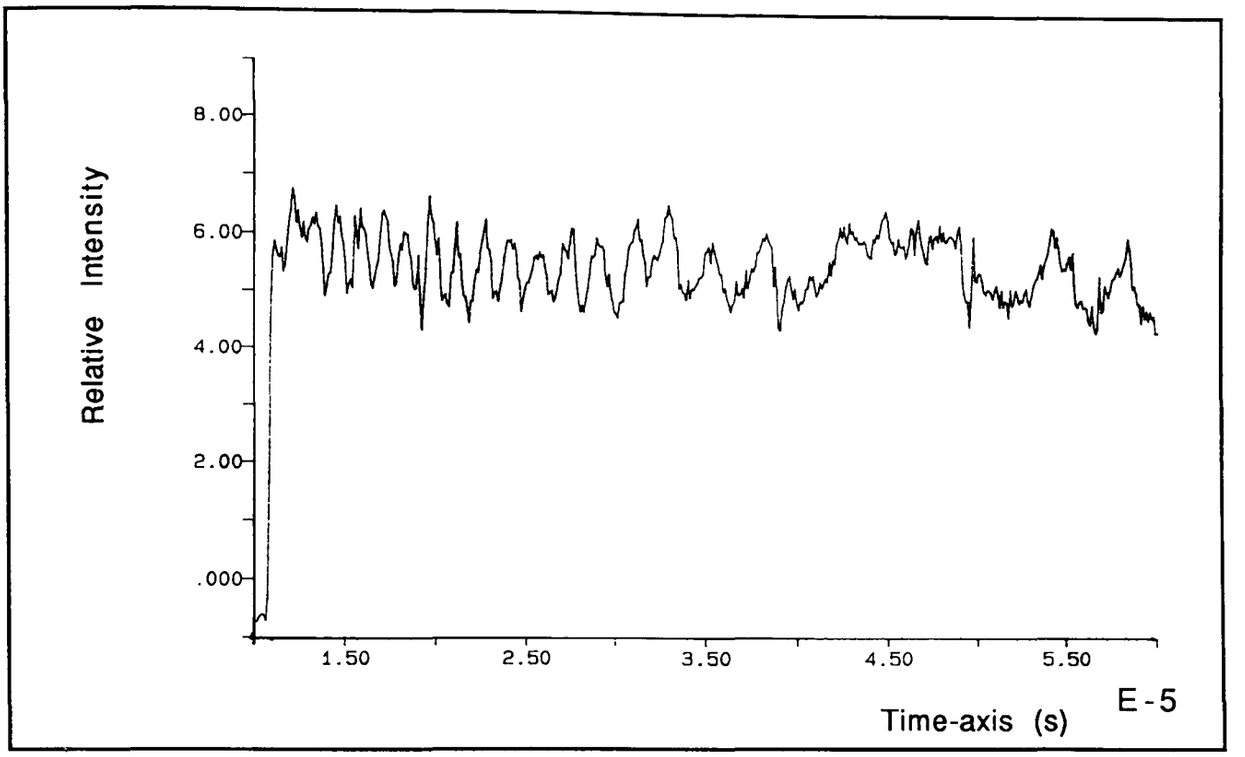

Optical noise of the CCD camera EEV46410

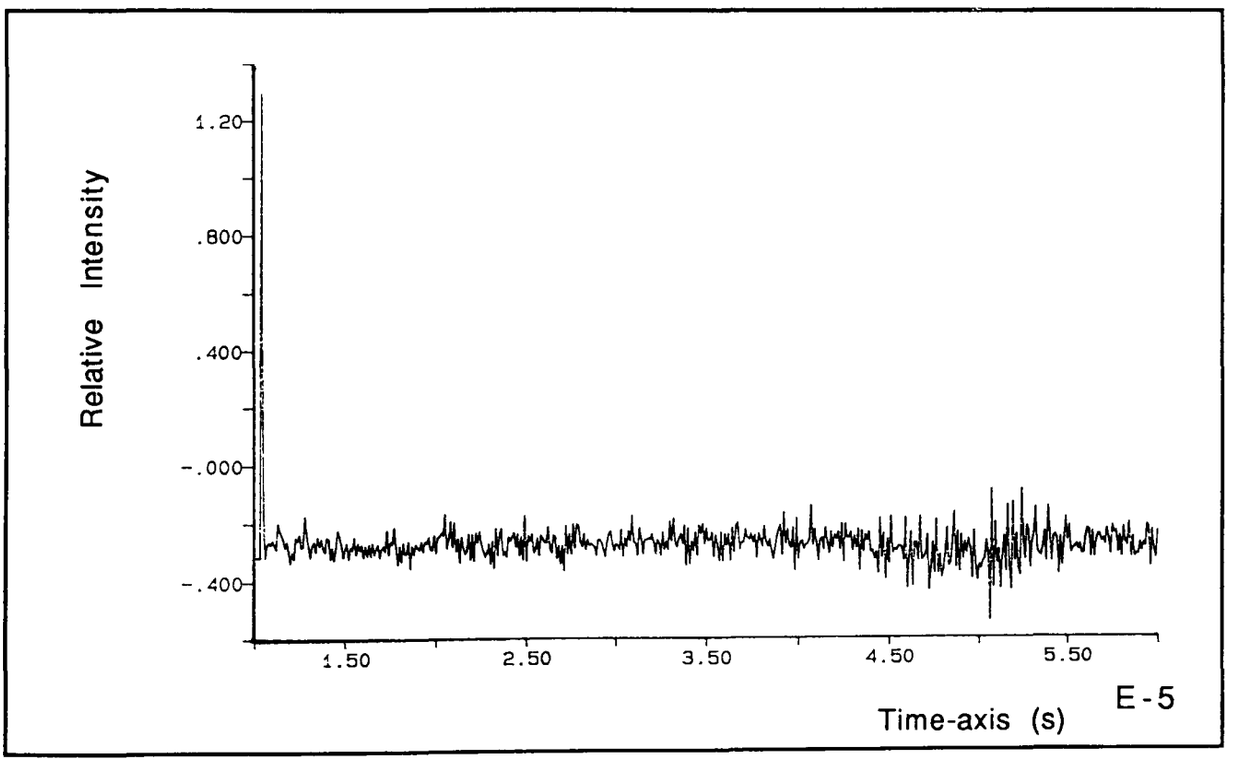

Optical noise of the video camera 109A from Link Electronics

FIG. (4.1.3) Comparison of the optical noise of the two cameras when coherently illuminated.

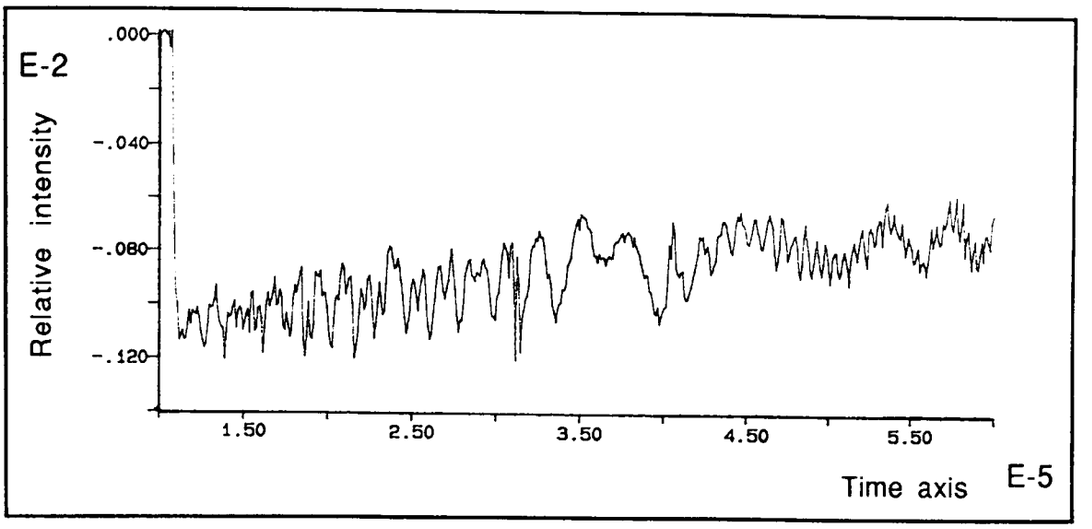

Without subtracting background (CCD camera)

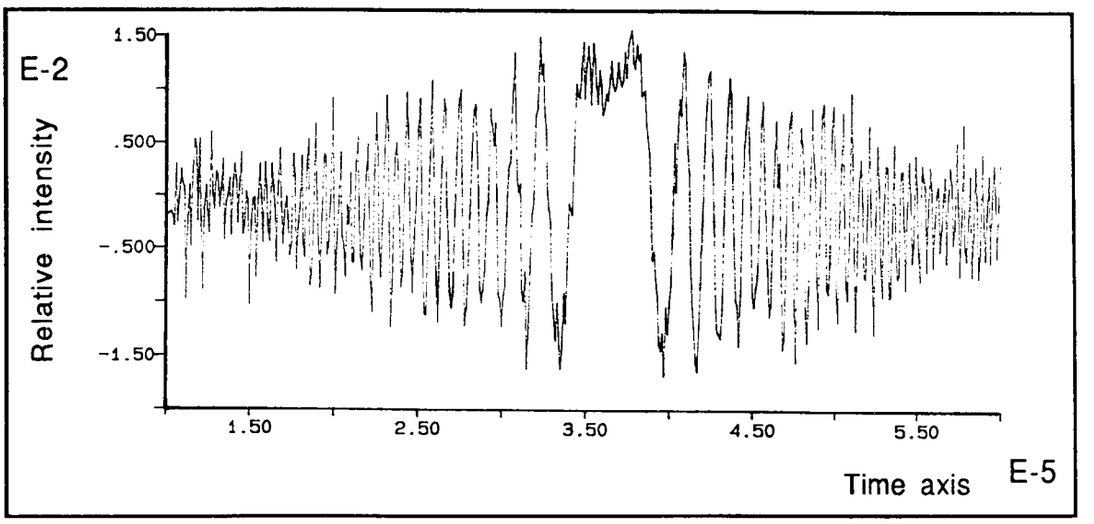

Using CCD camera

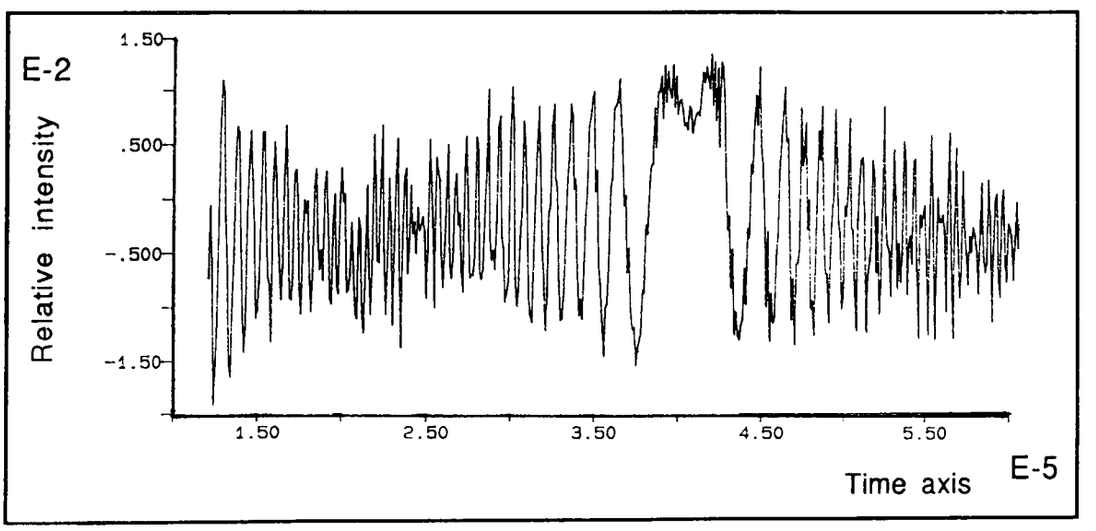

Using Video camera

FIG. (4.1.4) Diffraction Patterns arising from a thin wire (ϕ=25 μm).

arising from the thin protection glass window over the CCD chip. Resolution of the camera tube Ultricon II™ 5432/U, used in video camera 109A was determined experimentally and was found to be about 20 μm which was comparable with the pixel size of the CCD camera. Hence resolution of the image was not lost with the use of the video camera 109A. Therefore, the video camera 109A, because of its better performance with coherent light, was selected for the experiments discussed in this thesis.

A digital oscilloscope HP54501A was selected because of its ability to capture the data and send it to a computer in a automated test system. The other advantage of the digital oscilloscope is that it stores its trace in RAM, rather than in an electrically charged mesh which enables it to be displayed on the screen for an infinite period of time without change, and because of separate ADC for each channel, more than one channel can be viewed simultaneously without loosing any information. The most important feature is that the waveforms can be arranged and stored in internal memories for future use and comparison.

Two types of sources 60 Hz/525 lines and 50 Hz/625 lines may be applied to any of the four channels of the oscilloscope for TV triggering. Polarity can be selected for positive or negative

synchronising pulses. The triggering may be qualified by an edge, pattern, time qualified pattern or state. The trigger delay can be selected from 30 ns to 160 ms.

The waveform from the oscilloscope may be acquired in either averaging or envelope mode. Digitisation of the data is done in the averaging mode and the number *n* of averaging may be specified by the user in the powers of 2, up to 2048. On each acquisition, *1/n* times the new data is added to *(n-1)/n* of the previous value at each time co-ordinate.

The general purpose interface bus or GPIB provides a powerful, flexible standard for communication interface between computer and other devices. The advantage of GPIB over more specialised interfaces are twofold. First, the GPIB reduces the hardware requirements of the computer from many interfaces for each instrument to one interface or the entire system. Second, as a result of its hardware standerisation, GPIB allows the use of generalised software, such as Asystant GPIB from **Asyst Software technologies Inc.** It is actually a connection scheme for communication between different pieces of hardware. Information carried by the bus is sent over 24-way cable that connects the computer to each device on the bus. As specified by

the IEEE-488 standard, 14 devices can be connected to the computer by one bus. To facilitate communication, each device on the bus is assigned a unique address, which referred to as the primary address of the device and can range from 0 to 30.

Asystant GPIB is a commercially available PC package which enables the user to acquire data controlled through the GPIB. The data acquired may be manipulated, analysed, and graphically displayed.

Asystant GPIB allows the user to communicate with instruments on the GPIB bus through the commands that can be executed either immediately or used later in the programmable routines. In the experiment under discussion Asystant GPIB is used to acquire the waveform from the digital oscilloscope to analyse and display it graphically on the computer. For this purpose different subroutines were written through which different commands were executed for the different user defined conditions. The collection of commands executes automatically when the routine is run. Up to 30 routines can be written in one file and each routine can hold up to 20 commands, but routines can be nested by including the command "execute routine" in a routine and hence more commands can be executed in this fashion. Eight

subroutines were written to control the digital oscilloscope and to acquire, analyse and display the waveform on the computer. All the eight subroutines are given in the appendix B. A flowchart to show the logical setup for data acquisition and its analysis is shown in figure (4.1.5).

As in all experiments involving coherent light in optics, the background noise is an important parameter, therefore; the background noise level is stored in the memory 1 of the digital oscilloscope where the interference fringes arising from the the object is stored in the memory 2 of the scope. The difference of the two memories is computed and is stored in the memory 3 of the oscilloscope. This difference is the scan of the actual reconstructed image which is free from the variations in detector sensitivity and fixed fringes associated with the camera, however, this subtraction does not affect the levels of random noise in the image. Thus the data from memory 3 of the oscilloscope is acquired and is analysed on the computer.

The data acquisition system is tested by the experiments using a thin wire (ϕ'=25 μm). The results of the video line 131, acquired manually and using the data acquisition system discussed in this section, are represented in the figure (4.1.6) which shows

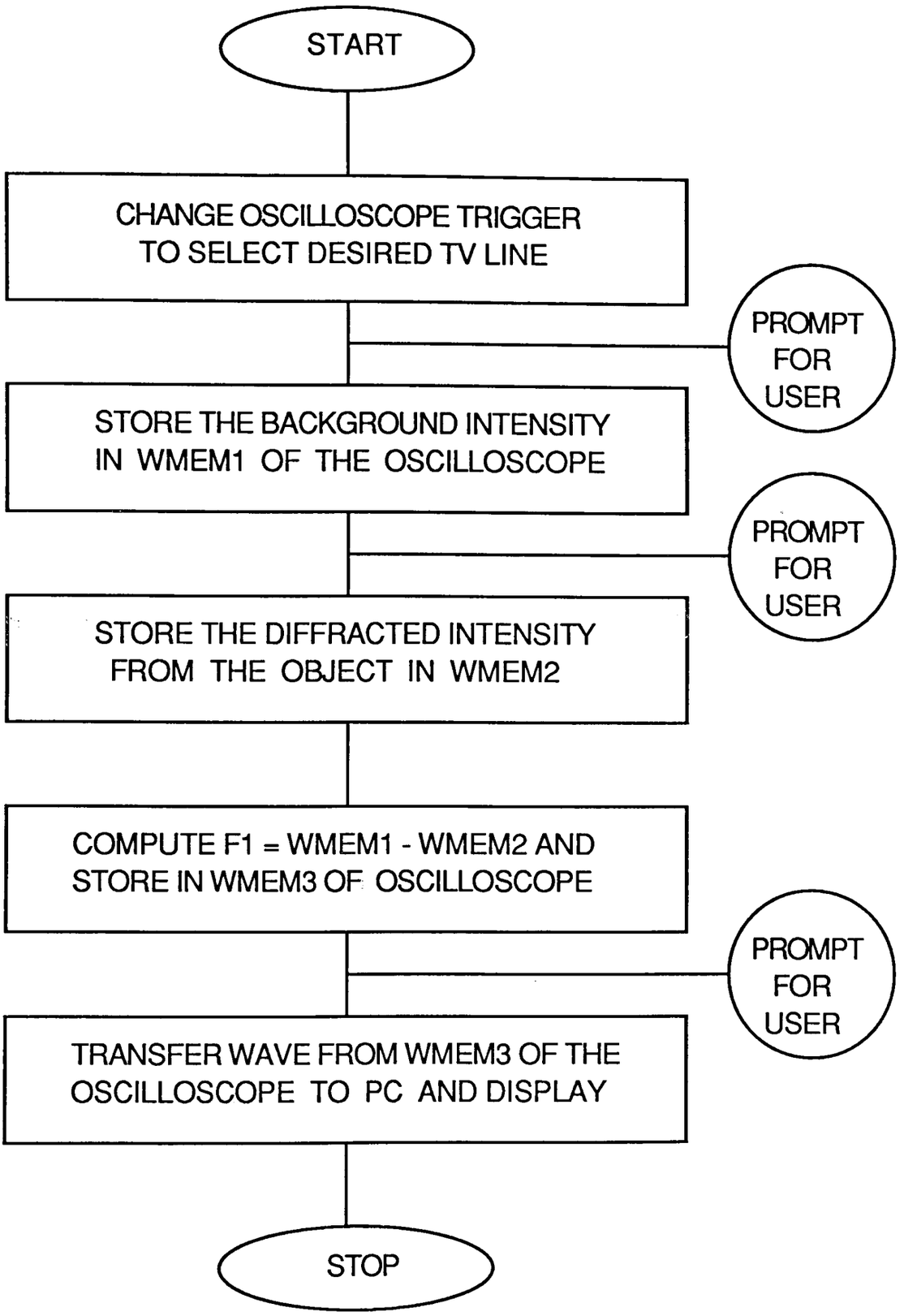

FIG. (4.1.5) Flow chart for the data acquisition using Asystant GPIB

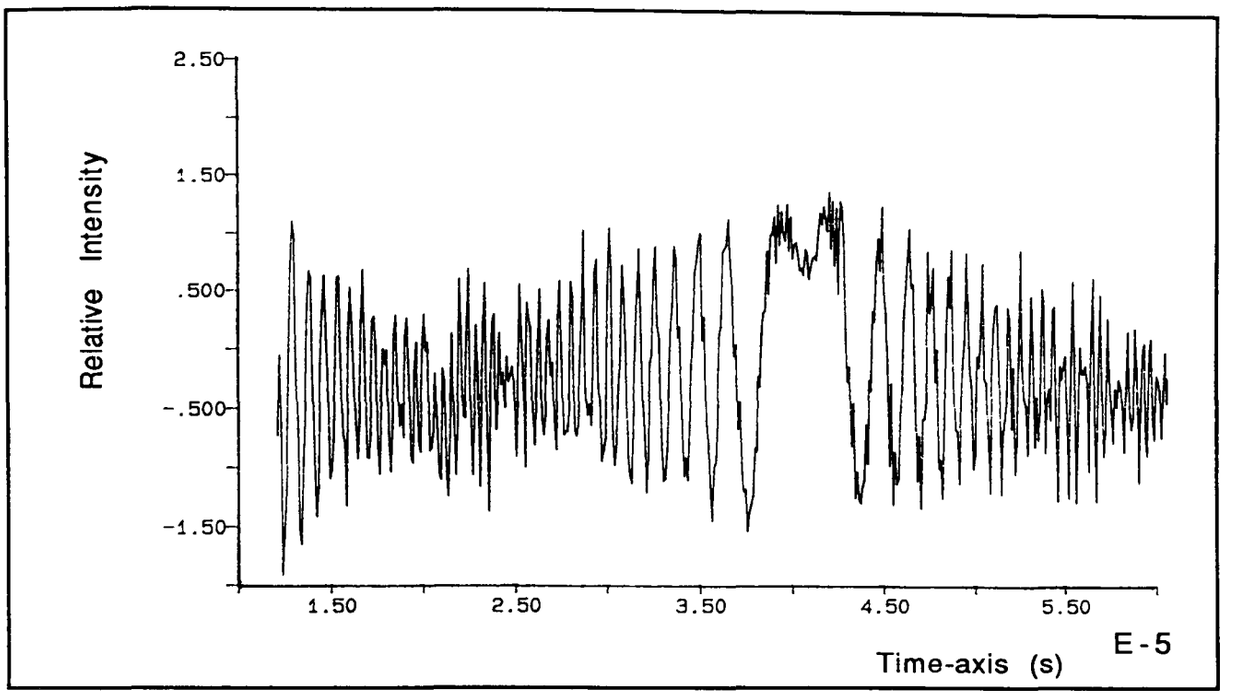

Acquired from the oscilloscope without using Asystant GPIB

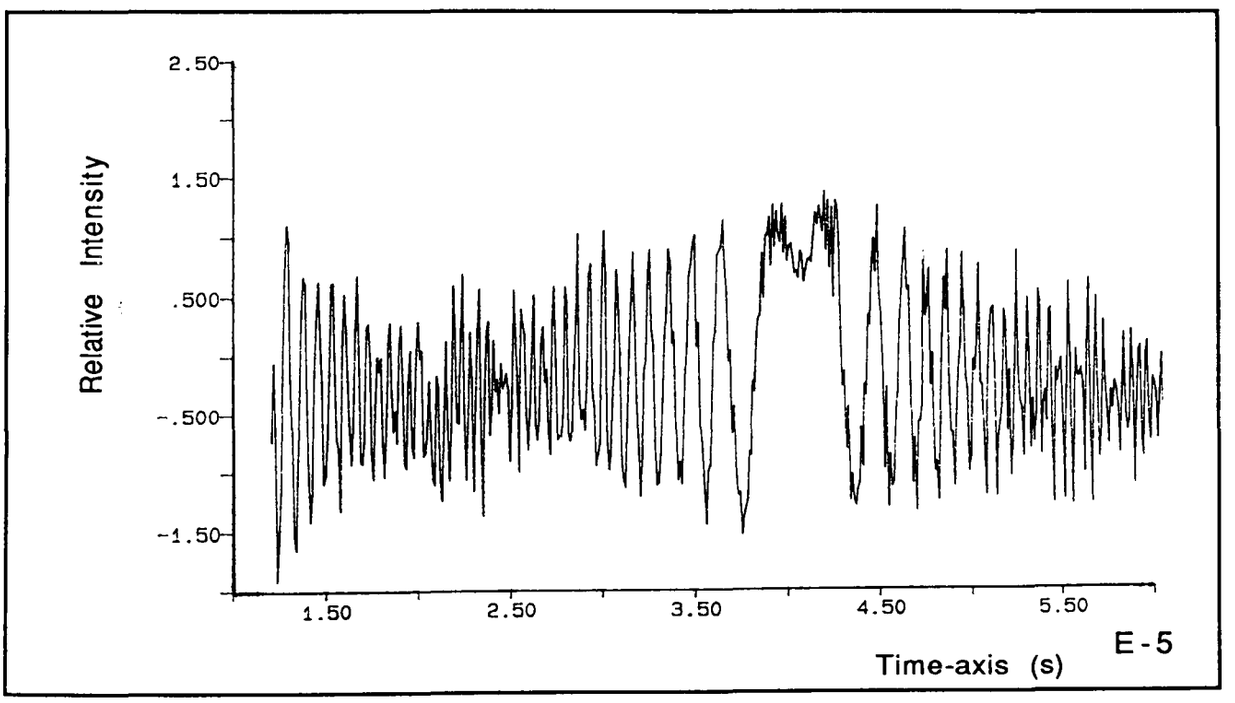

Acquired from the oscilloscope by using Asystant GPIB

FIG. (4.1.6) Comparison of the diffraction patterns arising from a thin wire (ϕ=25 μm) acquired with or without using Asystant GPIB, showing no difference.

that the data can be acquired accurately using Asystant GPIB.

The time scale of the oscilloscope was calibrated to distance scale by placing a thin edge on the micro positioner and the movement of the in focus image of the edge was recorded with corresponding to the actual movement of the edge. A graph between the two movements was plotted as shown in figure (4.1.7), which gives a straight line and shows that the scan of the video camera is linear.

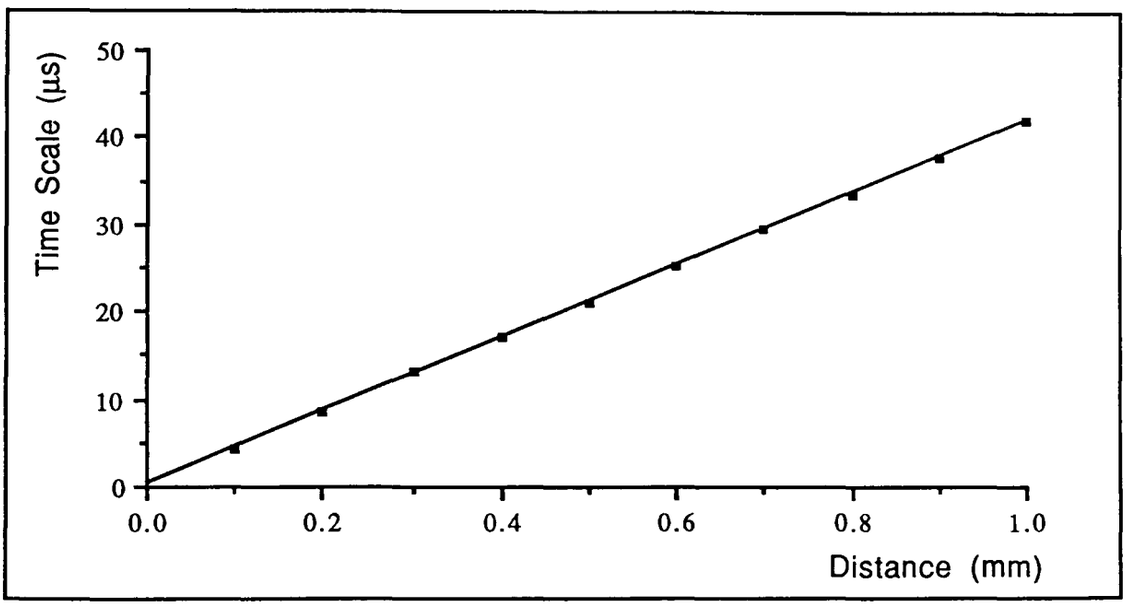

FIG. (4.1.7) GRAPH FOR THE CALIBRATION OF THE TIME SCALE

4.2 COLLIMATING ASSEMBLY

The output of the He-Ne from Melles Griot [05-HHR-321] laser was passed through a collimating assembly to get a highly collimated beam, free from noise. The collimating assembly consisted of a focusing lens, a spatial filter and a collimating lens.

4.2.1 SPATIAL FILTER

The simplest kind of spatial filter is a pinhole located in the focal plane of a microscopic objective, which acts as a low pass filter. This is commonly used to improve the quality of the laser beam by filtering it where the wave front is disturbed due to scattering, reflection or some other causes such as those intrinsic to the laser. The output from spatial filter is an expanded wave front free from noise. A simple spatial filter is shown in the figure (4.2.1).

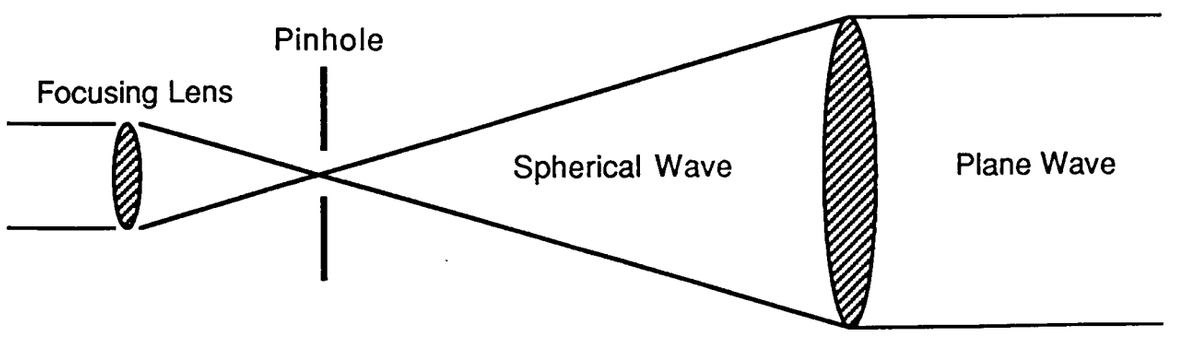

FIG. (4.2.1) A simple spatial filter with collimating lens.

The size of the pinhole should be selected carefully such that only the main lobe of the Fourier transform of the beam can go through. Then only the light rays with an angle of incidence parallel to optical axis before reaching the focusing lens, can pass through and all other rays will be eliminated. The size of the pinhole for a given microscopic objective of known focal length is given by **Micro Control (1988-1989)**.

$$D_p = f \left\{ \frac{2(1.22)\,\lambda}{d_b} + \alpha + 2k_a \left(\frac{d_b}{2f} \right)^3 \right\} \qquad .....(4.1.1)$$

where

f is a focal length of the microscopic objective.

λ is the wave length of the laser.

d_b is the beam diameter of the laser.

α is the divergence of the laser beam.

k_a is the parameter for spherical aberration.

For a He-Ne laser (λ=633 nm, k_a =0.27) of beam diameter (d_b =0.79 mm) and divergence (α =10^{-3} rad) combined with a microscopic objective of focal length (f = 10 mm), the diameter of the pinhole is calculated to be about 30 μm and was used in the experiment.

4.1.2 COLLIMATING LENS

The collimating lens is used to obtain a highly collimated laser beam. To achieve this, the pinhole of the spatial filter is placed at the focal point of the collimating lens. The diverging beam of the laser emerging from the pinhole when falls on the collimating lens, and plane wave is obtained as shown in the figure (4.2.1)

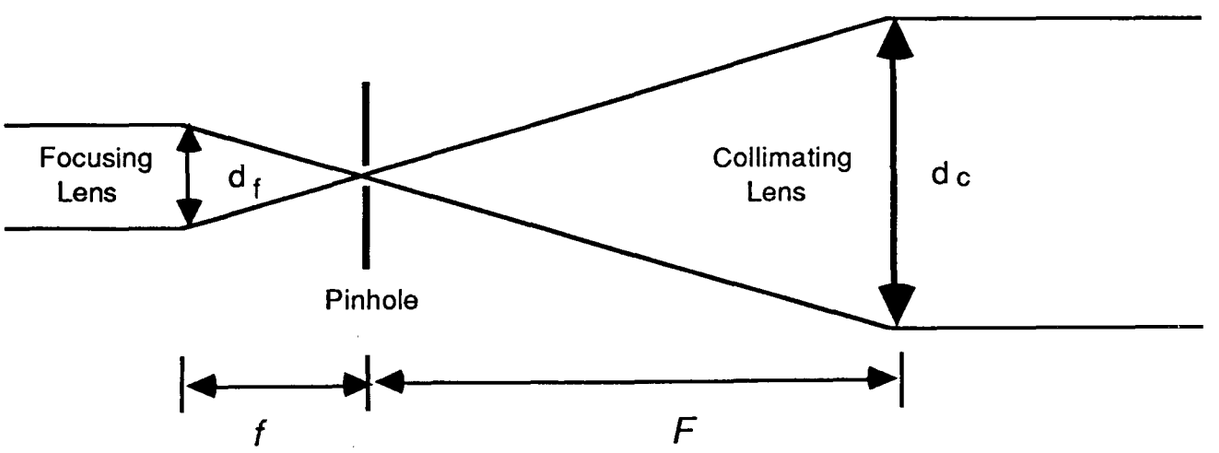

FIG. (4.2.2) Collimating lens with a pinhole and microscopic lens.

From the geometry of the figure (4.2.2), the focal length F of the collimating lens can be calculated by using a simple trigonometric formula:

$$F = \frac{d_f}{d_c} f \qquad \text{.....(4.1.2)}$$

with f = 10 mm, d_f = 0.79 mm and d_c = 50.8 mm, F = 625 mm was calculated. Because of the difficulty of getting a lens of this focal length, a collimating lens of focal length of 500.0 mm and diameter of 50.8 mm (PAC 091 from Newport Ltd.) was used.

4.3. EXPOSURE TIME

The response of the film to exposure by light usually expressed in logarithmic units. This is convenient for several reasons. First, the mass of the silver per unit area in the developed image is related to the logarithm of the transmittance of the film. Second, a characteristic curve plotted in logarithmic units has a long linear portion. Finally, the response of the human eye is approximately logarithmic in bright light **Young (1986)**.

The values of the exposure levels for transmittance Ta=0.5 corresponding to density D=0.6, and other parameters are as reported by **Agfa-Gevaert** given in the table (4.1).

FILM	GRAIN SIZE	RESOLVING POWER	EXPOSURE
10E 75	90.0 nm	3000 Lines/mm	0.50 $\mu J/cm^2$
8E 75HD	35.0 nm	5000 Lines/mm	10.0 $\mu J/cm^2$

TABLE (4.1) Characteristics of photographic emulsions [after Agfa-Gevaert]

For the measurement of exposure level, Ta/E curve is proffered because a hologram acts as a diffraction screen to the incident wave and hence the amplitude transmission is more important consideration. The Ta/E for the emulsions which are commonly used for holography involving red lasers, are shown in the figure (4.3.1) [**Hariharan P. (1989)**]:

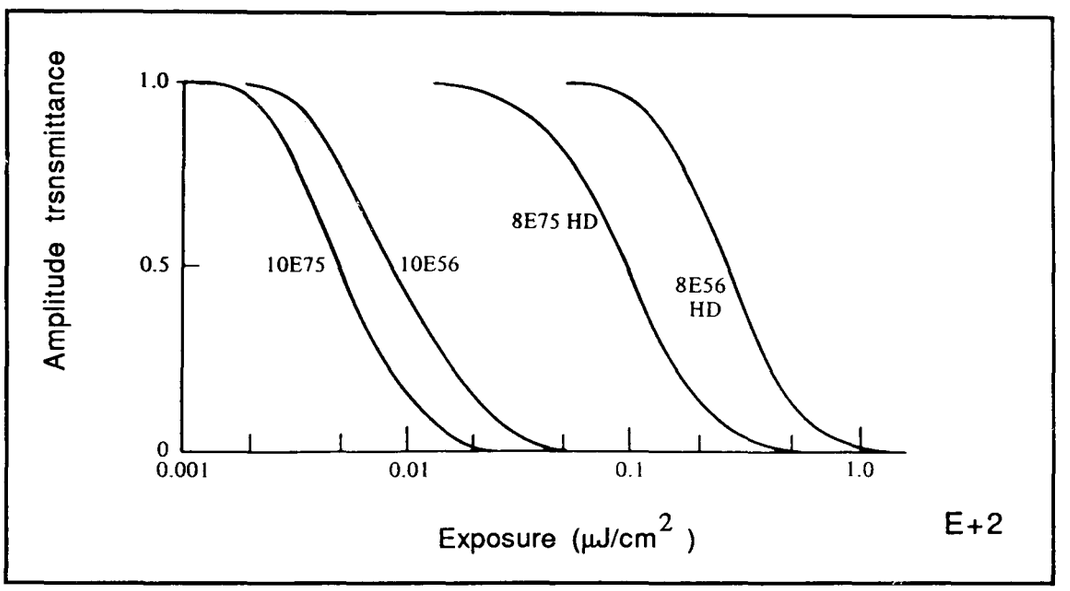

FIG. (4.3.1) Ta/E curves of commonly used emulsions [from Agfa-Gevaert]

If the exposure E for any material is known, the exposure time T can be calculated [**Collier R. J (1971)**].

$$E = \frac{\Phi}{A} \eta_t T \qquad .....(4.3.1)$$

where η_t is the power transfer efficiency from the laser to the recording material, Φ is the output power of the laser and A

is the cross sectional area of the beam illuminating the hologram plate.

As considerable amount of the laser output is lost in the optical arrangement to obtain a degree of uniformity of subject and hologram plate illumination and light incident on each air to glass interface of the optics, therefore; for practical exposure time T, η_t should not be taken more than 5%. [**Collier (1971)**].

In the experiment under discussion, a He-Ne laser with nominal 5 mW output power and cross sectional area for the illuminating beam of about A= 20 cm^2 was used. The exposure time for both the photographic emulsions is calculated and is given by:

T = 0.04 s	E =0.50 $\mu J/cm^2$	for 10E 75
T = 0.80 s	E =10.0 $\mu J/cm^2$	for 8E 75HD

Nassenstein at el.(1969) have shown that for optimum performance, a hologram should be given a finite exposure with little tolerance. The best exposure time for Agfa 8E 75HD emulsion was determined experimentally by recording an in-line hologram of a 25.0 μm thin wire, and is found to be about 1.0 s. All the optical components used in the experiment have been aligned carefully to within $\pm$100.0 μrad., using the back reflection technique. The holograms produced were developed using the

standard developing chemicals from **LAZA Holograms**. Details of the development procedure are given in appendix C.

4.4 DESIGN OF THE TEST OBJECT

It has been mentioned earlier that in the present study a system of two discs is investigated. For the sake of mathematical simplicity two discs of the same radius are considered lying in the same depth plane. Hence the test object is designed to test the theory cited in the chapter 3 and is shown in the figures (4.4.1) and (4.4.2). Diameter of each disc in each row is given in table (4.2).

Row indentifier	A	B	C	D	E
Diameter of Discs (μm)	50	100	150	200	300

Table (4.2) Diameter of discs in each row.

The figure (4.4.1) shows the location of these discs on the glass substrate. The pattern consists of five colmns and five rows. Separation between the discs of each pair, remains constant in each column where each row contain pairs of discs of same diameter but the separation between the discs of each pair is different for each column. Figure (4.4.2) shows the pattern of the pairs of opaque discs in each row. Care was taken to ensure the

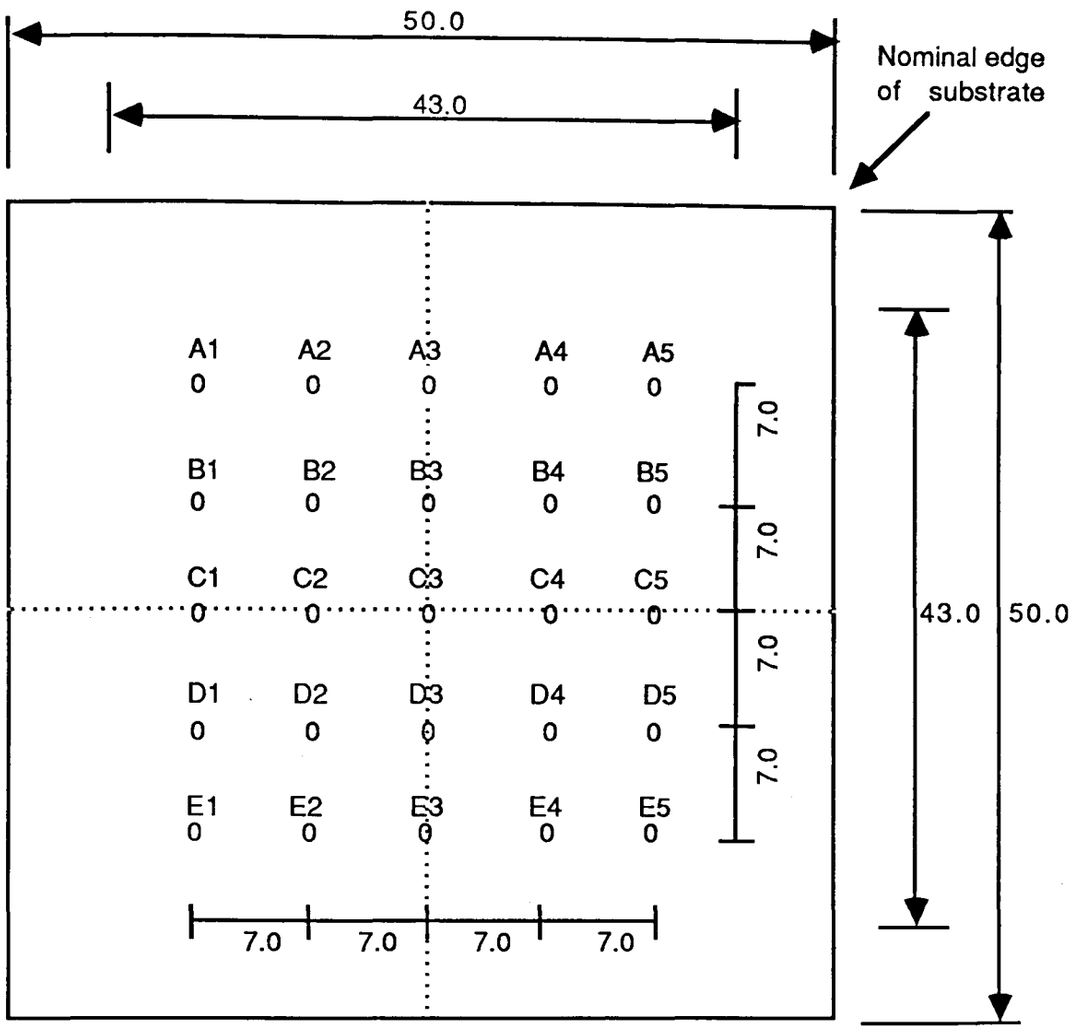

FIG. (4.4.1) Location of discs on substrate [measurements in mm]

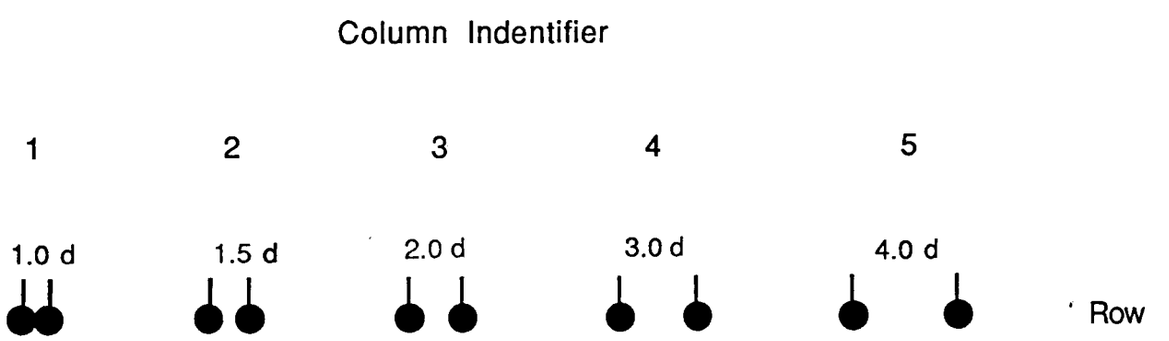

FIG. (4.4.2) Pattern of the opaque discs

uniformity of diameter in a given row rather than the absolute value.

The pattern was produced by thin film evaporation technique on a circular BK7 substrate of 75.0 mm diameter by **Datasights Ltd**. The technical details of the BK7 substrate are given in appendix D. After fabrication, the pattern on the substrate was carefully measured at the Department of Physics and Astronomy, University College, London. The measured values of the diameter ($2a$) of the discs and their separation in different rows are given in table (4.3).

ROWS	COLUMNS 1	2	3	4	5
$2a$ =50 μm					
A	0.0 μm	26 μm	50 μm	101 μm	150 μm
$2a$ =100 μm					
B	0.0 μm	50 μm	100 μm	200 μm	300 μm
$2a$ =150 μm					
C	0.0 μm	N.M	N.M	N.M	N.M
$2a$ =200 μm					
D	0.0 μm	N.M	N.M	N.M	N.M
$2a$ =300 μm					
E	0.0 μm	149 μm	299 μm	600 μm	900 μm

N.M Not measured.

Table (4.3) Measured diameter of discs and their separation, errors are ± 1.0 μm.

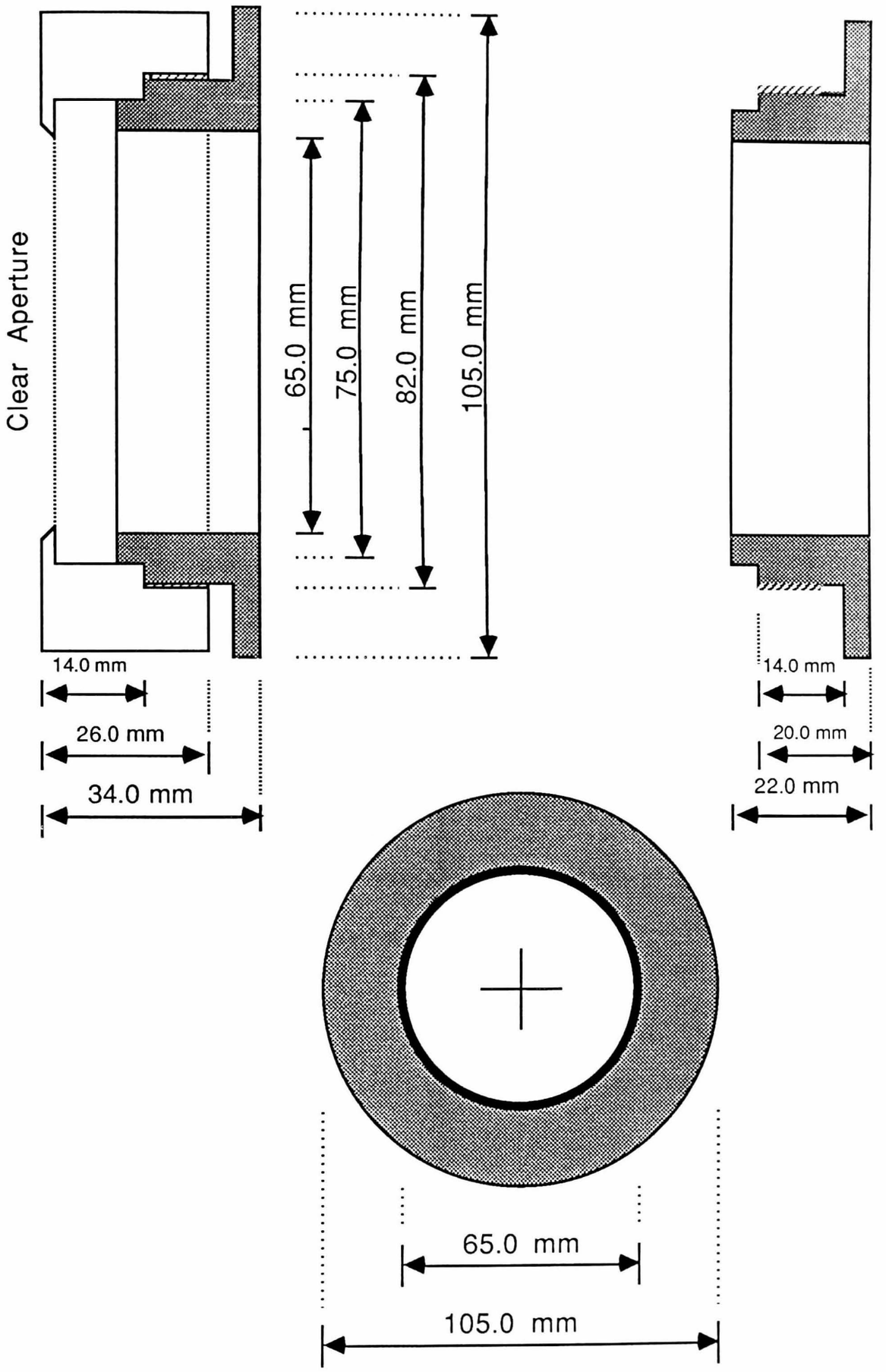

FIG (4.4.3) Drawing of the test object holder.

A circular holder was designed and fabricated to mount the test object on a three dimensional micro positioner base. The design of the circular holder is shown in figure (4.4.3). The three dimensional micro positioner base is assembled by using three manual micro positioners from Ealing Opto Electronics, which can readout to ± 10 μm.

4.5 PLACEMENT OF THE APERTURE

In the problem under investigation, the effect of the limiting aperture on the resolution of the hologram is an important parameter to be studied. In the theoretical model Ω is the limiting aperture parameter, thus different values of Ω (3.832, 7.016, 10.173, 13.324, 19.616) were chosen to limit the recorded information on the hologram. These values of Ω are the first, second , third, fourth, and sixth zeros of the Bessel function which correspond to the number of maxima in the diffraction pattern recorded on the hologram. Thus the number of maxima recorded on the hologram can be counted by choosing these value of Ω.

The information recorded on the hologram can be limited experimentally, by using a physical aperture and three different techniques of aperture limiting were tested. The size of an aperture can be calculated by the equation:

$$\Omega = \frac{kaH}{Z_1} \quad where \quad k = \frac{2\pi}{\lambda} \qquad .....(4.5.1)$$

Here H is the size of the aperture, a the radius of the disc and Z_1 is the recording distance of the hologram.

In the first technique a fixed aperture of 3.0x3.0 mm^2 was placed just after the collimating lens ($H = \pm 1.5$ mm). The required values of Ω were obtained by selecting a suitable recording distance Z_1. A hologram of the target disc group C2 (a =75 μm) was recorded and developed for Ω = 19.616. The results are shown in figure (4.5.1).

In the second technique the same fixed aperture was placed just before the recording plane and the results of the image of disc group C2 for Ω = 19.616 are shown in figure (4.5.2).

It was observed that the diffraction pattern from the aperture were also present in the reconstructed image. The other main disadvantage of these two techniques was that the recording distance is also limited because of the use of a fixed aperture since the recording distance is inversely proportional to Ω. Thus for higher values of Ω the recording distance is smaller than those for the smaller values of Ω.

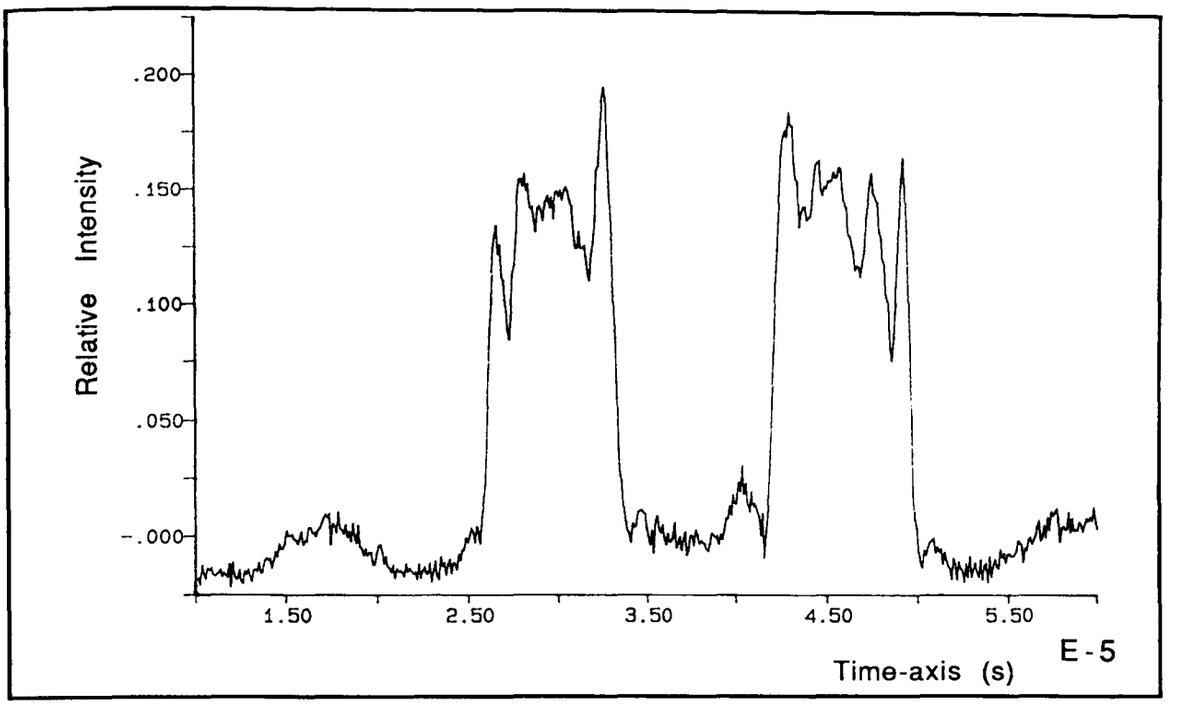

FIG. (4.5.1) Aperture placed just after the collimating lens [$H = \pm 1.5$ mm].

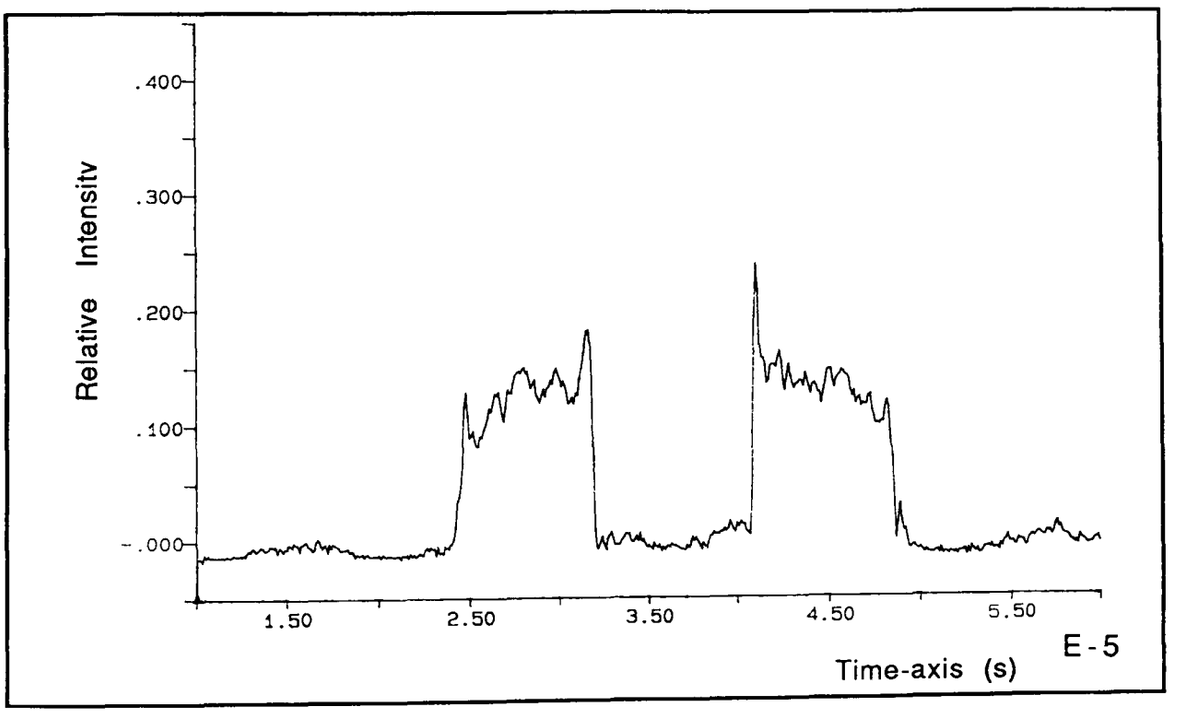

FIG. (4.5.2) Aperture placed just before the recording plane [$H = \pm 1.5$ mm].

Finally a hologram of the whole test substrate was recorded at the recording distance of 175.0 mm which corresponds a recording distance of 5 far-fields for discs of 150.0 μm in diameter. An aperture was placed on the non emulsion side of the developed hologram in the reconstruction stage. The results of the image from discs C2 for Ω = 19.616 are shown in figure (4.5.3) which is, because of low background noise and symmetry in the reconstructed image, clearly better than the previous results. This technique also allows full control over the recording distance which was kept constant at (Z_1 =175 mm) for different values Ω. Hence the effect of the recording distance can also be studied.

The only disadvantage of the technique is that aperture of different sizes corresponding to different values of Ω were to be used. The size of the aperture was calculated using equation (4.5.1). The recording distance (Z_1 = 175 mm) and the radius of the disc (a = 75 μm) was kept constant in the experiment. The calculated values of apertures for different values of Ω are given in table (4.4).

It is important to note that the the experimental results are highly repeatable, the repeatability of the experimental results is shown in figure (4.5.4).

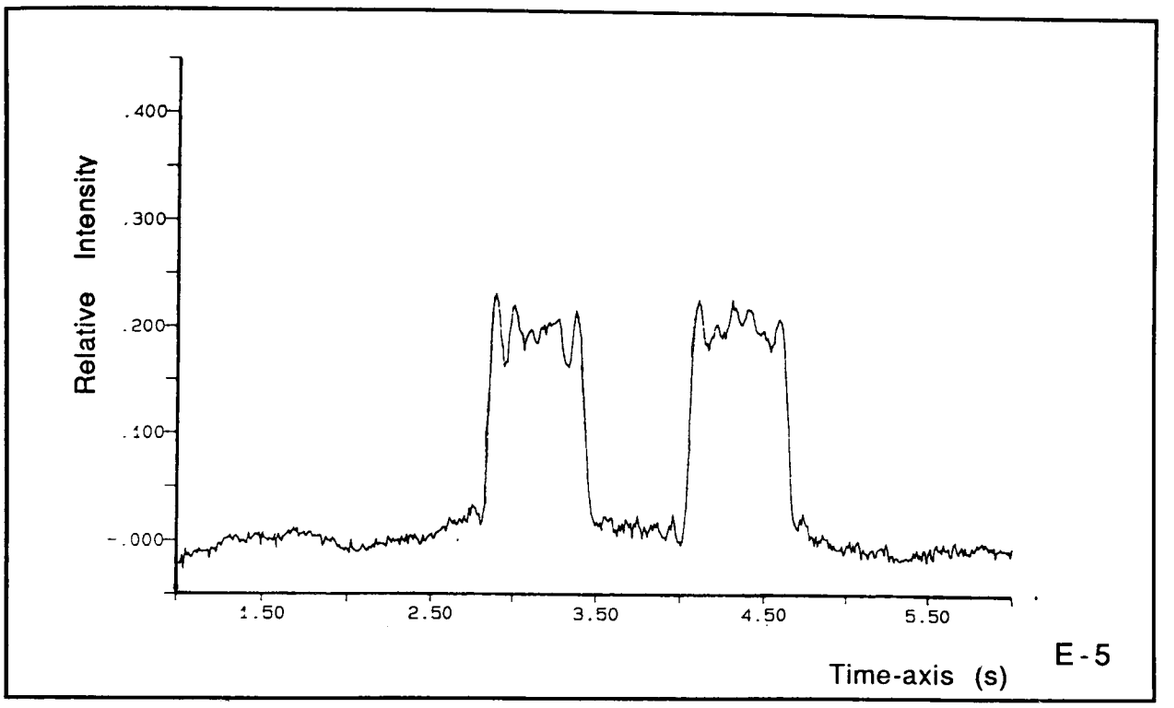

FIG. (4.5.3) Aperture placed on the developed hologram in the reconstruction stage.

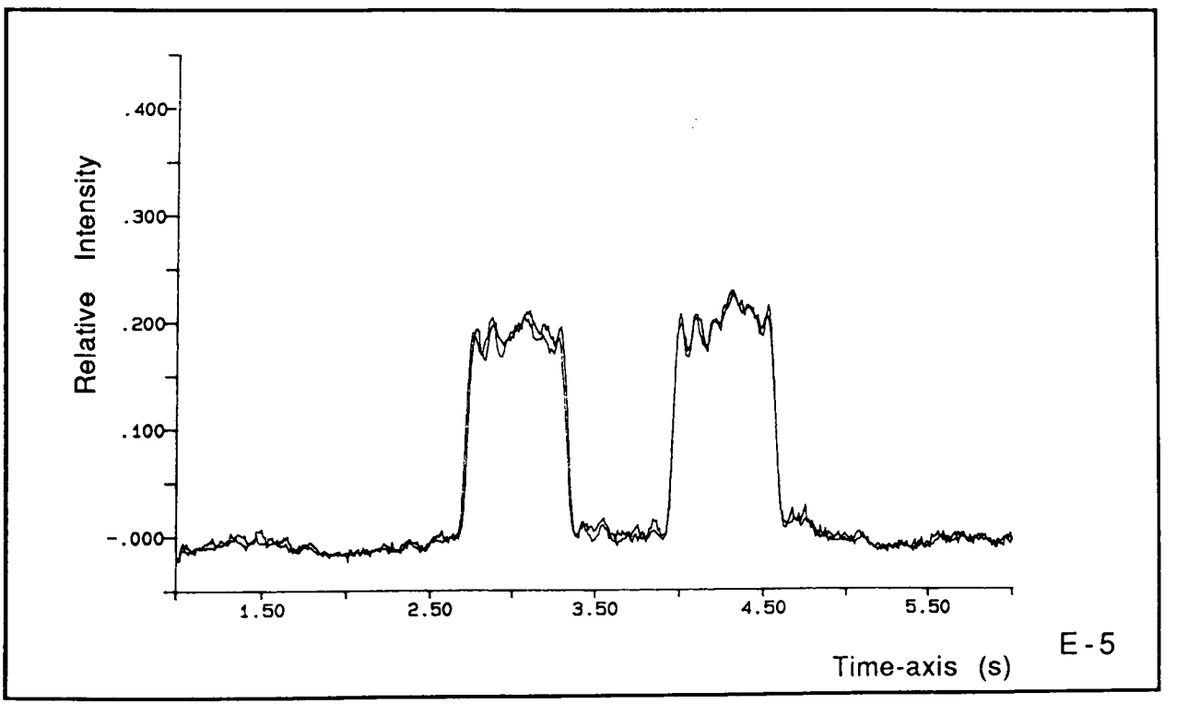

Fig. (4.5.4) repeatability of the experimental results.

VALUE OF Ω	CALCULATED SIZE (mm^2)	MEASURED SIZE (mm^2)	ERROR
3.832	1.8 x 1.8	1.6 x 1.6	-11.1%
7.016	3.3 x 3.3	3.0 x 3.0	-9.1%
10.173	4.8 x 4.8	4.6 x 4.6	-4.2%
13.324	6.3 x 6.3	6.1 x 6.1	-3.2%
19.616	9.2 x 9.2	8.9 x 8.9	-3.3%

$$\text{Errors (\%)} = \frac{\text{Measured - Calculated}}{\text{Calculated}} .100$$

TABLE (4.3) Calculated and measured sizes of the aperture [a =75 μm, Z_1 =175 mm].

CHAPTER 5

ANALYSIS OF RESULTS

In this chapter all the data acquired experimentally is presented and compared with theoretical values to verify the theory cited in chapter 3. The radius and separation of the discs was measured using three different criteria to evaluate the inherent theoretical errors. The same measurements were also done on the experimental data and the results are compared with those obtained with the theoretical values. Table (5.1) gives the values of all the parameters for which the data was collected and analysed.

5.1 THEORETICAL DATA AND ANALYSIS

The equation (3.3.19) which described the intensity distribution in the image formed from a finite aperture hologram can only be solved numerically. Because of the use of a square aperture in the experiment, the double integrals were solved over a square domain bounded on [-1,1 ; -1,1]. Both of the integrands are oscillatory functions and involve trigonometric functions with large radian arguments. These aspects lead to the use of double precision variables and a high order Gaussian Quadrature integration formula.

No.	Ω	GROUP	SEPARATION (2b)	ΔZ
1	3.832	C1	150 μm	0.0 mm
2	3.832	C2	225 μm	0.0 mm
3	3.832	C3	300 μm	0.0 mm
4	7.016	C1	150 μm	0.0 mm
5	7.016	C1	150 μm	-3.5 mm
6	7.016	C2	225 μm	0.0 mm
7	7.016	C2	225 μm	-3.5 mm
8	7.016	C3	300 μm	0.0 mm
9	7.016	C3	300 μm	-3.5 mm
10	10.173	C1	150 μm	0.0 mm
11	10.173	C2	225 μm	0.0 mm
12	10.173	C3	300 μm	0.0 mm
13	13.324	C1	150 μm	0.0 mm
14	13.324	C1	150 μm	-3.0 mm
15	13.324	C1	150 μm	-4.5 mm
16	13.324	C2	225 μm	0.0 mm
17	13.324	C2	225 μm	-3.0 mm
18	13.324	C2	225 μm	-4.5 mm
19	13.324	C3	300 μm	0.0 mm
20	13.324	C3	300 μm	-3.0 mm
21	13.324	C3	300 μm	-4.5 mm
22	19.616	C1	150 μm	0.0 mm
23	19.616	C1	150 μm	-3.0 mm
24	19.616	C1	150 μm	-4.5 mm
25	19.616	C2	225 μm	0.0 mm
26	19.616	C2	225 μm	-3.0 mm
27	19.616	C2	225 μm	-4.5 mm
28	19.616	C3	300 μm	0.0 mm
29	19.616	C3	300 μm	-3.0 mm
30	19.616	C3	300 μm	+3.0 mm
31	19.616	C3	300 μm	-4.5 mm
32	19.616	C3	300 μm	+4.5 mm

a 75 μm for all groups.
Ω The limiting aperture parameter.
2b Center to Center separation of the discs.
$\Delta Z = Z_2 - Z_1$ The focusing parameter.

Table (5.1) parameters for which the data was acquired

Gaussian Quadrature was chosen as the integration technique because of its ability to solve accurately the integrals involving high order polynomials [an n order technique will exactly solve a polynomial integral of order $(2n-1)$], and because of its simple extension to two dimensions. It should be noted that it is not the most efficient integrator for multiple dimensions, but in practice it is usually the method of choice [see **Belz R. A (1971)**]. A 96-point formula was used with coefficients and weights taken from **Abramowitz and Stegun (1970)**, and coded to 6 significant figures.

A computer programme was written by Dr. Hobson, Brunel University, in FORTRAN 77 to solve the double integrals for arbitrary values of the parameter Ω, Z_1, and Z_2. The wavelength was encoded as a parameter, and kept fixed at 633 nm. The range of the values in the image plane for which the integral was solved, were further freely chosen input parameters to the programme. For useful contour plots a naive calculation shows that the integrand must be evaluated about 10^7 times. This demanded efficient coding in order to limit computation time, even using a reasonably fast processor (a VAX station 3100 running VMS). Following initial tests using the performance analyser tool PCA,

the terms involving the Bessel function in the integral were separated out, since these are neither a function of the image plane co-ordinates nor of the integration variables. Thus these could be precalculated and taken out of each integral as a constant multiplicative factor. With further optimisation, the calculation time for a 96 by 96 point image was reduced to about 9 hours of CPU time, which was acceptable, given the access to several Batch queues overnight. The data was stored in a simple FORTRAN formatted file to allow it to be easily read into the two interactive programmes PAW and UNIMAP which were used to produce graphical plots.

Contour plots of all the in-focus and out-of-focus predicted images of group C3 for Ω=19.616 are shown in figures (5.1.2) to (5.1.9). Photographs taken from the monitor for the observed images of group C3 for Ω=19.616 and ΔZ = 0.0, -3.0 mm, -4.5 mm, are included in the figures (5.1.7) to (5.1.9) for a qualitative comparison of the theoretically calculated and experimentally obtained images. The contour plots show that the predicted images have a plane of mirror symmetry (μ=0.0).

Line scan through the centre of the observed image (υ=0) are also plotted for images whose parameters are listed in

table (5.1) and were compared with the respective computer plots through the center of the predicted images. Line scans of all the in focus computed and observed images were used to take the measurement of the discs diameter and separation. Three measurements criteria are explained in figure (5.1.1).

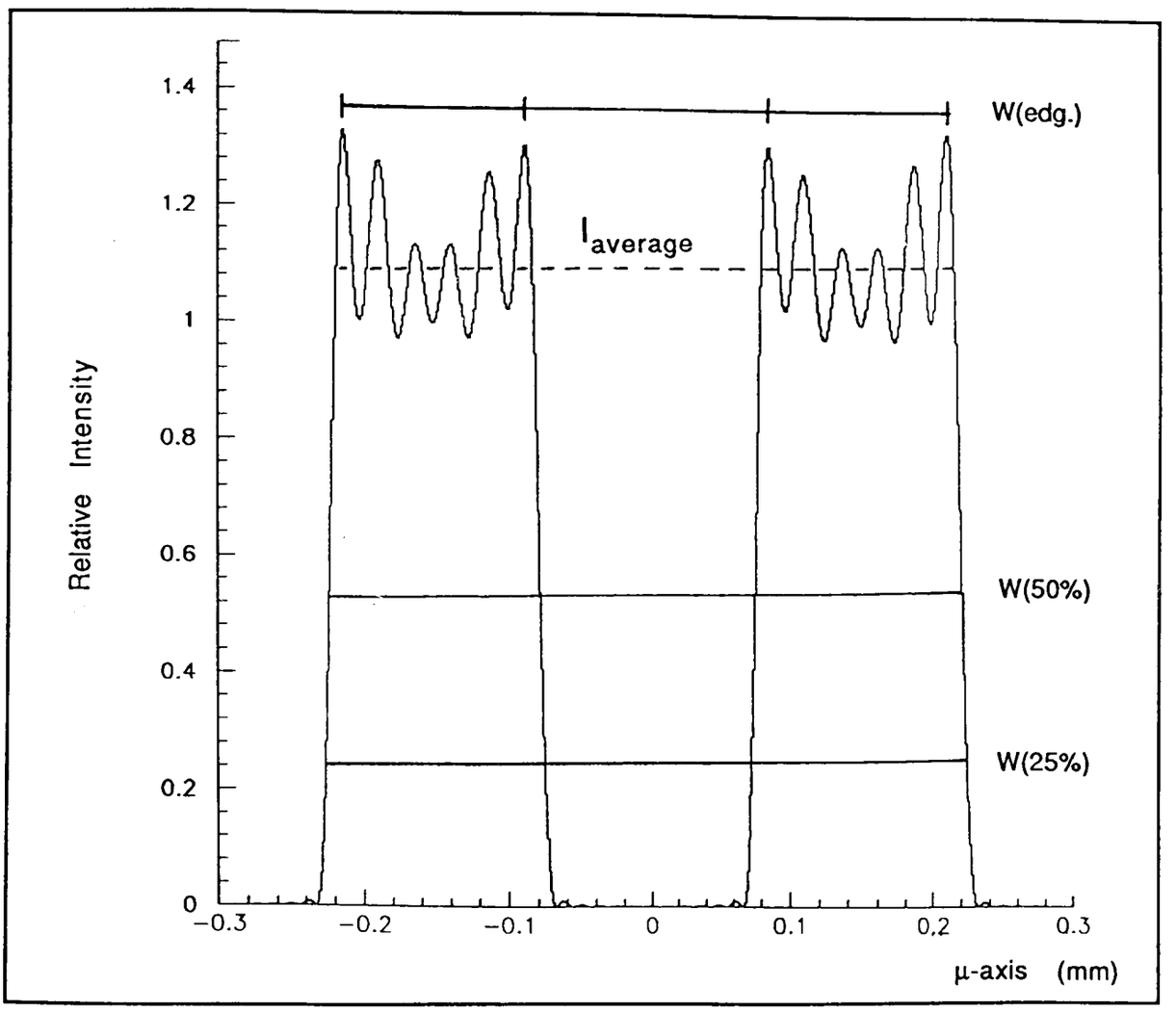

W(25%) = 25% of the center intensity.

W(edg.) = Separation of the two outer most peaks.

W(50%) = 50% of the average image intensity.

FIG. (5.1.1) Computed plot through the center of in focus image of the group C3 [a=75 μm, 2b=300 μm] for Ω=19.616, showing the measurement criteria.

W(25%) is the width measured where the edge intensity is 25% of the center intensity of each disc in the image. Because of two touching discs in group C1, W(25%) was measured where the edge intensity was 25% of the intensity at the center of the entire image. These measurements are tabulated in table (5.2).

GROUP	7.016	10.173	13.324	19.616
Actual: 300 μm				
C1	0.0%	0.8%	0.0%	-1.5%
Actual: 150 μm				
C2(d)	4.6%	-1.5%	0.0%	0.0%
Actual: 75 μm				
C2(s)	-13.9%	4.6%	-1.5%	-1.5%
Actual: 150 μm				
C3(d)	4.6%	-1.5%	0.0%	0.0%
Actual: 150 μm				
C3(s)	-7.6%	1.5%	0.0%	0.0%

C(d) measurement of the diameter.
C(s) measurement of the separation.

$$\text{Error \%} = \frac{\text{Measured - Actual}}{\text{Actual}} .100\%$$

Table (5.2) Table of accuracy of measurements W(25%) [W(25%) = 25% of the center intensity].

W(edg.) is the separation of the outermost peaks of intensity in the image and the errors arising from these measurements are listed in table (5.3).

GROUP	7.016	10.173	13.324	19.616
Actual: 300 μm				
C1	-20.0%	-16.2%	-13.1%	-9.2%
Actual: 150 μm				
C2(d)	-44.6%	-35.4%	-26.2%	-16.9%
Actual: 75 μm				
C2(s)	90.8%	66.2%	53.9%	29.2%
Actual: 150 μm				
C3(d)	-44..6%	-35.4%	-26.2%	-16.9%
Actual: 150 μm				
C3(s)	46.2%	38.5%	26.2%	13.8%

C(d) measurement of the diameter.
C(s) measurement of the separation.

$$\text{Error \%} = \frac{\text{Measured - Actual}}{\text{Actual}} .100\%$$

Table (5.3) Table of percentage errors for measurements W(edg.) [W(edg.) = Separation of the two outer most peaks].

W(50%) is the width measured where the edge intensity is 50% of the average image intensity in the region of the disc and the errors inherent to these measurements are tabulated in table (5.4).

GROUP	7.016	10.173	13.324	19.616
Actual: 300 μm				
C1	-3.1%	-3.1%	-3.1%	-3.1%
Actual: 150 μm				
C2(d)	-6.2%	-9.2%	-4.6%	-3.1%
Actual: 75 μm				
C2(s)	7.6%	20.0%	4.6%	4.6%
Actual: 150 μm				
C3(d)	-6.2%	-9.2%	-4.6%	-3.1%
Actual: 150 μm				
C3(s)	4.6%	7.7%	6.2%	1.5%

C(d) measurement of the diameter.
C(s) measurement of the separation.

$$\text{Error \%} = \frac{\text{Measured - Actual}}{\text{Actual}} .100\%$$

Table (5.4) Table of percentage errors for measurements W(50%) [W(50%) = 50% of the average image intensity].

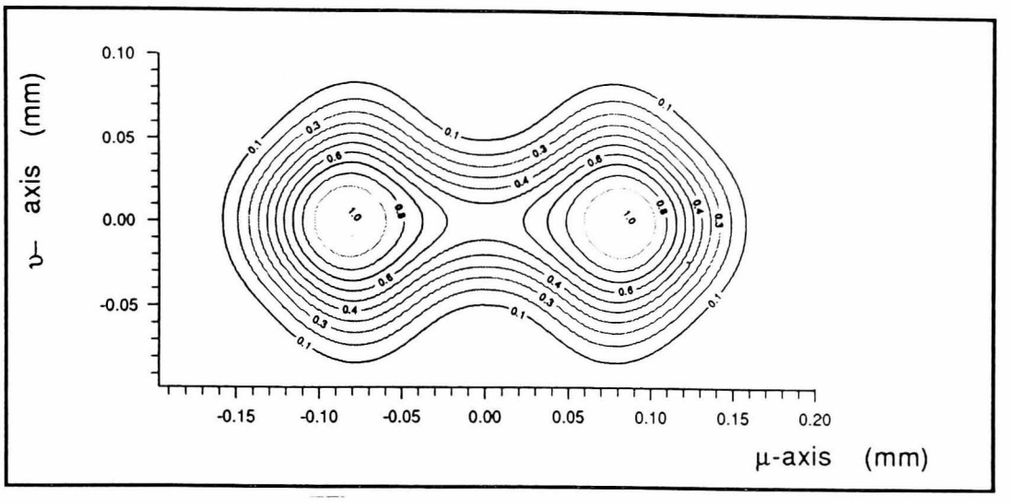

Group C1, Two touching Discs a=75 μm, 2b=150 μm

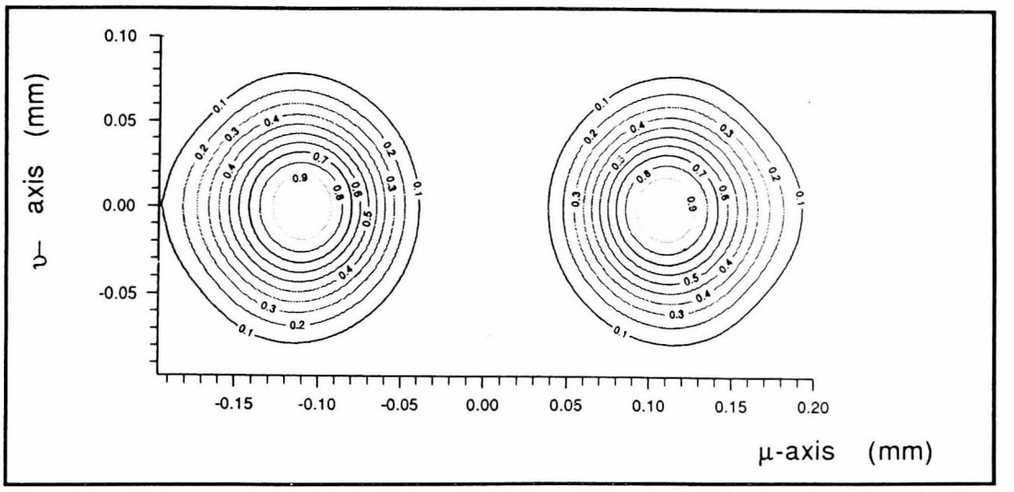

Group C2, a=75 μm, 2b=225 μm

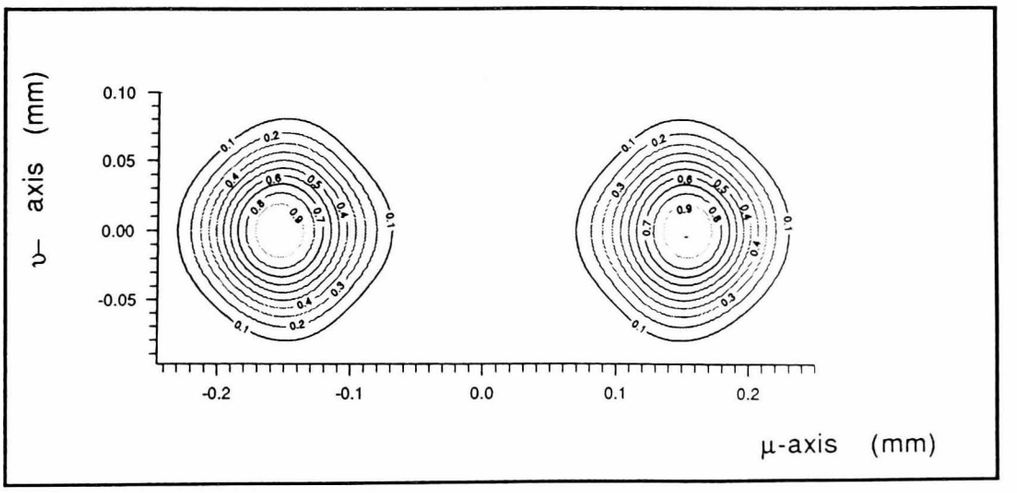

Group C3, a=75 μm, 2b=300 μm

FIG. (5.1.2) Contour plots of in-focus images for for Ω = 3.832 [ΔZ=0.0]

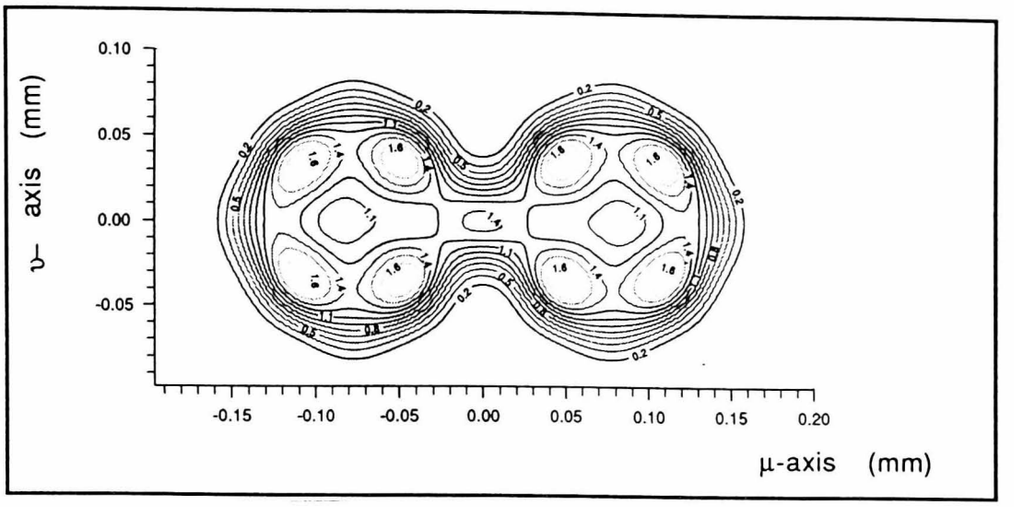

Group C1, Two touching Discs a=75 μm, 2b=150 μm

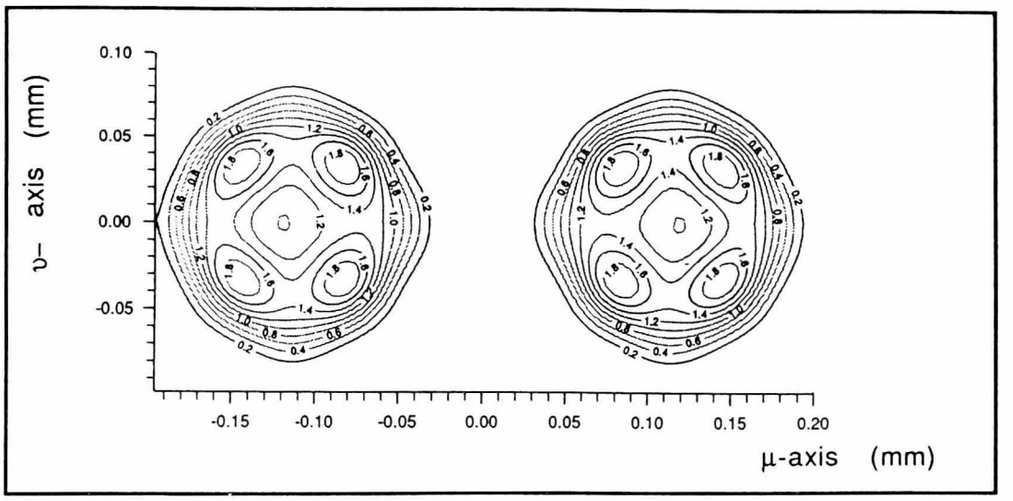

Group C2, a=75 μm, 2b=225 μm

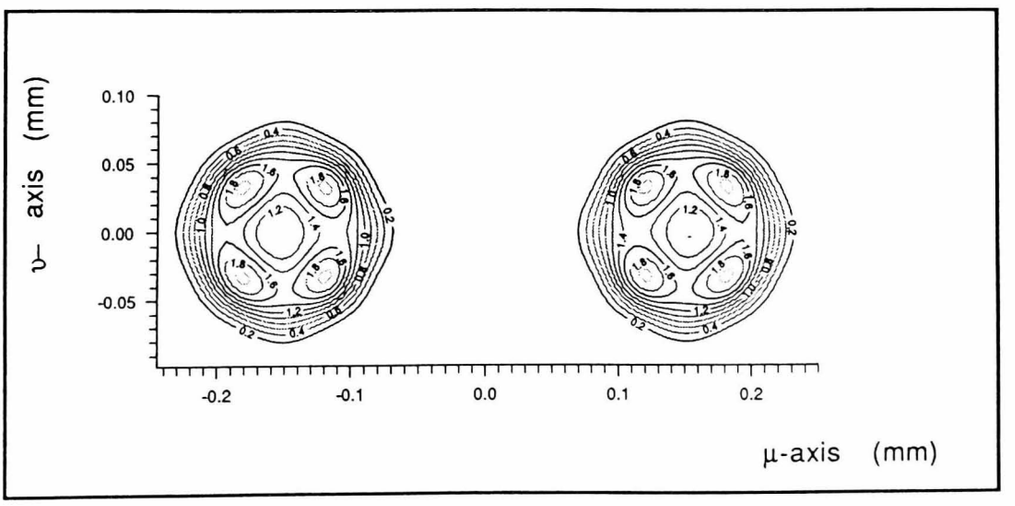

Group C3, a=75 μm, 2b=300 μm

FIG. (5.1.3) Contour plots of in-focus images for for Ω = 7.016 [ΔZ=0.0]

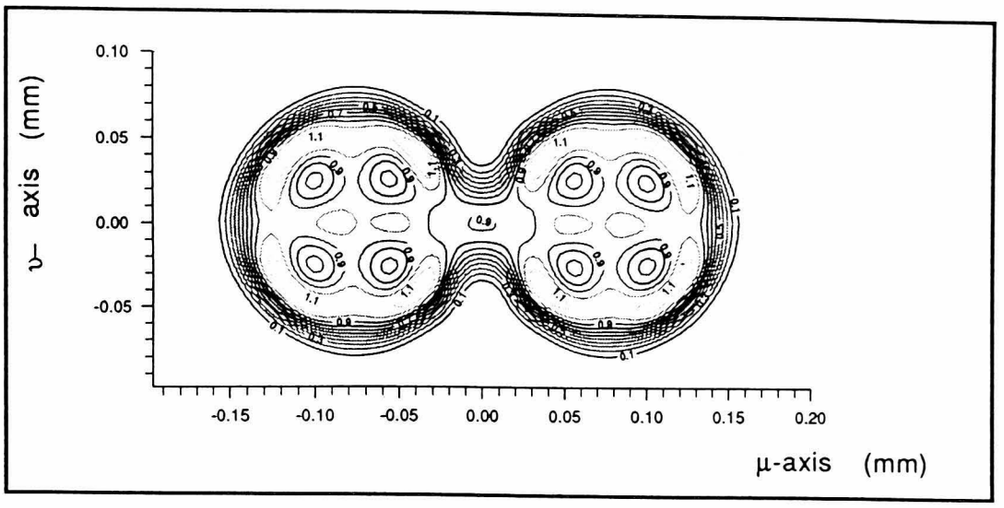

Group C1, Two touching Discs a=75 μm, 2b=150 μm

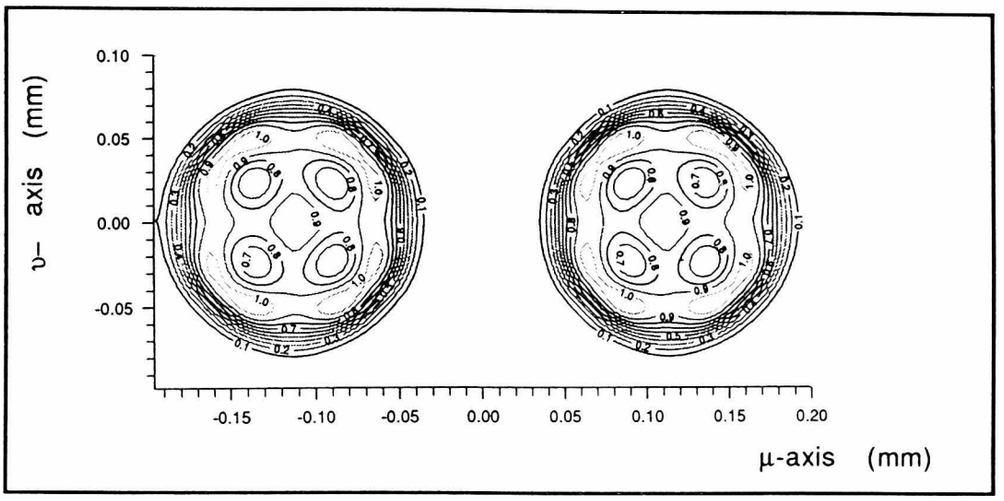

Group C2, a=75 μm, 2b=225 μm

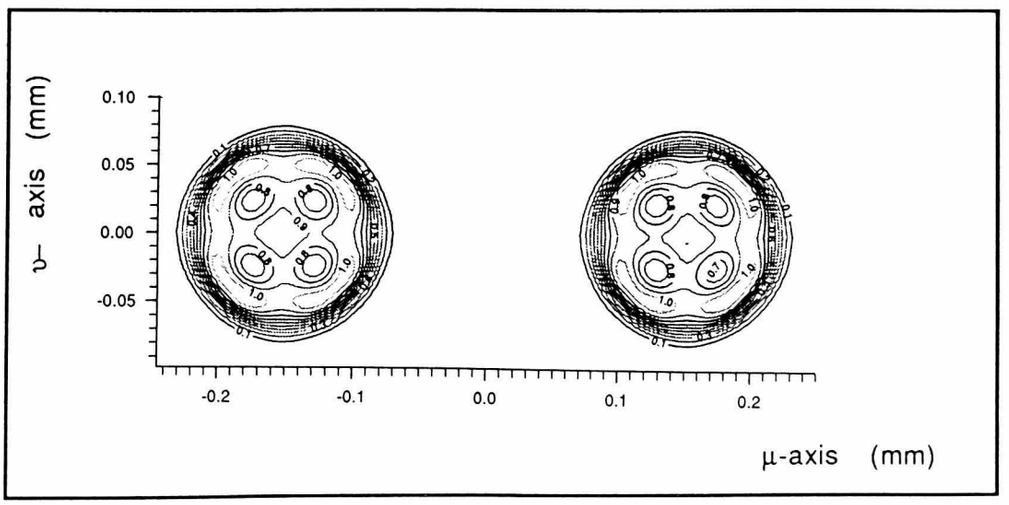

Group C3, a=75 μm, 2b=300 μm

FIG. (5.1.4) Contour plots of in-focus images for for Ω = 10.173 [ΔZ=0.0]

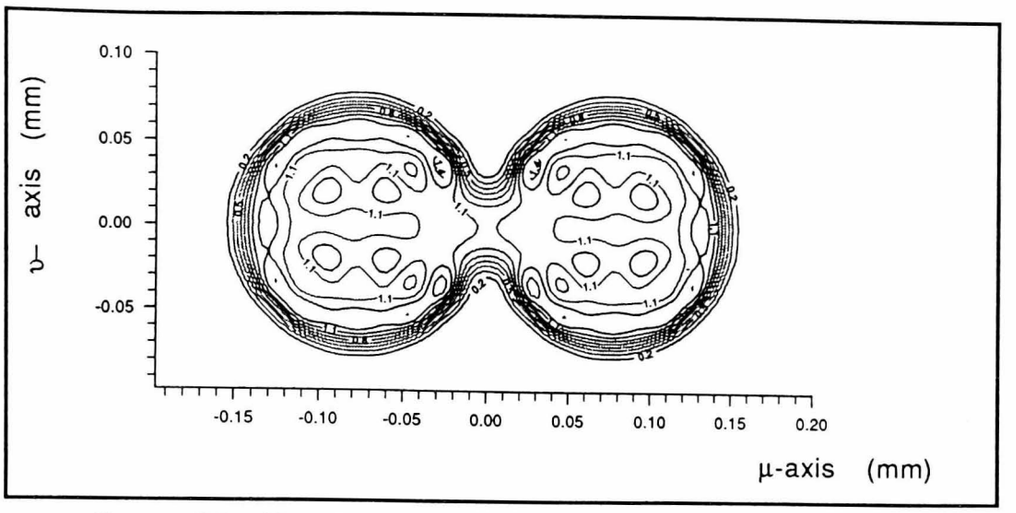

Group C1, Two touching Discs a=75 μm, 2b=150 μm

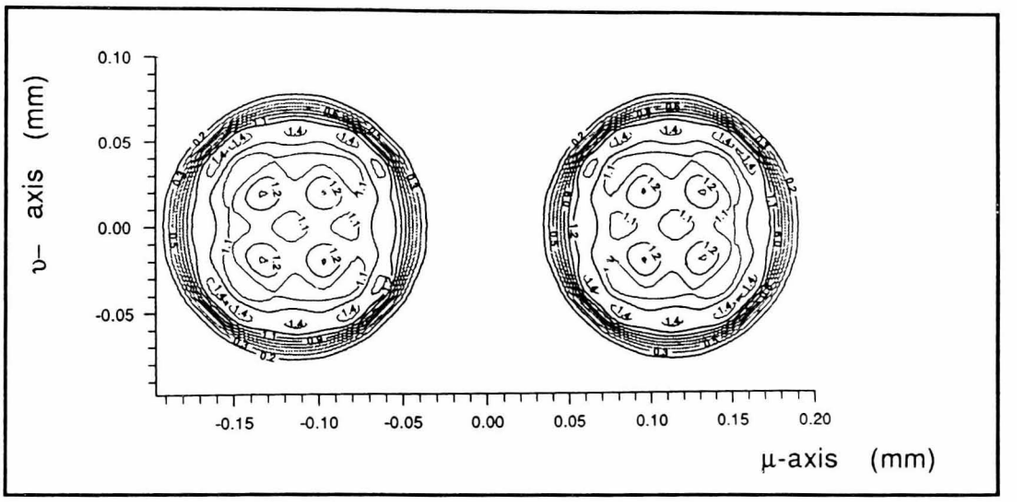

Group C2, a=75 μm, 2b=225 μm

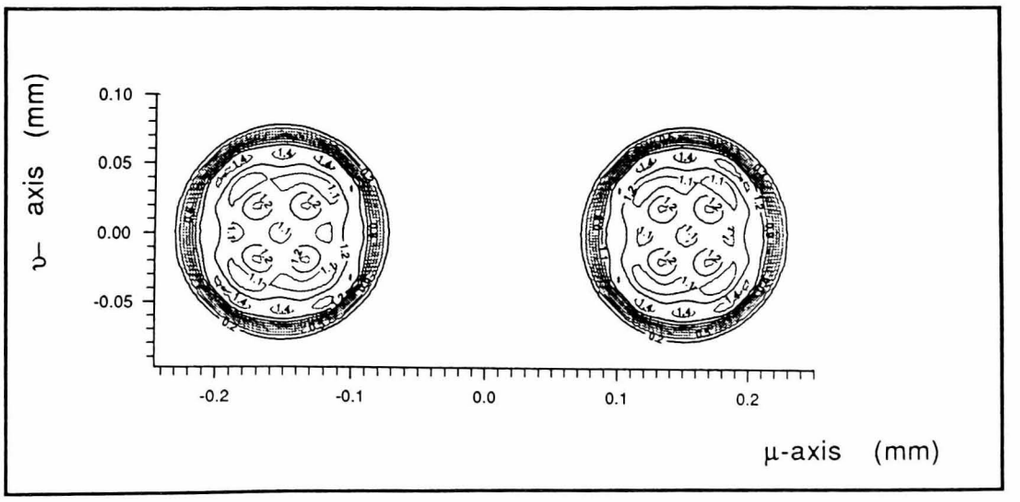

Group C3, a=75 μm, 2b=300 μm

FIG. (5.1.5) Contour plots of in-focus images for for Ω = 13.324 [ΔZ=0.0]

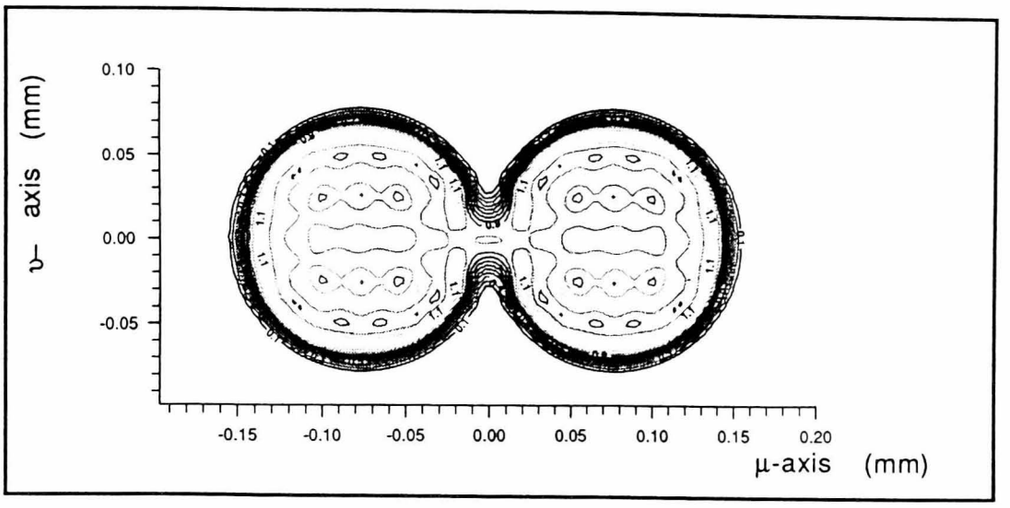

Group C1, Two touching Discs a=75 μm, 2b=150 μm

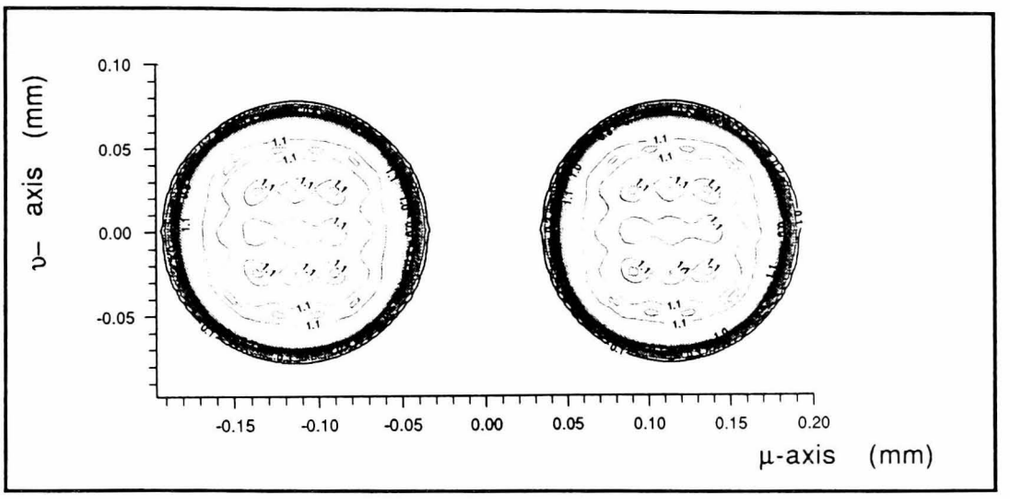

Group C2, a=75 μm, 2b=225 μm

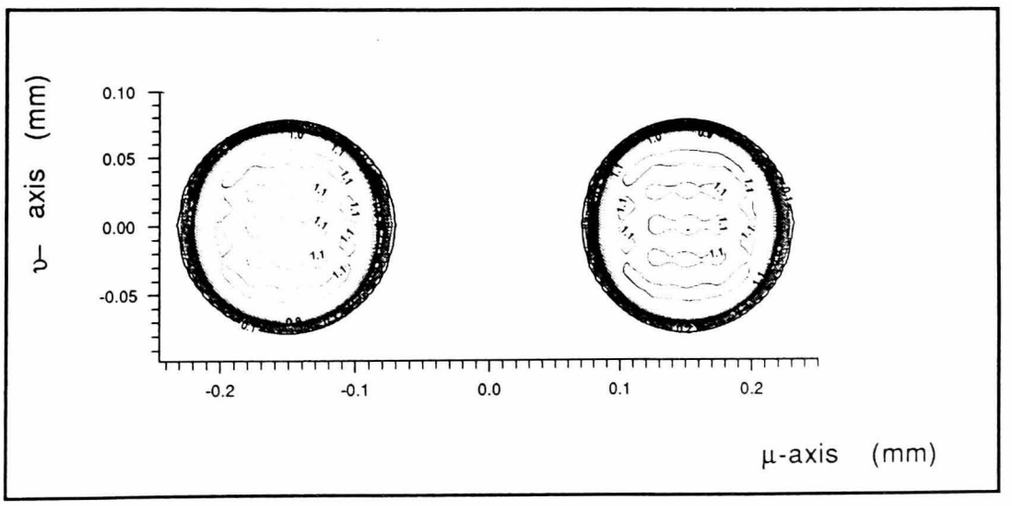

Group C3, a=75 μm, 2b=300 μm

FIG. (5.1.6) Contour plots of in-focus images for Ω = 19.616 [ΔZ=0.0]

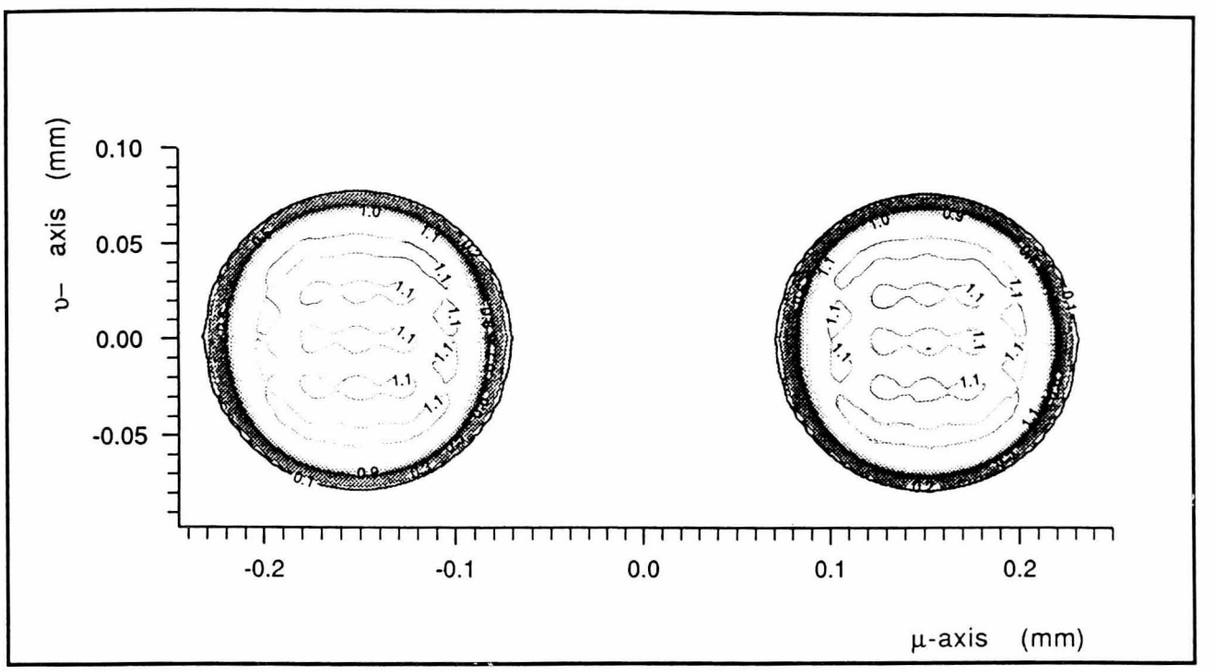

Contour plot

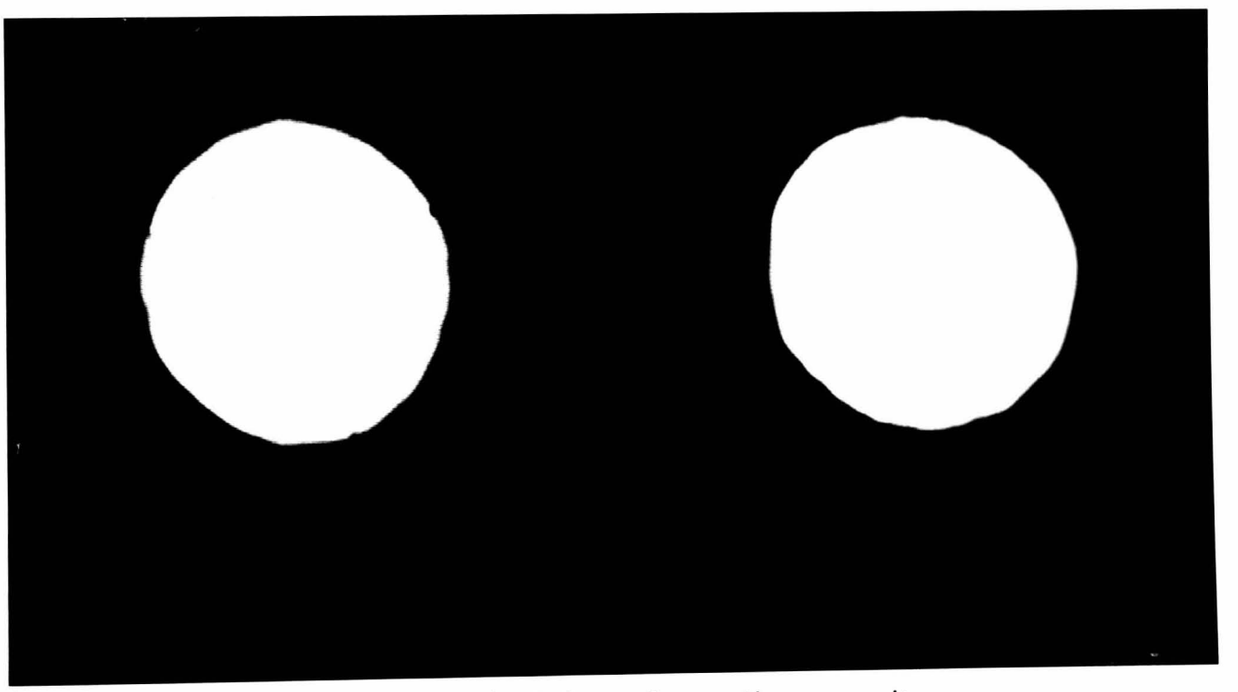

Photograph taken from the monitor

FIG. (5.1.7) In-focus image of group C3

[a=75 μm, 2b=300 μm, ΔZ=0.0, Ω=19.616],

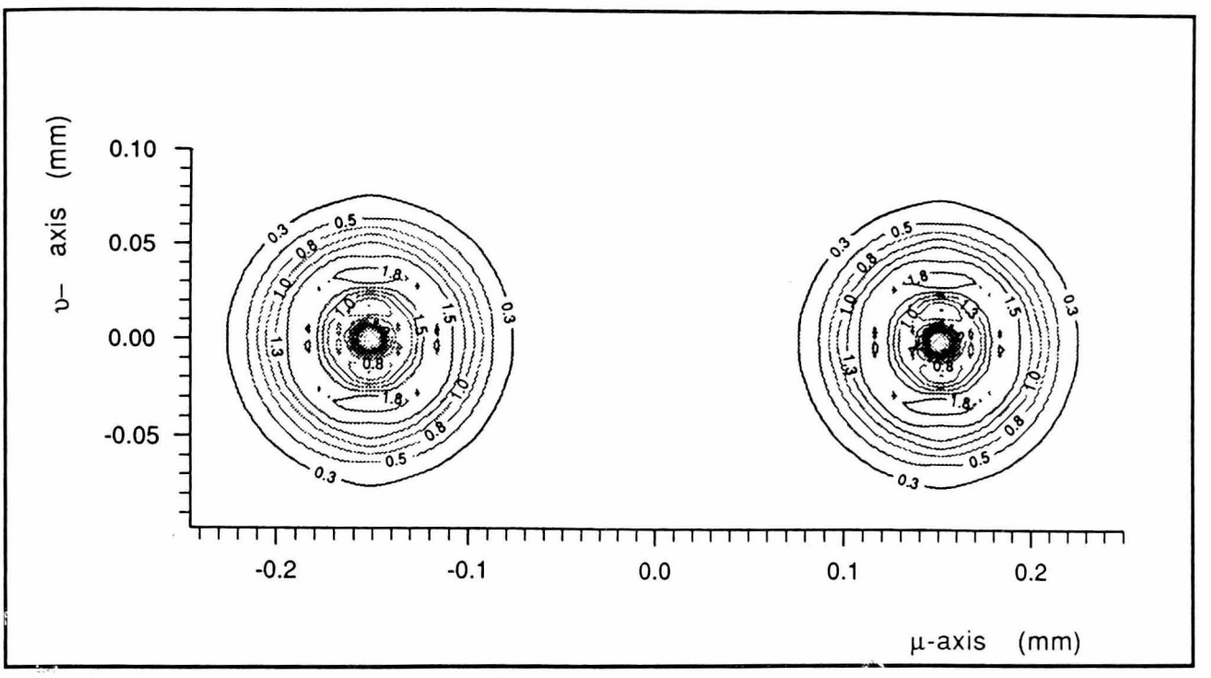

Contour plot

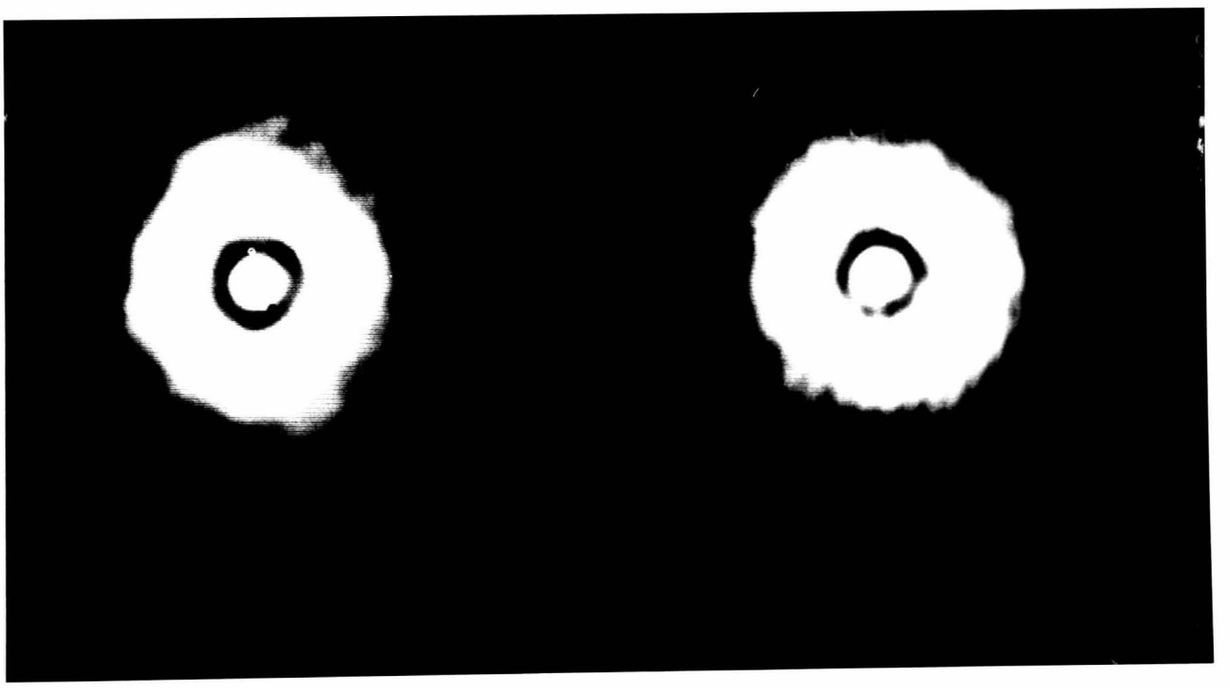

Photograph taken from the monitor

FIG. (5.1.8) Out of focus image of group C3

[a=75 μm, 2b=300 μm, ΔZ=-3.0 mm, Ω=19.616]

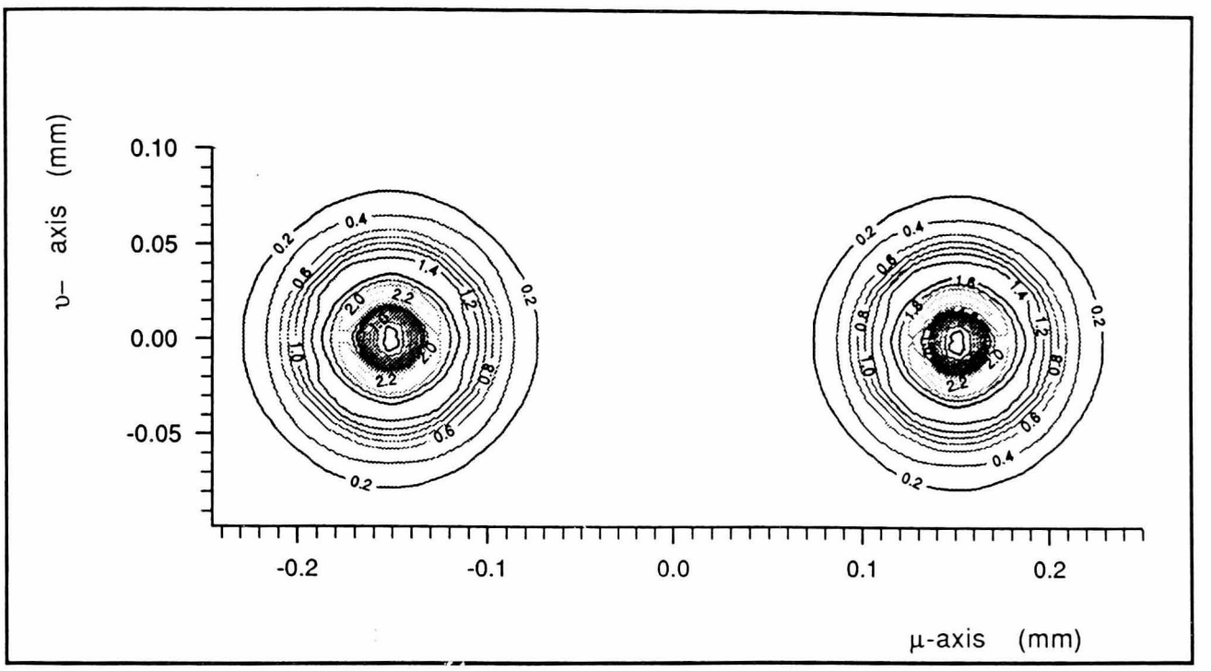

Contour plot

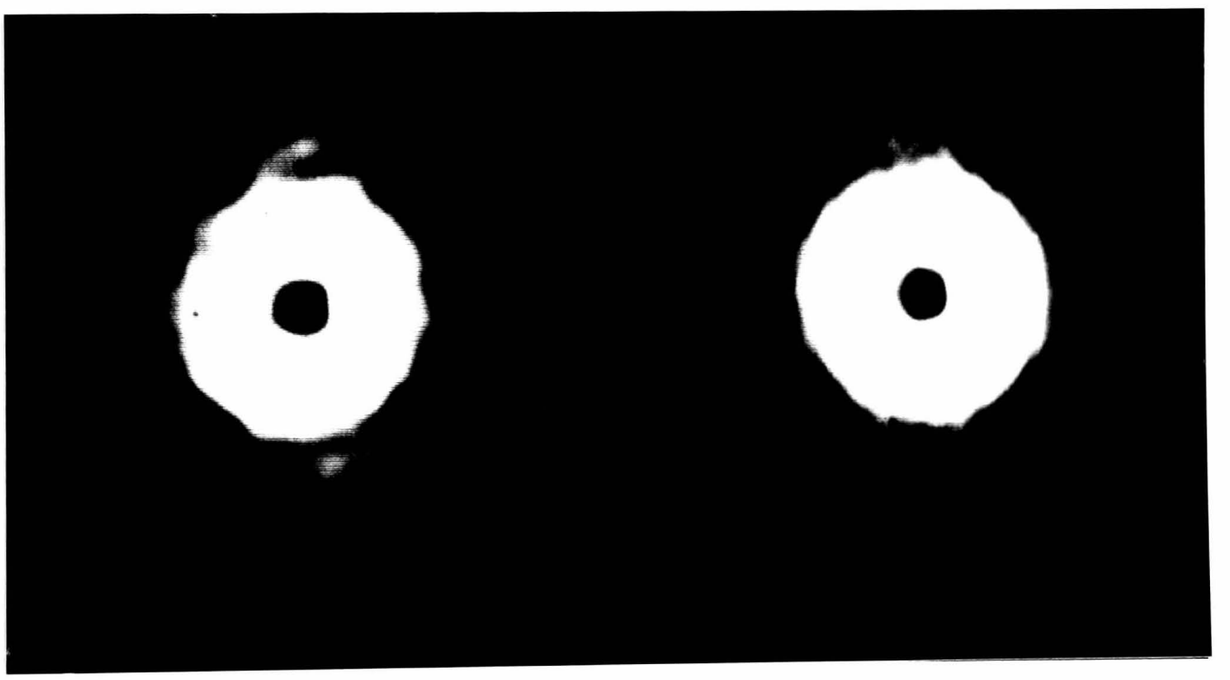

Photograph taken from the monitor

FIG. (5.1.9) Out of focus image of group C3

[a=75 μm, 2b=300 μm, ΔZ=-4.5 mm, Ω=19.616]

5.2 EXPERIMENTAL RESULTS AND ANALYSIS

Line scans through the center of all the holographic images whose parameters are listed in table (5.1), were recorded experimentally. The techniques of acquiring the data experimentally was discussed in chapter 4. Triggering through the oscilloscope was used to find video line numbers of the upper and the lower edges of the image under observation, and hence the central video line number was calculated, scanned and recorded using Asystant GPIB. Determination of the video line numbers of the upper and the lower edges eliminated any guess work about the central video line number of the image under observation. These line scans were compared with the theoretical plots and are presented in figures (5.2.1) to (5.2.32).

Measurements W(25%), W(edg.), and W(50%), as discussed in the previous section using the same criteria, were taken from the scans of all the in-focus images. The results of these measurements are tabulated in tables (5.5) to (5.7).

It has been noted that although the width W(25%) was more accurate theoretically and give less errors when measured on the predicted images, it has less practical significance because of the noise arising from the hologram and the coherent noise from

the optical components used in the experiment. Another source of errors in measuring the image was found to occur in determining where the intensity at the edge is 25% of the central intensity. Background noise in the reconstruction results in large errors in locating this point.

The width W(50%) was measured where the intensity on the edge of the disc image was halfway between the average image intensity and the average background noise level. These measurements were found to be more accurate, because the problem of noise in the reconstruction was minimised.

It is important to note here that the image intensity of the in-focus images presented in the theoretical plots, was normalised to the intensity at expected geometric center of each disc. The out-of-focus image intensities, for the same value of Ω, were plotted using the same normalisation to establish a relation between intensities between the in-focus and out-of-focus images.

In the figures (5.2.1) [page 107] to (5.2.32) [page 138],

C_d is the measurement of the diameter of the discs.

C_s is the measurement of the separation between inner edges of the discs.

GROUP	7.016	10.173	13.324	19.616
Actual: 300 μm				
C1	-3.7% (0.0%)	0.3% (0.8%)	-3.7% (0.0%)	-1.7% (-1.5%)
Actual: 150 μm				
C2(d)	13.3% (4.6%)	0.0% (-1.5%)	-2.7% (0.0%)	-2.0% (0.0%)
Actual: 75 μm				
C2(s)	-45.3% (-13.9%)	12.0% (4.6%)	-8.0% (-1.5%)	8.0% (-1.5%)
Actual: 150 μm				
C3(d)	6.0% (4.6%)	0.0% (-1.5%)	0.0% (0.0%)	-3.3% (0.0%)
Actual: 150 μm				
C3(s)	-13.3% (-7.6%)	-7.3% (1.5%)	-7.3% (0.0%)	-3.3% (0.0%)

Theoretical results are included within parentheses for comparison with the experimental measurements.

C(d) measurement of the diameter.
C(s) measurement of the separation.

$$\text{Error \%} = \frac{\text{Measured - Actual}}{\text{Actual}} .100\%$$

Table (5.5) Table of measurements using criteria W(25%)
[W(25%) = 25% of the center intensity].

GROUP	7.016	10.173	13.324	19.616
Actual: 300 μm				
C1	-22.7% (-20.0%)	-17.0% (-16.2%)	-14.3% (-13.1%)	-11.3% (-9.2%)
Actual: 150 μm				
C2(d)	-36.7% (-44.6%)	-26.7% (-35.4%)	-22.7% (-26.2)	-17.3% (-16.9%)
Actual: 75 μm				
C2(s)	50.7% (90.8%)	38.7% (66.2%)	38.7% (53.9%)	24.0% (29.2%)
Actual: 150 μm				
C3(d)	-46.0% (-44.6%)	-30.7% (-35.4%)	-22.7% (-26.2)	-22.7% (-16.9%)
Actual: 150 μm				
C3(s)	38.7% (46.2%)	27.3% (38.5%)	16.0% (26.2%)	16.0% (13.8%)

Theoretical measurements are included within parentheses for comparison with the experimental measurements.

C(d) measurement of the diameter.
C(s) measurement of the separation.

$$\text{Error \%} = \frac{\text{Measured - Actual}}{\text{Actual}} .100\%$$

Table (5.6) Table for measurements W(edg.)
[W(edg.) = Separation of the two outer most peaks].

GROUP	7.016	10.173	13.324	19.616
Actual: 300 μm				
C1	-7.7% (-3.1%)	-3.7% (-3.1%)	-5.6% (-3.1%)	-3.7% (-3.1%)
Actual: 150 μm				
C2(d)	0.7% (-6.2%)	-6.0% (-9.2%)	-6.0% (-4.6%)	-3.3% (-3.1%)
Actual: 75 μm				
C2(s)	-14.7% (7.6%)	-4.0% (20.0%)	-4.0% (4.6%)	-4.0% (4.6%)
Actual:150 μm				
C3(d)	-3.3% (-6.2%)	-6.0% (-9.2%)	-3.3% (-4.6%)	-8.0% (-3.1%)
Actual: 150 μm				
C3(s)	-3.3% (4.6%)	0.0% (7.7%)	-3.3% (6.2%)	-2.0% (1.5%)

Theoretical measurements are included within parentheses for comparison with the experimental measurements.

C(d) measurement of the diameter.
C(s) measurement of the separation.

$$\text{Error \%} = \frac{\text{Measured - Actual}}{\text{Actual}} .100\%$$

Table (5.7) Table for measurements W(50%)
[W(50%) = 50% of the average image intensity].

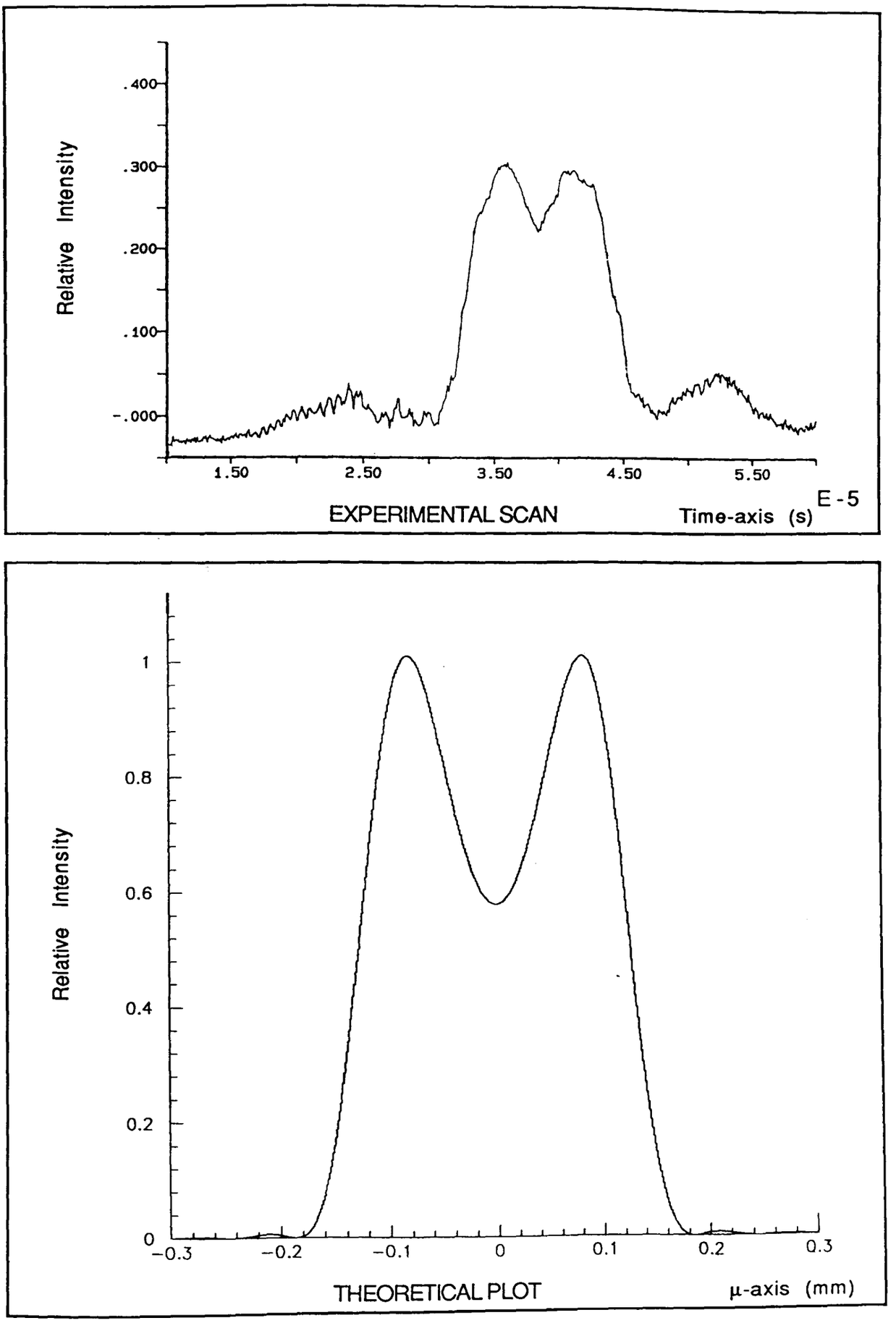

FIG. (5.2.1) Group C1 [C = 300 μm] for Ω=3.832, ΔZ=0.0 mm

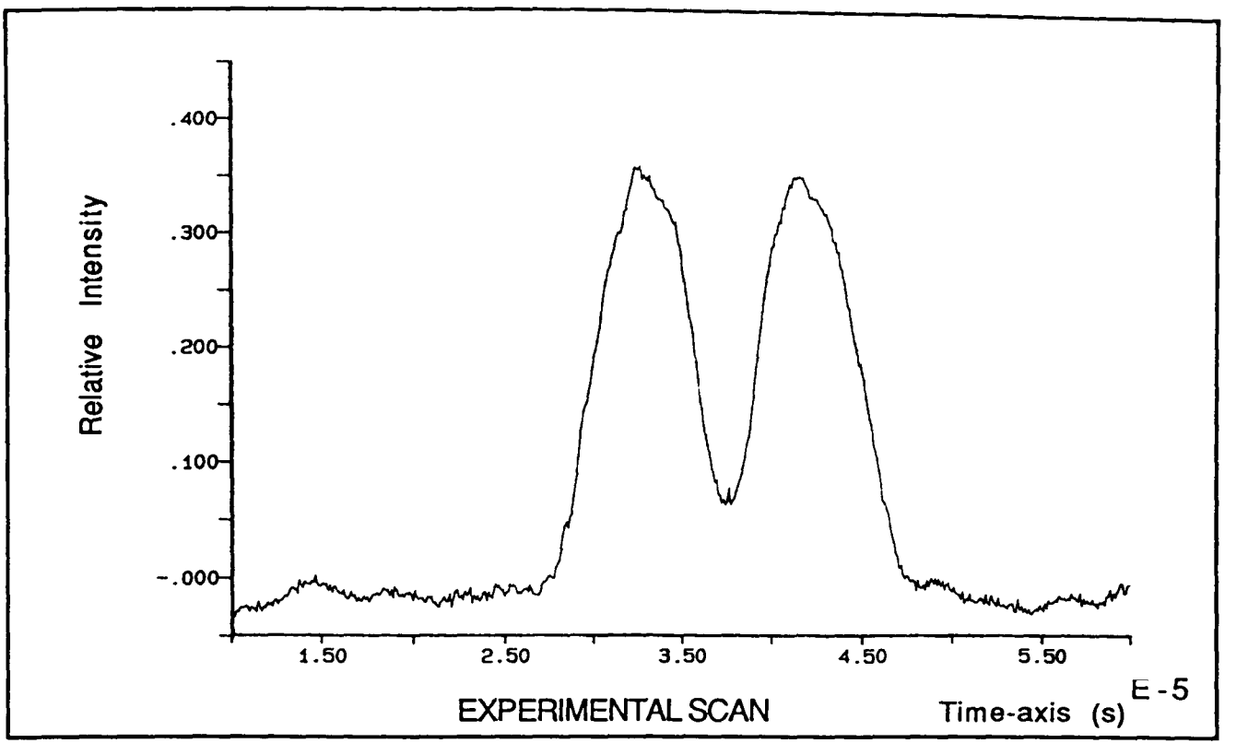

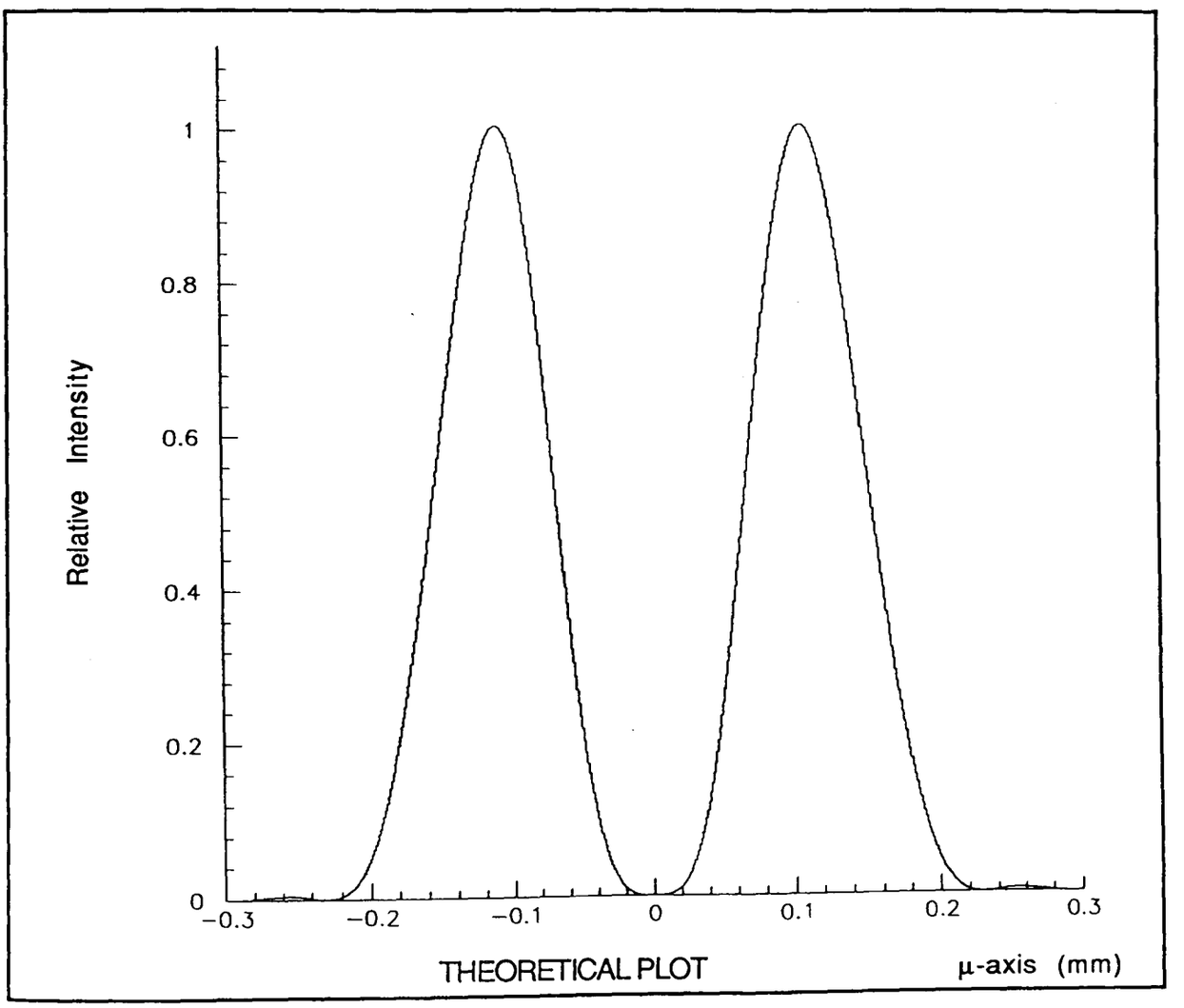

FIG. (5.2.2) Group C2 [C_d = 150 μm, C_s=75 μm] for Ω=3.832, ΔZ=0.0 mm

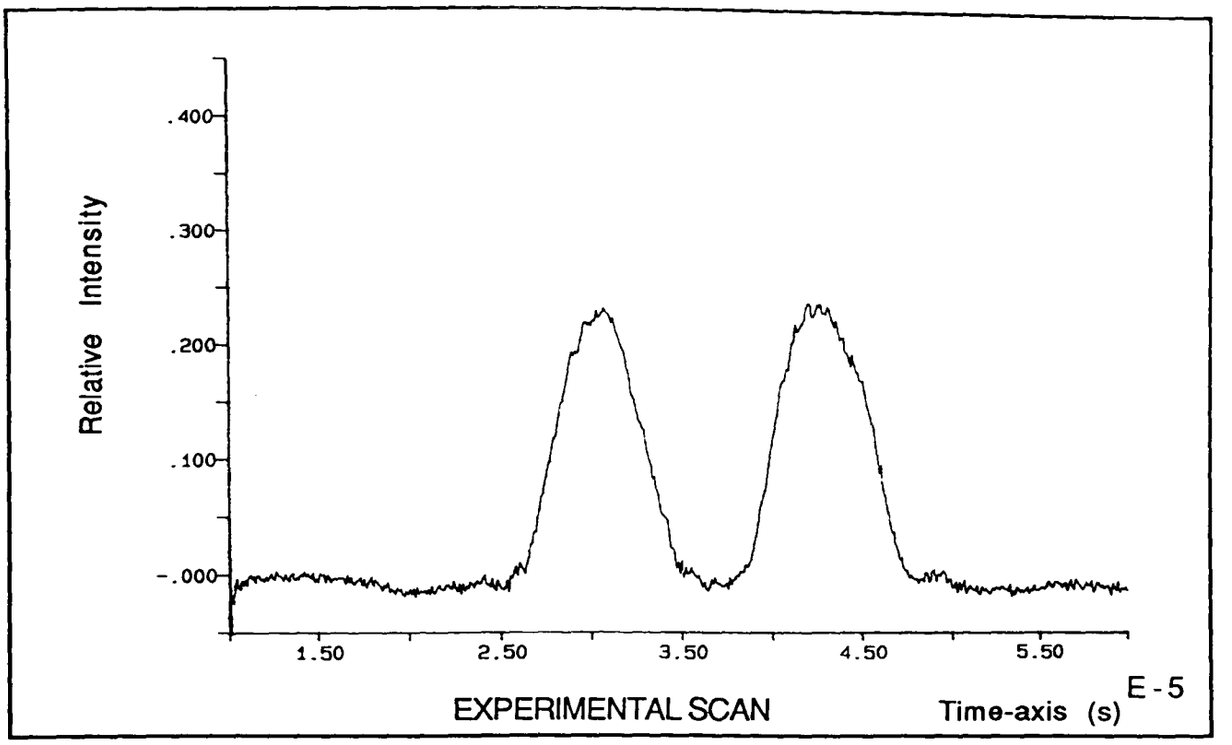

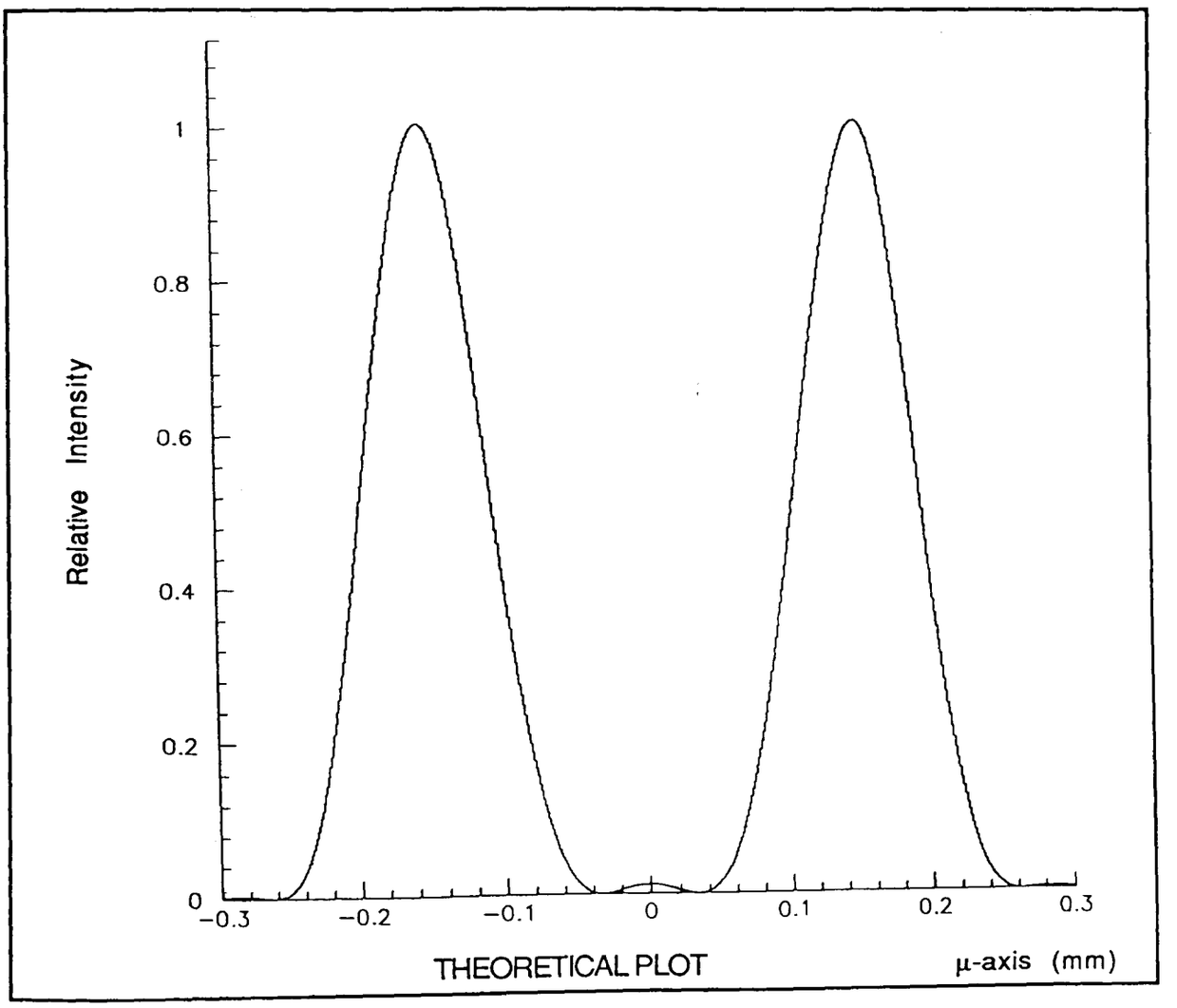

FIG. (5.2.3) Group C3 [C_d = 150 μm, C_s=150 μm] for Ω=3.832, ΔZ=0.0 mm

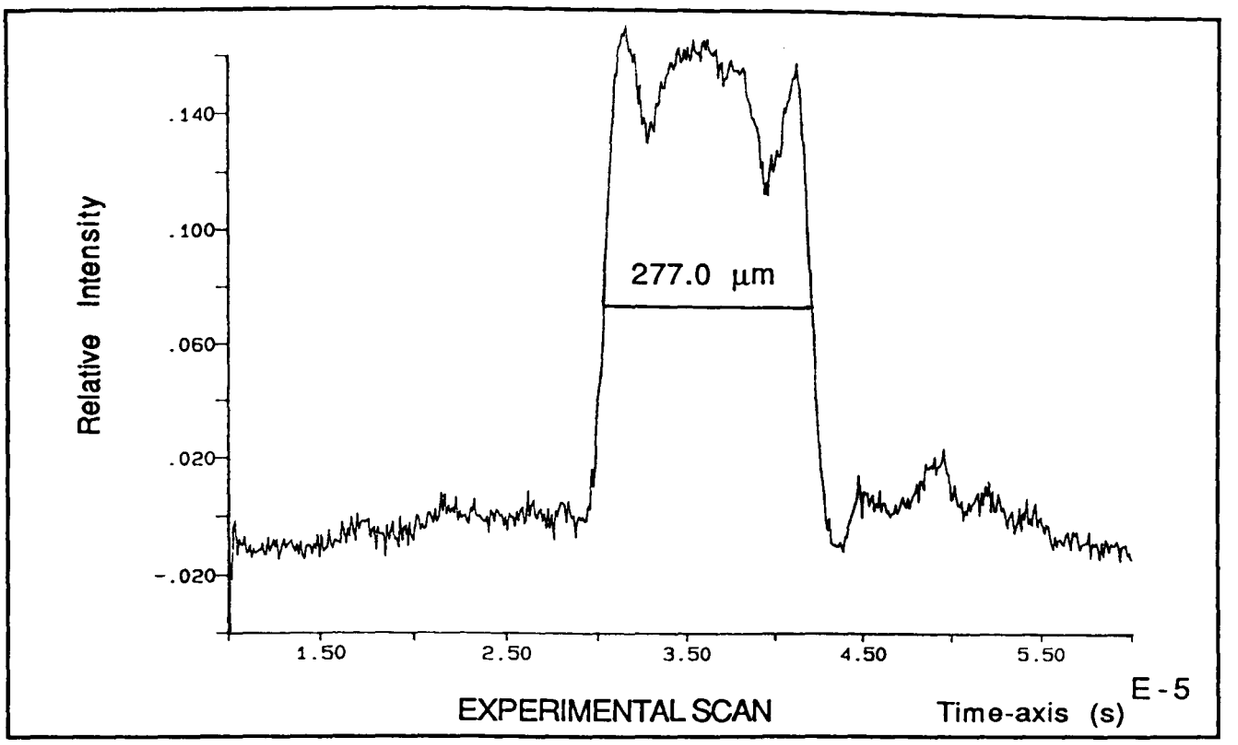

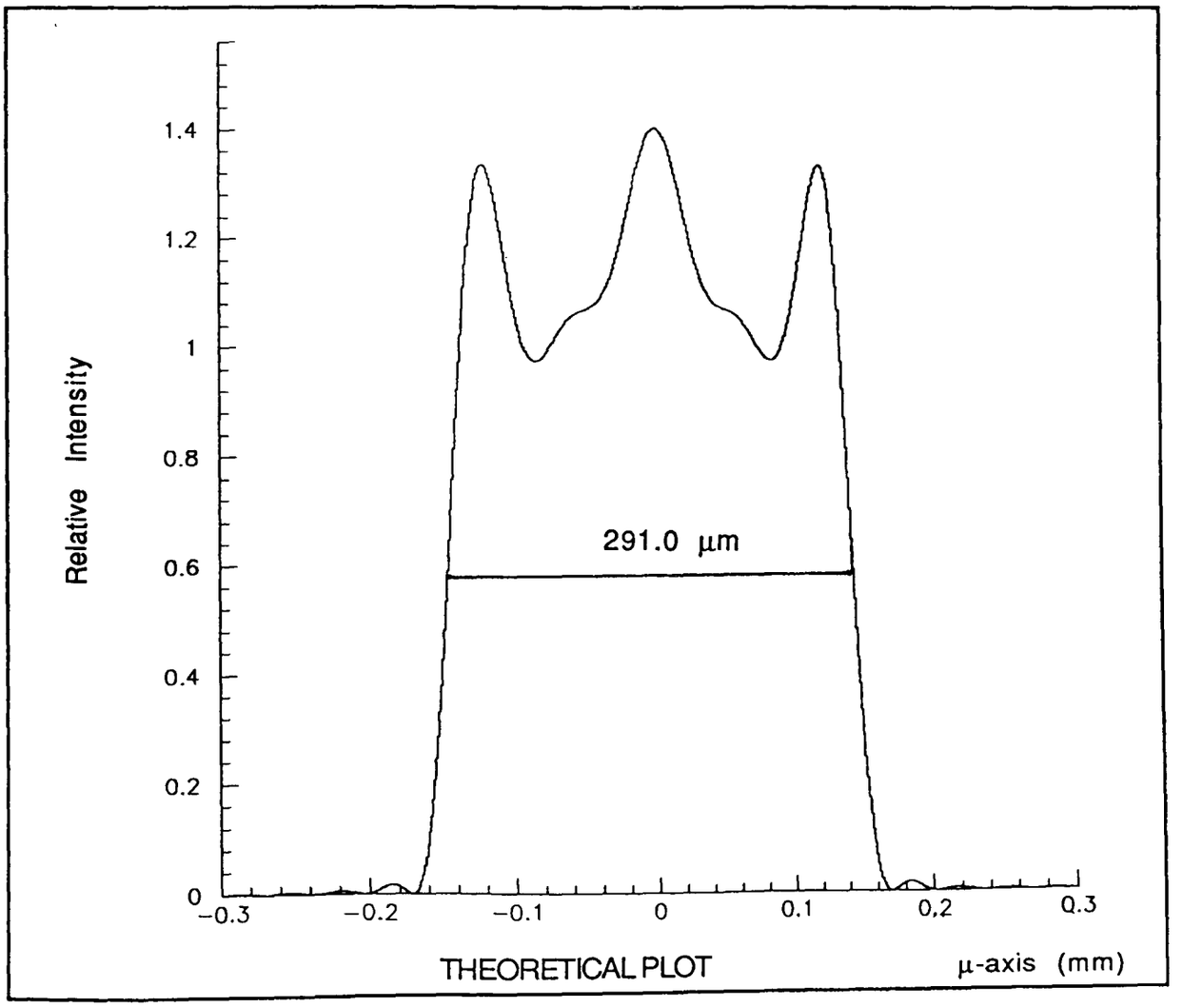

FIG. (5.2.4) Group C1 [C = 300 µm] for Ω=7.016, ΔZ=0.0 mm

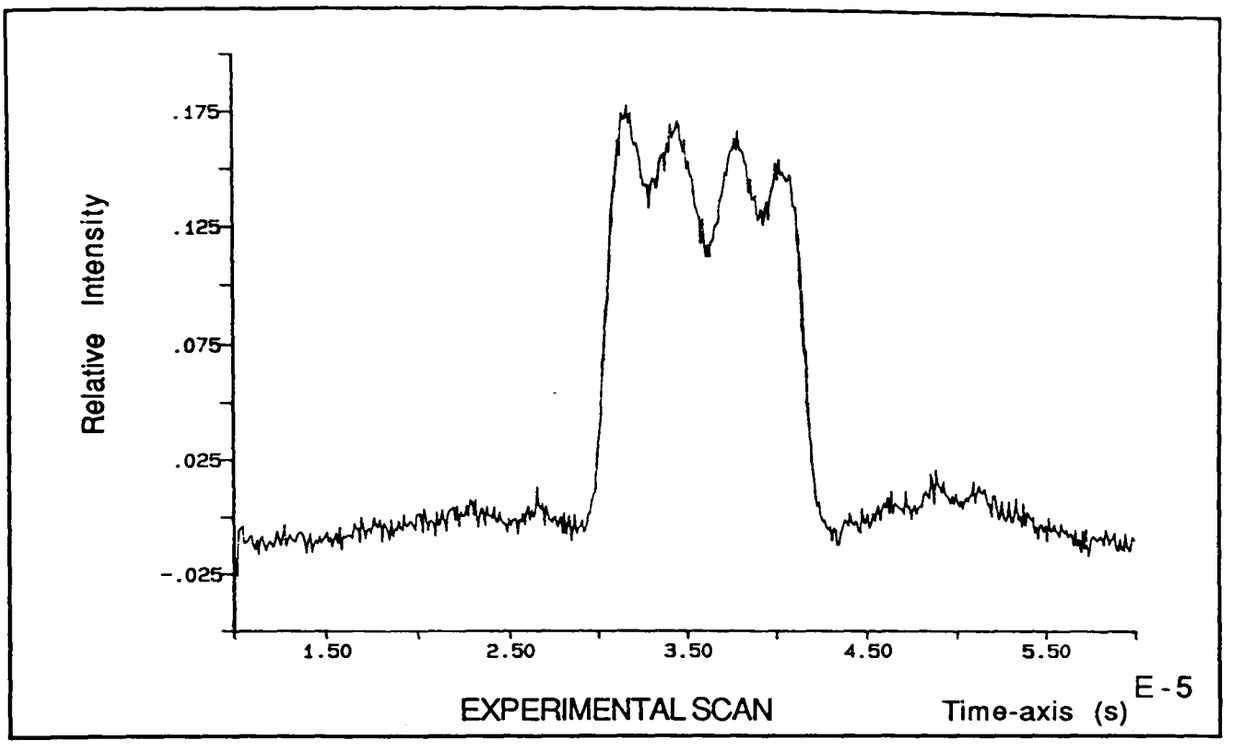

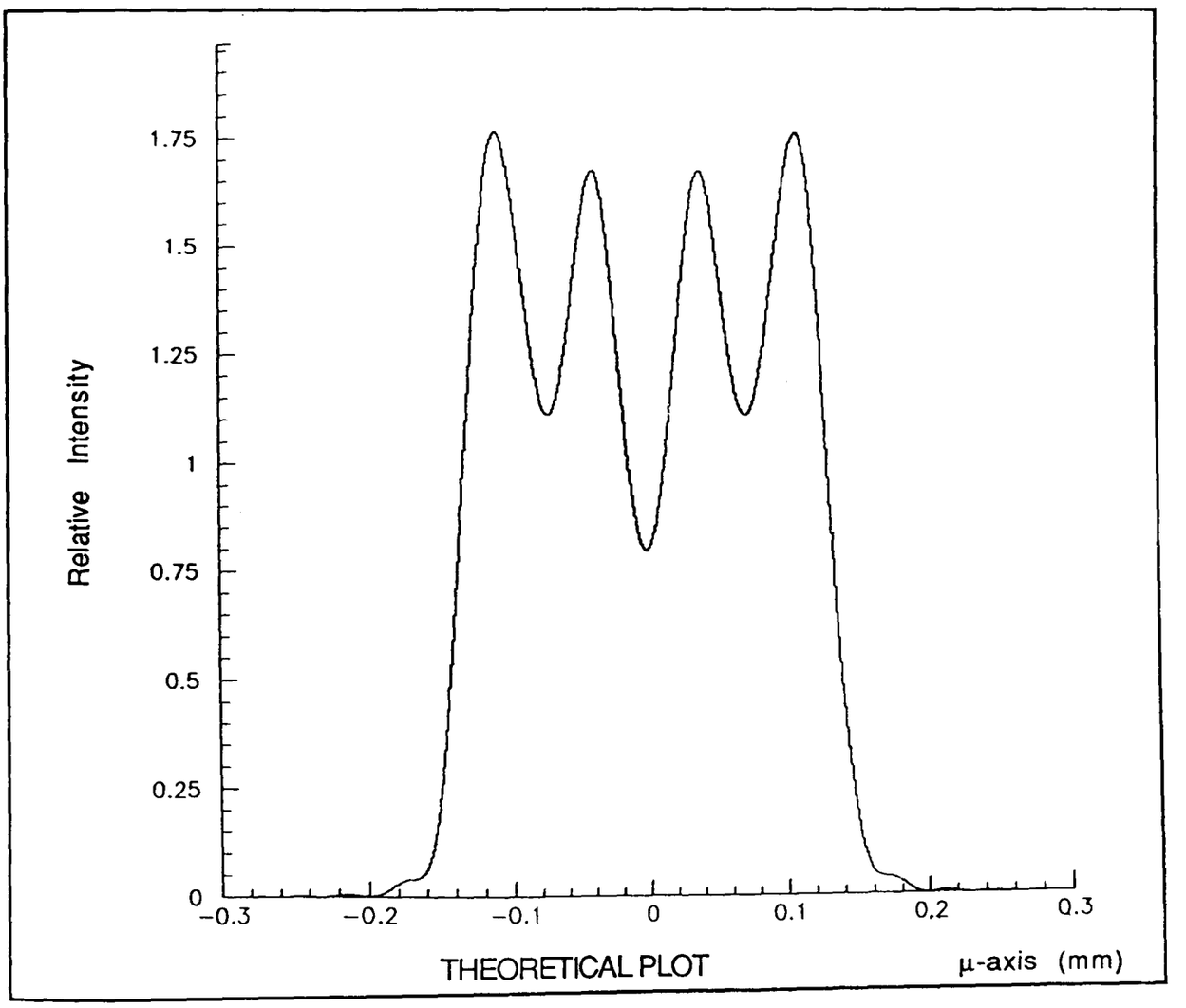

FIG. (5.2.5) Group C1 [C = 300 μm] for Ω=7.016, ΔZ=-3.5 mm

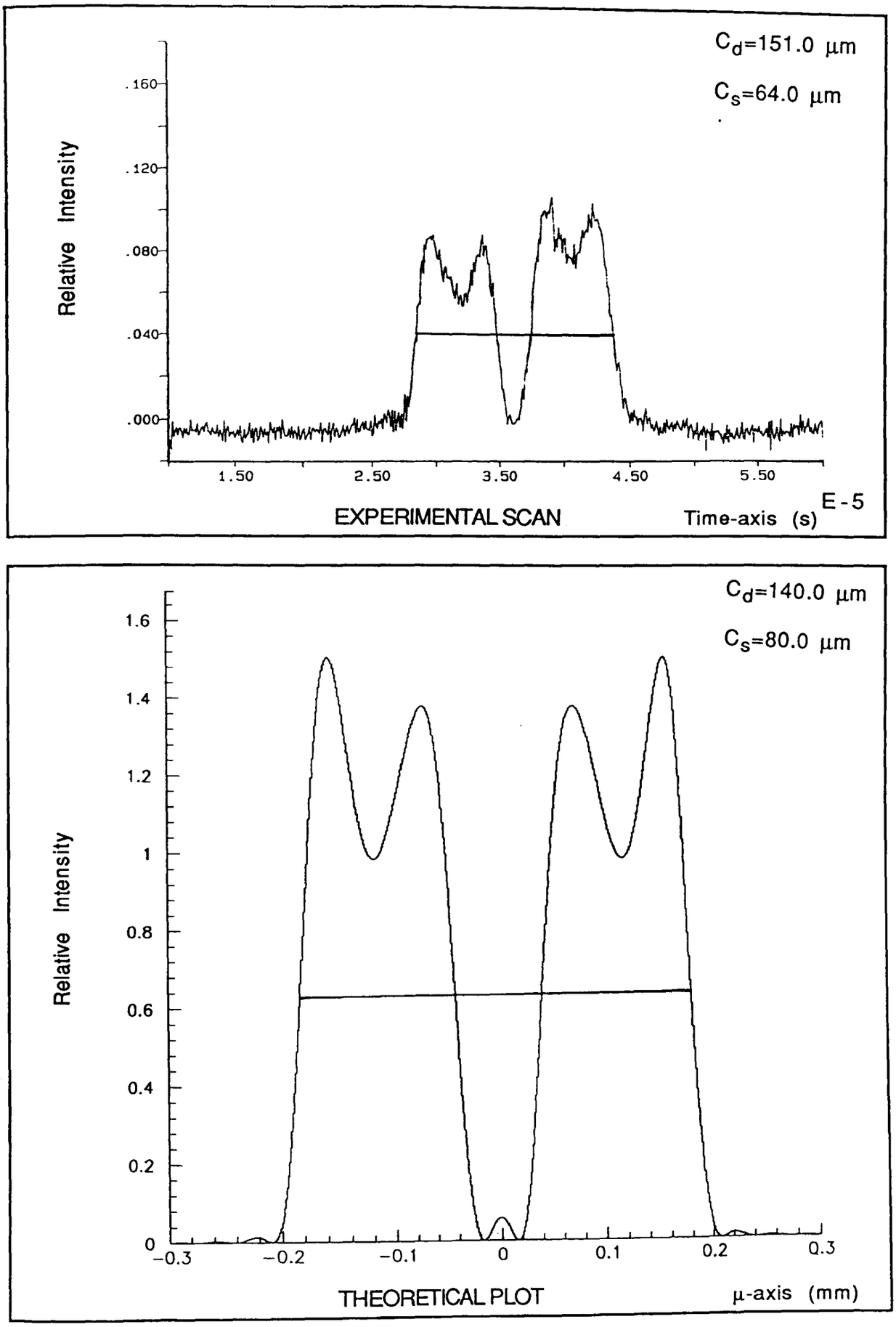

FIG. (5.2.6) Group C2 [C_d = 150 μm, C_s=75 μm] for Ω=7.016, ΔZ=0.0 mm

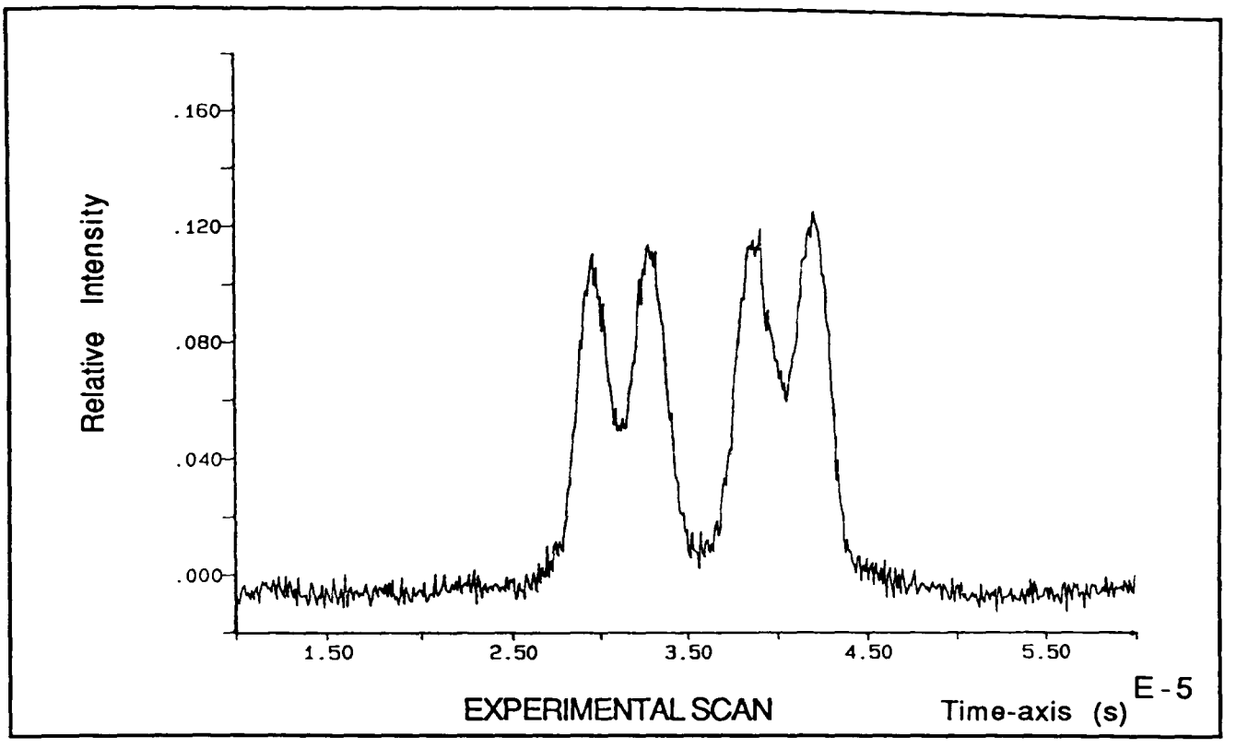

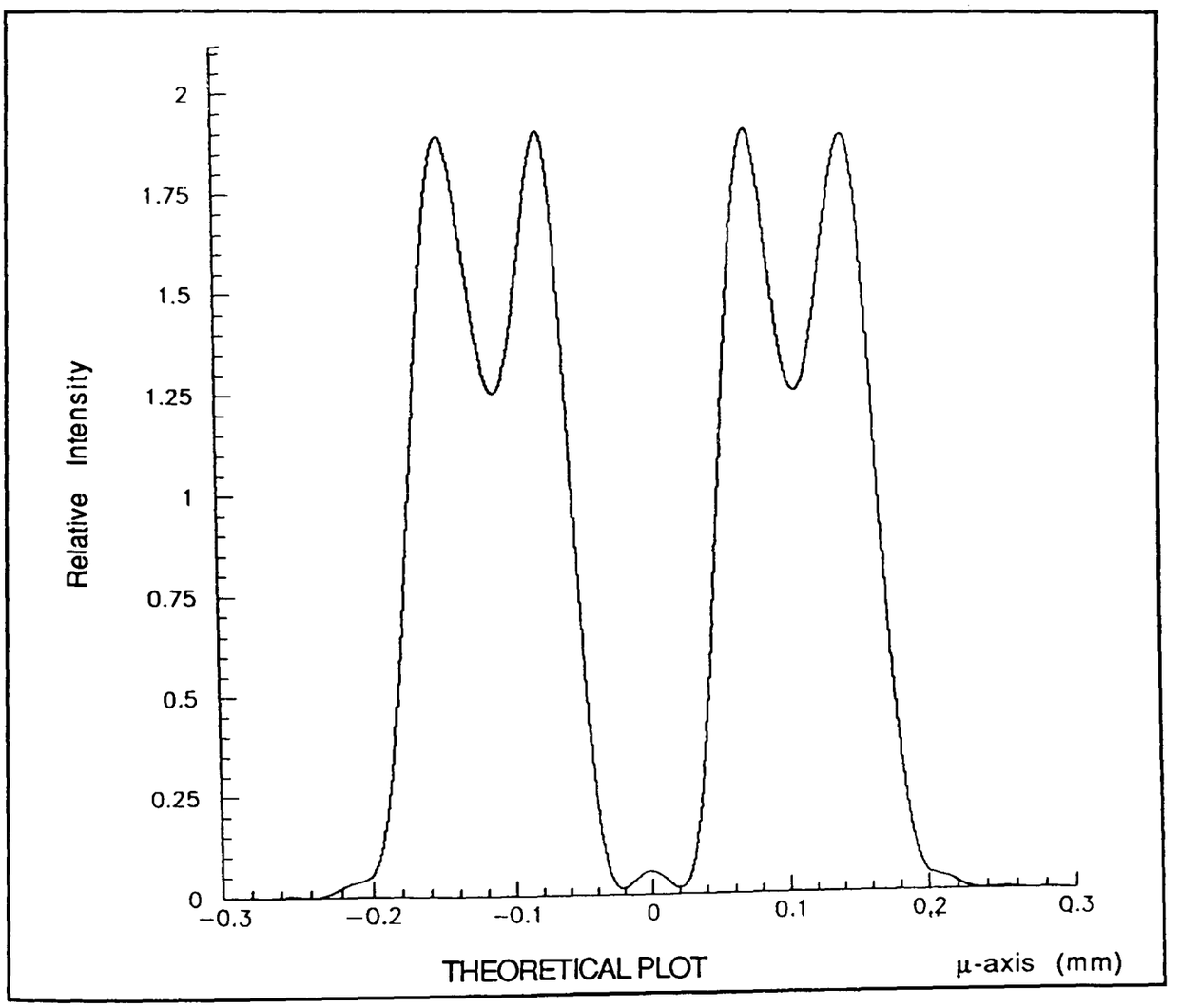

FIG. (5.2.7) Group C2 [C_d = 150 μm, C_s=75 μm] for Ω=7.016, ΔZ=-3.5 mm

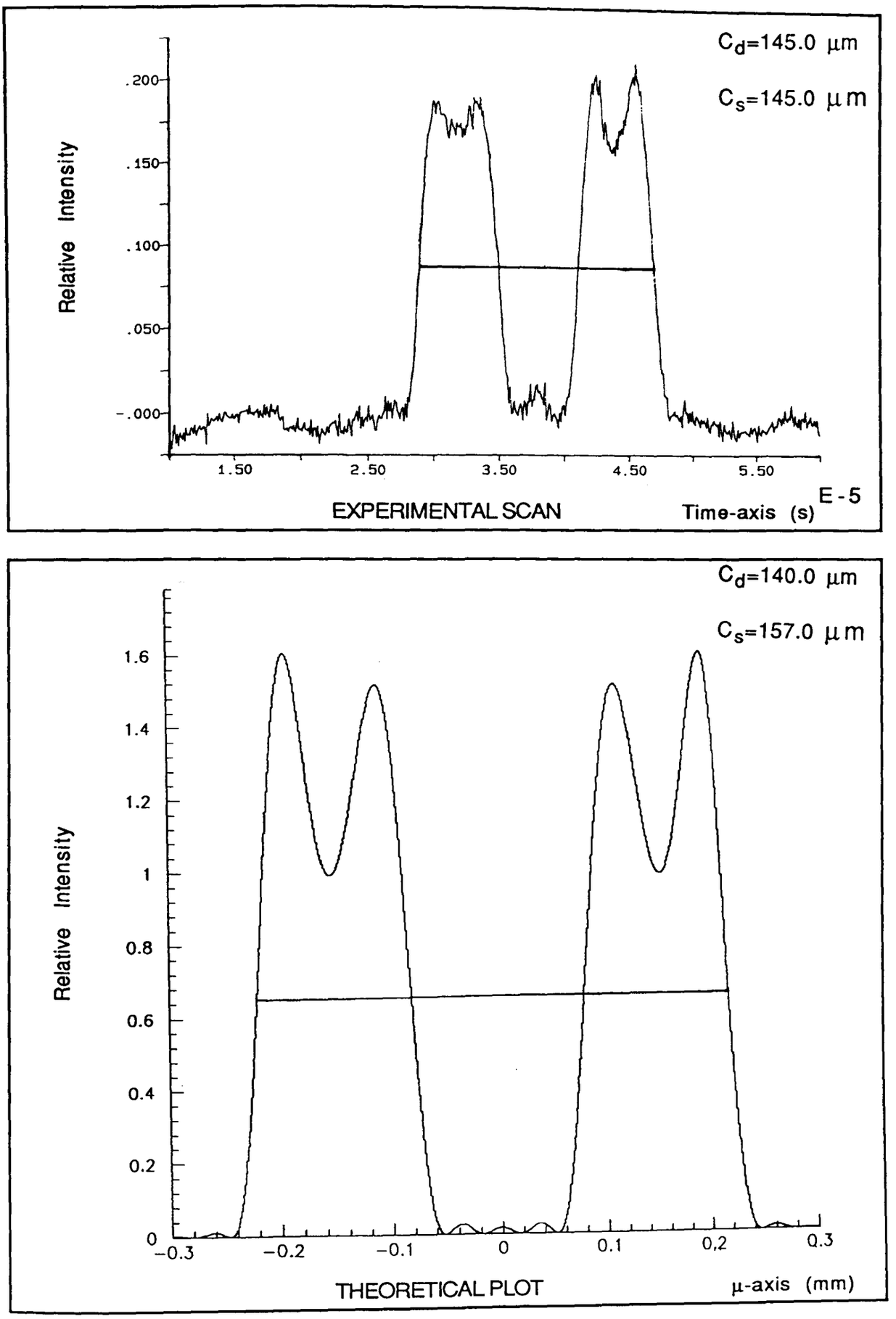

FIG. (5.2.8) Group C3 [C_d = 150 μm, C_s=150 μm] for Ω=7.016, ΔZ=0.0 mm

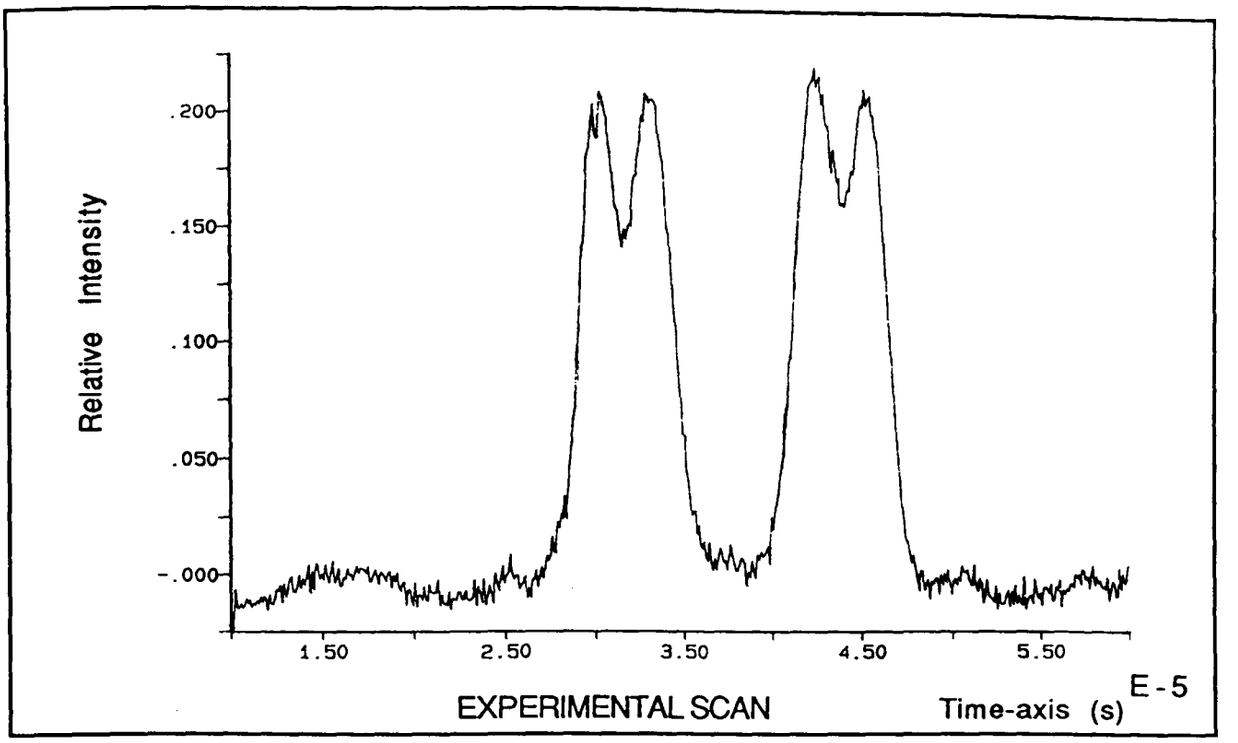

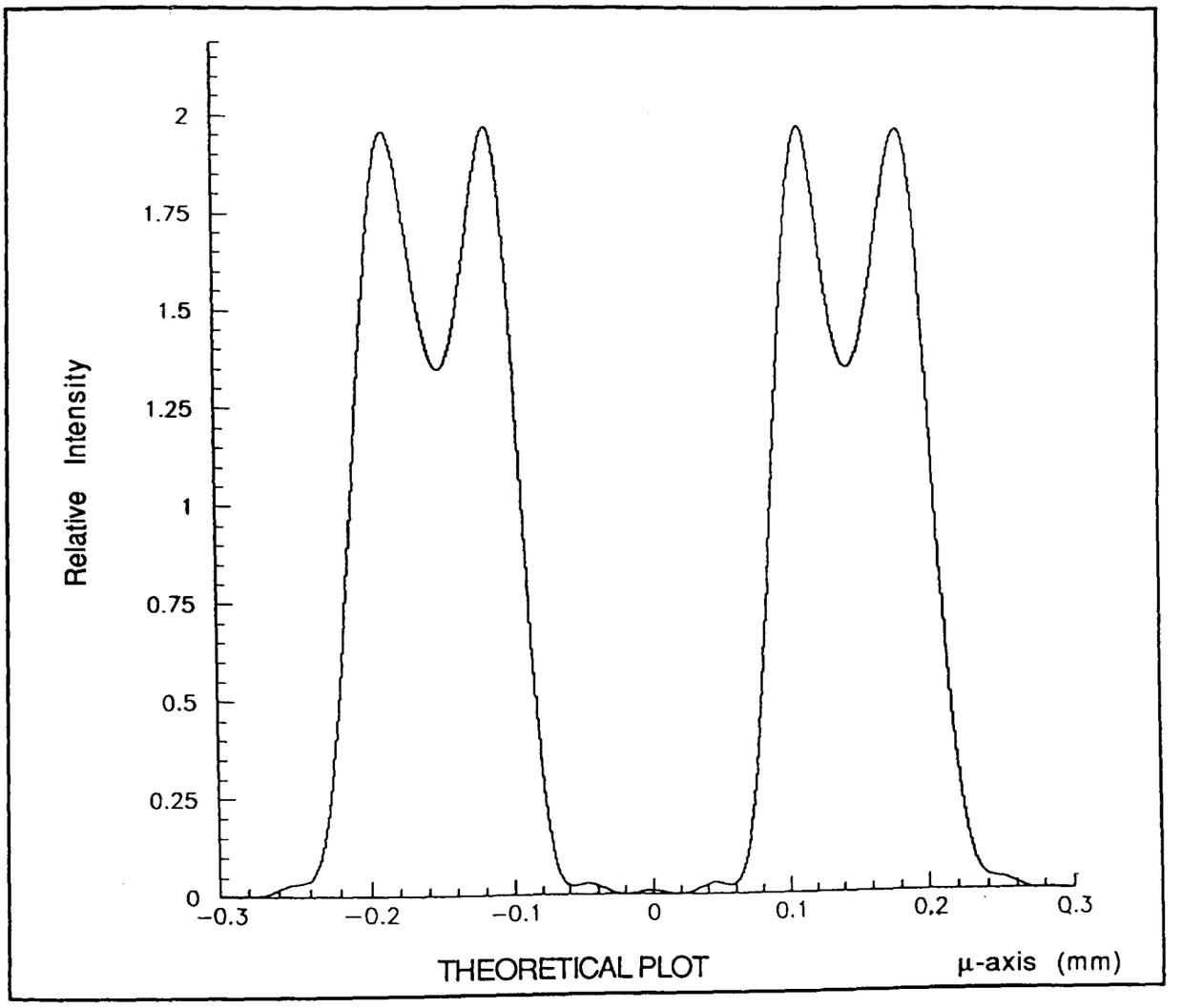

FIG. (5.2.9) Group C3 [C_d = 150 μm, C_s=150 μm] for Ω=7.016, ΔZ=-3.5 mm

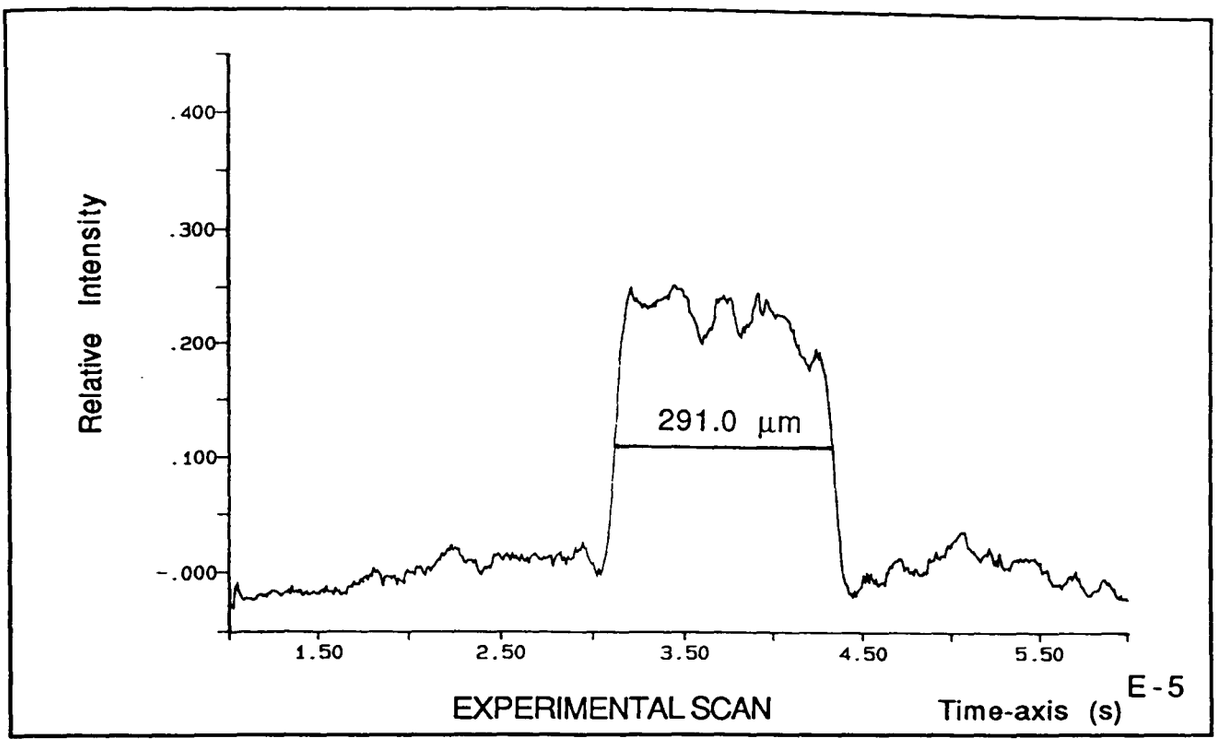

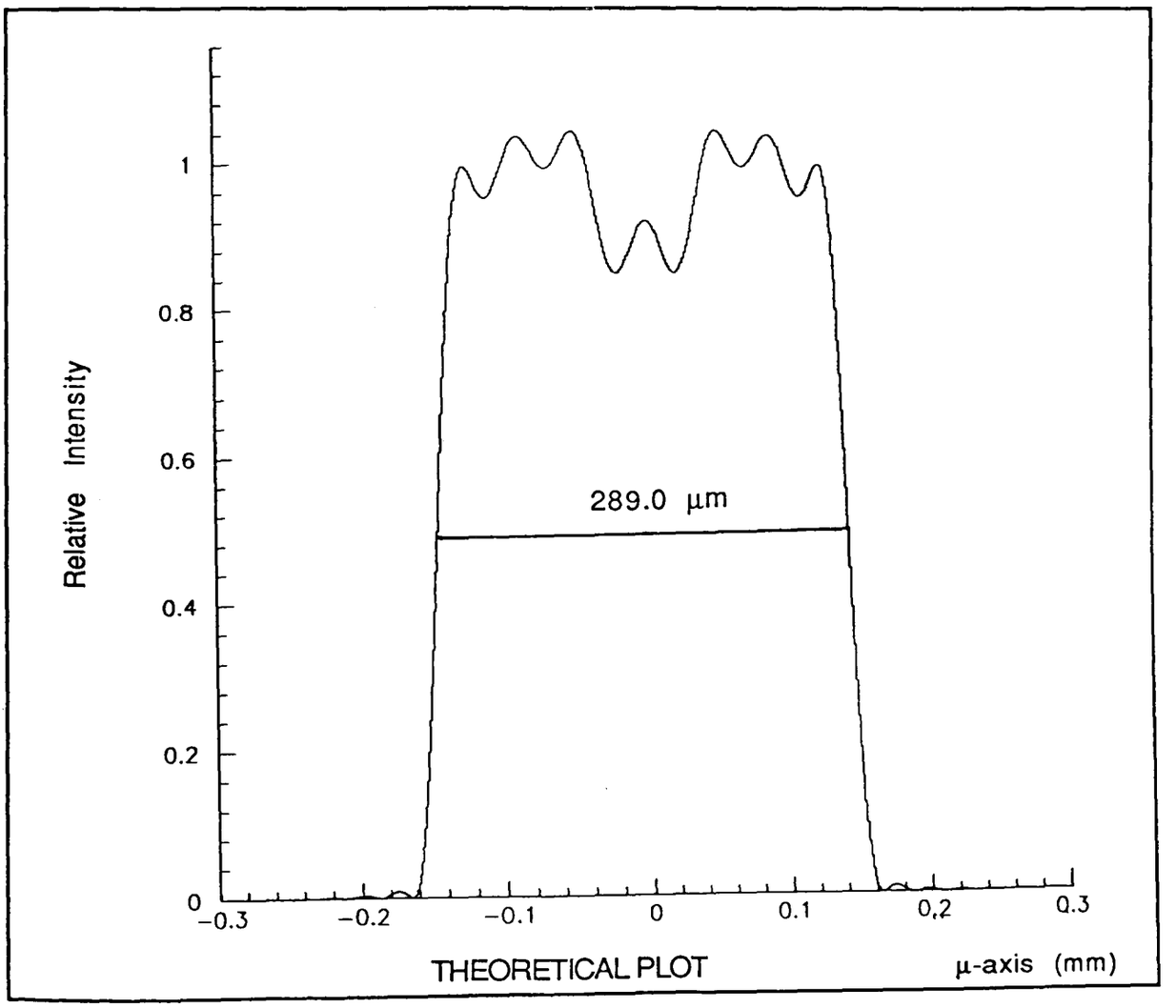

FIG. (5.2.10) Group C1 [C = 300 μm] for Ω=10.173, ΔZ=0.0 mm

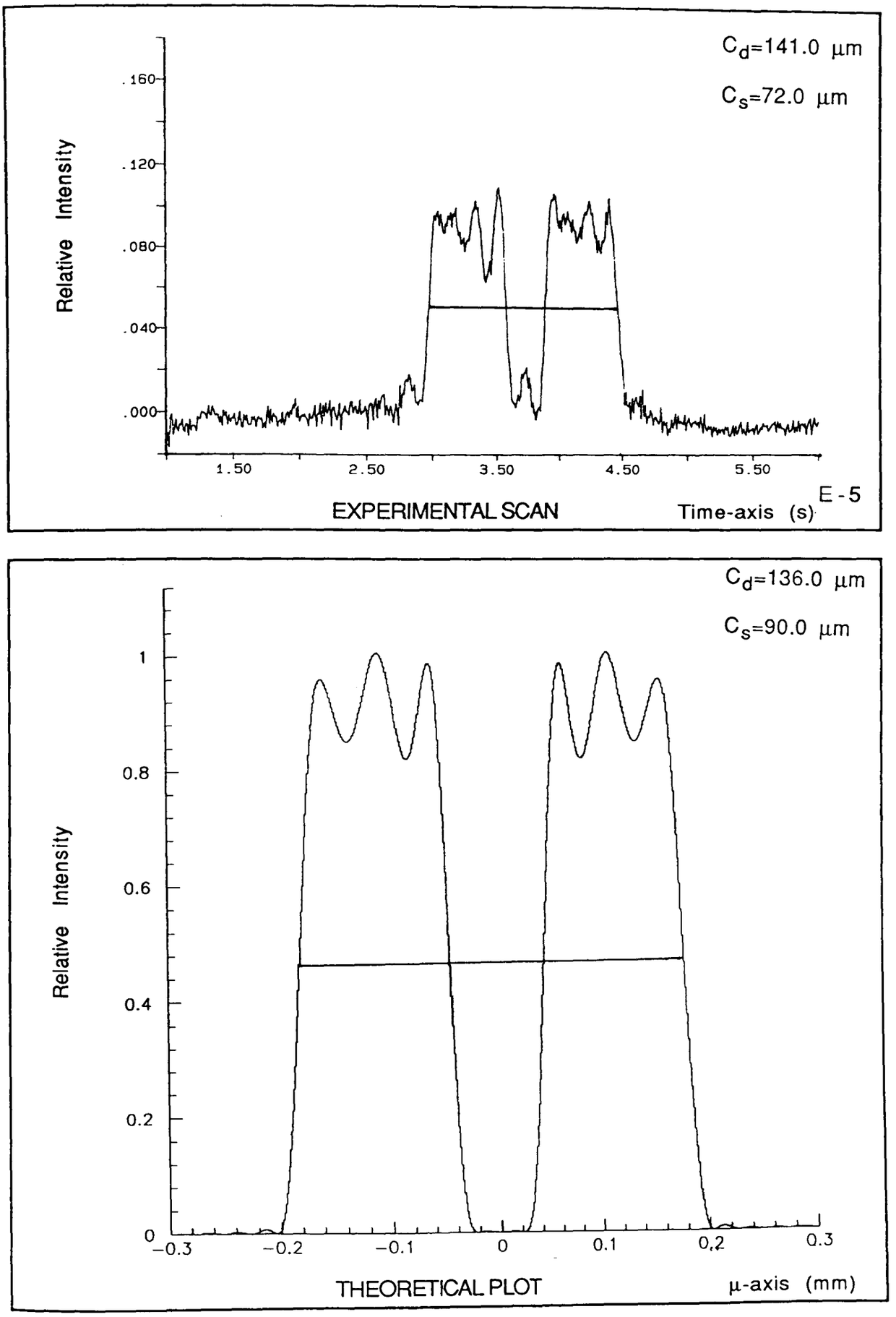

FIG. (5.2.11) Group C2 [C_d = 150 μm, C_s=75 μm] for Ω=10.173, ΔZ=0.0 mm

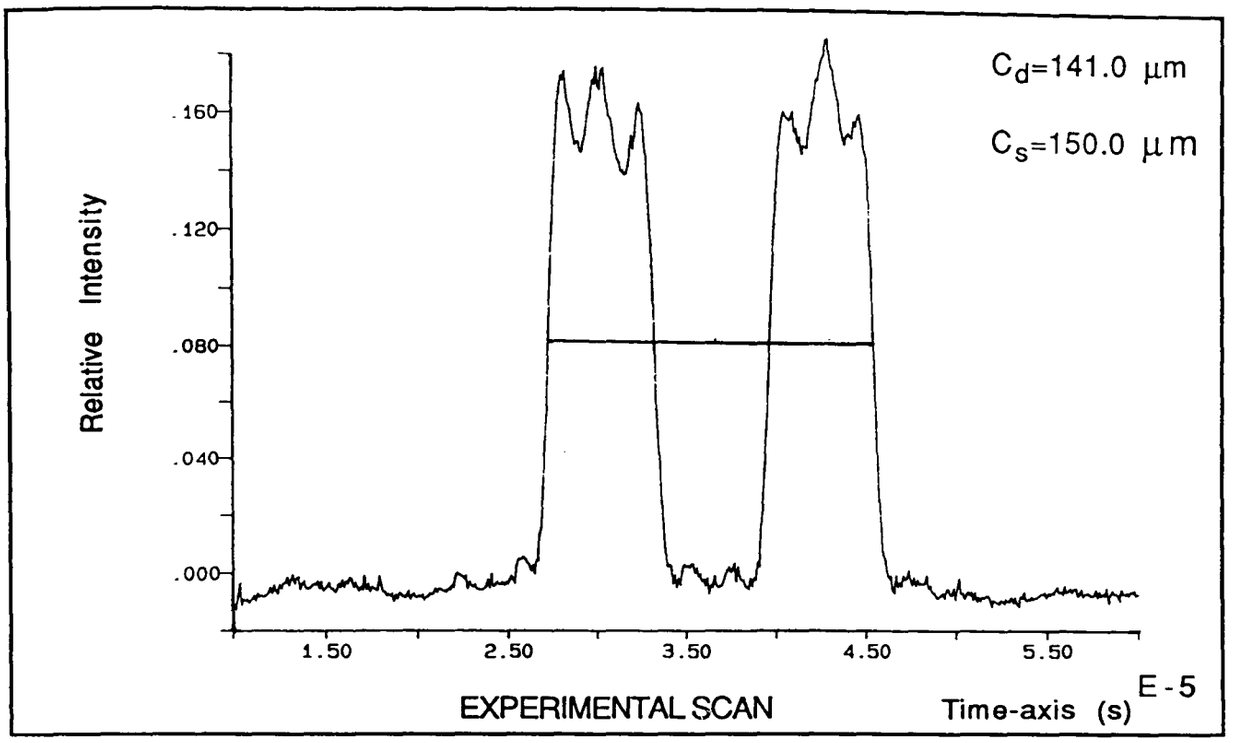

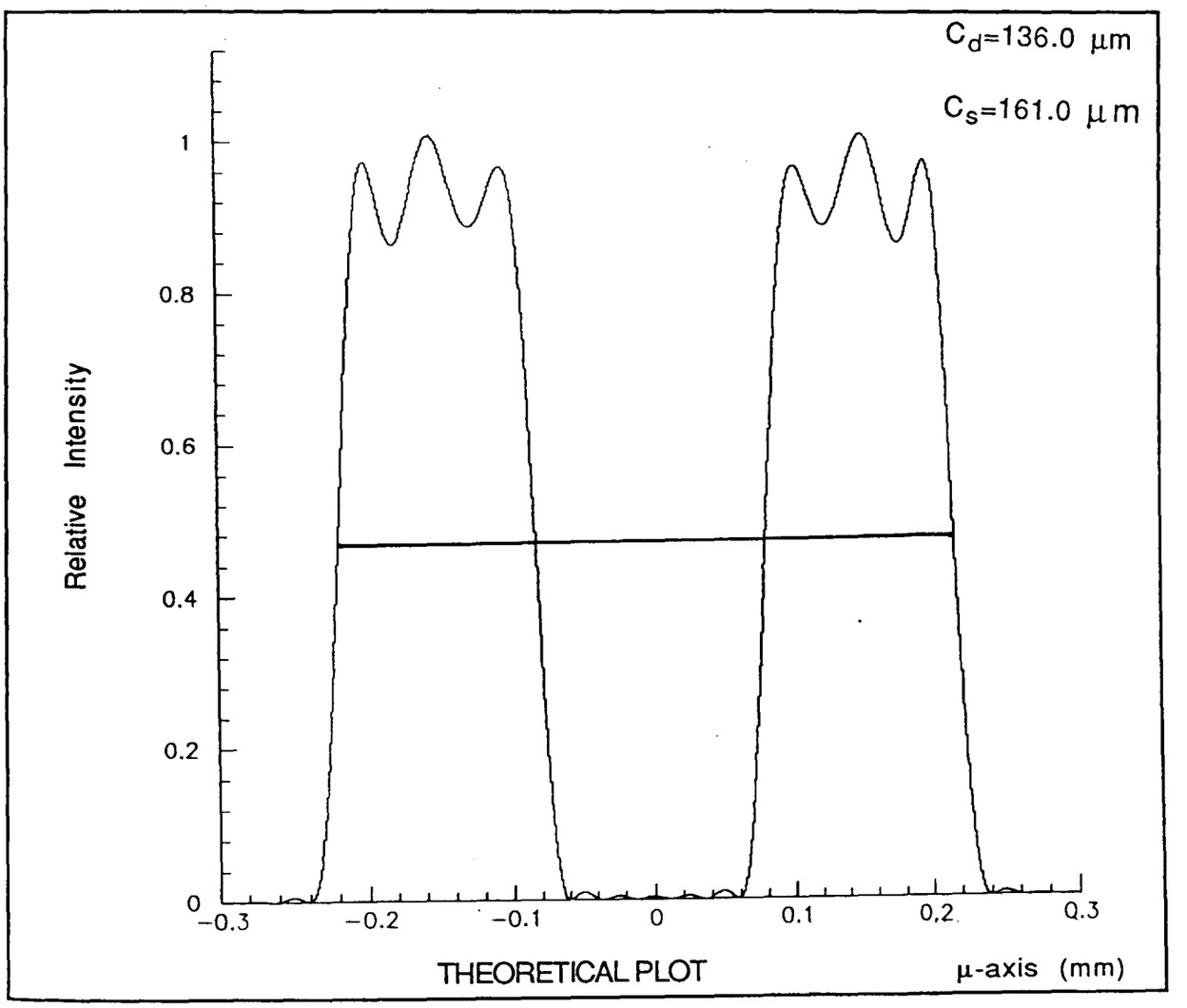

FIG. (5.2.12) Group C3 [C_d = 150 μm, C_s=150 μm] for Ω=10.173, ΔZ=0.0 mm

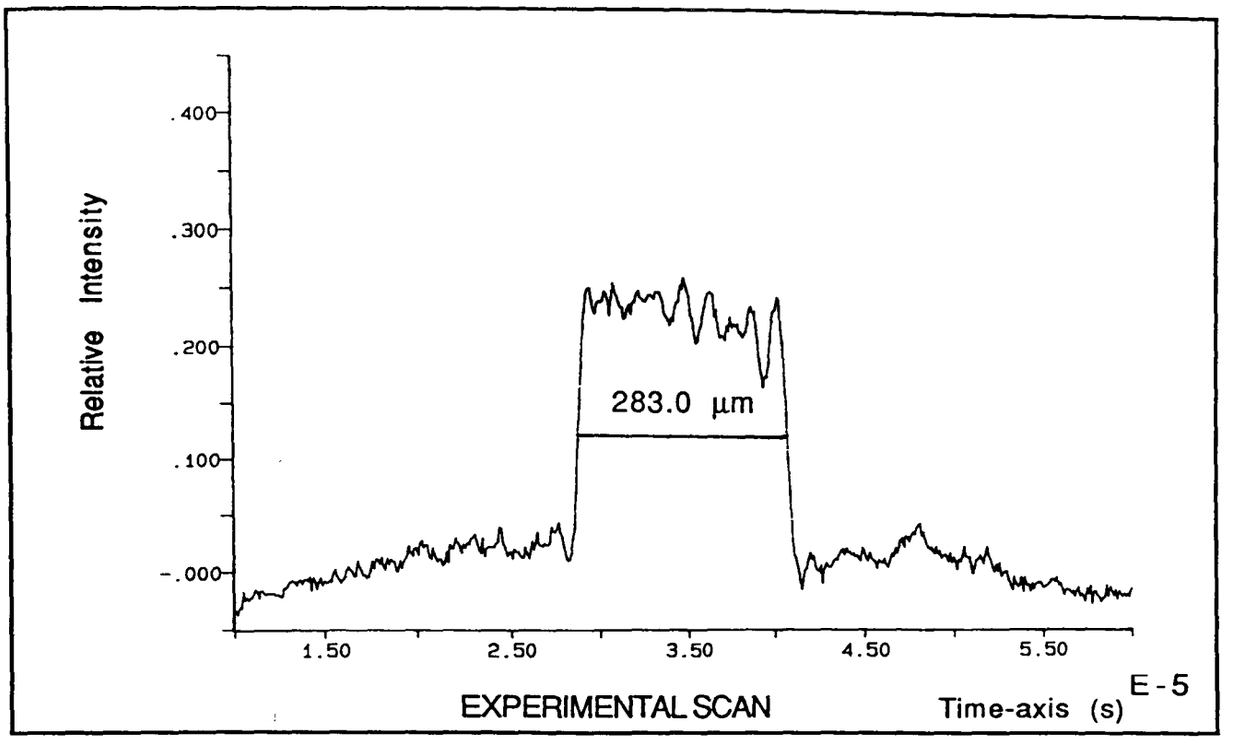

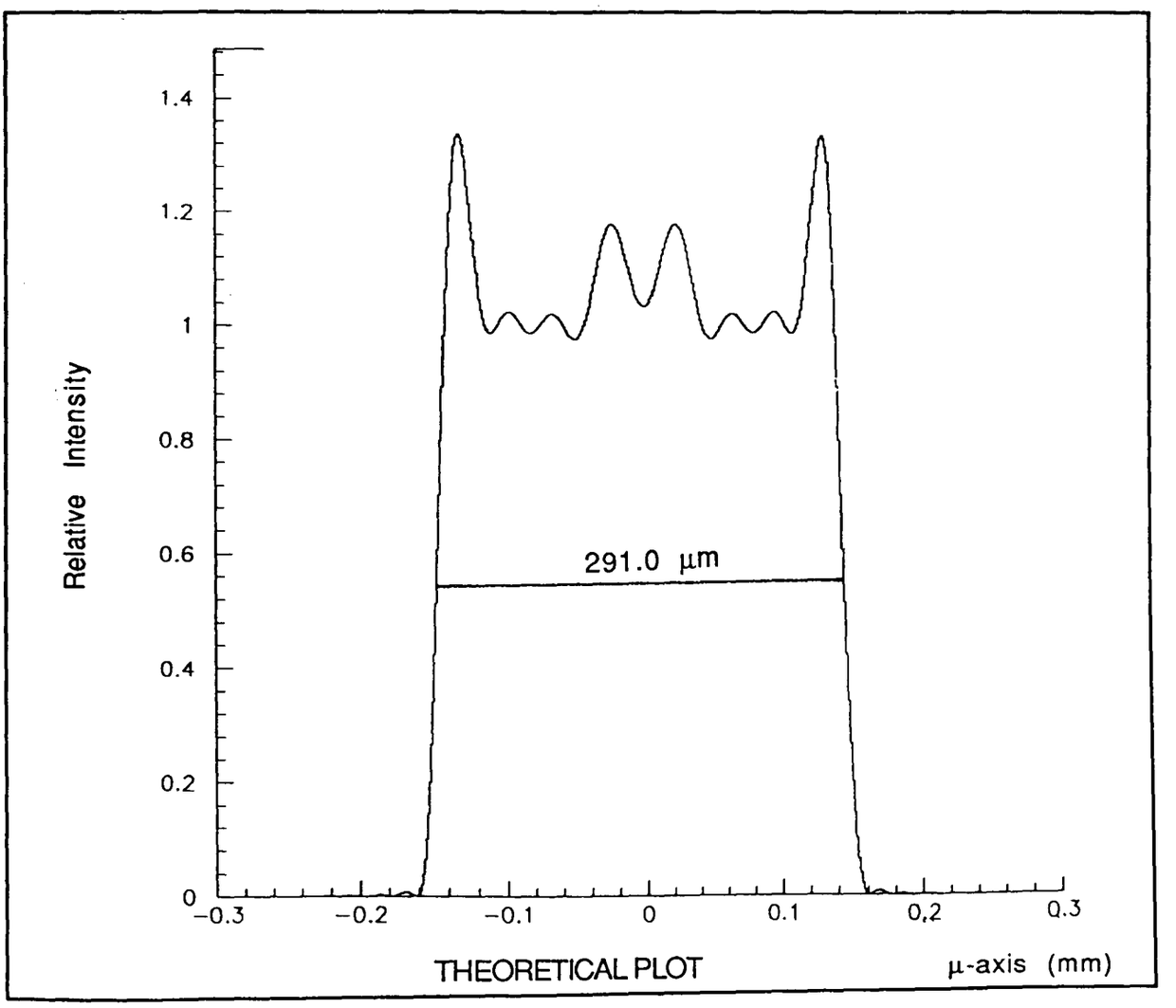

FIG. (5.2.13) Group C1 [C = 300 µm] for Ω=13.324, ΔZ=0.0 mm

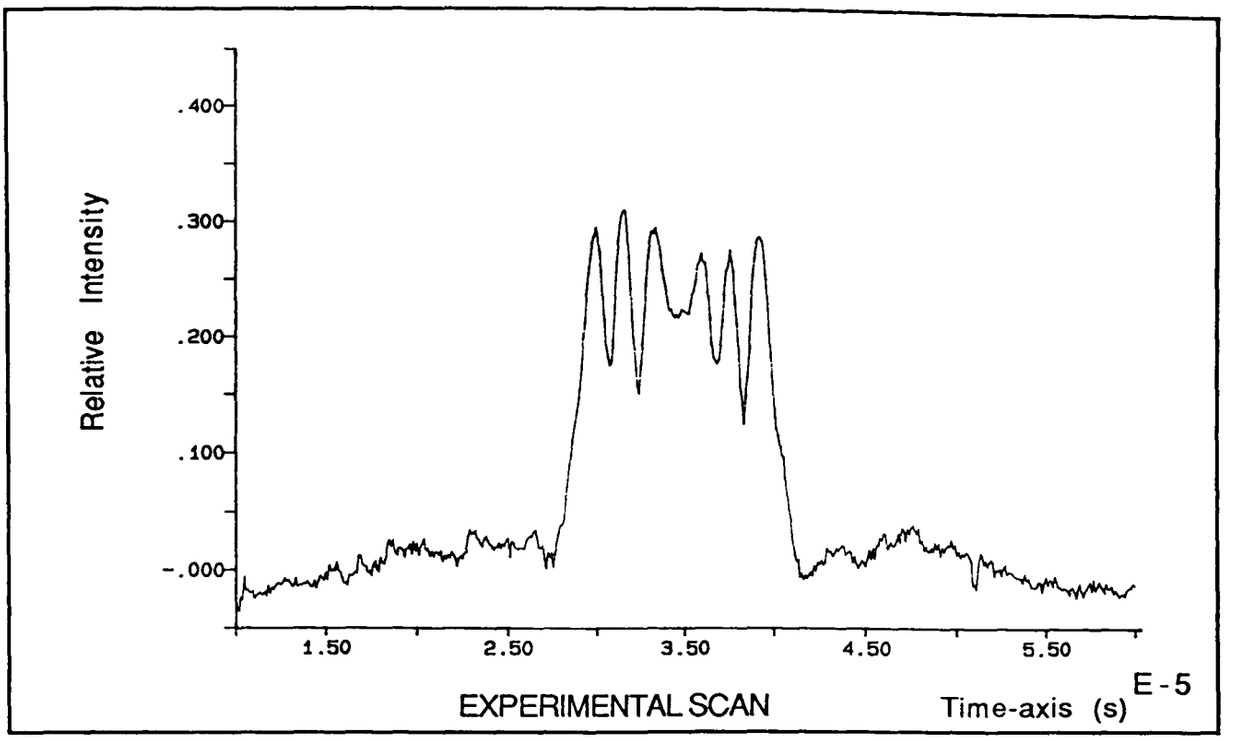

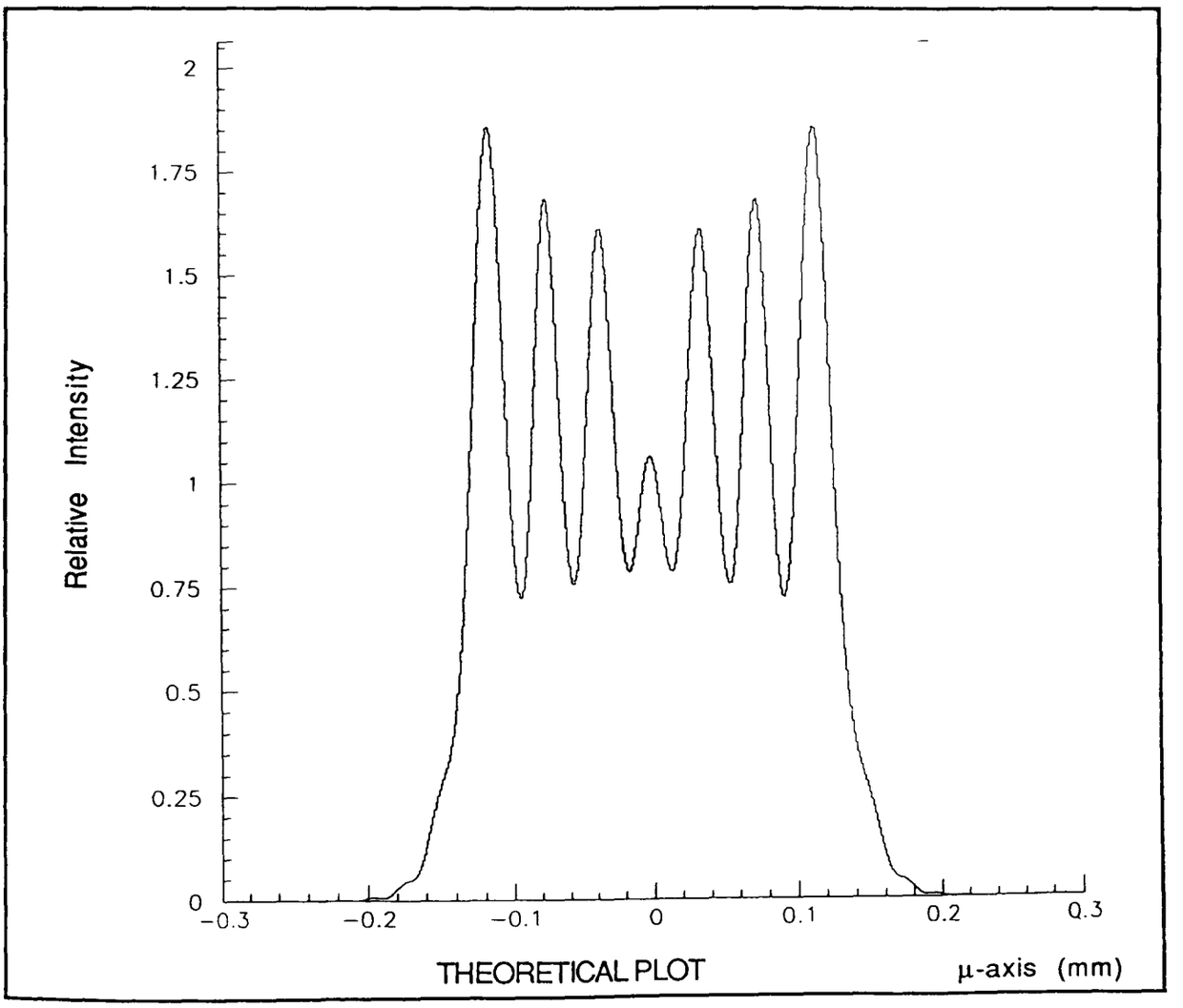

FIG. (5.2.14) Group C1 [C = 300 μm] for Ω=13.324, ΔZ=-3.0 mm

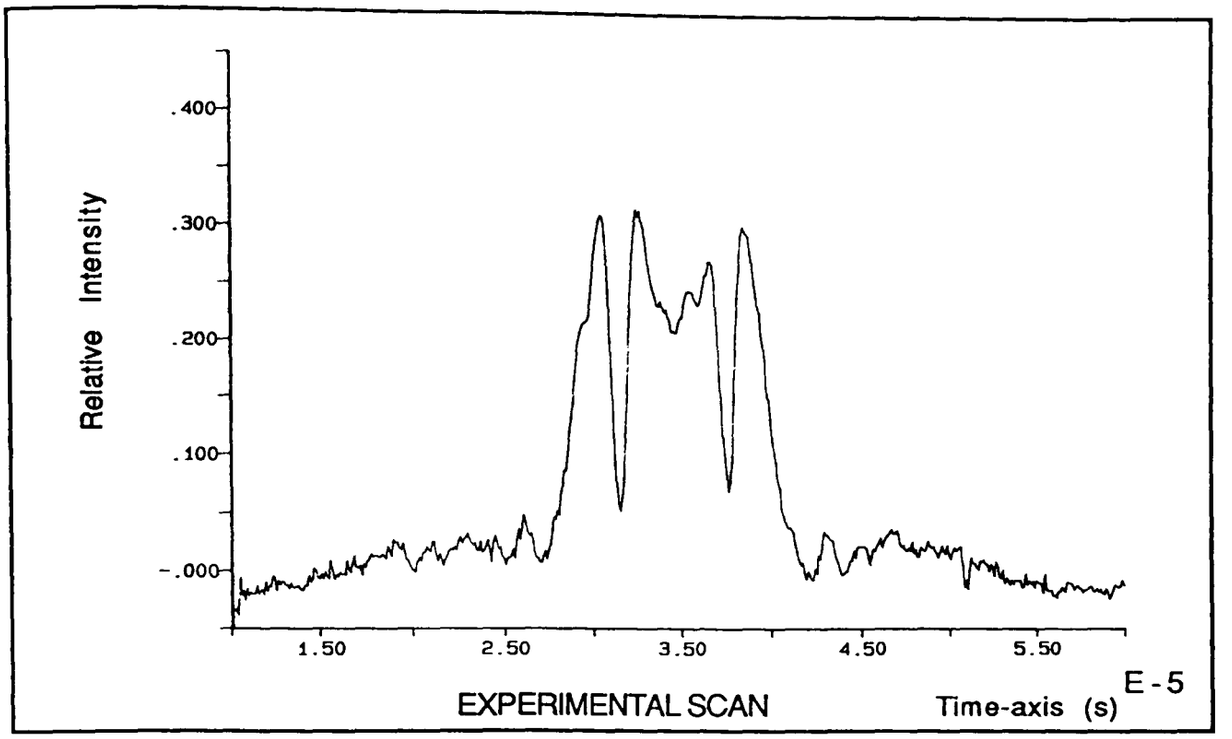

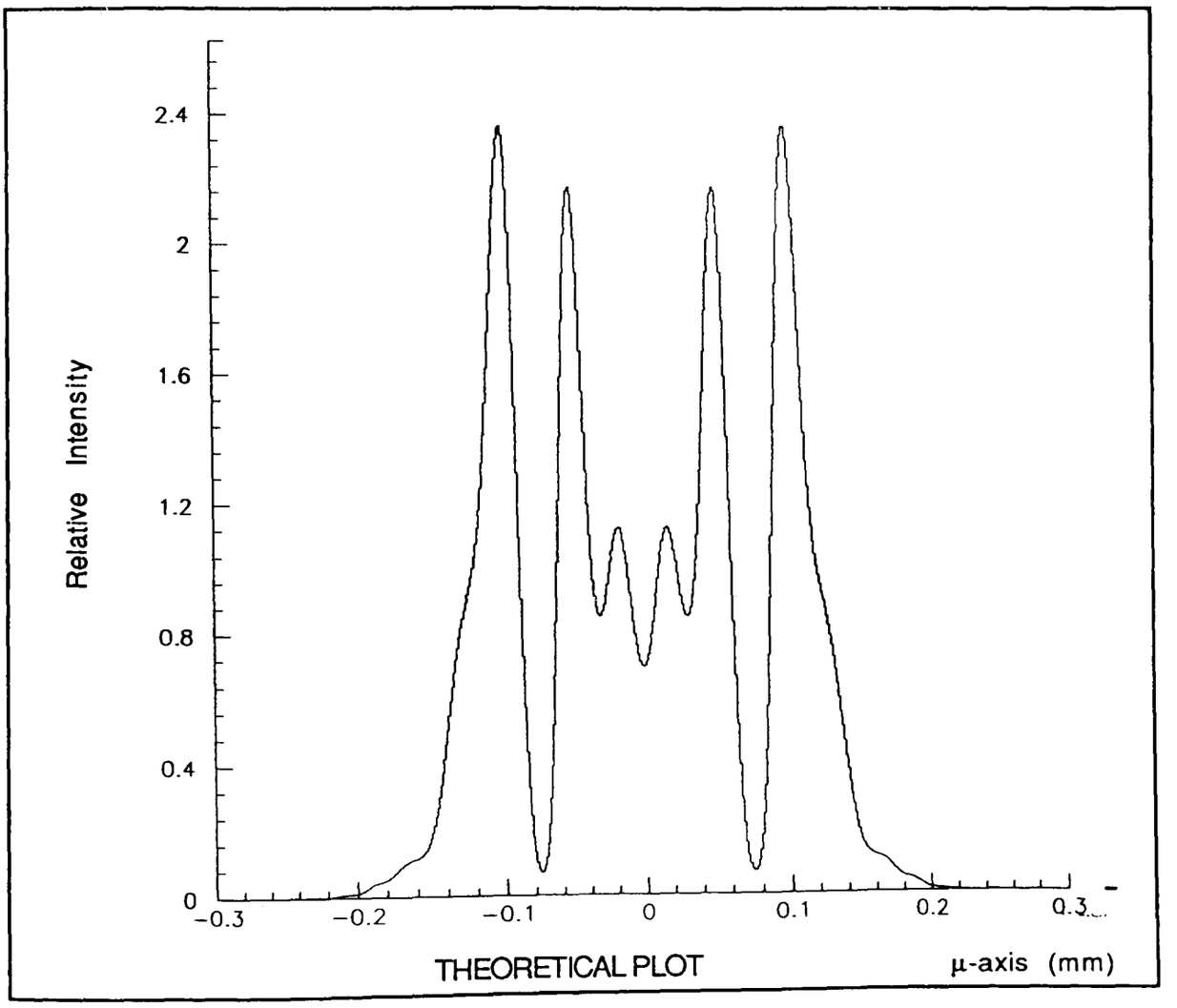

FIG. (5.2.15) Group C1 [C = 300 μm] for Ω=13.324, ΔZ=-4.5 mm

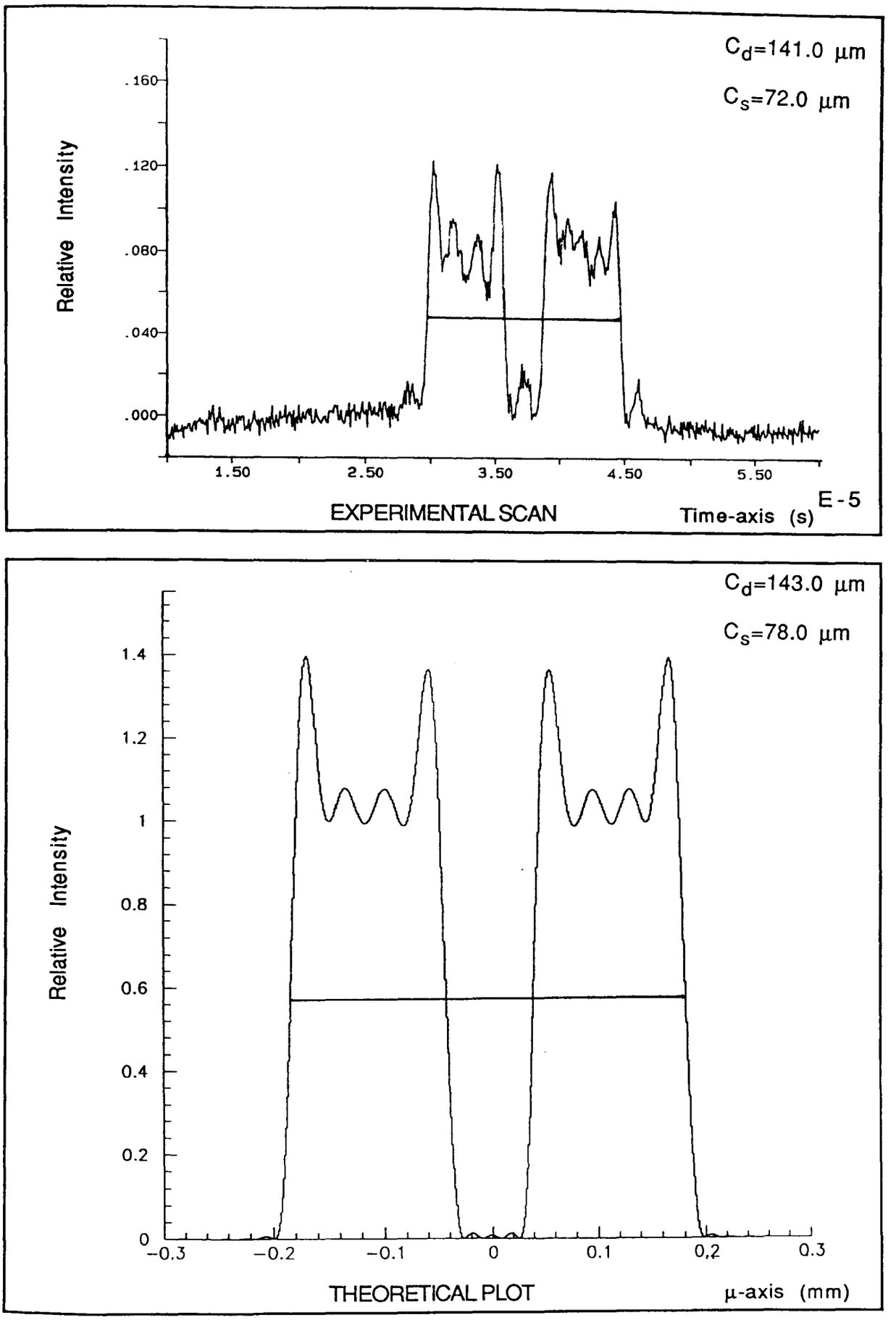

FIG. (5.2.16) Group C2 [C_d = 150 μm, C_s=75 μm] for Ω=13.324, ΔZ=0.0 mm

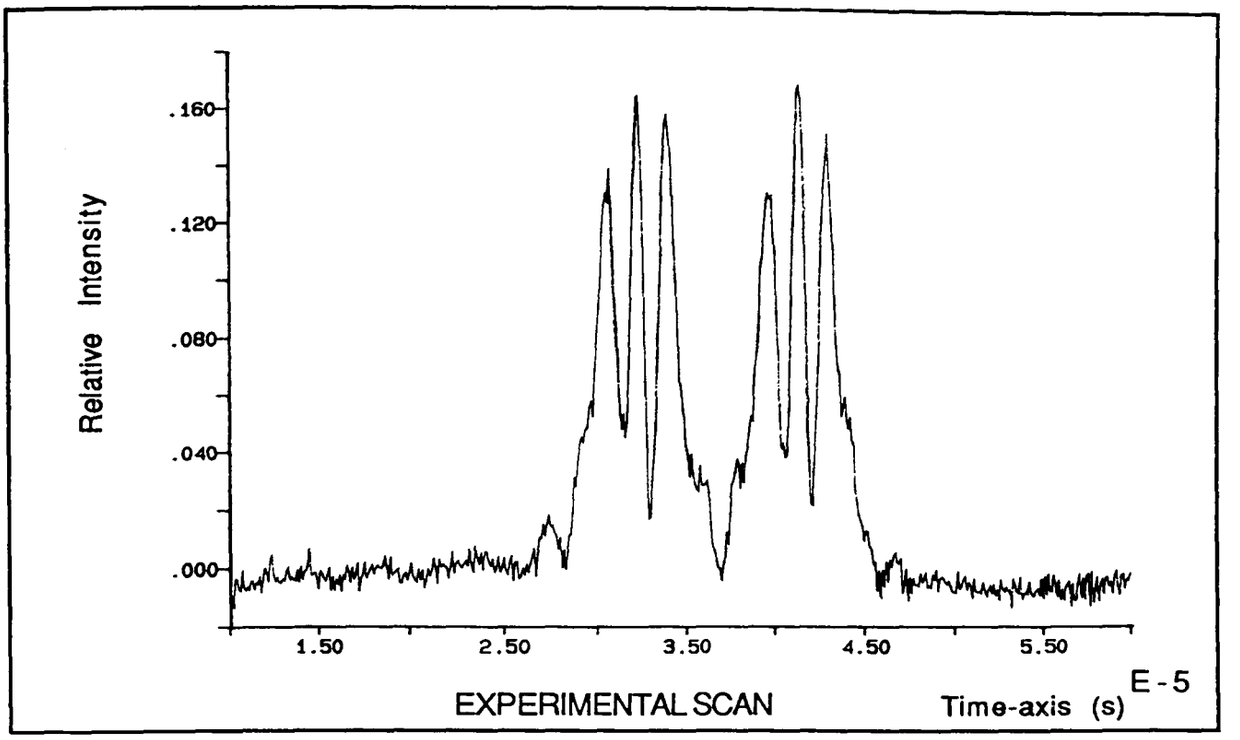

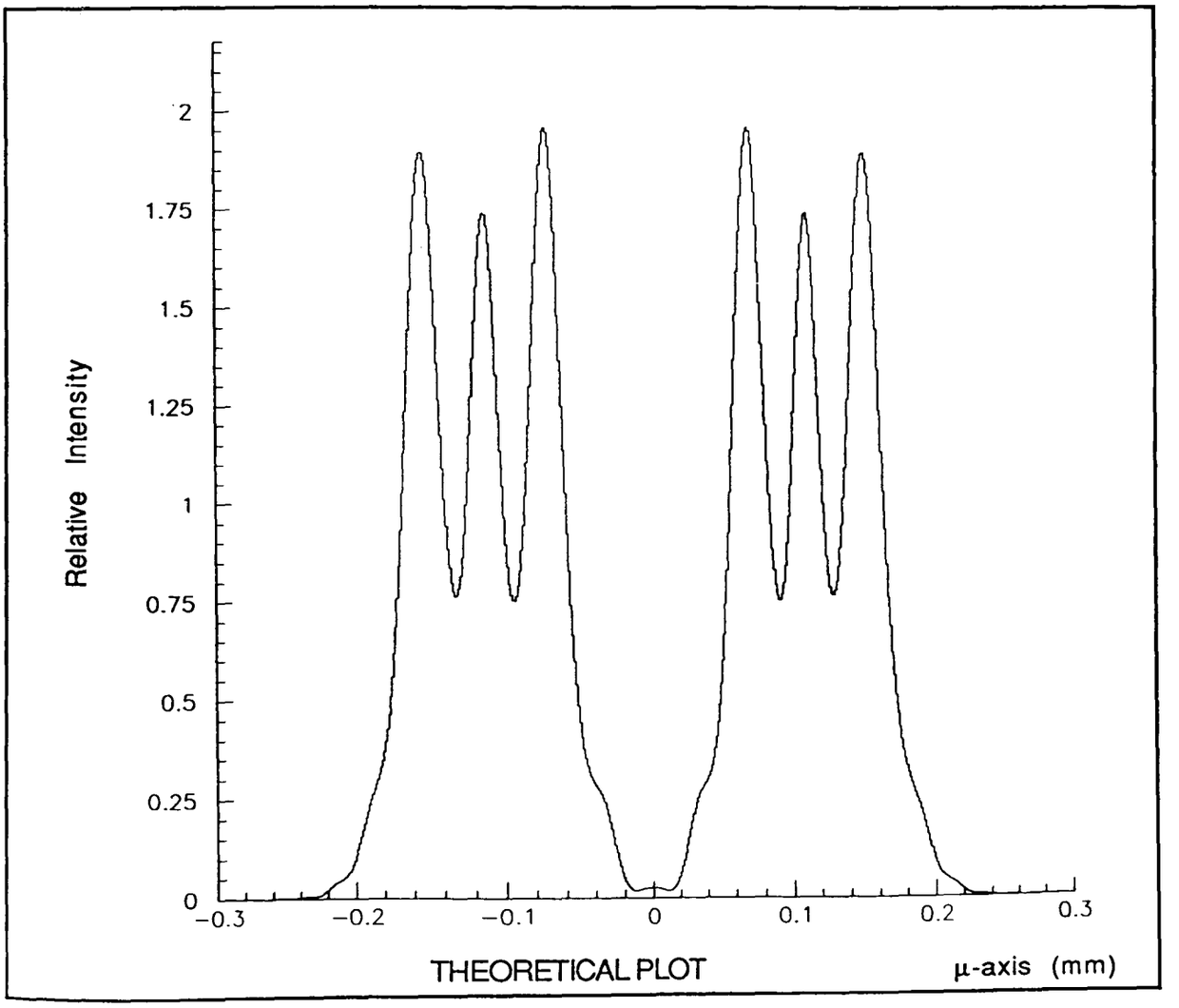

FIG. (5.2.17) Group C2 [C_d = 150 μm, C_s=75 μm] for Ω=13.324, ΔZ=-3.0 mm

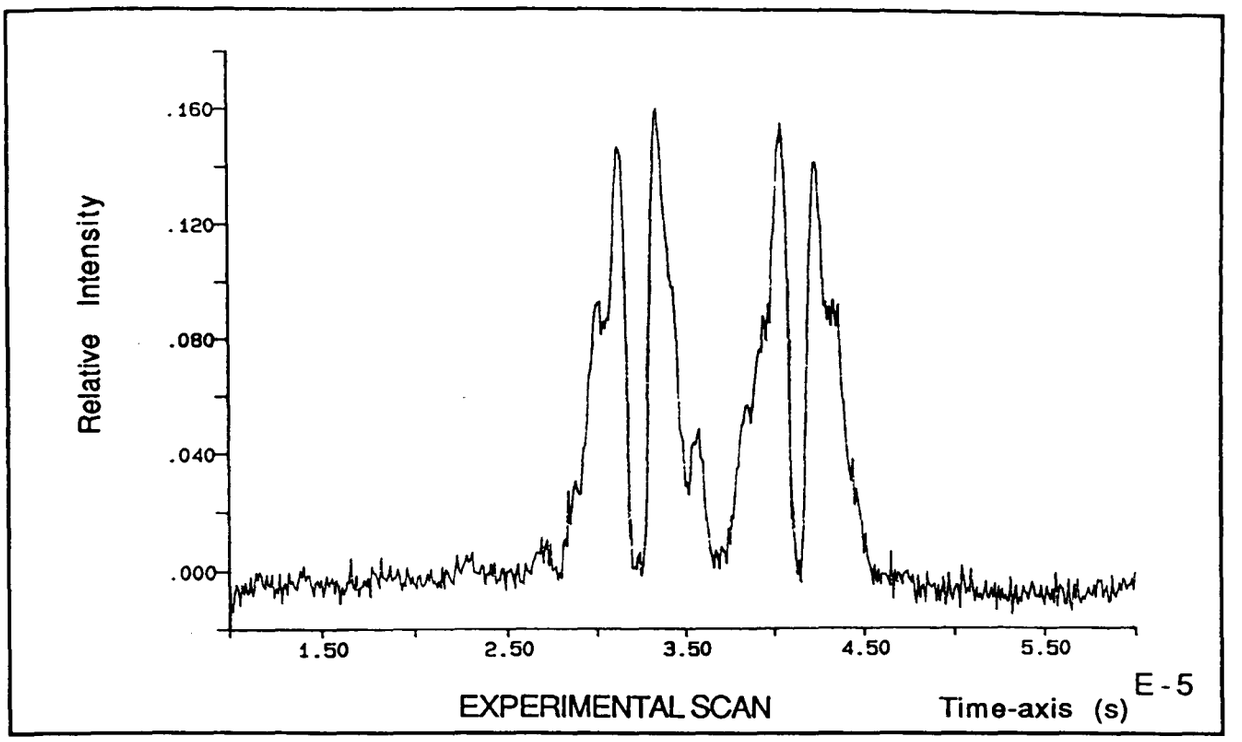

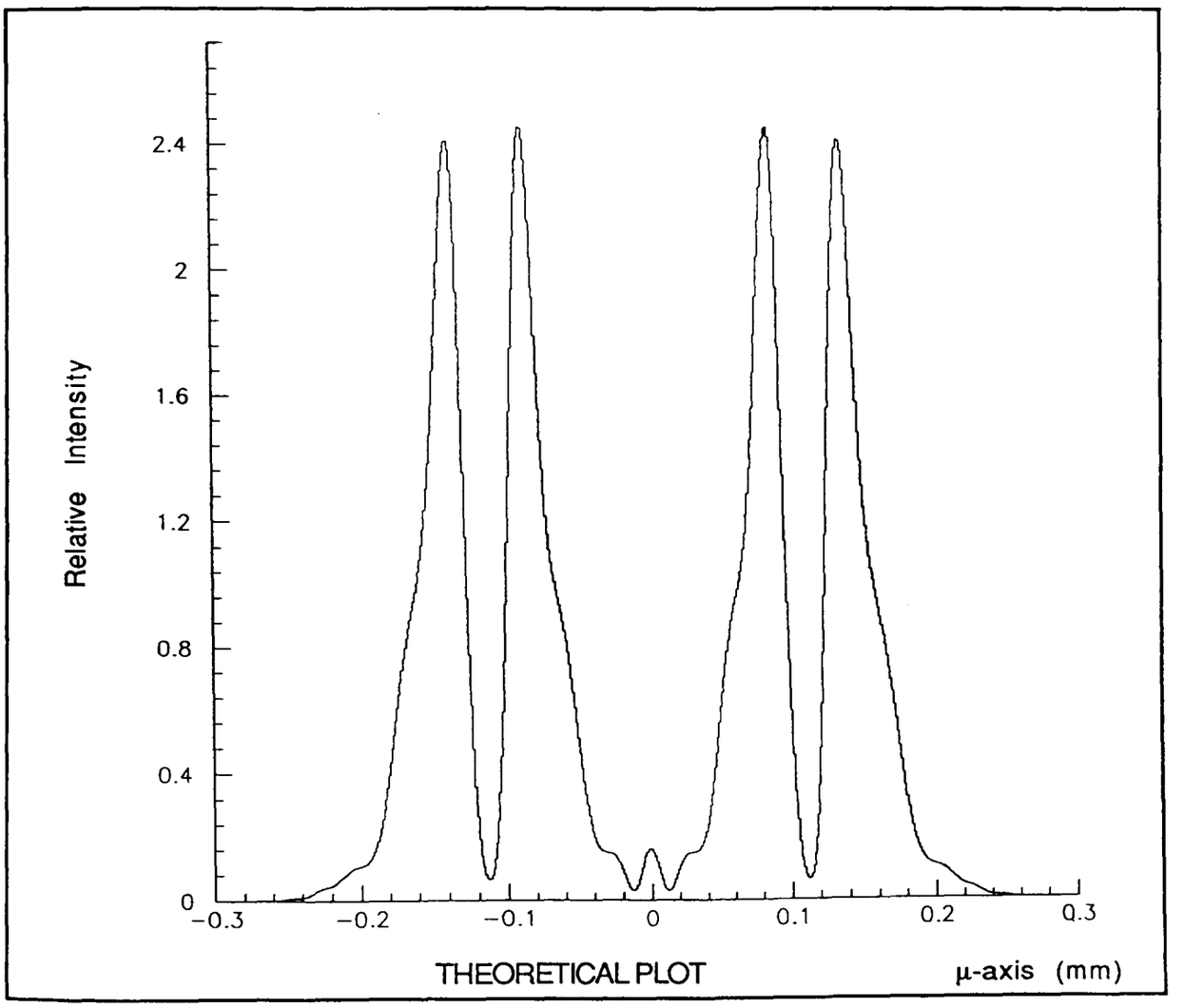

FIG. (5.2.18) Group C2 [C_d = 150 μm, C_s=75 μm] for Ω=13.324, ΔZ=-4.5 mm

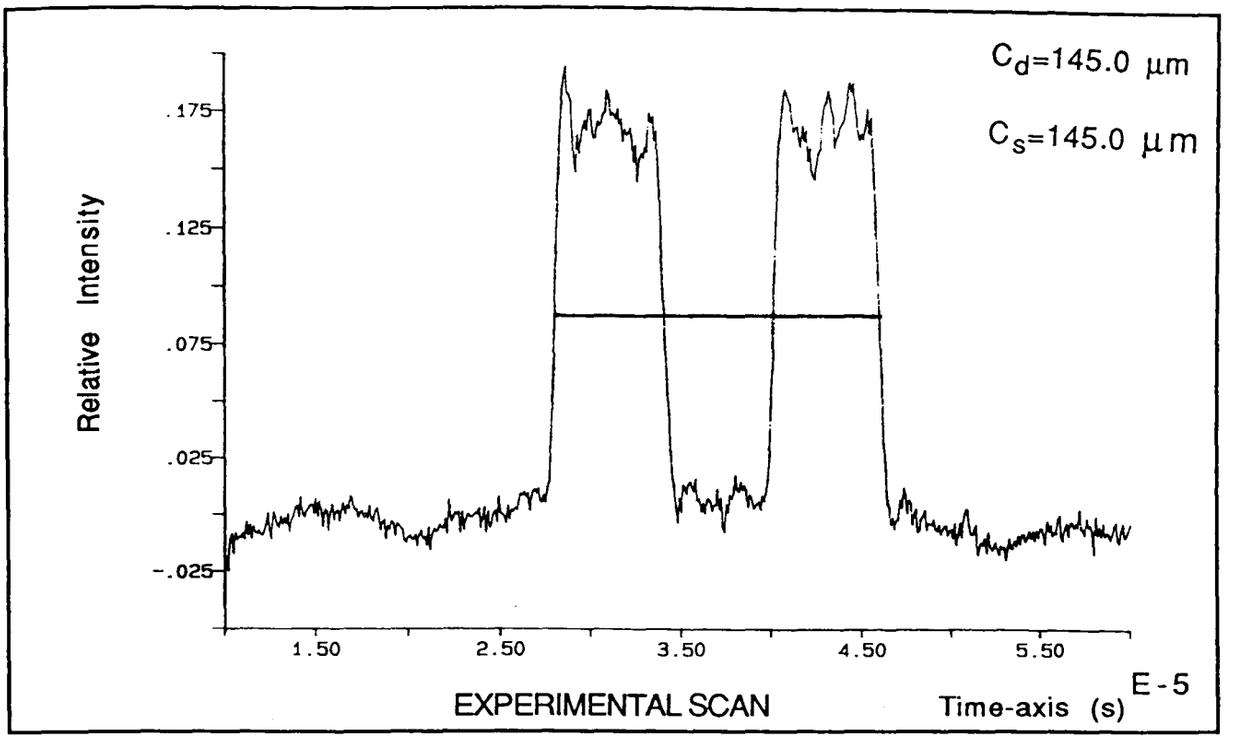

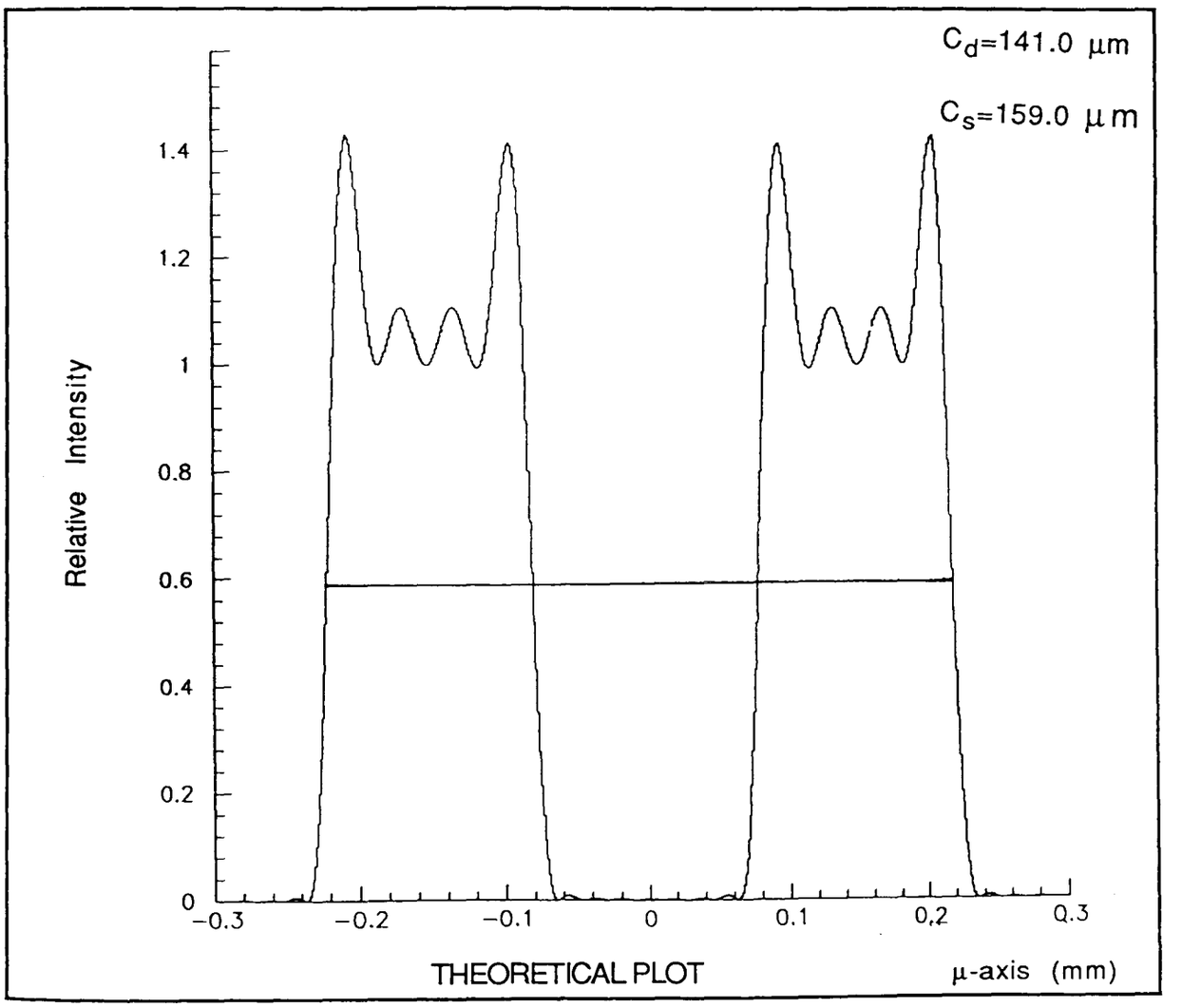

FIG. (5.2.19) Group C3 [C_d = 150 μm, C_s=150 μm] for Ω=13.324, ΔZ=0.0 mm

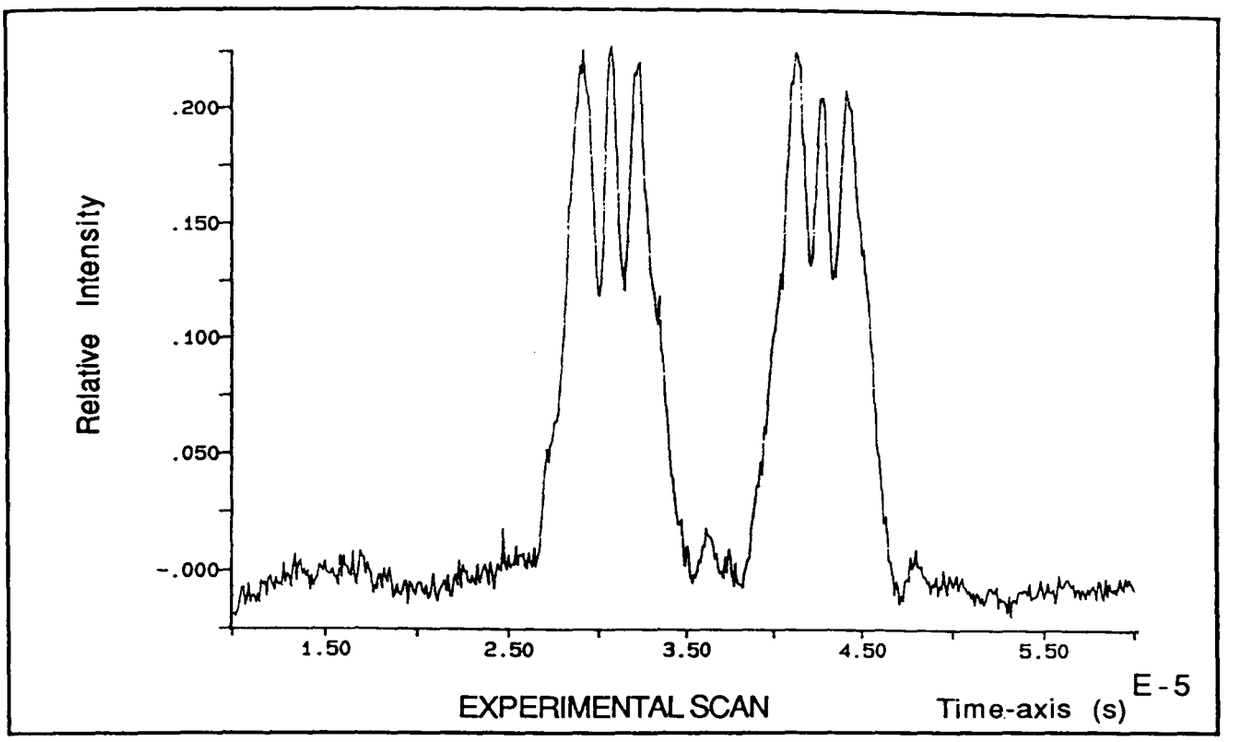

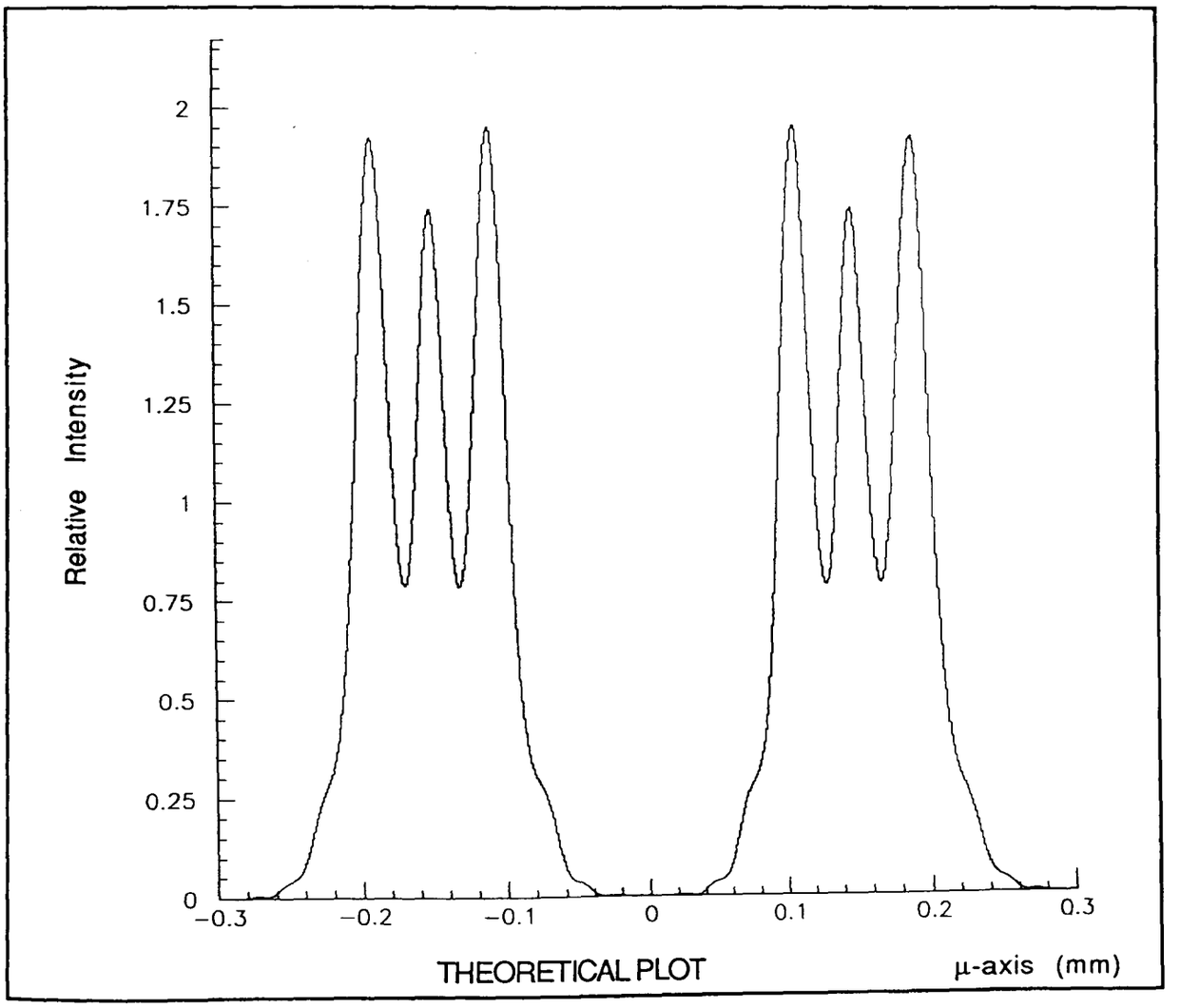

FIG. (5.2.20) Group C3 [C_d = 150 μm, C_s=150 μm] for Ω=13.324, ΔZ=-3.0 mm

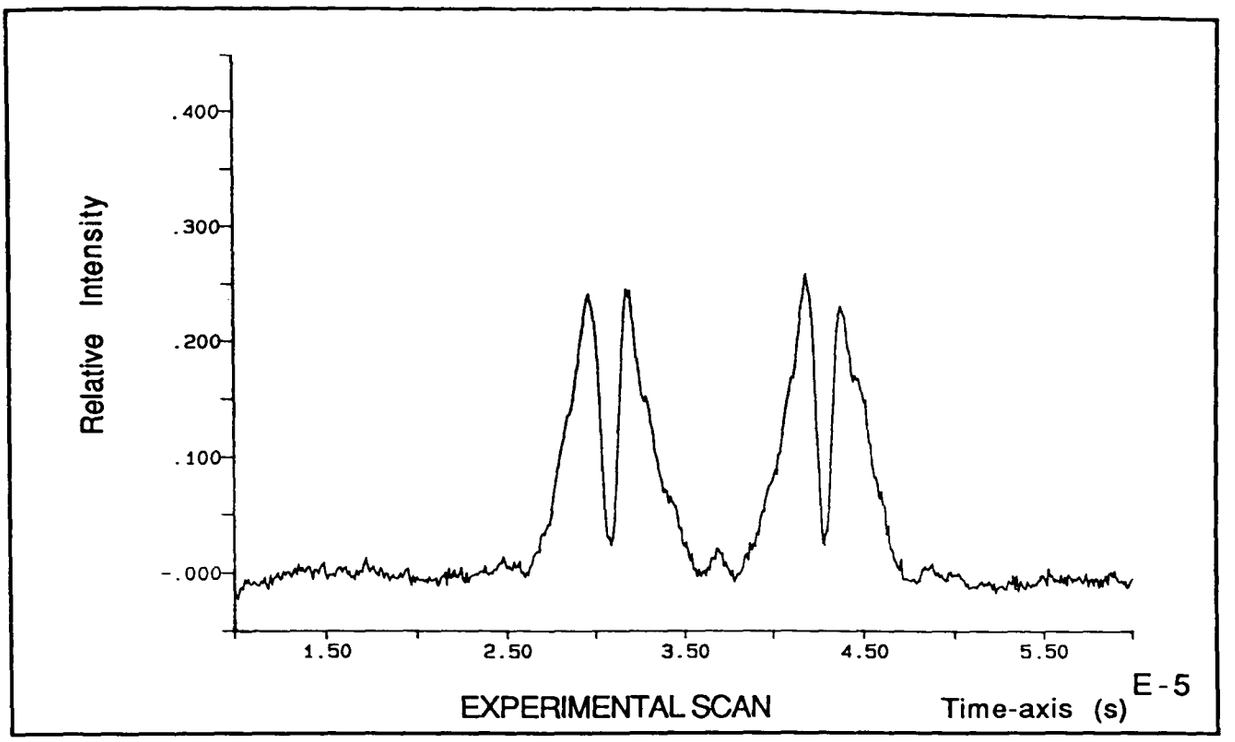

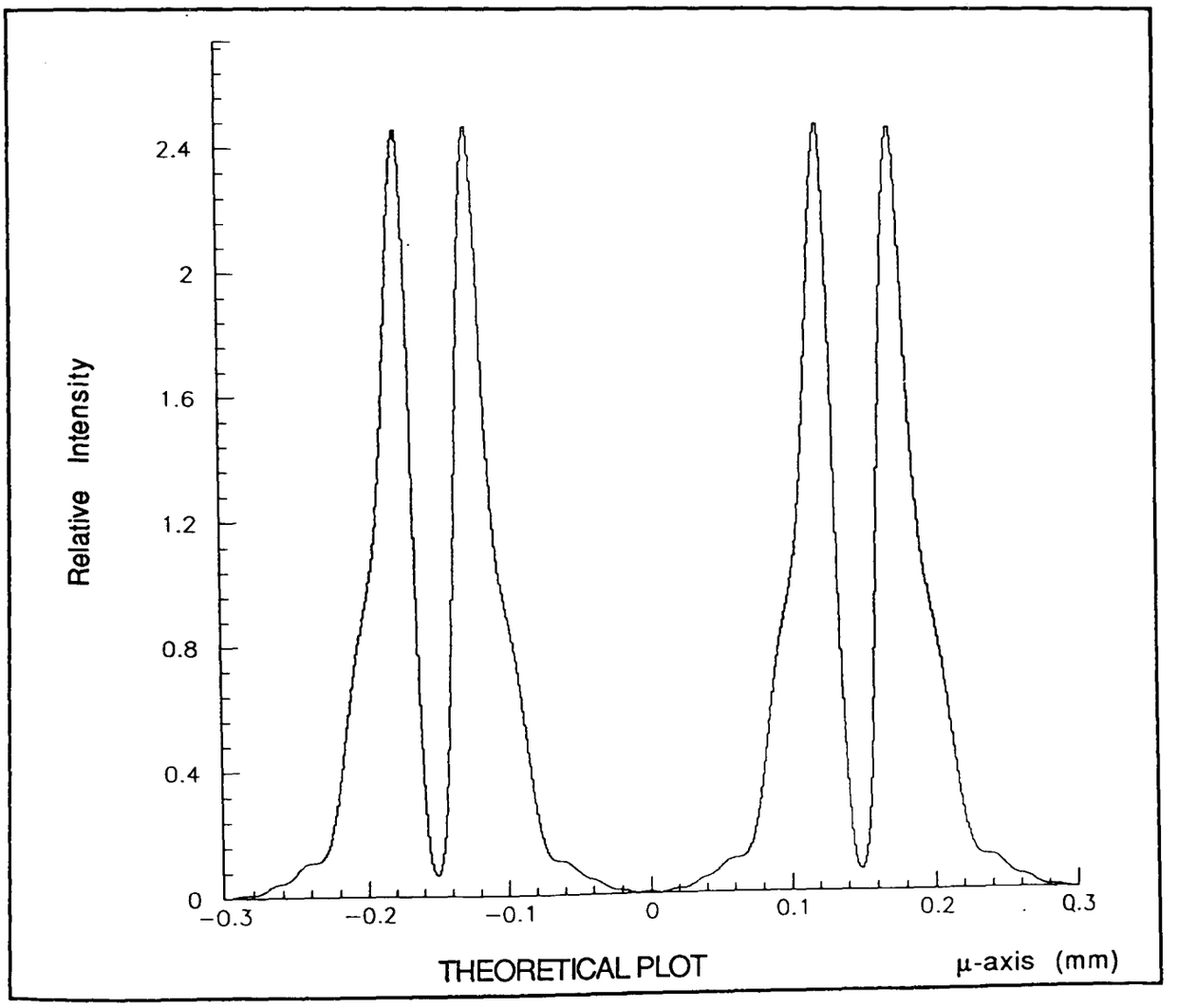

FIG. (5.2.21) Group C3 [C_d = 150 μm, C_s=150 μm] for Ω=13.324, ΔZ=-4.5 mm

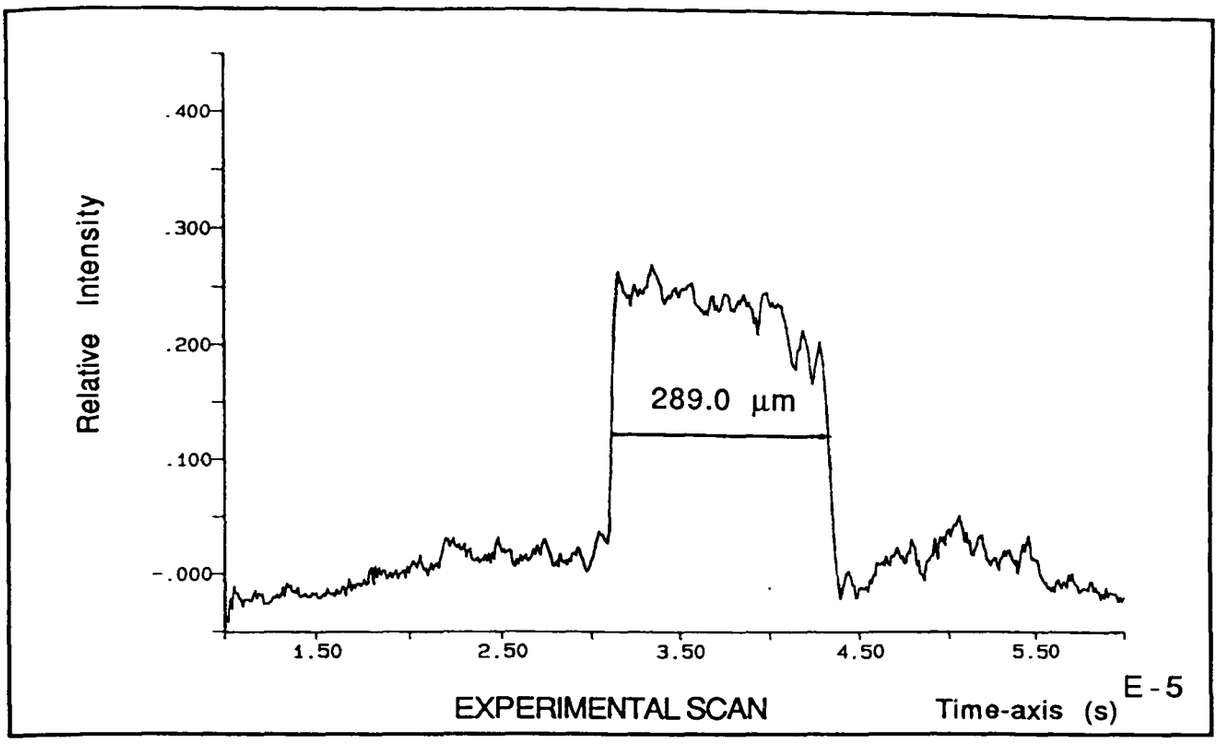

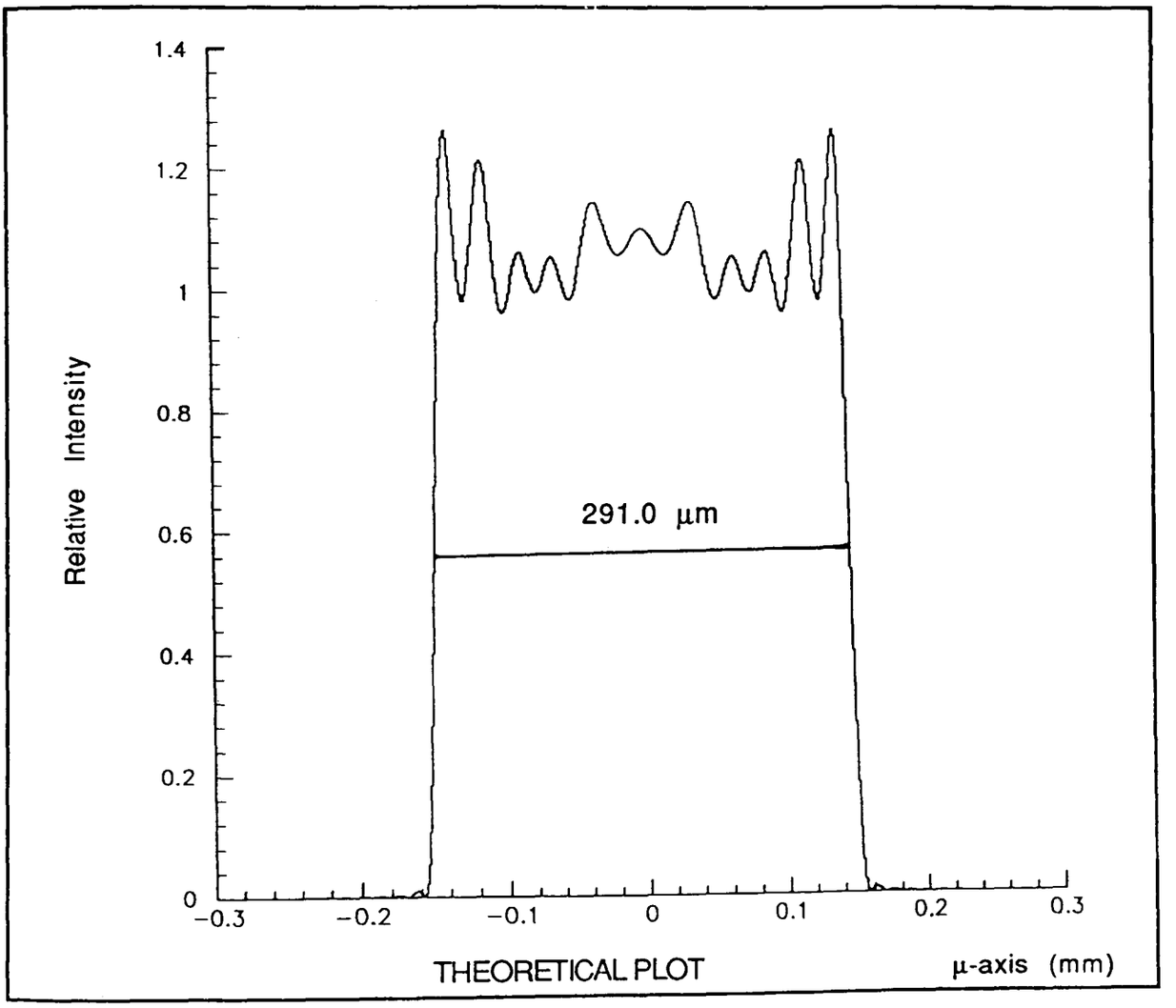

FIG. (5.2.22) Group C1 [C = 300 µm] for Ω=19.616, ΔZ=0.0 mm

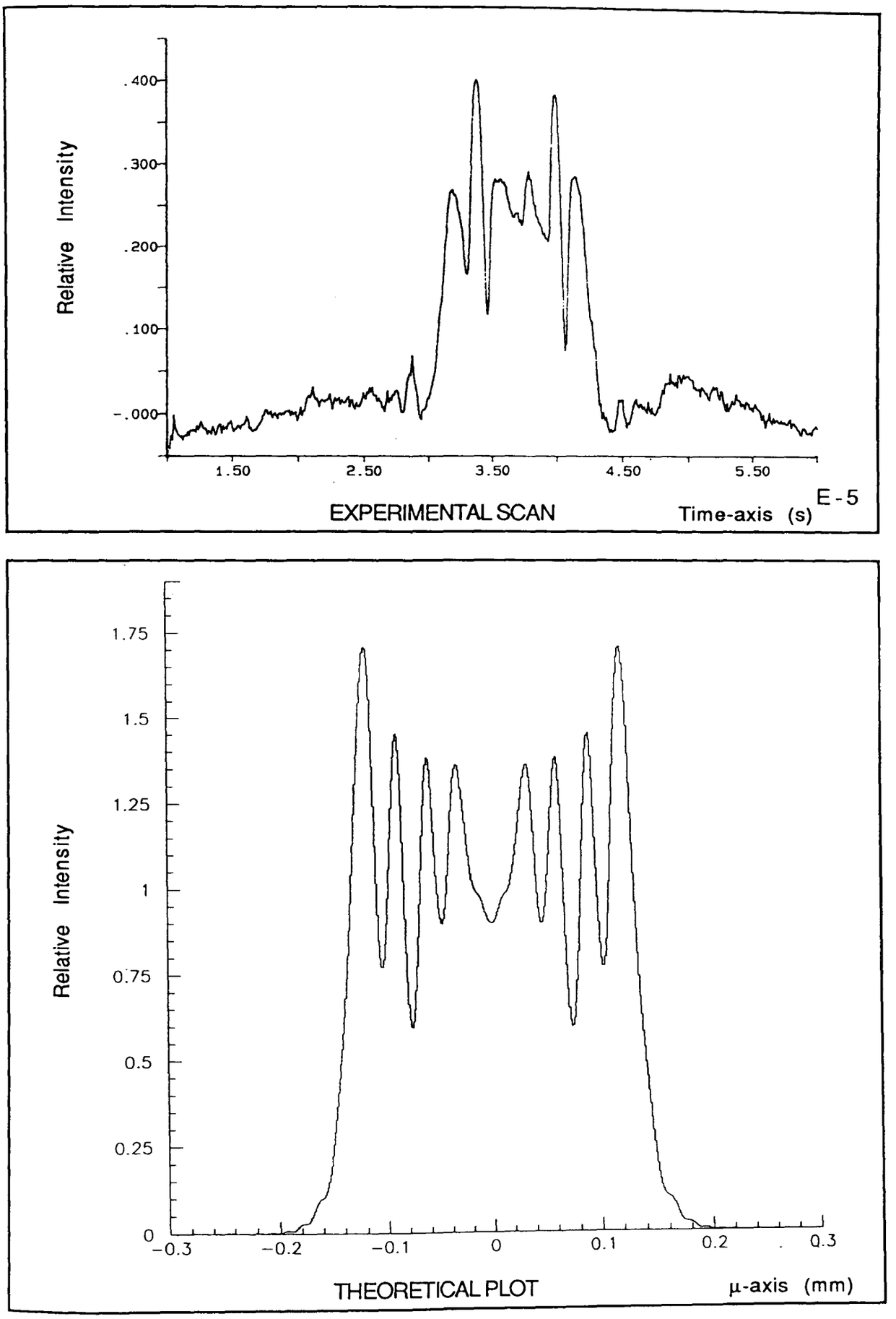

FIG. (5.2.23) Group C1 [C = 300 μm] for Ω=19.616, ΔZ=-3.0 mm

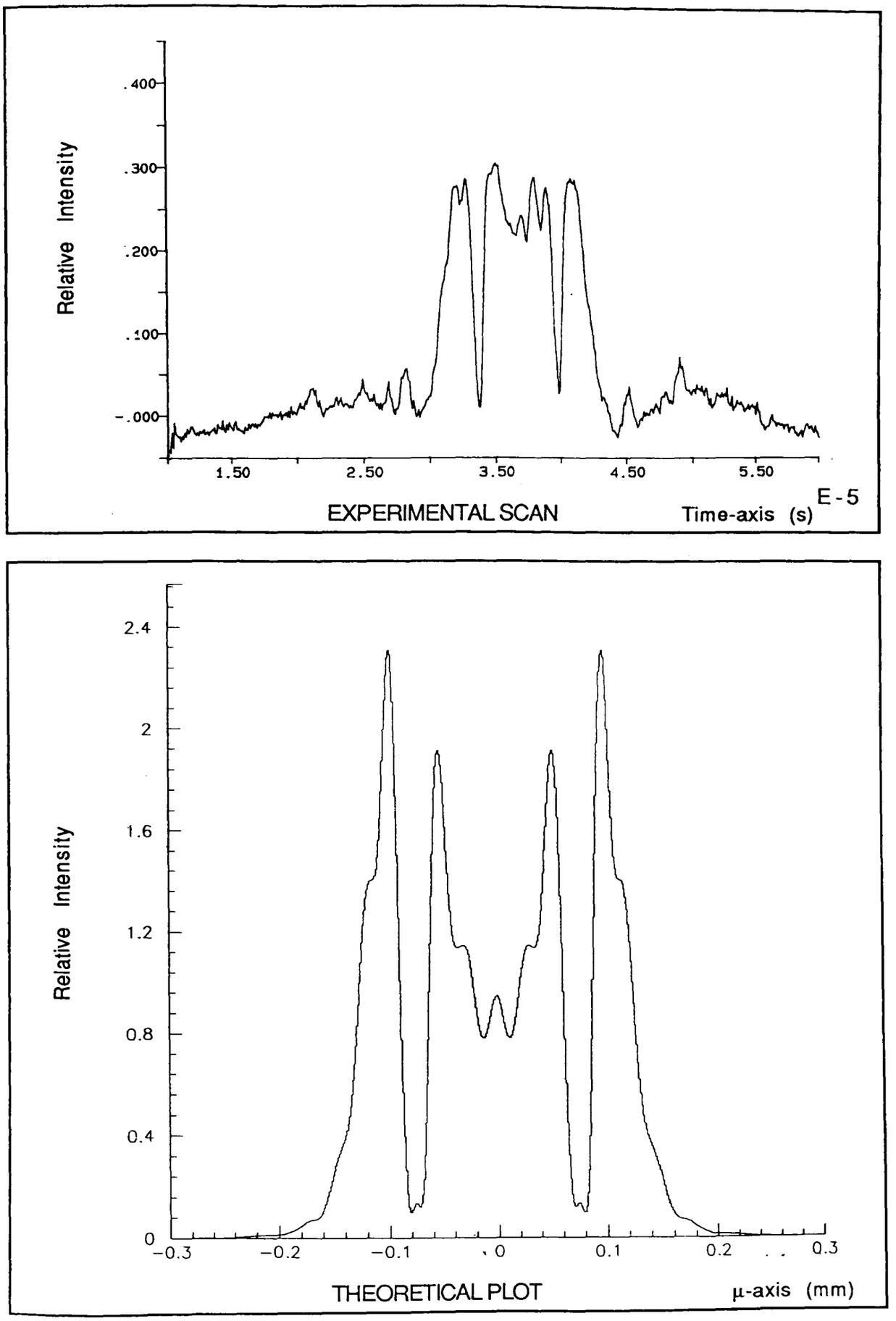

FIG. (5.2.24) Group C1 [C = 300 μm] for Ω=19.616, ΔZ=-4.5 mm

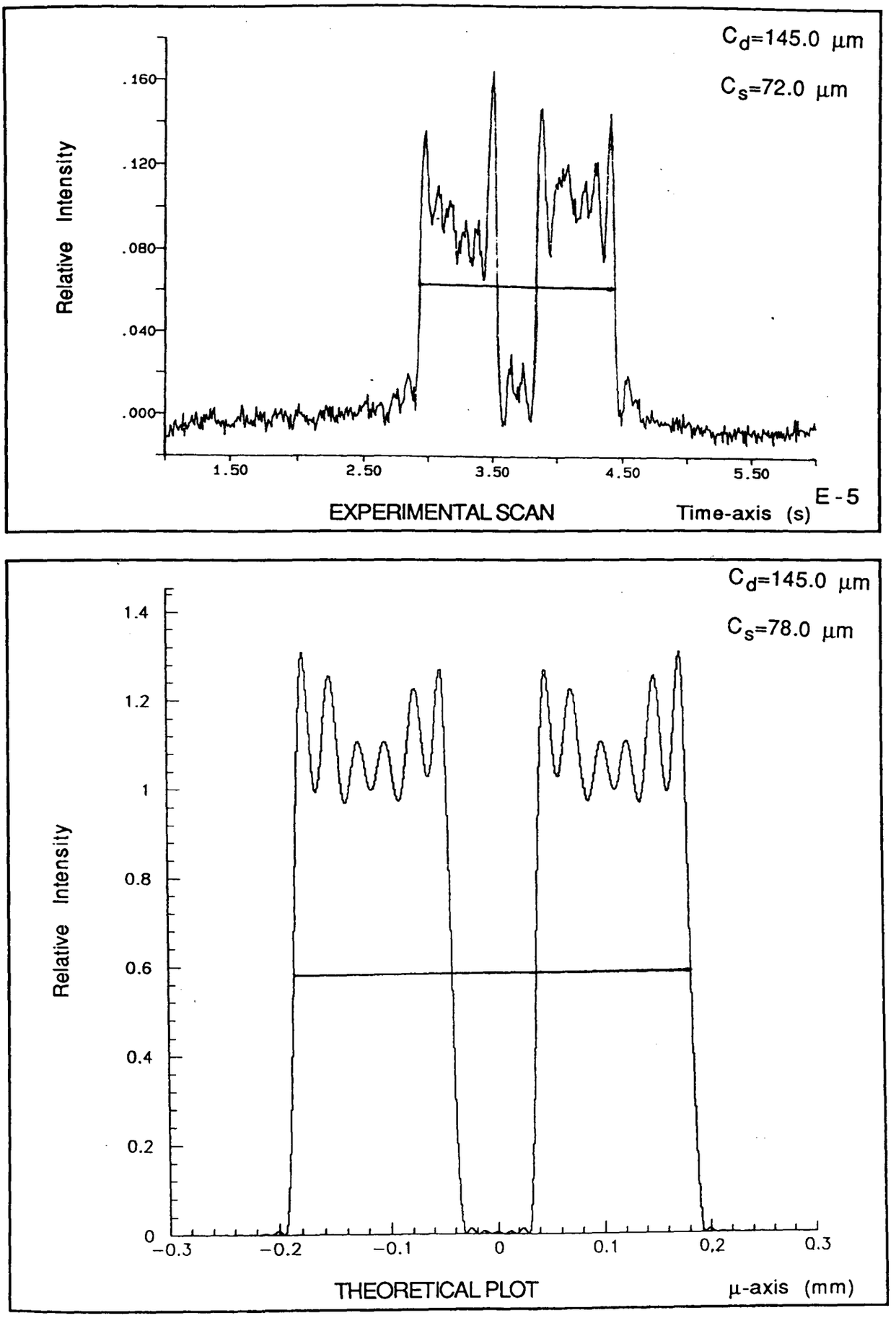

FIG. (5.2.25) Group C2 [C_d = 150 μm, C_s=75 μm] for Ω=19.616, ΔZ=0.0 mm

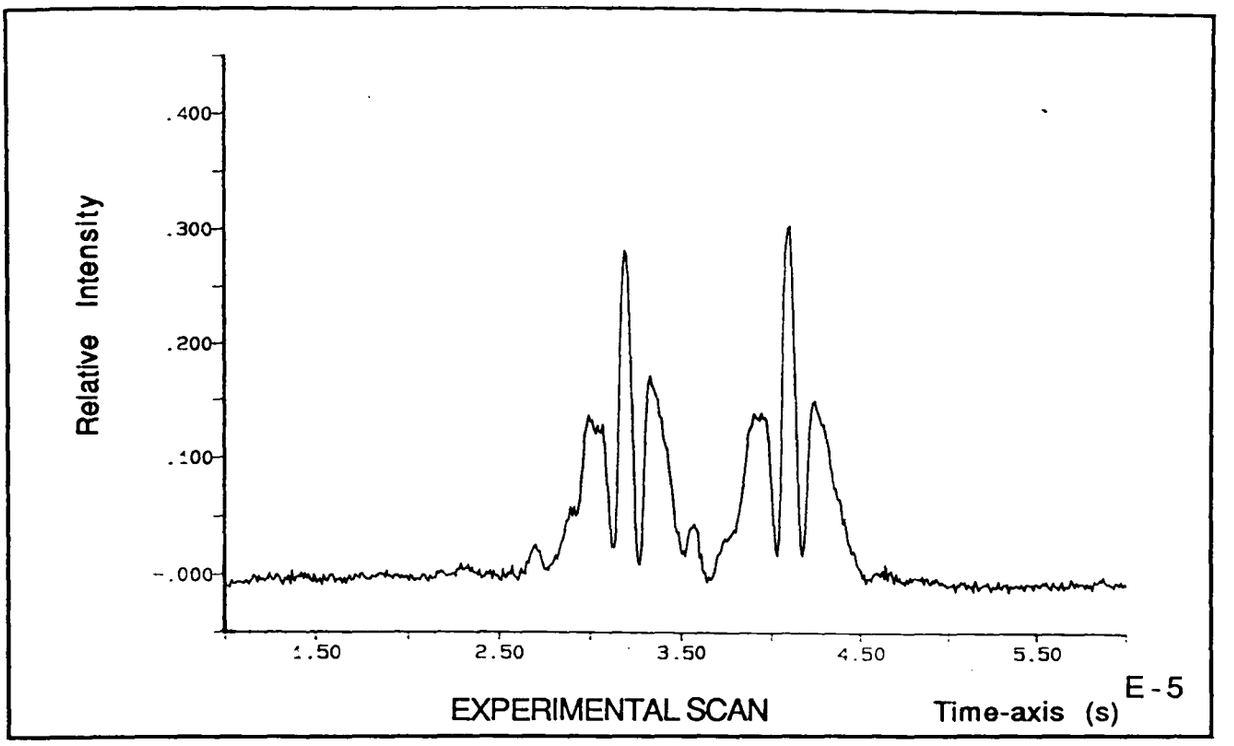

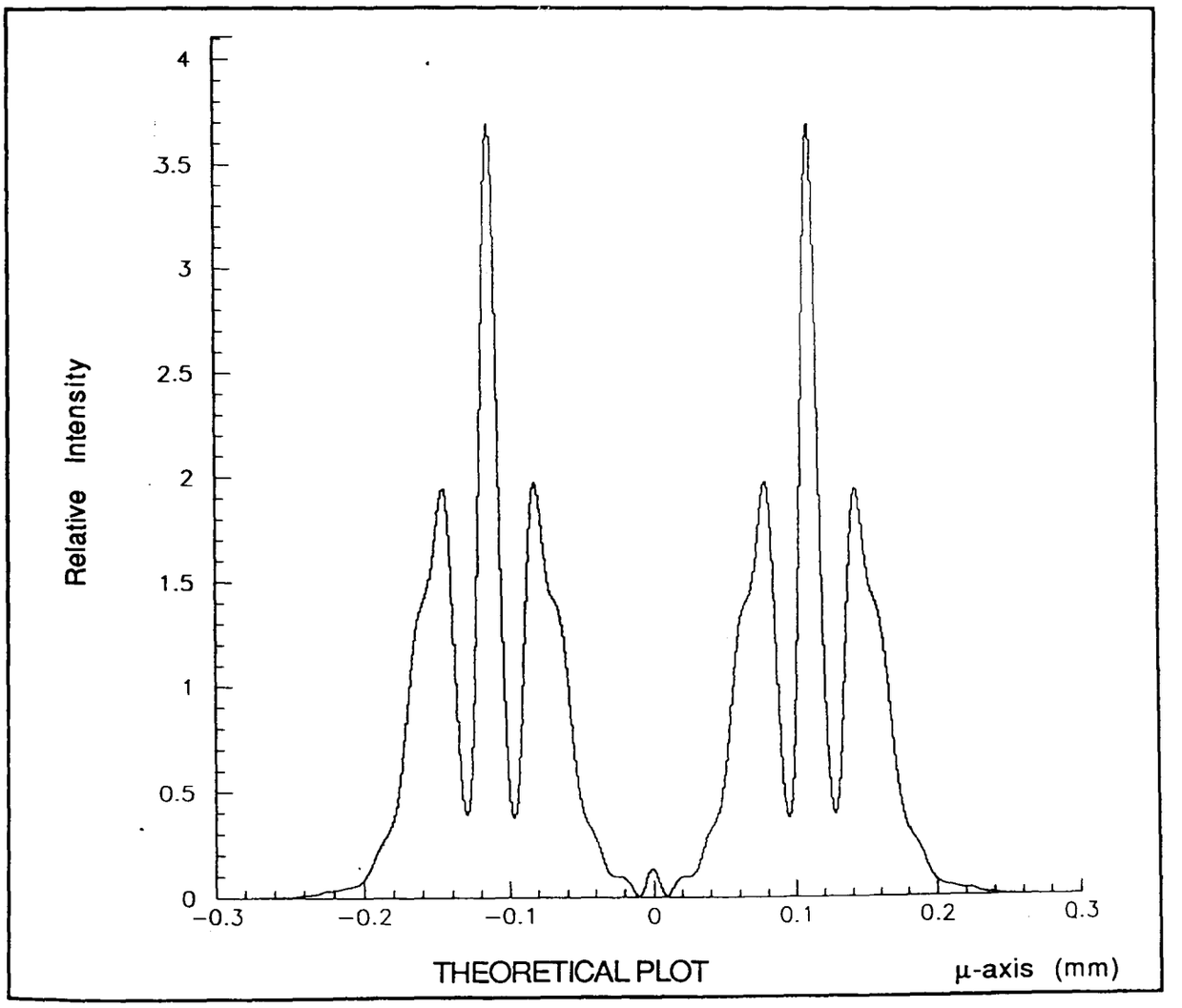

FIG. (5.2.26) Group C2 [C_d = 150 μm, C_s=75 μm] for Ω=19.616, ΔZ=-3.0 mm

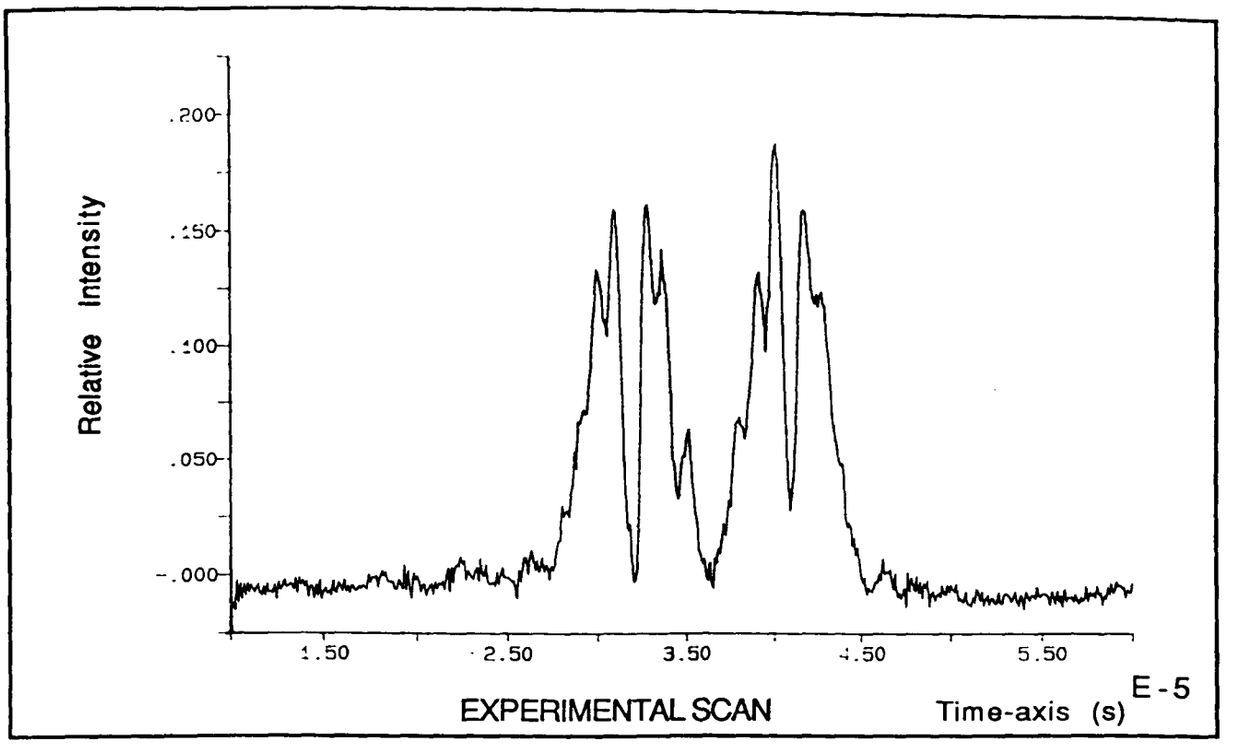

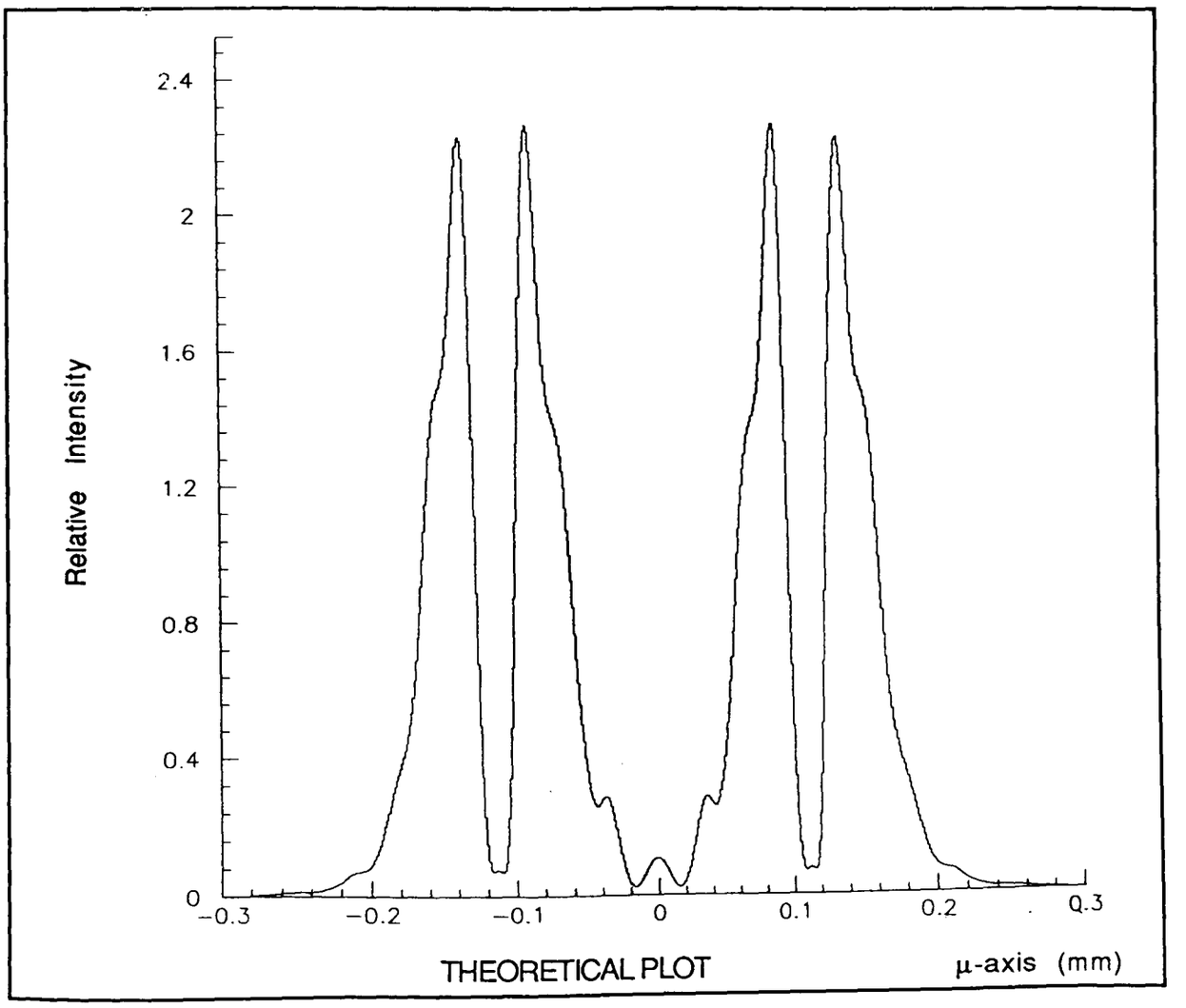

FIG. (5.2.27) Group C2 [C_d = 150 μm, C_s=75 μm] for Ω=19.616, ΔZ=-4.5 mm

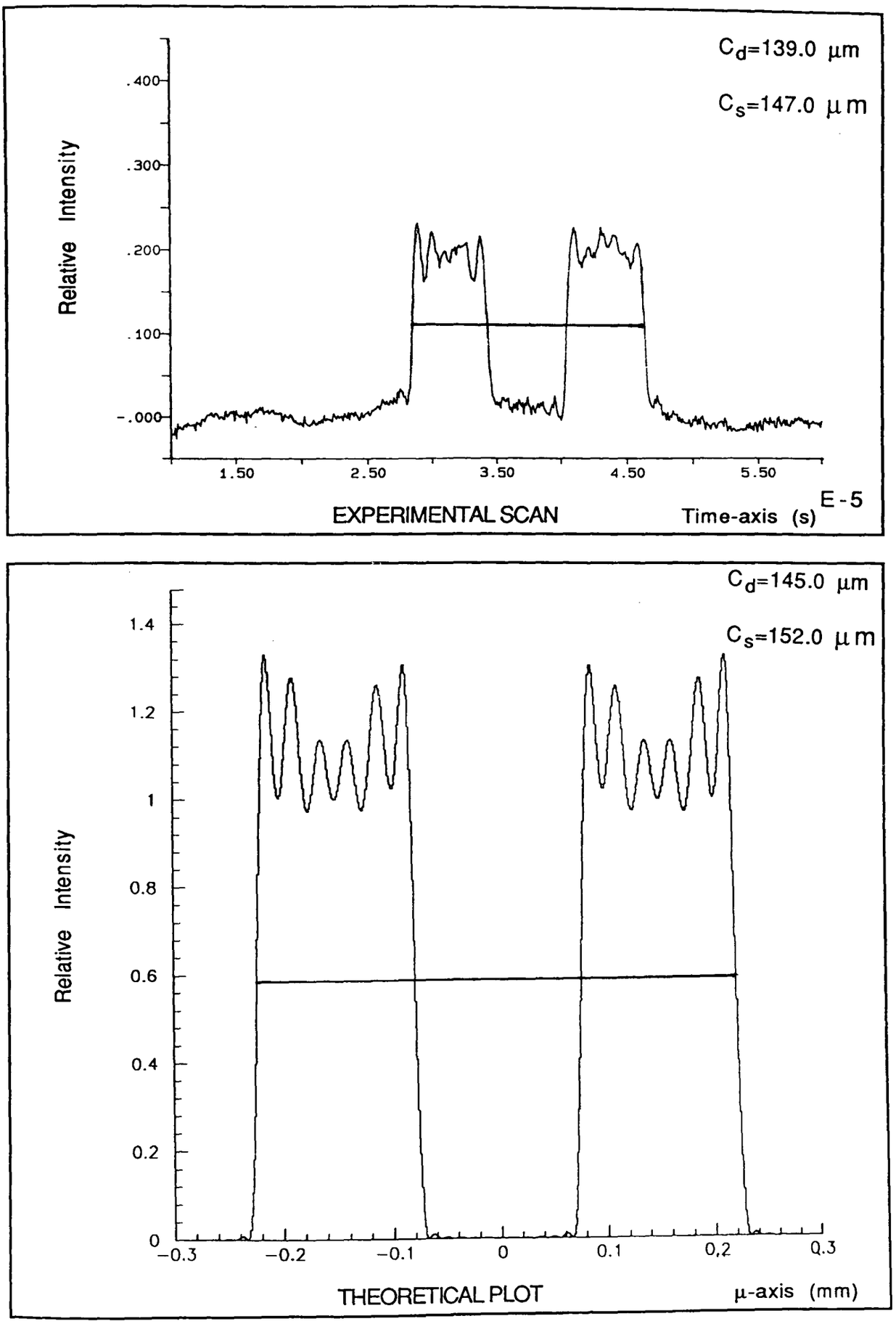

FIG. (5.2.28) Group C3 [C_d = 150 μm, C_s=150 μm] for Ω=19.616, ΔZ=0.0 mm

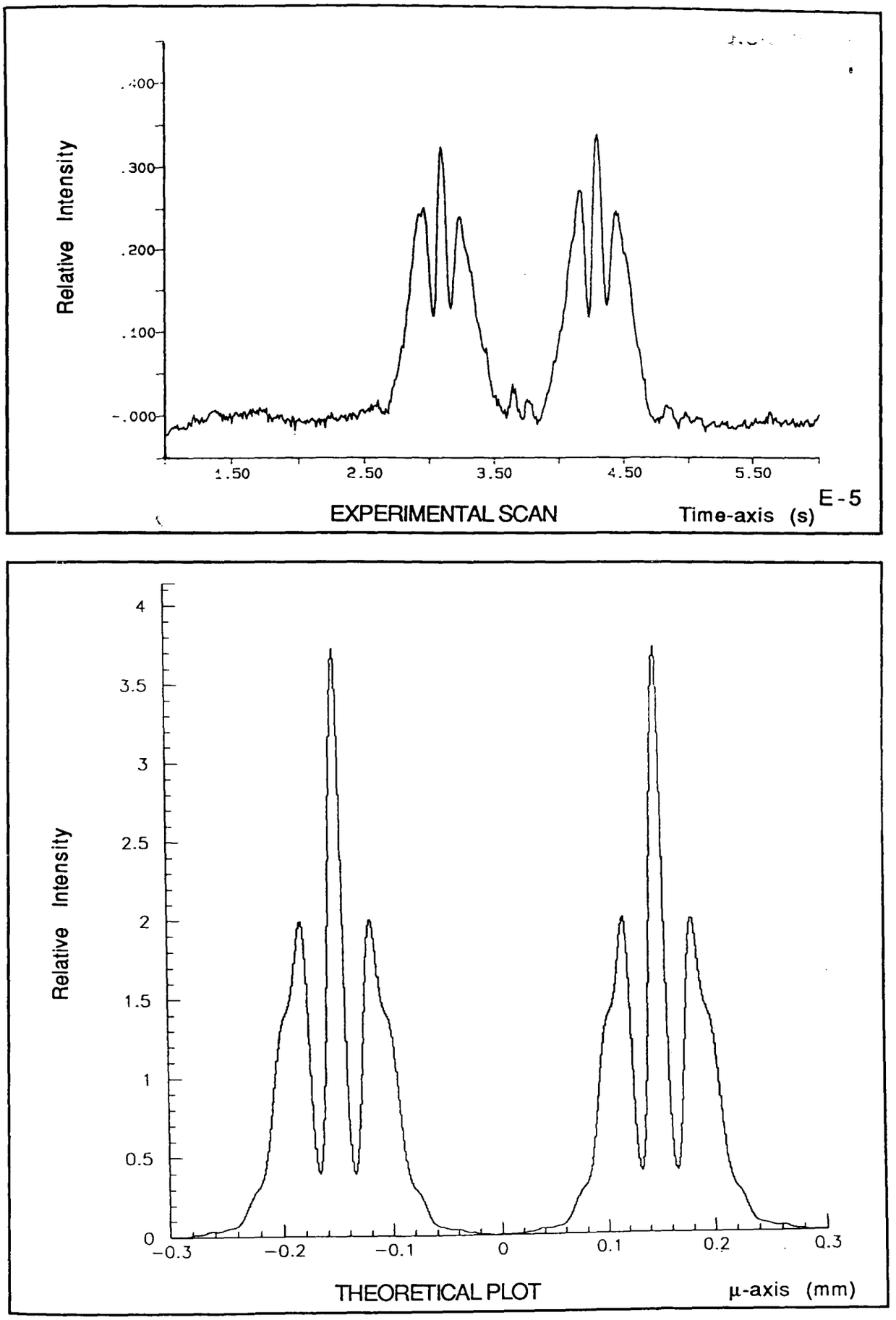

FIG. (5.2.29) Group C3 [C_d = 150 μm, C_s=150 μm] for Ω=19.616, ΔZ=-3.0 mm

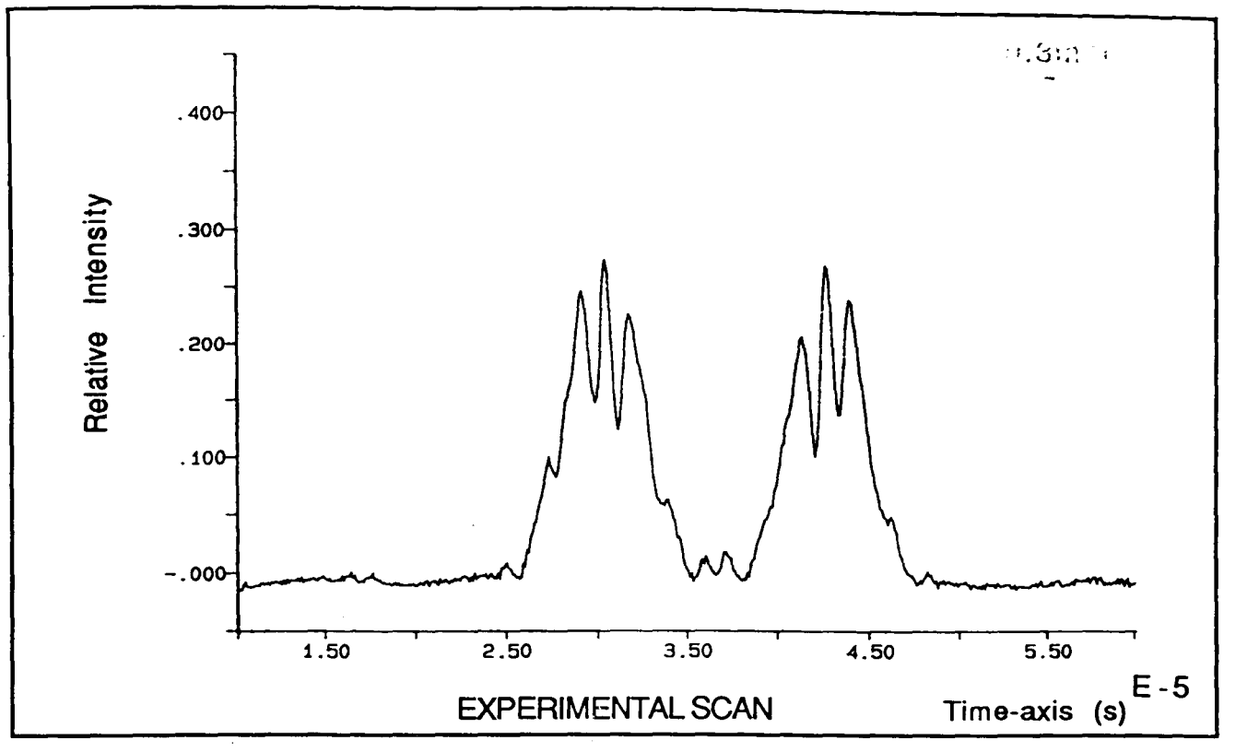

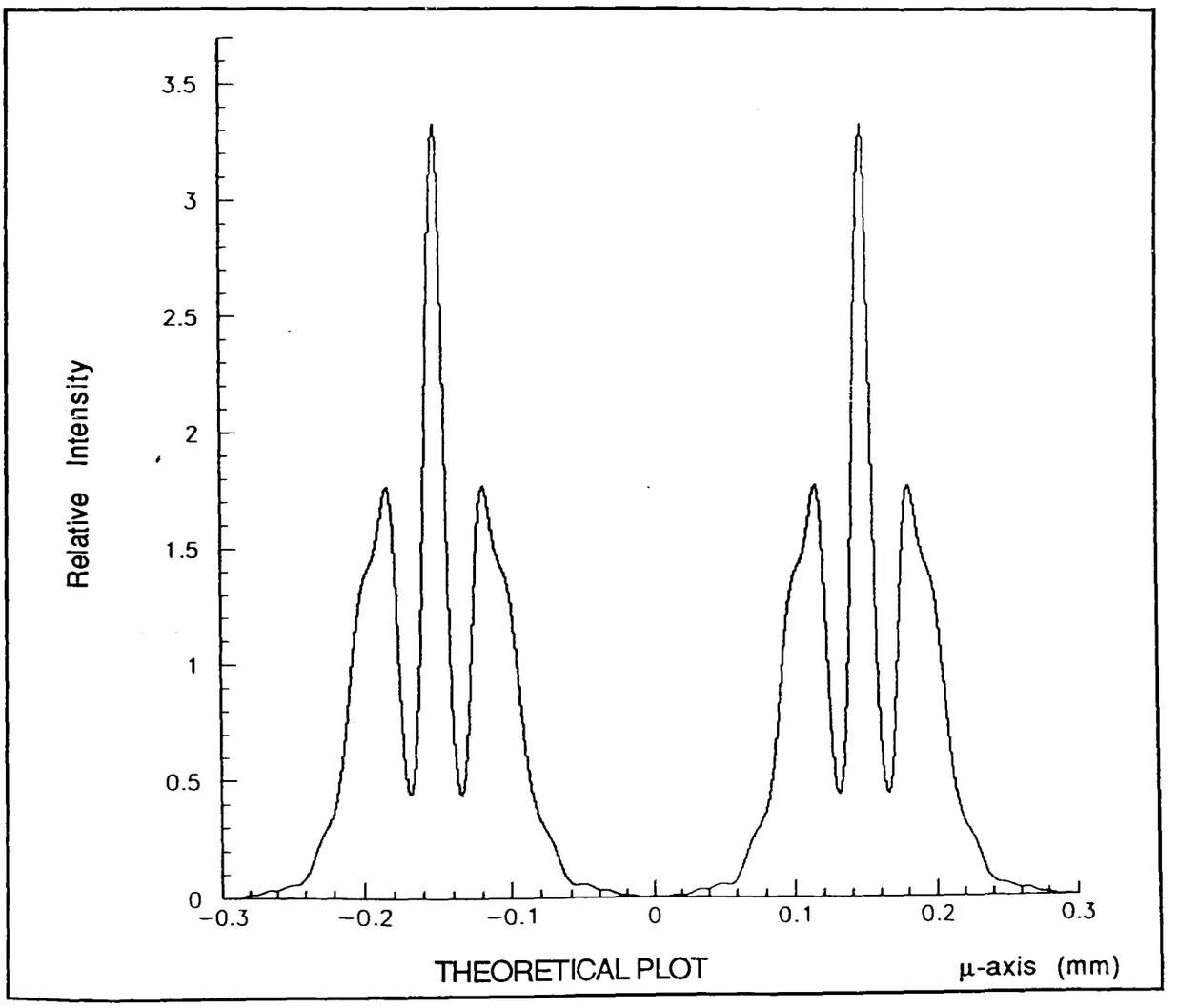

FIG. (5.2.30) Group C3 [C_d = 150 μm, C_s=150 μm] for Ω=19.616, ΔZ=+3.0 mm

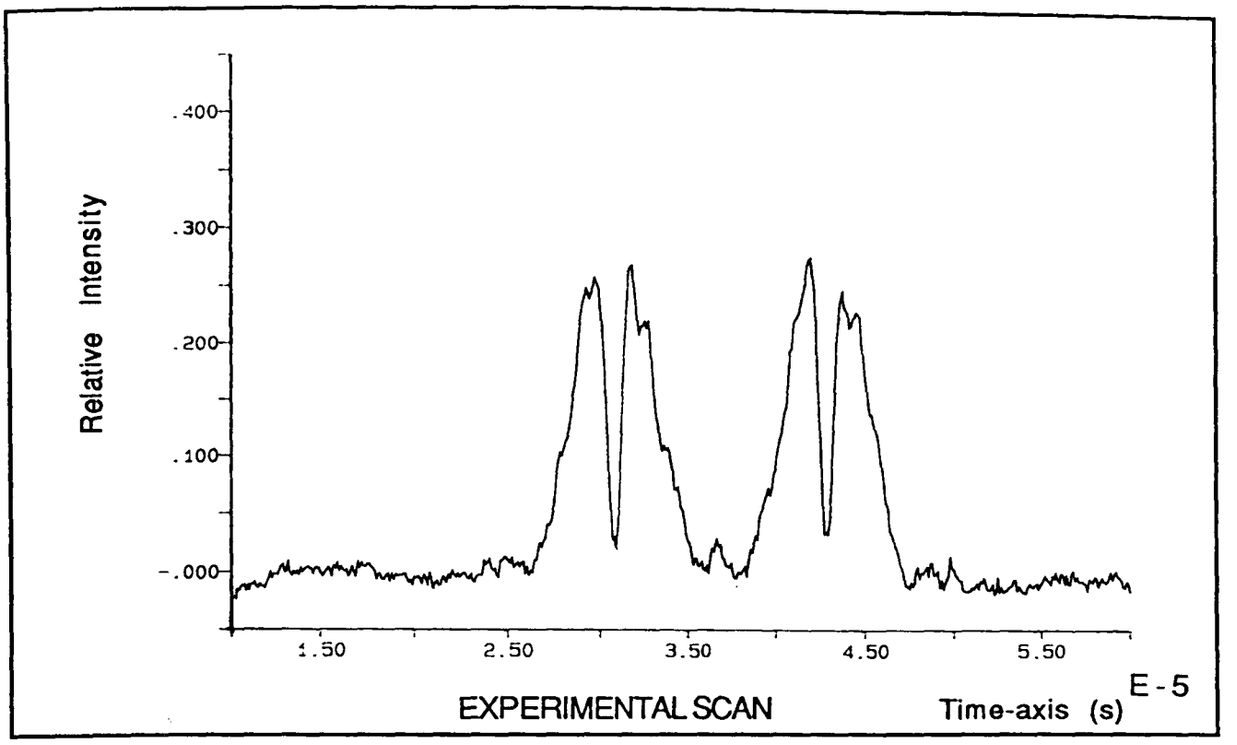

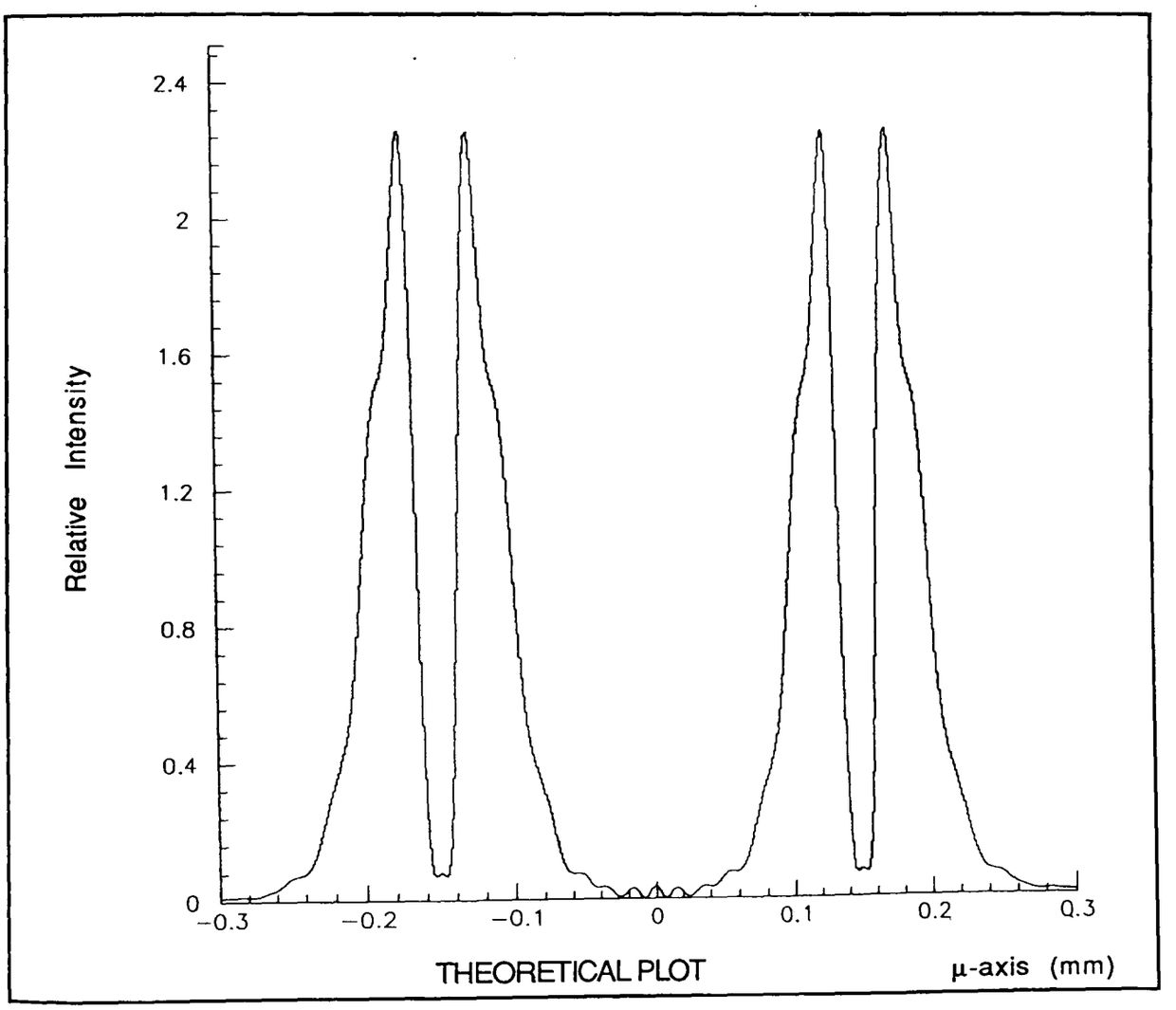

FIG. (5.2.31) Group C3 [C_d = 150 μm, C_s=150 μm] for Ω=19.616, ΔZ=-4.5 mm

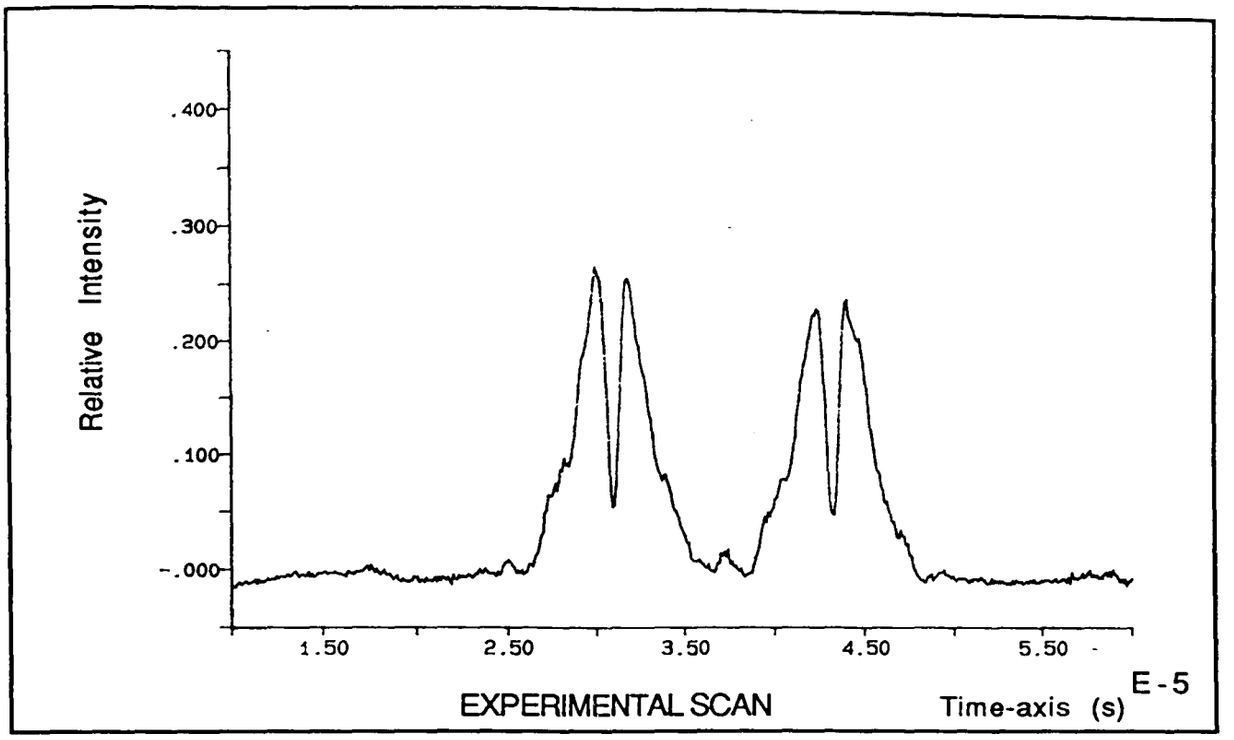

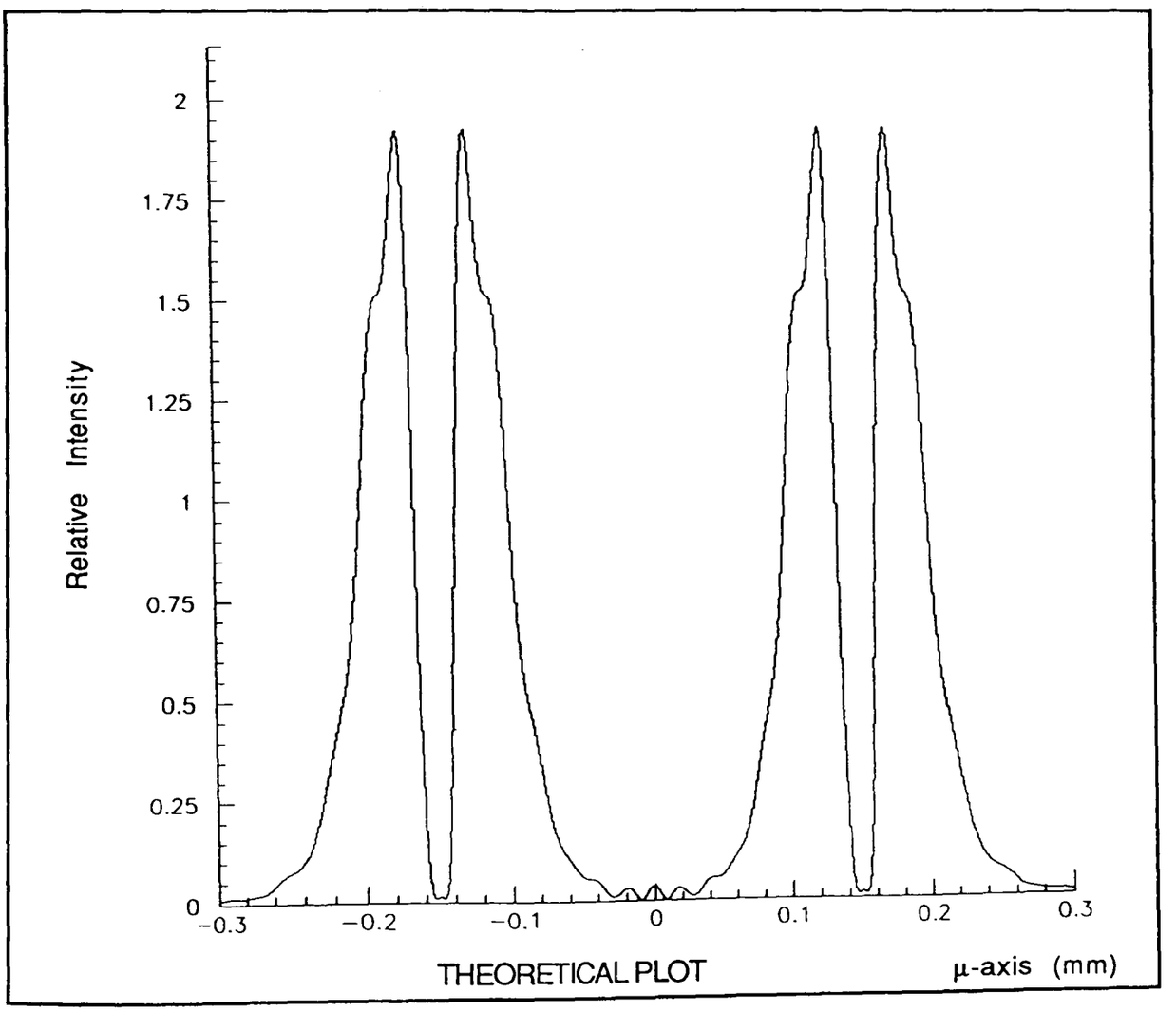

FIG. (5.2.32) Group C3 [C_d = 150 μm, C_s=150 μm] for Ω=19.616, ΔZ=+4.5 mm

CHAPTER 6

DISCUSSION OF THE RESULTS

All the experimental and theoretical data have been shown in Chapter 5 along with the discussion of different measurement criteria. In this Chapter, the computed and the observed images will be discussed in detail and different features of the predicted images will be compared with the experimental results to verify the theory discussed in Chapter 3.

Figure (5.2.1) [page 107], shows an experimental scan and a theoretical plot of an in-focus image of group C1 [a =75 μm, $2b$ =150 μm] for Ω=3.832. In the theoretical plot, a relatively low intensity in the center of the computed image, is observed surrounded by two peaks indicating the image of two touching discs, and the same dip can also be observed in the experimental scan. In the theoretical plot the intensity at the touching point of the discs is about 55% of the maximum intensity where it is about 66% in the experimental scan which indicates a lower contrast within the observed image. The other difference between the two images is the presence of small broad peaks indicating a ring of low amplitude around the observed image. The reason of this extra

structure has not been investigated, but two touching discs can easily be resolved in both the experimental scan and the theoretical plot.

Figure (5.2.3) [page 109] shows an experimental scan and a theoretical plot of an in-focus image of group C3 [a =75 μm, $2b$ =300 μm] for Ω=3.832. The figure shows an excellent agreement between the two plots. In both, the experimental scan and the theoretical plot, two well separated peaks indicating that two separated discs can be observed. It is important to note that in both plots the intensity in the separated region of the two discs is about the average background noise. Low background noise, indicating the good quality of the reconstructed image, can be observed in the experimental scan.

Figure (5.2.25) [page 131] shows an experimental scan and a theoretical plot of an in-focus image of group C2 [a =75 μm, $2b$ =225 μm] for Ω=19.616. The images of two well separated discs can be observed in both the experimental scan and the theoretical plot. Low background noise can be observed in the experimental scan, but the intensity in the separation region of the two discs shows two peaks which are not present in the predicted image. A total of six peaks are present within the predicted image

of each individual disc and can be counted in the experimental scan of the left disc where in the scan of the right hand side disc, because of the overlapping of two peaks due to noise, five peaks can easily be counted. Low contrast within the observed image of individual disc can also be observed in the experimental scan.

The experimental scans and the theoretical plots of out-of-focus images are found to be comparable to each other i.e. see figure (5.2.26) [page 132] and figure (5.2.27) [page 133]. The figure (5.2.26) shows the presence of central bright central spot surrounded by an alternative dark and bright ring in both the observed and the predicted image of an individual disc. In the figure (5.2.27) a dark central spot surrounded by a bright ring can be observed in both the experimental scan and the theoretical plot. The low background noise level in the experimental scans of both figures indicates that the quality of the out- of-focus image did not degraded.

Three different measurement criteria have been discussed in the Chapter 5. The effect of the finite aperture on the measurements of radius and separation of the predicted images are explained graphically in figures (6.1) to (6.3).

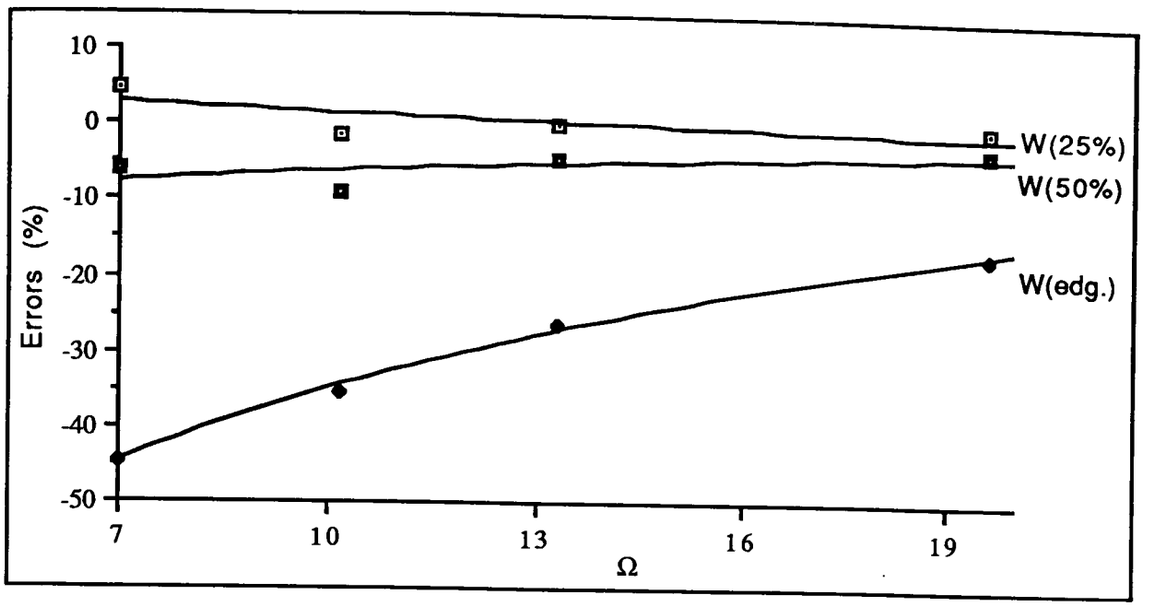

Error trends for the measurement of the diameter

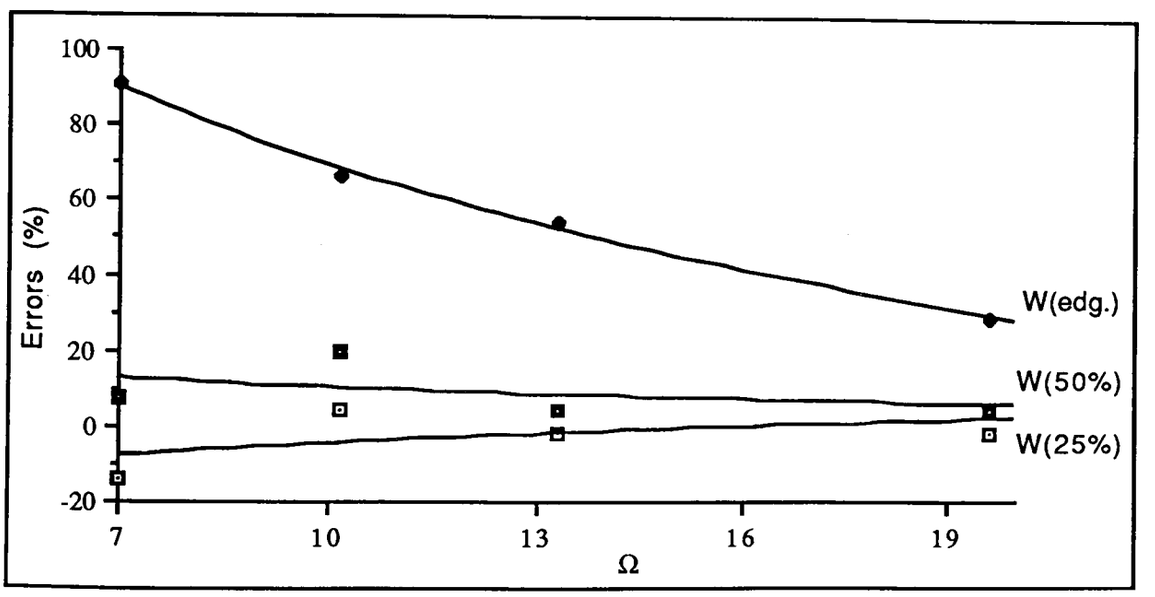

Error trends for the measurement of the separation

FIG. (6.1) Graphical representation of the errors for group C2

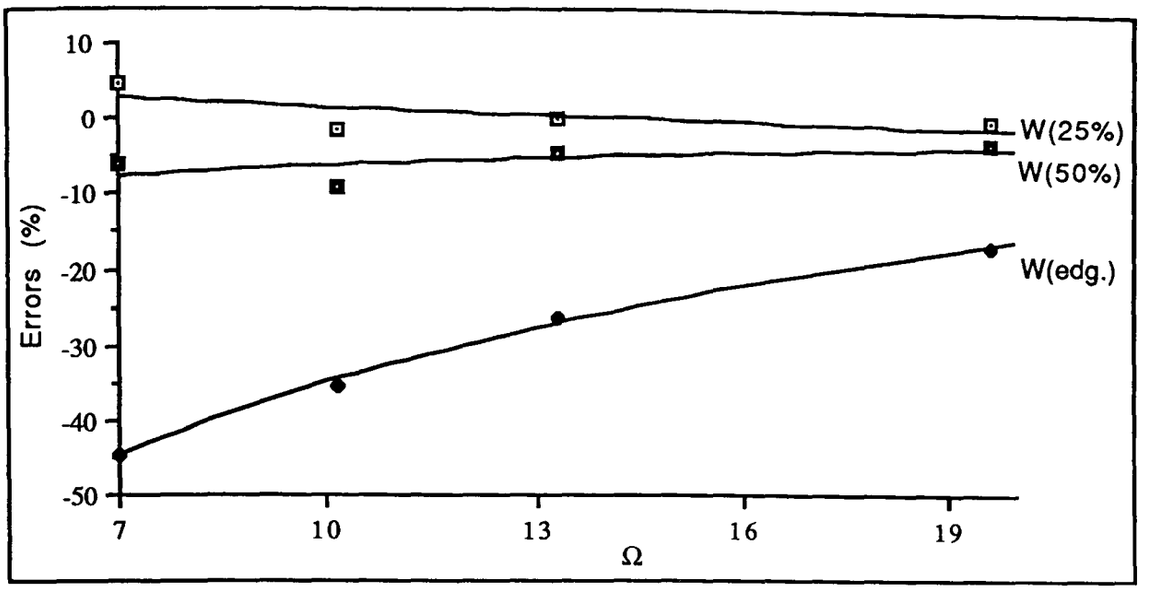

Error trends for the measurement of the diameter

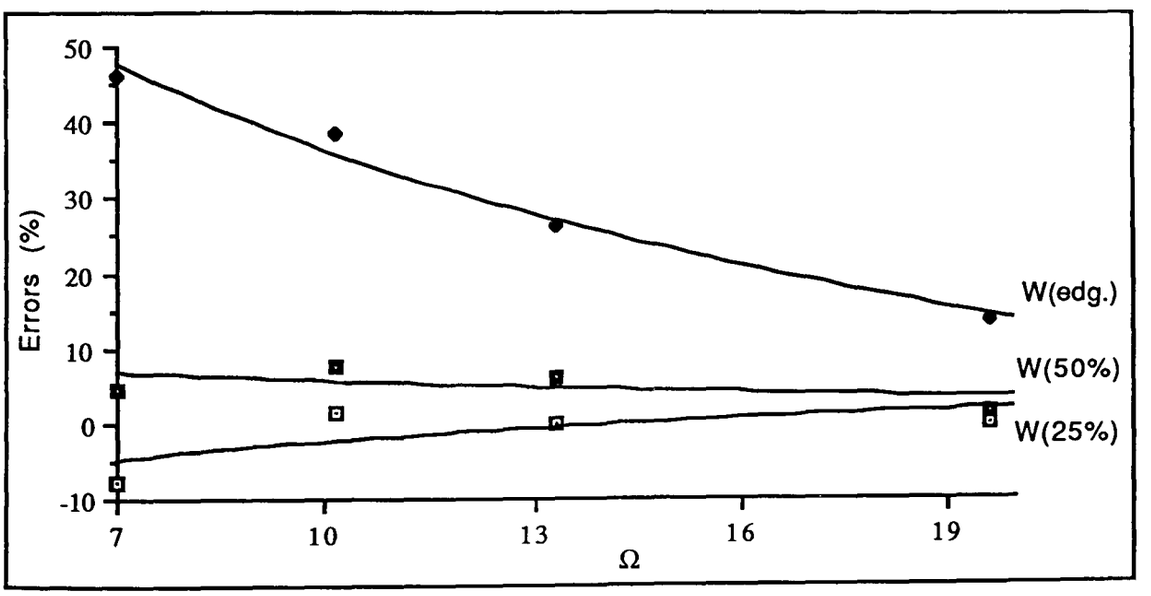

Errors trends for the measurement of the separation

FIG. (6.2) Graphical representation of the errors for group C3

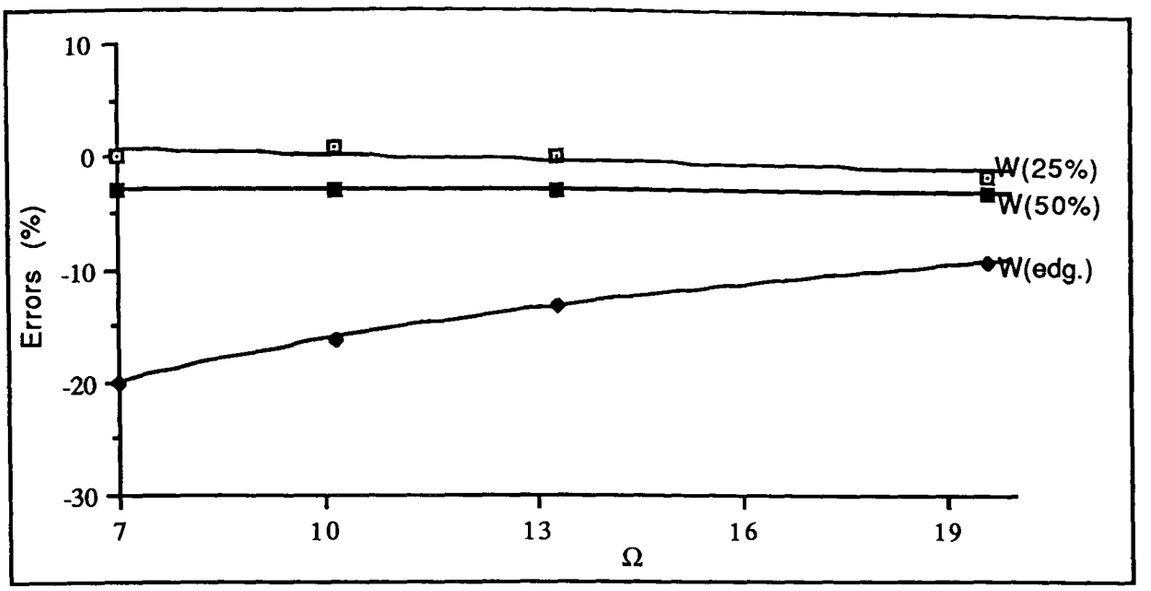

FIG. (6.3) Graphical representation of errors for group C1

It has been observed that measurements W(25%) shows positive errors where measurements W(50%) shows negative errors. This suggests that the point of real measurements lies somewhere between the measurements W(25%) and W(50%). The exact position of this measurement criteria was not investigated because, as has been mentioned in the Chapter 5, W(25%) is the most accurate criteria for the measurements on the computed images but W(50%) is the most practical measurement criteria. The comparison of results of measurement W(50%), W(25%) and W(edg.), predicted by the theory with those obtained experimentally, is given in table (6.1), (6.2) and (6.3). It should be noted that non-linearities in the vidicon line scan limit the

Ω	7.016	10.173	13.324	19.616
Group				
C1				
Actual:	300.0 μm	300.0 μm	300.0 μm	300.0 μm
Theoretical:	291.0 μm	291.0 μm	291.0 μm	291.0 μm
Experimental:	277.0 μm	289.0 μm	283.0 μm	289.0 μm
C2(d)				
Actual:	150.0 μm	150.0 μm	150.0 μm	150.0 μm
Theoretical:	140.0 μm	136.0 μm	143.0 μm	145.0 μm
Experimental:	151.0 μm	141.0 μm	141.0 μm	145.0 μm
C2(s)				
Actual:	75.0 μm	75.0 μm	75.0 μm	75.0 μm
Theoretical:	80.0 μm	90.0 μm	78.0 μm	78.0 μm
Experimental:	64.0 μm	72.0 μm	72.0 μm	72.0 μm
C3(d)				
Actual:	150.0 μm	150.0 μm	150.0 μm	150.0 μm
Theoretical:	140.0 μm	136.0 μm	141.0 μm	145.0 μm
Experimental:	145.0 μm	141.0 μm	145.0 μm	139.0 μm
C3(s)				
Actual:	150.0 μm	150.0 μm	150.0 μm	150.0 μm
Theoretical:	157.0 μm	161.0 μm	159.0 μm	152.0 μm
Experimental:	145.0 μm	150.0 μm	145.0 μm	147.0 μm

Table (6.1) Measurements W(50%)

[W(50%) is the measurement at the 50% of the average intensity]

Ω	7.016	10.173	13.324	19.616
GROUP				
C1				
Actual:	300.0 μm	300.0 μm	300.0 μm	300.0 μm
Theoretical:	300.0 μm	302.0 μm	300.0 μm	295.0 μm
Experimental:	289.0 μm	301.0 μm	289.0 μm	295.0 μm
C2(d)				
Actual:	150.0 μ m	150.0 μ m	150.0 μ m	150.0 μ m
Theoretical:	157.0 μm	148.0 μm	150.0 μm	150.0 μm
Experimental:	170.0 μm	150.0 μm	146.0 μm	147.0 μm
C2(s)				
Actual:	75.0 μm	75.0 μm	75.0 μm	75.0 μm
Theoretical:	65.0 μm	78.0 μm	74.0 μm	74.0 μm
Experimental:	41.0 μm	66.0 μm	69.0 μm	69.0 μm
C3(d)				
Actual:	150.0 μ m	150.0 μ m	150.0 μ m	150.0 μ m
Theoretical:	157.0 μm	148.0 μm	150.0 μm	150.0 μm
Experimental:	160.0 μm	150.0 μm	150.0 μm	145.0 μm
C3(s)				
Actual:	150.0 μ m	150.0 μ m	150.0 μ m	150.0 μ m
Theoretical:	138.0 μ m	154.0 μ m	150.0 μ m	150.0 μ m
Experimental:	130.5 μ m	139.0 μ m	139.0 μ m	145.0 μ m

Table (6.2) Measurements W(25%)

[W(25%) is the measurement at the 25% of the center intensity]

Ω	7.016	10.173	13.324	19.616
GROUP				
C1				
Actual:	300.0 μm	300.0 μm	300.0 μm	300.0 μm
Theoretical:	240.0 μm	252.0 μm	261.0 μm	272.0 μm
Experimental:	232.0 μm	249.0 μm	257.0 μm	266.0 μm
C2(d)				
Actual:	150.0 μm	150.0 μm	150.0 μm	150.0 μm
Theoretical:	83.0 μm	97.0 μm	111.0 μm	125.0 μm
Experimental:	95.0 μm	110.0 μm	116.0 μm	124.0 μm
C2(s)				
Actual:	75.0 μm	75.0 μm	75.0 μm	75.0 μm
Theoretical:	143.0 μm	125.0 μm	115.0 μm	97.0 μm
Experimental:	113.0 μm	104.0 μm	104.0 μm	93.0 μm
C3(d)				
Actual:	150.0 μ m	150.0 μ m	150.0 μ m	150.0 μ m
Theoretical:	83.0 μm	97.0 μm	111.0 μm	125.0 μm
Experimental:	81.0 μm	104.0 μm	116.0 μm	116.0 μm
C3(s)				
Actual:	150.0 μ m	150.0 μ m	150.0 μ m	150.0 μ m
Theoretical:	219.0 μ m	208.0 μ m	189.0 μ m	171.0 μ m
Experimental:	208.0 μ m	191.0 μ m	174.0 μ m	147.0 μ m

Table (6.3) Measurements W(edg.)

[W(edg.) is the separation of the outermost peaks]

accuracy to these results to about ± 5 μm.

It can be observed that the measurements on the real images generaly show larger errors than those predicted by the theory. This was because of the difficulty in locating the exact point of measurements in the presence of noise which can not be illuminated from the data acquisition system. This difficultly of locating the exact point, can be observed by noting that if the radius of an individual disc is measured smaller than the actual diameter, the separation is measured larger, in experimental measurements, confirming the overall width of the image is very close to the actual width. This difficulty was mainly due to the presence of electronic noise present in the data acquisition system which caused the acquired line scan from the video camera to fluctuate. This might be reduced by improving the data acquisition system.

It has also been observed for measurements W(edg.), on computed and experimental images, the errors decrease rapidly as Ω increases. This indicates that the rise interval, (where the image intensity of the computed images rises from 10% to 90% of its maximum edge intensity), decreases as the Ω increases. This

effect of image edge sharpness has also been verified by the measuring the rise time of the experimental images from which the rise interval has been calculated for its comparison with the predicted results. These results of the rise interval for group C2 have been tabulated in table (6.4). Figure (6.4) shows graphically, the change of rise interval with respect to the change in Ω.

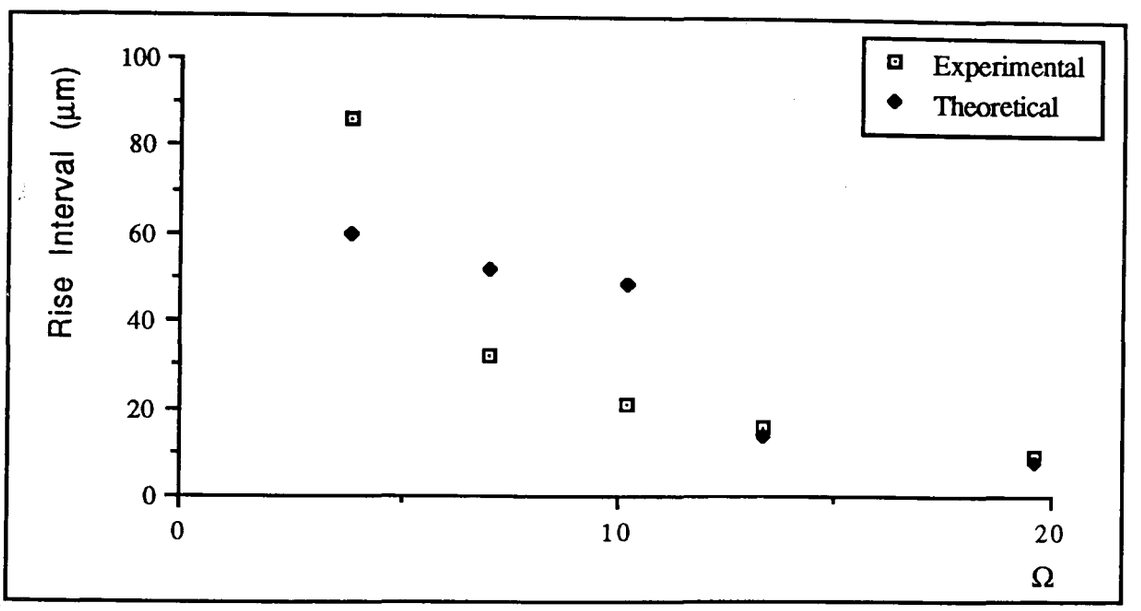

FIG. (6.4) Change of rise interval with respect to Ω

Ω	EXPERIMENTAL	THEORETICAL
3.832	86 μm	60 μm
7.016	32 μm	52 μm
10.173	21 μm	49 μm
13.324	16 μm	14 μm
19.616	9 μm	8 μm

TABLE (6.4) Change of rise interval with respect to Ω

The figure (6.4) shows that the predicted images were found in good agreement with the observed images for Ω=13.324 and Ω=19.616, but show poor agreement for smaller values of Ω, i.e. Ω=3.832, 7.016 and 10.173. It is also inyeresting to note that the change of rise interval of the in-focus images is very smooth in the experimental data.

Table (6.5) gives the comparison of the rise intervals of predicted and observed images of group C3 for Ω=19.616. It can be seen from figure (6.5), which is a graphical comparison of the change of rise time with respect to the change of ΔZ, the focusing parameter, that the computed images are asymmetrical.

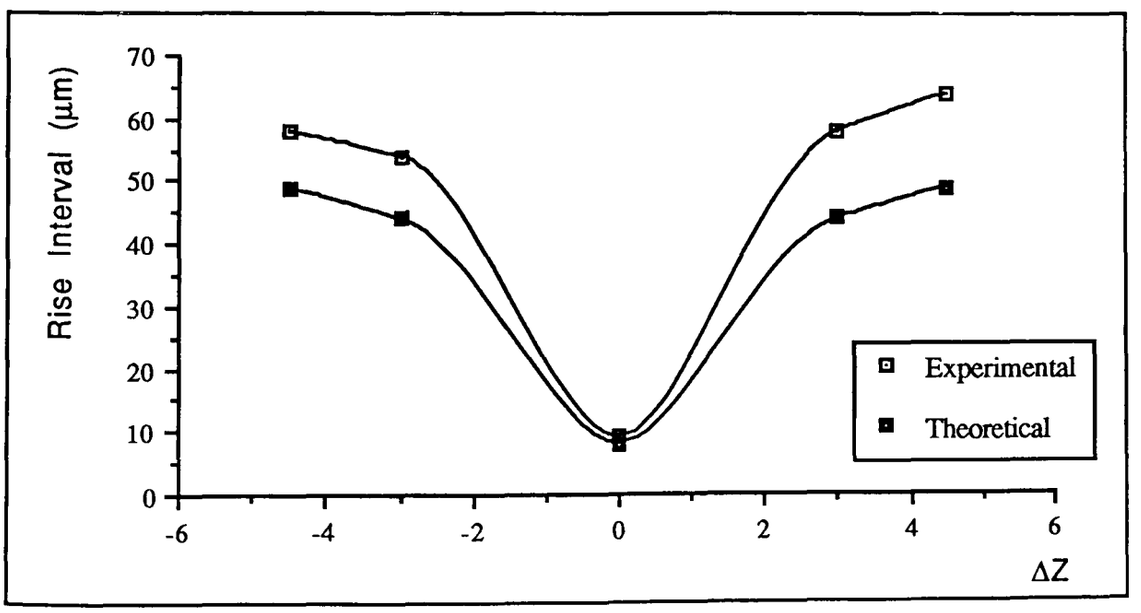

FIG. (6.5) Change of rise interval with respect to ΔZ.
[The curves drawn are to guide eye only]

ΔZ	EXPERIMENTAL	THEORETICAL
0.0	90.0 μm	82.0 μm
-3.0 mm	54.0 μm	44.0 μm
+3.0 mm	58.0 μm	44.0 μm
-4.5 mm	58.0 μm	49.0 μm
+4.5 mm	64.0 μm	49.0 μm

TABLE (6.5) Change of rise interval with respect to ΔZ.

Another difference between the predicted images and observed images which has been observed is that the ratio of minima to maxima of the extrema within the the image is less for observed images than those predicted theoretically. This was mainly due to the dynamic range of the video camera, beyond which its response is not suppose to be linear. The observed image will have a maximum contrast if the background is close to the minimum detectable intensity by the video camera, and the signal intensity is about the maximum detectable intensity by the video camera. This condition could not be achieved in the experiment because of our interest in investigating the effects of limited aperture on the reconstructed images and hence the hologram of the whole test volume was recorded and the aperture was placed on reconstruction (the techniques of masking the aperture have been

discussed in Chapter 4). Therefore, the recorded hologram was of varying density which has its effects on the contrast of the reconstructed images. The intensity in the computed images has been normalised the the expected center of the disc and it was free from errors introduced by the video system, hence it shows maximum possible contrast within the image.

It has been observed that the in-focus computed images of each disc of group C2 and group C3 for Ω=3.832 [figures (5.2.2) page 108 and (5.2.3) page 109] has only a single peak where for Ω=7.016 [figure (5.2.6) page 112 and (5.2.8) page 114], the intensity at the center of the computed image of an individual disc is minimum showing two outer peaks. Similarly 7 extrema can be observed in the computed in-focus images of Group C2 and Group C3 for Ω=13.173 [figure (5.2.16) page 122 and (5.2.19) page 125] where 11 extrema exist within the computed in-focus image of an individual disc of group C2 and C3 for Z=19.616 [figure (5.2.25) page 131 and (5.2.28) page134]. The number of extrema within the predicted image of an individual disc, increases with Ω and are found to be proportional to the recorded information on the hologram. It was concluded that $N_{(extrema)}$, the number of these extrema is directly related to the number of zeros *n* of the Bessel

function J_1 as:

$$N_{(extrema)} = 2n - 1 \qquad \text{.....(6.1)}$$

The same effect of increasing number of extrema with increasing Ω, was also pointed out by **Belz R. A. (1971)**. The increase of extrema with increasing Ω has been verified experimentally. It was noted from the experimental data that the extrema within the image of an individual disc are not very clearly observable for Ω=19.616. This was due to the smaller amplitude of maxima which could be overcome by the background noise and also due to the smaller width of the peaks within the observed image which become smaller than the resolution of the video camera.

Due to these ripples which exists within the in-focus computed images of each individual disc, the expected center of the individual disc must fall, either on the top of a ripple or on the trough between the two ripples. It has been observed that the expected center of an in-focus predicted image of an individual disc falls on the crest of a ripple if n , the number of zero of the Bessel function J_1, is odd and falls on trough if n is even.

Similarly some peaks are also observed in the separated region of the discs, in the computed images of group C3

and the number of these peaks is found to be proportional to Ω, i.e. one peak for Ω=3.832 [figure (5.2.3) page 109], three peaks for Ω=7.016 [figure (5.2.8) page 114], five peaks for Ω=10.173 [figure (5.2.12) page 118] and so on. It was concluded that $N_{(peaks)}$, the number of these peaks is directly related to the number of zeros *n* of the Bessel function J_1 as:

$$N_{(peaks)} = 2n - 1 \qquad \text{.....(6.2)}$$

Although some peaks can be observed within the separated region of the discs in the computed images of group C2, but no such relation was formed.

It has been observed that for two separated discs i.e. group C2 and C3, the shape of the predicted or the observed image for Ω=7.016, does not change significantly, if it was moves out-of-focus. i.e. figure (5.2.5) [page 111] to figure (5.2.9) [page 115], but for higher values of Ω the image changes quite rapidly as it was moved out-of-focus. The number of extrema within the image of individual disc, decreases with an increase in $|\Delta Z|$, the focusing parameter. For ΔZ=-3.00mm a bright spot was observed in the center of the predicted as well as the observed image of each individual disc i.e. figure (5.2.17) [page 123], (5.2.20) [page

126], (5.2.26) [page 132] and (5.2.29) [page 135]. This central bright spot was surrounded by an alternative dark and bright ring giving three peaks and five total extrema within the image of individual disc. Similarly for ΔZ=-4.50 mm i.e. figure (5.2.18) [page 124], (5.2.21) [page 127], (5.2.27) [page 133] and (5.2.31) [page 137], a central dark spot surrounded by bright ring, giving three extrema, was observed for both the experimental scan and the theoretical plot.

From this discussion, it is concluded that the predicted images are in good agreement with the observed images and many features of the predicted images are observed experimentally. Despite of a small differences between the experimental and computed images, in some of the measurements, the theory discussed in Chapter 3, has been experimentally verified with a good degree of accuracy.

CHAPTER 7

SUMMARY AND CONCLUSIONS

The main contribution of this work is a theoretical derivation of the reconstructed real image from an in-line Fraunhofer hologram for two identical three dimensional targets and its experimental verification. The theory cited in Chapter 3 gives mathematical explanation of the construction and the reconstruction process of in line Fraunhofer holography for more than one target disc. In particular, characteristic effects of limited recorded information on the reconstruction of the real images were found. This finite information is discussed in terms of a limiting aperture on the hologram and the results of the analysis are corroborated by experimental data. In addition, size and separation measurements of the target discs and focal tolerance are determined for the images reconstructed by aperture limited holograms along with the possible measurement criteria.

The intensity distribution in the reconstruction were presented in terms of useful contour plots. This gave information about the reconstructed image as a whole. The contour plots group C3 for Ω=19.616, were compared with the photographs of observed images taken from the monitor. A good qualitative agreement was

found between the contour plots and the photographs of the real images. It was found that for all the in-focus images, the number of intensity maxima depends upon the number of zeros of the first order Bessel function J_1 recorded, and as the image moves out of focus the number of these maxima decreases. It is clear from the contour plots that the reconstructed images have a plane of mirror symmetry. It was also observed that the images are asymmetrical about the focal plane. All the theoretically predicted results were verified by the corresponding experimental data presented in Chapter 5. The results of experimental observations and the theoretical predictions are discussed in Chapter 6.

For the three measurement criteria discussed in chapter 5, width W(25%) which was measured where the intensity at the edge was 25% of the central intensity, was found accurate for theoretical measurements. Because errors ware introduced due to the electronic readout system and the background noise, it was observed that the width W(50%) which was measured along the halfway between the average image intensity and the average background noise level, is more accurate for experimental measurements.

In addition to the experimental verification of the

theory cited in Chapter 3, a new useful approach of acquiring the experimental data from the real images, using Asystant GPIB, was also developed and discussed in Chapter 4. This new data acquisition technique was different from the previously cited techniques. It does not include the densitometry of the photographs of the real images and was found more rapid and flexible than those data acquisition systems already cited in literature.

Performance of the CCD camera and a video camera 109A from link electronics were tested and it was found that although the dark current for the CCD camera was less than the video camera, the video camera 109A had better imaging performance when used in a coherent light and hence was chosen in preference for use in the data acquisition system.

Finally the techniques of masking the hologram to get an aperture limited effect are also discussed in Chapter 4. Three different techniques were tried and it was found that masking the hologram with an aperture in the reconstruction is the best technique.

For the future work, different algorithms may also be established experimentally, to find the true focal plane of the real

images and hence an automatic system may be developed to display the in focus images. The data acquisition system may be improved by using a CCD camera without having a glass plate on the CCD chip. The subroutines governing the data acquisition using Asystant GPIB can also be improved the capture the whole image instead of the line scan through the center of the image.

The discs of different sizes may be included in the theory. A more complicated case of more than two discs may also be analysed and the theory may be enhanced to the pair of discs in different Z-planes. For the case of the pair of discs in different Z-plane, the coordinate geometry of recording and reconstruction process, could be as shown in figure (7.1)

The diffracted wavefront from the disc D1 will also diffract from the disc D2. The complex interference of the two diffracted waves and the coherent background will be recorded on the film.

For experimental verification of the theory the test object should be designed accordingly, and the glass substrate with the test object should be placed in a liquid of same refractive index as that of the substrate, before recording the hologram.

Similarly the problem of two one dimensional objects

(a thin wire) lying in the same and different planes, may also be solved analytically.

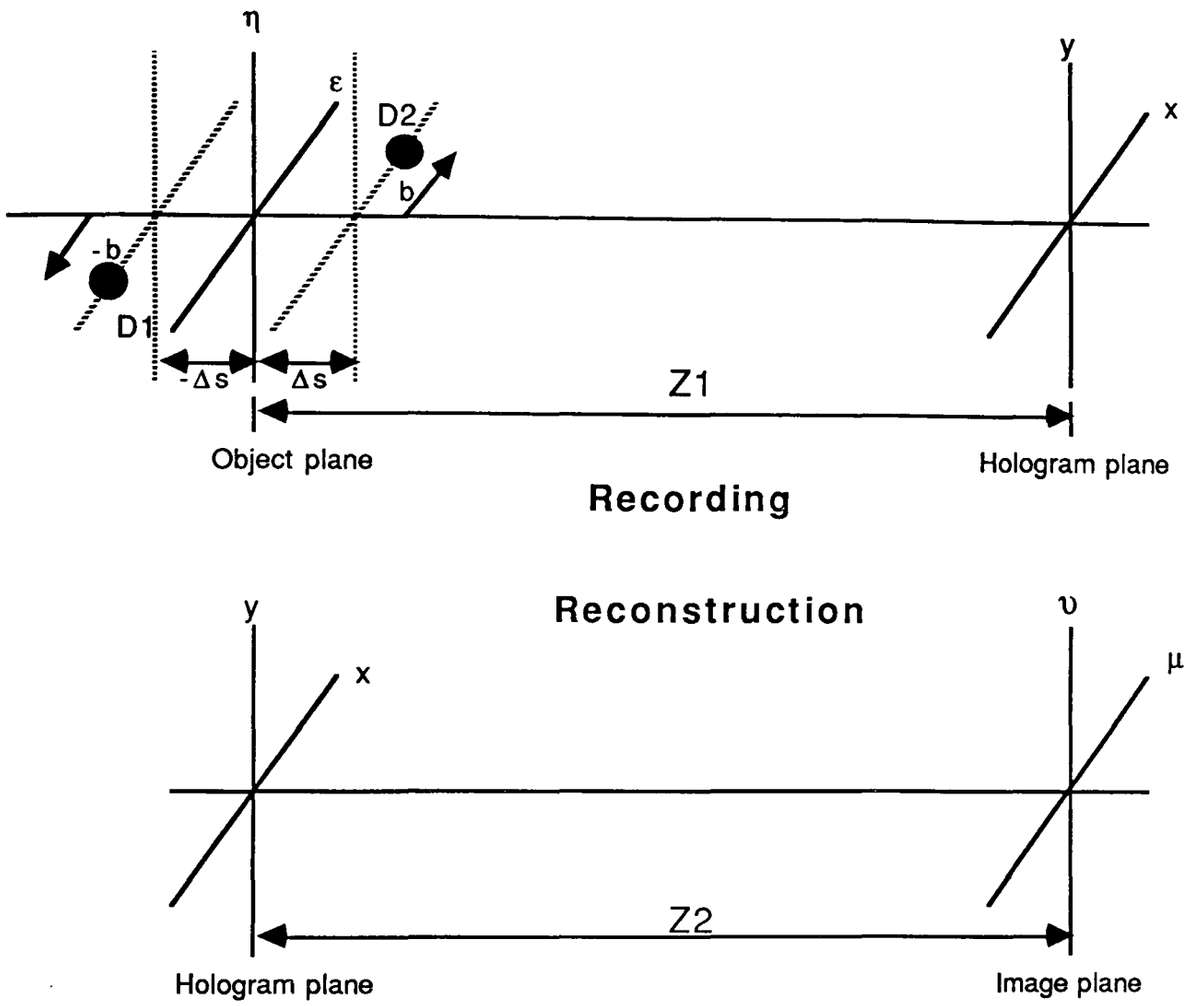

FIG. (6.1) Coordinate geometry of the proposed future work

APPENDICES

APPENDIX A1

TECHNICAL INFORMATION FOR THE CCD CAMERA EEV46410

The CCD camera EEV46410 has the following important features.

Number of picture elements:	
Horizontal	385
Vertical	288
Picture element size:	
Horizontal	16.5μm
Vertical	16.5 μm
Image area:	
Horizontal	6.4 mm
Vertical	4.8 mm
Integration time:	20 ms
Scanning system:	CCIR
Field frequency:	50 Hz
Video output	0.7 V_{p-p}
Number of active lines:	576
Image sensor structure:	1/2 inch transfer

APPENDIX A2

TECHNICAL INFORMATION FOR THE VIDEO CAMERA 109A

It is a self contained monochrome TV camera fitted with one inch diameter 4532/U Ultricon II™ tube. The camera has the following important features.

i - A fully interlaced dual standard sync. pulse generator.

ii - Broadcast quality output.

iii - Variable gamma correction (1.0 to 0.3).

iv - Low noise FET head amplifier.

v - Two video outputs.

vi - TV standard 625 or 525 lines, selectable by two internal links.

ULTRICON II™ 4532/U TUBE (RCA)

The tube have following characteristics.

Focusing method:	Magnetic
Normal scan area:	12.8 X 9.6 mm^2
Typical dark current:	12 nA
TV lines at 40% modulation:	450

APPENDIX B

SUBROUTINES WRITTEN FOR ASYSTANT GPIB

Following eight subroutines were written to acquire and plot the experimental data using Asystant GPIB.

i -	TVTRIG	Setup scope for TV trig.
ii -	MAIN	Runs routines 3, 4, 5.
iii -	AVER-1	Store noise in WMEM1.
iv -	AVER-2	Store diffraction intensity in WMEM2.
v -	GET-PLOT	Gets wave of WMEM3 and plots.
vi -	GET-WAVE	Gets wave from scope.
vii -	SCALE-1	Set vertical scale.
viii -	SCALE-2	Set horizontal scale.

TVTRIG is an independent subroutine which was used for TV triggering, video line for triggering may be selected directly from the oscilloscope.

MAIN is the subroutine which performs the execution of the entire data acquisition programme by calling subroutines AVER-1, AVER-2 and GET-PLOT.

AVER-1 is the subroutine which stores the background intensity in memory WMEM1 of the oscilloscope and AVER-2 is the

subroutine which stores the diffraction intensity in memory WMEM2 of the oscilloscope, subtract the background intensity from the diffracted intensity to get noise free diffraction intensity and store it in memory WMEM3 of the oscilloscope.

GET-PLOT is the subroutine which acquires data from the oscilloscope and plots it by calling subroutines GET-WAVE, SCALE-1 and SCALE-2.

Subroutine GET-WAVE acquires the data from the oscilloscope, where subroutines SCALE-1 and SCALE-2 sets the vertical and horizontal axis of the graphical output.

These routines have litral strings which are specific to the Hewlett Packard (HP) oscilloscope. Their detailed functions are described in the HP Oscilloscope Programme Reference Manual.

TVTRIG

This subroutine sets up TV triggering. The video line number for triggering may be selected directly from the oscilloscope.

Routine Name: < TVTRIG >

Comment: < SET UP SCOPE FOR TV TRIG >

No. of Iteration:	< 1 >
SQR (Y/N):	<N>
Key typed (Y/N):	<N>
Comparison (Y/N):	<N>
Edit Command (Y/N):	<Y>

TALK:

LITERAL: :TRIG:SOUR CHAN1

LITERAL: :LEV -150 MV

LITERAL: :TIM:RANG 50.0 US;DEL 10.0 US

LITERAL: :CHAN1:COUP DC;HFR ON

LITERAL: :CHAN1:RANG 1.6 V;OFFS 0.0 MV

Segment Terminator

ASCII Value (No. / None):	<N>
Send EOI with last byte?	<Y>
Quit / Continue:	<C>

END ROUTINE

MAIN

This is the main routine which controls the entire data acquisition programme.

Routine Name: < MAIN >

Comment: < RUNS THE ROUTINES 3, 4, 5 >

No. of Iteration:	< 1 >
SQR (Y/N):	<N>
Key typed (Y/N):	<N>
Comparison (Y/N):	<N>
Edit Command (Y/N):	<Y>

SET DEVICE: SCOPE

TALK:

LITERAL: : CHAN1:OFFS 0

Segment Terminator

ASCII Value (No. / None):	<N>
Send EOI with last byte?	<Y>
Quit / Continue:	<C>

WAIT: DELAY

Wait for SQR (Y/N):	<N>
Wait for key (Y/N):	<N>
Wait for time (Sec.):	< 30.0 >

MASSAGE: PRESS ANY KEY TO CONTINUE...

WAIT: KEY

Wait for SQR (Y/N):	<N>

Wait for key (Y/N): <Y>

Wait for time (Sec.): < 0.0 >

MASSAGE END

EXEC ROUT NO. 3 AVER-1

MESSAGE: BACKGROUND NOISE IS STORED IN MEMORY-1,

MESSAGE: PRESS ANY KEY TO PROCEED FURTHER TO

MESSAGE: STORE DIFFRACTION INTENSITY IN MEMORY-2.

WAIT: KEY

Wait for SQR (Y/N): <N>

Wait for key (Y/N): <Y>

Wait for time (Sec.): < 0.0 >

MESSAGE END

EXEC ROUT NO. 4 AVER-2

MESSAGE: PRESS ANY KEY TO PLOT THE GRAPH

WAIT: KEY

Wait for SQR (Y/N): <N>

Wait for key (Y/N): <Y>

Wait for time (Sec.): < 0.0 >

MESSAGE END

EXEC ROUT NO. 5 GET-PLOT

END: ROUTINE

AVER-1

This subroutine stores the background noise in memory WMEM1 of the oscilloscope.

Routine Name: < AVER-1 >

Comment: < STORE NOISE IN WMEM1 >

No. of Iteration:	< 1 >
SQR (Y/N):	<N>
Key typed (Y/N):	<N>
Comparison (Y/N):	<N>
Edit Command (Y/N):	<Y>

SET DEVICE: SCOPE

TALK:

LITERAL: :ACQ:TYPE AVER;COUNT 32;COMP 100

Segment Terminator

ASCII Value (No. / None):	<N>
Send EOI with last byte?	<Y>
Quit / Continue:	<C>

WAIT: DELAY

Wait for SQR (Y/N):	<N>
Wait for key (Y/N):	<N>
Wait for time (Sec.):	< 30.0 >

TALK:

LITERAL: :STORE CHAN4,WMEM1

Segment Terminator

ASCII Value (No. / None):	<N>
Send EOI with last byte?	<Y>
Quit / Continue:	<C>

WAIT: DELAY

Wait for SQR (Y/N):	<N>
Wait for key (Y/N):	<N>
Wait for time (Sec.):	< 30.0 >

GOTO LOCAL

END ROUTINE

AVER-2

This subroutine stores the diffraction intensity into memory WMEM2 of the oscilloscope, subtract WMEM1 - WMEM2 to get noise free diffraction intensity and store it into memory WMEM3 of the oscilloscope.

Routine Name: < AVER-2 >

Comment: < STORE DIFF. INT. IN WMEM1 >

No. of Iteration:	< 1 >
SQR (Y/N):	<N>
Key typed (Y/N):	<N>
Comparison (Y/N):	<N>
Edit Command (Y/N):	<Y>

SET DEVICE: SCOPE

TALK:

LITERAL: :ACQ:TYPE AVER;COUNT 32;COMP 100

Segment Terminator

ASCII Value (No. / None):	<N>
Send EOI with last byte?	<Y>
Quit / Continue:	<C>

WAIT: DELAY

Wait for SQR (Y/N):	<N>
Wait for key (Y/N):	<N>
Wait for time (Sec.):	< 30.0 >

TALK:

LITERAL: :STORE CHAN4,WMEM2

	Segment Terminator
ASCII Value (No. / None):	<N>
Send EOI with last byte?	<Y>
Quit / Continue:	<C>

WAIT: DELAY

Wait for SQR (Y/N):	<N>
Wait for key (Y/N):	<N>
Wait for time (Sec.):	< 30.0 >

TALK:

LITERAL: :FUNC1:SUBT WMEM1,WMEM2

	Segment Terminator
ASCII Value (No. / None):	<N>
Send EOI with last byte?	<Y>
Quit / Continue:	<C>

WAIT: DELAY

Wait for SQR (Y/N):	<N>
Wait for key (Y/N):	<N>
Wait for time (Sec.):	< 30.0 >

TALK:

LITERAL: :VIEW FUNC1

Segment Terminator	
ASCII Value (No. / None):	<N>

	Send EOI with last byte?	<Y>
	Quit / Continue:	<C>

WAIT: DELAY

Wait for SQR (Y/N):	<N>
Wait for key (Y/N):	<N>
Wait for time (Sec.):	< 30.0 >

TALK:

LITERAL: :STOR FUNC,WMEM3

Segment Terminator	
ASCII Value (No. / None):	<N>
Send EOI with last byte?	<Y>
Quit / Continue:	<C>

WAIT: DELAY

Wait for SQR (Y/N):	<N>
Wait for key (Y/N):	<N>
Wait for time (Sec.):	< 30.0 >

GOTO LOCAL

END ROUTINE

GET-PLOT

This is the subroutine which acquire data from memory WMEM3 of the oscilloscope and plot a graph of relative intensity and X-axis.

Routine Name: < GET-PLOT >

Comment: < GETS WAVE OF WMEM3 & PLOT >

No. of Iteration:	<1>
SQR (Y/N):	<N>
Key typed (Y/N):	<N>
Comparison (Y/N):	<N>
Edit Command (Y/N):	<Y>

SET DEVICE: SCOPE

TALK:

LITERAL: :WAV:SOUR WMEM3

Segment Terminator

ASCII Value (No. / None):	<N>
Send EOI with last byte?	<Y>
Quit / Continue:	<C>

WAIT: DELAY

Wait for SQR (Y/N):	<N>
Wait for key (Y/N):	<N>
Wait for time (Sec.):	< 30.0 >

EXEC ROUT NO. 6: GET-WAVE

EXEC ROUT NO. 7: SCALE-1

EXEC ROUT NO. 8: SCALE-2

SETUP: [F] AUTO Y(X)

SETUP

Full/Top/Bottom:	<F>
Auto/Data/Axis plot:	<A>
Plot Y vs. Index/X:	<X>
X Label:	< X-axis >
Y Lebel:	< Relative Intensity >
Quit/Continue:	<C>

DRAW: [F] R ALL

DATA DRAW

Full/Top/Bottom:	<F>
Last listen Index/X:	<X>
Y array:	<R>
X array:	<T>
Overlay plot (Y/N):	<N>
Quit/Continue:	<C>

DEVICE CLEAR

INITIALIZED

GOTO LOCAL

END ROUTINE

GET-WAVE

This subroutine collects data from the oscilloscope.

Routine Name: < GET-WAV >

Comment: < GETS WAVE FROM SCOPE >

No. of Iteration:	< 1 >
SQR (Y/N):	<N>
Key typed (Y/N):	<N>
Comparison (Y/N):	<N>
Edit Command (Y/N):	<Y>

SET DEVICE: SCOPE

TALK:

LITERAL: :WAV:FORM WORD

LITERAL: :WAV:DATA?

Segment Terminator

ASCII Value (No. / None):	<N>
Send EOI with last byte?	<Y>
Quit / Continue:	<C>

WAIT: DELAY

Wait for SQR (Y/N):	<N>
Wait for key (Y/N):	<N>
Wait for time (Sec.):	< 30.0 >

LISTEN:

WASTE BASKET

VARIABLE R

Name of variable:	<R>
Append or Overwrite:	<O>
ASCII or Binary:	<A>
Integer or Real:	<R>
ASCII element separator:	< 44 >
Segment Terminator	
ASCII EOS value (No./None):	< 10 >
Send EOI with last byte?	<Y>
Quit/Continue:	<C>

WAIT: DELAY

Wait for SQR (Y/N):	<N>
Wait for key (Y/N):	<N>
Wait for time (Sec.):	< 30.0 >

COMMAND: R < 1,A > STORE R

WAIT: DELAY

Wait for SQR (Y/N):	<N>
Wait for key (Y/N):	<N>
Wait for time (Sec.):	< 30.0 >

GOTO LOCAL

END ROUTINE

SCALE-1

This subroutine sets the vertical scale which corresponds to relative image intensity.

Routine Name: < SCALE-1 >

Comment: < SET VOLT SCALE >

No. of Iteration:	< 1 >
SQR (Y/N):	<N>
Key typed (Y/N):	<N>
Comparison (Y/N):	<N>
Edit Command (Y/N):	<Y>

TALK:

LITERAL: :WAV:YREF?

Segment Terminator

ASCII Value (No. / None):	<N>
Send EOI with last byte?	<Y>
Quit / Continue:	<C>

WAIT: DELAY

Wait for SQR (Y/N):	<N>
Wait for key (Y/N):	<N>
Wait for time (Sec.):	< 30.0 >

LISTEN:

VARIABLE S

Name of variable:	<S>

Append or Overwrite: <O>

ASCII or Binary: <A>

Integer or Real: <R>

ASCII element separator: < 44 >

Segment Terminator

ASCII EOS value (No./None): < 10 >

Send EOI with last byte? <Y>

Quit/Continue: <C>

COMMAND: S [I] STORE B

WAIT: DELAY

Wait for SQR (Y/N): <N>

Wait for key (Y/N): <N>

Wait for time (Sec.): < 30.0 >

TALK:

LITERAL: :WAV:YINC?

Segment Terminator

ASCII Value (No. / None): <N>

Send EOI with last byte? <Y>

Quit / Continue: <C>

WAIT: DELAY

Wait for SQR (Y/N): <N>

Wait for key (Y/N): <N>

Wait for time (Sec.): < 30.0 >

LISTEN:

VARIABLE S

Name of variable: <S>

Append or Overwrite: <O>

ASCII or Binary: <A>

Integer or Real: <R>

ASCII element separator: < 44 >

Segment Terminator

ASCII EOS value (No./None): < 10 >

Send EOI with last byte? <Y>

Quit/Continue: <C>

COMMAND: S [I] STORE C

WAIT: DELAY

Wait for SQR (Y/N): <N>

Wait for key (Y/N): <N>

Wait for time (Sec.): < 30.0 >

TALK:

LITERAL: :WAV:YOR?

Segment Terminator

ASCII Value (No. / None): <N>

Send EOI with last byte? <Y>

Quit / Continue: <C>

WAIT: DELAY

Wait for SQR (Y/N): <N>

Wait for key (Y/N): <N>

Wait for time (Sec.): < 30.0 >

LISTEN:

VARIABLE S

Name of variable:	<S>
Append or Overwrite:	<O>
ASCII or Binary:	<A>
Integer or Real:	<R>
ASCII element separator:	< 44 >
Segment Terminator	
ASCII EOS value (No./None):	< 10 >
Send EOI with last byte?	<Y>
Quit/Continue:	<C>

COMMAND: S [I] STORE D

WAIT: DELAY

Wait for SQR (Y/N):	<N>
Wait for key (Y/N):	<N>
Wait for time (Sec.):	< 30.0 >

COMMAND: R B - C * D + STORE R

WAIT: DELAY

Wait for SQR (Y/N):	<N>
Wait for key (Y/N):	<N>
Wait for time (Sec.):	< 30.0 >

GOTO LOCAL

END ROUTINE

SCALE-2

This subroutine sets the horizontal time scale which corresponds to the X-axis.

Routine Name: < SCALE-2 >

Comment: < SET TIME SCALE >

No. of Iteration:	< 1 >
SQR (Y/N):	<N>
Key typed (Y/N):	<N>
Comparison (Y/N):	<N>
Edit Command (Y/N):	<Y>

TALK:

LITERAL: :WAV:XREF?

Segment Terminator

ASCII Value (No. / None):	<N>
Send EOI with last byte?	<Y>
Quit / Continue:	<C>

WAIT: DELAY

Wait for SQR (Y/N):	<N>
Wait for key (Y/N):	<N>
Wait for time (Sec.):	< 30.0 >

LISTEN:

VARIABLE S

Name of variable:	<S>

Append or Overwrite: <O>

ASCII or Binary: <A>

Integer or Real: <R>

ASCII element separator: < 44 >

Segment Terminator

ASCII EOS value (No./None): < 10 >

Send EOI with last byte? <Y>

Quit/Continue: <C>

COMMAND: S [I] STORE B

WAIT: DELAY

Wait for SQR (Y/N): <N>

Wait for key (Y/N): <N>

Wait for time (Sec.): < 30.0 >

TALK:

LITERAL: :WAV:XINC?

Segment Terminator

ASCII Value (No. / None): <N>

Send EOI with last byte? <Y>

Quit / Continue: <C>

WAIT: DELAY

Wait for SQR (Y/N): <N>

Wait for key (Y/N): <N>

Wait for time (Sec.): < 30.0 >

LISTEN:

VARIABLE S

Name of variable:	<S>
Append or Overwrite:	<O>
ASCII or Binary:	<A>
Integer or Real:	<R>
ASCII element separator:	< 44 >
Segment Terminator	
ASCII EOS value (No./None):	< 10 >
Send EOI with last byte?	<Y>
Quit/Continue:	<C>

COMMAND: S [I] STORE C

WAIT: DELAY

Wait for SQR (Y/N):	<N>
Wait for key (Y/N):	<N>
Wait for time (Sec.):	< 30.0 >

TALK:

LITERAL: :WAV:XOR?

Segment Terminator	
ASCII Value (No. / None):	<N>
Send EOI with last byte?	<Y>
Quit / Continue:	<C>

WAIT: DELAY

Wait for SQR (Y/N):	<N>
Wait for key (Y/N):	<N>
Wait for time (Sec.):	< 30.0 >

LISTEN:

VARIABLE S

Name of variable:	<S>
Append or Overwrite:	<O>
ASCII or Binary:	<A>
Integer or Real:	<R>
ASCII element separator:	< 44 >
Segment Terminator	
ASCII EOS value (No./None):	< 10 >
Send EOI with last byte?	<Y>
Quit/Continue:	<C>

COMMAND: S [I] STORE D

WAIT: DELAY

Wait for SQR (Y/N):	<N>
Wait for key (Y/N):	<N>
Wait for time (Sec.):	< 30.0 >

COMMAND: A N:RAMP B - C * 8 + STORE T

WAIT: DELAY

Wait for SQR (Y/N):	<N>
Wait for key (Y/N):	<N>
Wait for time (Sec.):	< 30.0 >

GOTO LOCAL

END ROUTINE

APPENDIX C

PROCESSING OF THE HOLOGRAMS

The hologram were processed with the chemicals from **LAZA holograms**; using the prescribed processing method as following.

i - RLD1 developer part A was developed according to the instructions as given in information sheet LI21 by **LAZA holograms**, where the RLD1 developer part B was made up as normal.

ii - 150ml of part A and 150ml of part B of RLD1 developer were taken in two different bottles. The two parts of the developer were mixed just before the use, in one tray and the exposed holographic plate was placed in the tray and rocked gently from side to side for about 2min. The two parts of the developer were mixed just before the use in the dark and as turn brown due to oxidation in air hence were discarded after the processing of two holographic plates. It was highly desirable to maintain the temperature of the solution at $20^{o}C$, the tray of the mixed solution was placed in a

container of hot water at suitable temperature.

iii- The holographic plates were washed in running water for about 5min to remove all the traces of the developer and after washing thoroughly they were placed in a standard Kodak fixer for about 2min.

iv- After fixing the holographic plates, they were washed again in running water for about 5min., and rinsed with and Agfa wetting agent for about 30s which allowed them for even "streak free" squeegeeing before drying.

APPENDIX D

TECHNICAL DETAILS OF THE BK7 SUBSTRATE

The BK7 substrate is made with special annealed platinum free BK7 material. The technical details of the substrate are as following.

Diameter tolerance:	0.0mm to 0.15mm
Thickness tolerance:	± 0.15mm
Parallelism:	2 arc minutes
Surface quality:	Ultra fine laser polish.
	Scratch dig 10 - 5.
Surface flatness:	λ/10 over central 90% of the
(Both Sides)	full aperture at 633nm.

APPENDIX E

IMAGE INTENSITY IN BELZ AND SHOFNER'S IMAGING MODEL [From Belz R. A. (1971)]

If a circular opaque disc of radius *a* is illuminated with a plane wave ofcoherent light (centeral portion of the collimated laser beam) as shown in figure (E-1), the intensity in the hologram plane at a distance Z_1 is givn by.

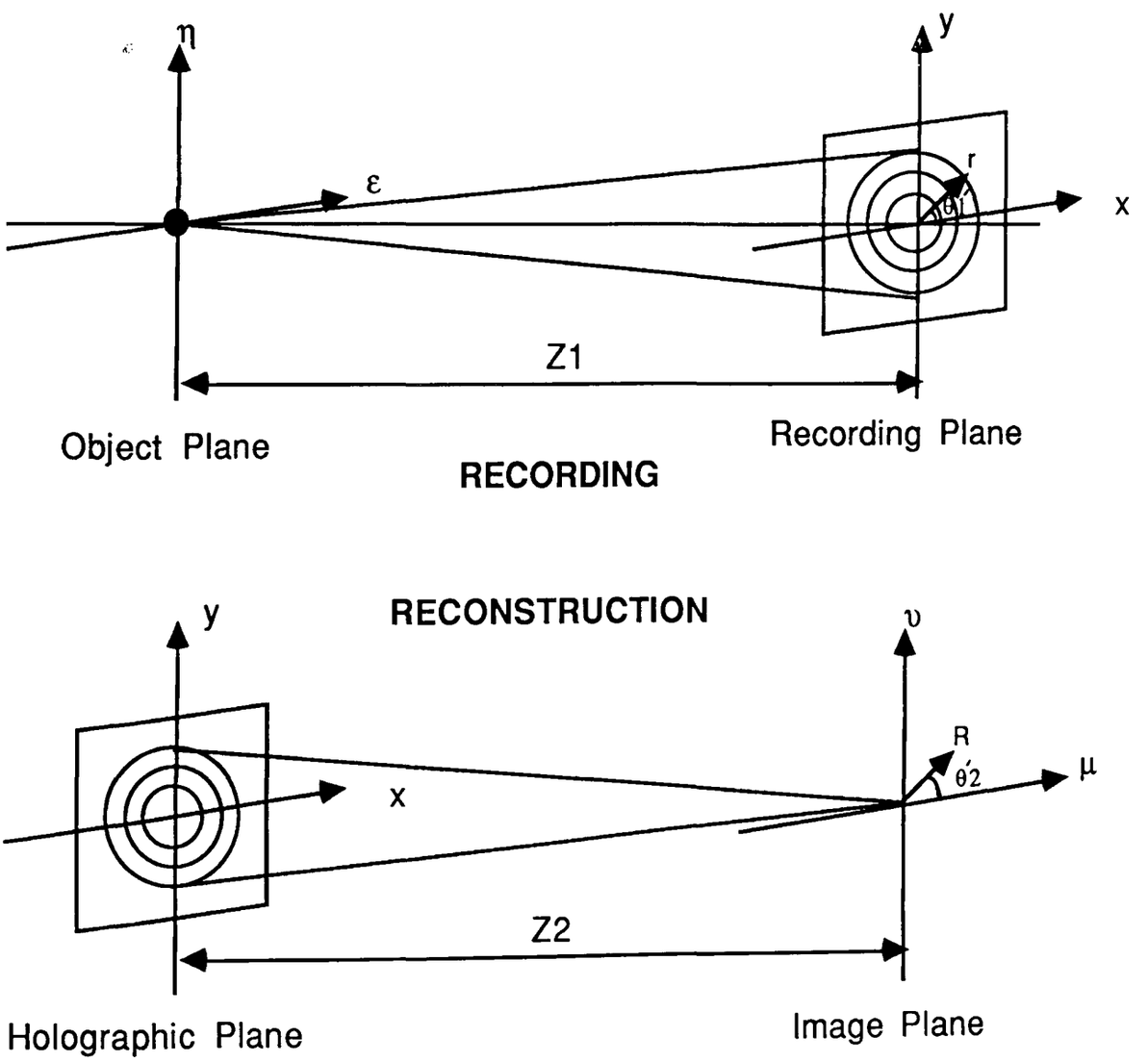

FIG. (E-1) Recording and reconstruction of in-line hologram

$$I_{(\mu,\upsilon)} = 1 + \frac{a^2}{r^2} J_1^2\left(\frac{kar}{Z_1}\right) - \frac{a}{r} J_1\left(\frac{kar}{Z_1}\right) \sin\left(\frac{kr^2}{2Z_1}\right) \quad ...(E.1)$$

The third term in this equation represents the coherence interference of the object wave and the reference wave and is responsible for the reconstruction of images from the hologram. This term mey be wrtitten in complex form by using the relation.

$$\sin\theta = \frac{\exp(i\theta) - \exp(-i\theta)}{2i}$$

As we are interested in the real image only which is represented by a negative exponent, thus the term responsible for the reconstruction of real image may be written as.

$$I_A = -i \frac{a}{2r} J_1\left(\frac{kar}{Z_1}\right) \exp\left(-i \frac{kr^2}{2Z_1}\right) \quad ...(E.2)$$

If the hologram is illuminated with the same wave which was used for recording, the reconstructed field at a distance Z2 is given by:

$$\Psi_{(\mu,\upsilon)} = \frac{-i}{\lambda Z_2} \exp\left[i k\left(Z_2 + \frac{R^2}{2Z_2}\right)\right] \int_0^{\bar{r}} I_A . \exp\left[i k\left(\frac{r^2}{2Z_2} - \frac{r.R}{Z_2}\right)\right] d\bar{r} \quad .....(E.3)$$

But

$d\bar{r} = r\, dr d\theta$ and $r.R = \cos(\theta_1' - \theta_2')$

Therefore equation (E.3) may be written as:

$$\psi_{(\mu,\upsilon)} = \frac{-i}{\lambda Z_2} \exp[i\,k(Z_2 + \frac{R^2}{2Z_2})] \int_0^r I_A \exp(i\,k\frac{r^2}{2Z_2}) \left[\int_0^{2\pi} i\,k\,\frac{rR}{Z_2} \cos(\theta_1' - \theta_2')d\theta \right] dr \quad \text{.....(E.4)}$$

But

$$\int_0^{2\pi} i\,k\,\frac{rR}{Z_2} \cos(\theta_1' - \theta_2')d\theta = 2\pi J_o(\frac{krR}{Z_2})$$

The equation (E.4) may be written as:

$$\psi_{(\mu,\upsilon)} = \frac{-i}{\lambda Z_2} \exp[i\,k(Z_2 + \frac{R^2}{2Z_2})] \int_0^r I_A\, 2\pi\, J_o(\frac{krR}{Z_2}) \exp(i\,k\frac{r^2}{2Z_2})\, dr \quad \text{.....(E.5)}$$

The reconstructed field can be determined by subsituting the I_A from equation (E.2) in equation (E.5) and is given by:

$$\psi_{(\mu,\upsilon)} = \frac{2\pi}{\lambda Z_2} \exp[i\,k(Z_2 + \frac{R^2}{2Z_2})] \int_0^r \frac{a}{2r} J_1(\frac{kar}{Z_1})\; J_o(\frac{krR}{Z_2}) \exp[i\;\frac{kr^2}{2}(\frac{1}{Z_1} - \frac{1}{Z_2})]\, dr \quad \text{.....(E6)}$$

To reduce the terms in the above equation suppose that:

$$\frac{2\pi}{\lambda Z_2} \exp[i\,k(Z_2 + \frac{R^2}{2Z_2})] = C$$

Similarly using Euler's equation [$i\,\theta$ = cos θ - i sin θ] it can be written that:

$$\exp[i\;\frac{kr^2}{2}(\frac{1}{Z_1} - \frac{1}{Z_2})] = \cos[\frac{kr^2}{2}(\frac{1}{Z_1} - \frac{1}{Z_2})] - i\,\sin[\frac{kr^2}{2}(\frac{1}{Z_1} - \frac{1}{Z_2})]$$

The reconstructed field at a distance Z2 ca be obtained given by subsituting these values in equation (E.6) and is given by:

$$\psi_{(\mu,\upsilon)} = C\int_0^r \frac{a}{2r} J_1\left(\frac{kar}{Z_1}\right) J_0\left(\frac{krR}{Z_2}\right)\left[\cos\left[\frac{kr^2}{2}\left(\frac{1}{Z_1}-\frac{1}{Z_2}\right)\right] - i\sin\left[\frac{kr^2}{2}\left(\frac{1}{Z_1}-\frac{1}{Z_2}\right)\right]\right] dr \quad ...(E.7)$$

Similarly:

$$\overset{*}{\psi}_{(\mu,\upsilon)} = C\int_0^r \frac{a}{2r} J_1\left(\frac{kar}{Z_1}\right) J_0\left(\frac{krR}{Z_2}\right)\left[\cos\left[\frac{kr^2}{2}\left(\frac{1}{Z_1}-\frac{1}{Z_2}\right)\right] + i\sin\left[\frac{kr^2}{2}\left(\frac{1}{Z_1}-\frac{1}{Z_2}\right)\right]\right] dr \quad ...(E.8)$$

The reconstructed image intensity caqn be determined by the relation $I_{(\mu.\upsilon)} = \psi^*_{(\mu.\upsilon)} \cdot \psi_{(\mu.\upsilon)}$ and is given by:

$$I_R = C^2\left\{\begin{array}{l}\left[\int_0^r J_1\left(\frac{kar}{Z_1}\right) J_0\left(\frac{kRr}{Z_2}\right)\cos\left[\frac{kr^2}{2}\left(\frac{1}{Z_1}-\frac{1}{Z_2}\right) dr\right]\right]^2 \\ +\left[\int_0^r J_1\left(\frac{kar}{Z_1}\right) J_0\left(\frac{kRr}{Z_2}\right)\sin\left[\frac{kr^2}{2}\left(\frac{1}{Z_1}-\frac{1}{Z_2}\right) dr\right]\right]^2\end{array}\right\} \quad .....(3.1.1)$$

REFERENCES

Abramowitz and Stegun (1970)
Handbook of mathematical functions,
Doven, New York, USA. Table: 25.4 P.919

Agfa-Gevaert
DIS/NDT Technical Information.

Asyst Software technologies Inc.
100 Coporate woods, Rochester, NY146321, USA.

Belz R. A (1971)
An investigation of the real image reconstructed
by an in line Fraunhofer hologram aperture limited
by film effects.
University of Tennessee, USA. Ph. D Thesis

Belz R. A. and Shofner F. M. (1972)
Applied Optics (1972), Vol. 11, No. 10 P.2215-2222

Biederman K. and Johanssom S. (1975)
Journal of Physics E: Scientific Instruments (1975)
Vol. 8 P.751-757

Bracewell R. N. (1978)
The Fourier Transform and its Application
McGraw-Hill Kogahusha Ltd., Tokyo

Butters J. N. (1971)
Holography and its Technology, Peter Peregrinus Ltd.
Printed on behalf of IEE.

Cartwright S. L; Dunn P; Thompson B. J. (1980)
Optical Engineering (1980), Vol. 19, No. 5 P. 727-733

Collier R. J (1971)
Optical Holography, Academic Press, New York P.269

Datasight Ltd.
Alma Road, Podera end, Endfield, Middx., EN3 7BB, UK.

DeVelis J. B; Parrent G. B; Thompson B. J (1966)
Journal of Optical Society of America (1966)
Vol. 56, No. 4 P. 423-427

Dunn P. and Thompson B. J. (1982)
Optical Engineering (1982), Vol. 21, No. 2 P. 327-332

Hariharan P. (1989)
Optical Holography, Cambridge University Press
New York, Port Chester, Melburn, Sydney. P.91

Hobson P. R (1984)
The design and construction of a holographic
film mechine for the heavy bubble chamber
HOBC and a determination of the crossection
for CHARM production by 360GEV protons.
University College London, UK. Ph. D Thesis. P.61

Hobson P. R (1988)
Journal of Physics E: Scientific Instruments, Vol. 21, P.139-145

LAZA HOLOGRAMS
Technical information sheets: LI21, LI22, LI23, LI24, LI25
47 Alpine Street Reading, RG1 2PY, UK.

Lehman M. (1970)
Holography, The Focal Press, London, New York.

Micro Control (1988-1989)
Technical Information Catalogue.
4320 First Avenue, Newbury Bisiness park,
London Road, Newbury RG13 2PZ Berks, UK. P.257

Nassentein H, Dedden H. (1969)
Photographic. Society Engineering. (1969) P.194-199

Ozkul C. (1986)
Optics and Laser Technology (1986), Vol. 11 P. 36-38

Parrent G. B; Thompson B. J. (1964)
Optica Acta (1964), Vol. 11 P.183-193

Murata K., Fujiwara H (1970)
Engineering uses of holography
Edited by Robert E. R. (1970) P. 289-300

Schaub A, Alexander D. R, Barton J. B (1989)
Optical Engineering (1989), Vol. 28, No. 5 P. 565-571

Thompson B. J. (1965)
Japan Journal Applied Physics (1965) Suppl.14 P.302

Thompson B. J and Mayak (1985)
SPIE, Particle Sizing and Spray Analysis, Vol 573 P.12-20

Tayler G. A. and Thompson B. J (1976)
Optica Acta (1976), Vol. 23, No. 9 P.665-700

Van Ligten R. F. (1966)
Journal of Optical Society of America (1966)
Vol. 56, No. 1 P.1-9
or Vol. 56, No. 8 P.1009-1014

Vikram C. S. and Billet M. L (1984-a)
Applied Optics (1984), Vol. 23, No. 18 P.3091-3094

Vikram C. S. and Billet M. L (1984-b)
Applied Physics B (1984), Vol. 23 P.149-153

Vikram C. S. and Billet M. L (1984-c)
Applied Optics (1984), Vol. 23, No. 12 P.1995-1998

Witherow W. K. (1979)
Optical Engineering (1979), Vol.18, No. 3 P.249-255

Wolf R. N, Marchend E. W, Depalma J. J (1968)
Journal of Optical Society of America (1968)
Vol. 58 , No. 9 P.1245-1256

Young M. (1986)
Optics and Lasers, Springer Verlag P.24